OPTICAL STUDIES OF THE MESOSPHERIC REGION

By

Jonathan Woithe, B.Sc. (Hons)

Thesis

submitted for the degree of

DOCTOR OF PHILOSOPHY

at the

UNIVERSITY OF ADELAIDE

(Department of Physics and Mathematical Physics)

November 2000

Contents

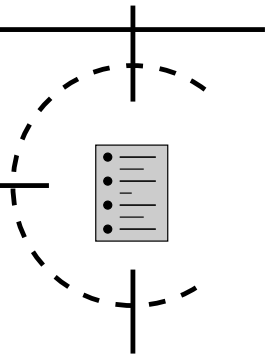

Abstract **vii**

Originality declaration **ix**

Acknowledgements **xi**

List of Figures **xvi**

List of Tables **xvii**

1 Introduction **1**

1.1 The earth's atmosphere 1

1.2 Motivation and thesis overview 3

2 Background and Theory **7**

2.1 Atmospheric airglow 7

2.2 Origin of the airglow 8

2.2.1 OH emission 9

2.2.2 OI emission 11

2.3 Atmospheric gravity waves 12

2.4 Gravity wave effects on the atmosphere 17

2.4.1 Airglow intensity . . . 17
2.4.2 Background winds . . . 18
2.5 Previous studies . . . 20
2.5.1 Historical development . . . 20
2.5.2 Recent gravity wave research . . . 22

3 Equipment **27**
3.1 Buckland Park three field photometer . . . 27
3.1.1 Physical description . . . 27
3.1.2 Control system . . . 30
3.1.3 Instrument operation . . . 33
3.1.4 Operational difficulties . . . 35
3.2 Davis three field photometer . . . 40
3.2.1 Differences from Buckland Park photometer . . . 40
3.2.2 Instrument operation . . . 42
3.3 Buckland Park MF radar . . . 42
3.3.1 Hardware . . . 42
3.3.2 Software improvements . . . 46
3.3.3 Spaced antenna operation . . . 47
3.3.4 Doppler beam steering operation . . . 47
3.3.5 Operational difficulties . . . 48
3.4 Davis MF radar . . . 50

4 Data processing and analysis **51**
4.1 Photometer data . . . 51
4.1.1 Data preprocessor . . . 52
4.1.2 Background filter techniques . . . 55
4.1.2.1 Subtraction of an average background . . . 56
4.1.2.2 Fourier amplitude filter . . . 57
4.1.2.3 Fourier phase filter . . . 62

4.1.2.4 Wavelet filter method 62
4.1.2.5 Filter method summary 71
4.1.3 Cross spectral analysis 72
4.1.4 Uncertainty estimations 78
4.1.5 Instrumental selection 80
4.1.6 Davis photometer data 81
4.2 MF radar Doppler analysis 84
4.3 MF radar spaced antenna analysis using FCA 87
4.4 Intrinsic wave parameters from optical data 90
4.5 Flux estimation from optical data 91
4.6 Long-term analysis 95
4.6.1 Lomb analysis 99
4.6.2 Cross spectral calculations 102

5 Short period gravity wave analysis 105
5.1 Acquisition of wave parameters 105
5.2 Observed wave parameters 111
5.3 Intrinsic wave parameters 116
5.4 Optical flux estimations 130
5.4.1 Original Swenson approach 130
5.4.2 Refinement of method 132
5.4.3 Revised flux estimates 136
5.4.4 Considerations arising from the method 143
5.5 Summary 145

6 Long-term airglow variability 147
6.1 Optical intensity data 147
6.1.1 Bright nights 155
6.1.2 Harmonic analysis 155
6.2 Variance of optical intensity 164

6.3 Spectral variations 174
6.4 MF Wind data 178
6.5 Radar–photometer intercomparison 186
6.5.1 Cross spectral comparisons 190
6.6 Summary 193

7 Conclusions and further work **195**
7.1 Gravity wave analysis 195
7.2 Airglow variability 197
7.3 Further research 199

A Davis MF radar **203**
A.1 Hardware 203
A.2 Radar operation 204

B Trends of airglow imager obervations **205**

C Analysis and interpretation of gravity waves **213**

References **233**

Abstract

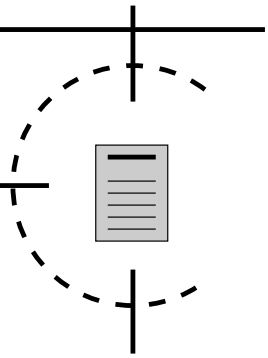

A three-field photometer has been employed at the University of Adelaide's Buckland Park field site to collect optical observations of the 557.7nm OI and 730nm OH airglow emissions. Data have been collected on an almost continuous basis since May 1995 through to May 2000, with observations made whenever the moon was not up.

Techniques and analysis procedures have been developed which allow routine extraction of the parameters of gravity waves observed each night. A cross-spectral analysis was performed on processed data from the photometer to identify short period ($\lesssim$3 hours) wave activity on nights where the impact of clouds on the data was minimal. The resulting wave parameters are analysed for seasonal variability and used to build up a climatology of wave parameters over the 5 years of observation. No consistent seasonal variation was observed, although there was a strong eastward perference to the wave's propagation direction. Implications of this finding are discussed.

A co-located MF radar has been operating in spaced antenna mode providing wind data concurrent with the optical observations for most of the acquisition period. When available the wind data allowed calculation of the intrinsic parameters for waves identified in the optical data. The seasonal variablility of these parameters was investigated. An evaluation of energy and momentum fluxes estimated using the method of Swenson & Liu (1998) was carried out. Approximations made in this method were found to be inappropriate for the waves detected by the photometer, and a refined procedure was

therefore developed. This gave more realistic results, although large number of physically unreasonable momentum flux measurements were reported. Possible reasons for these were explored, and the need for further investigations emphasised.

The five year dataset also allowed investigation of the long-term behaviour of the airglow. Both the intensity and variance were analysed using the Lomb-Scargle method across the complete dataset to identify the dominant periods present. Following similar treatment, the MF spaced antenna winds were compared with the optical results; this utilised a complex spectrum extension to the basic Lomb algorithm. Seasonally related periodicities of two years, one year, one half of a year and one third of a year were observed in the optical data, along with a possible signature of a five and a half year period potentially linked to the eleven year solar cycle. The radar data did not have stong signatures of the one third of a year periodicity although the presence of an five and a half year periodicity could not be ruled out. Gravity wave activity, as measured by the optical intensity variance, reached a maximum during autumn with a secondary maximum occurring in spring. The annual variability of the wave spectrum detected by the photometer was also studied which showed a falloff in the wave energy at short periods (less than thirty minutes) during autumn and spring. This suggested that the enhanced wave activity at these times consisted mainly of waves with periods greater than thirty minutes.

Originality declaration

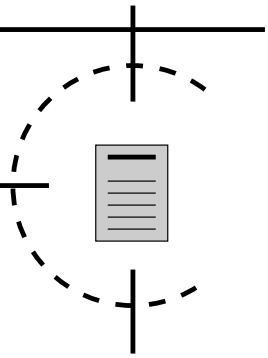

This work contains no material which has been accepted for the award of any other degree or diploma in any university or other tertiary institution and, to the best of my knowledge and belief, contains no material previously published or written by another person, except where due reference has been made in the text.

I give consent to this copy of my thesis, when deposited in the University Library, being available for loan and photocopying.

Signed: ..... dated: .....

Jonathan Woithe, B.Sc. (Hons)

Acknowledgements

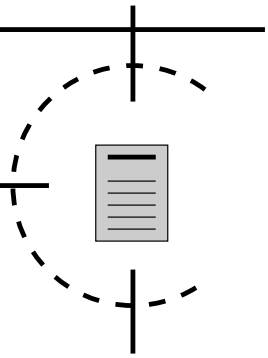

This thesis is the culmination of four years' work carried out between 1996 and 2000, and indirectly, all the years of my life preceding it. The teaching afforded by many experiences and people in the years before its commencement and during the candidature have helped in many ways during this PhD. Everyone who has had any part to play in helping me bring this volume to its eventual fruition is to be thanked for their support. In the interests of brevity and to keep the size of this thesis within reasonable limits, I would like to particularly thank the following people (in no particular order):

- my supervisor, Dr Iain Reid, for hours of useful discussions and general guidance over the last four years;

- Dr Bob Vincent, for numerous clarifications and other helpful assistance as the need arose;

- fellow students in the Atmospheric Group during my time here, many of whom have now finished or are about to — Daniel Badger, Steven Grant, Bridget Hobbs, Ali Kazempo, Andrew MacKinnon, Sujata Kovalam, Rupa Vuthaluru and Florian Zink — I would say that together we have managed to remain sane despite the best efforts of the university lifestyle, although others might well disagree;

- Mike Shorthose: for assistance with some electronic aspects of the photometer's operation, for putting up (and generally agreeing) with my numerous put-downs of a certain computer operating system from Redmond, California;

- Bob Hurn whose help with debugging a variety of photomultiplier faults has been appreciated;

- Authors of Linux-based free software everywhere, including but not limited to Linus Torvalds and the kernel team, the XFree86 guys, Donald Knuth and the LaTeX2e people, Robert Maier of GNU PlotUtils fame and the wxWindows developers: for making it possible to conduct an entire PhD on a stable, dependable computer platform without having to worry about when the next crash will come;

- Dallas Kirby, Lyn Birchby and Carmel Palumbo for being friendly, efficient administration people, of which there are far too few; and

- Malcolm Kirby and Alex Didenko, for checking up on equipment at Buckland Park and carrying out often obscure instructions delivered by the tenuous telephone link, thereby saving me ninety minutes of driving for the sake of a five minute activity.

In addition to the above, special thanks is due to my family: mum and dad for giving me valued opportunities and guidance during my initial years on this planet; my wife Kylie, for love, understanding, companionship, for being willing and able to proof this thesis, and for many other things which could easily fill a second thesis volume if written down; and my brothers Brendan and Adrian, for their special and unique contributions to my life experience. Finally, and most importantly, thanks to God for making me what I am, giving me the abilities I have, and for being my friend and Saviour.

Jonathan Woithe

November 2000

List of Figures

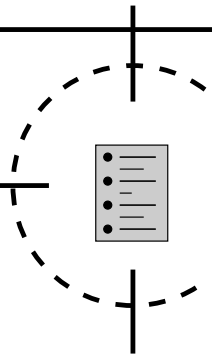

1.1 The earth's atmosphere 2

3.1 Schematic depiction of the Buckland Park three field photometer. . . . 28

3.2 Arrangement of filters on the filter wheel 30

3.3 System block diagram of the three field photometer 31

3.4 System flowchart for control of the photometer 34

3.5 Schematic diagram of revised lightning detector 38

3.6 Davis three field photometer field arrangement 41

3.7 The Buckland Park MF antenna array 44

4.1 Data from 2 August 1996 showing a peak of 2 minutes' duration 53

4.2 Typical performance of the average background subtraction 57

4.3 Detail of data and average background signals 58

4.4 Simulated photometer data used to evaluate filter methods 59

4.5 Typical performance of the Fourier amplitude filter 60

4.6 Performance of the Fourier amplitude filter on uncontaminated data . . 61

4.7 Typical performance of the Fourier phase filter 63

4.8 Performance of the Fourier phase filter on uncontaminated data 64

4.9 Schematic representation of the functionality of the wavelet filter. . . . 67
4.10 Typical performance of wavelet based filter 69
4.11 Response of the wavelet filter to uncontaminated data 70
4.12 Filter performance on contaminated data shown by wavelet transforms 73
4.13 Filter performance on uncontaminated data shown by wavelet transforms 74
4.14 Method of calculating phase velocities given three component velocities 76
4.15 Example of typical Davis photometer data 82
4.16 15 minute averaged 730nm intensity data from 1996 at Davis 83
4.17 Illustration showing estimation method for average 730nm intensity. . . 92
4.18 Difference between the alternative methods of amplitude estimation . . 96
4.19 Arrangement of 2D data array used for long-term analysis 98

5.1 Typical uncontaminated photometer timeseries 106
5.2 Effect of cloud on preprocessed photometer time series data 107
5.3 Cloud effects on wavelet-filtered data 108
5.4 Typical phase velocity plot from photometer data 109
5.5 Wavelet-filtered data for a cloudless night 110
5.6 Summary of all observed wave parameters 112
5.7 Summary of historical wave parameters inferred from optical data . . . 113
5.8 Composite plot of data shown in figure 5.7 114
5.9 Occurrence histograms of summer gravity wave parameters 117
5.10 Occurrence histograms of autumn gravity wave parameters 118
5.11 Occurrence histograms of winter gravity wave parameters 119
5.12 Occurrence histograms of spring gravity wave parameters 120
5.13 Summary of intrinisic wave parameters from photometer observations . 122
5.14 Histograms of summer gravity wave intrinsic parameters 123
5.15 Histograms of autumn gravity wave intrinsic parameters 124
5.16 Histograms of winter gravity wave intrinsic parameters 125
5.17 Histograms of spring gravity wave intrinsic parameters 126

5.18 Vertical wavelength vs horizontal period for all waves observed 129
5.19 Momentum flux estimations for all identified waves 131
5.20 Polar plot of energy and momentum flux derived from optical data . . . 133
5.21 Revised momentum fluxes of waves from the 730nm emission 137
5.22 Revised polar plot of energy and momentum flux from 730nm data . . 138
5.23 Energy and momentum flux greater than 0.1mWm^{-2} and 1m^{2}s^{-2} respectively 140
5.24 Momentum flux distribution, and average flux within 5km vertical wavelength bins 142
5.25 Seasonal variation of zonal and meridional momentum flux components 144

6.1 Overview of 557.7nm intensity data recorded at Buckland Park 148
6.2 Overview of 730nm intensity data recorded at Buckland Park 149
6.3 Three hour averaged 557.7nm intensity data from Buckland Park . . . 152
6.4 Three hour averaged 730nm intensity data from Buckland Park 153
6.5 Normalised Lomb periodogram of 557.7nm OI intensity data 156
6.6 Normalised Lomb periodogram of data with moon-induced gaps present 158
6.7 Normalised Lomb periodogram of data without moon-induced gaps . . 159
6.8 Three hour averaged OI data with fitted harmonic timeseries 162
6.9 Comparison between 10.7cm solar flux and 557.7nm intensity 165
6.10 Normalised Lomb periodogram of 730nm airglow intensity 166
6.11 Variance of 557.7nm photometer data relative to overall mean 167
6.12 Periodogram of 557.7nm variance 169
6.13 557.7nm variance data relative to daily mean intensities 170
6.14 730nm variance data relative to daily mean intensities 171
6.15 Lomb periodogram of 557.7nm local variance data 172
6.16 Lomb periodogram of 730nm local variance data 173
6.17 Example half-month averaged photometer spectrum 175
6.18 Normalised averaged photometer spectra from Buckland Park 177

6.19 84–88km wind components 179
6.20 92–96km wind components 180
6.21 Lomb periodogram of 84–88km wind components 181
6.22 Lomb periodogram of 92–96km wind components 182
6.23 Eight-day averaged variance of 84–88km wind components 184
6.24 Eight-day averaged variance of 92–96km wind components 185
6.25 Periodogram of MF wind variance between 84km and 88km 187
6.26 Periodogram of MF wind variance between 92km and 96km 188
6.27 Example cross spectrum obtained using the Lomb method 191

A.1 Davis MF radar antenna arrangement 204

List of Tables

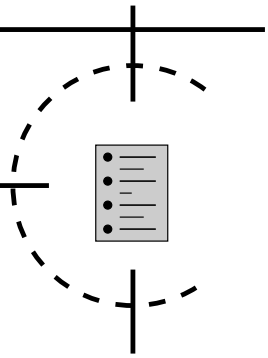

5.1 Assignment of months to seasons used in seasonal parameter plots . . . 116

5.2 Number of gravity wave events observed per season 116

5.3 Number of gravity wave events observed per season for which background wind data (and hence intrinsic parameters) were available. . . . 121

6.1 Cross spectral phases: 557.7nm vs 92km–98km winds 192

6.2 Cross spectral phases: 730nm vs 84km–90km winds 192

6.3 Cross spectral phases: 557.7nm vs 730nm 192

chapter 1

Introduction

1.1 The earth's atmosphere

Over the past century we have become increasingly aware of the complexity and diversity of dynamical processes within the earth's atmosphere. In recent times issues such as the 'greenhouse effect' and drops in ozone abundance over the polar regions have received extensive press coverage, bringing some of these to the attention of the general public. Even though our scientific understanding of the atmosphere — its makeup and processes — have progressed dramatically over the last fifty years, it seems that there is still much which we do not know or do not fully understand.

Strictly speaking, the atmosphere extends many hundreds of kilometres out from the earth's surface, although for most practical purposes its range is limited to between 150km to 200km. The action of gravity means that the atmosphere is more dense at the surface and gets progressively rarified with increasing altitude. Furthermore, because the optical depth of the atmosphere changes according to the radiation being considered, various dissociative reactions occur at a range of heights, dependent on the optical depth encountered by the radiation required for each particular reaction. Thus a variety of reactions involving atmospheric constituents occur at different heights throughout the atmosphere. The radiative and chemical processes set up a temperature profile which is indicated in figure 1.1. This profile is often used

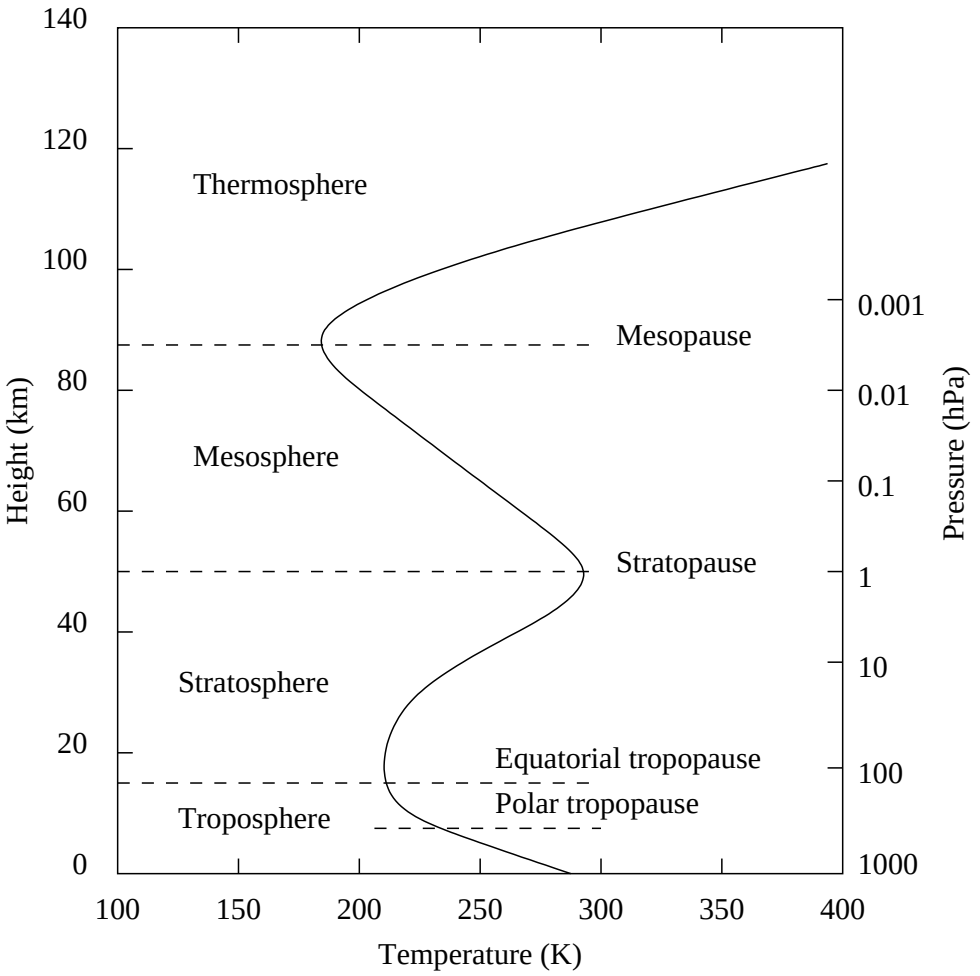

Figure 1.1: Schematic diagram of the earth's atmosphere showing an example temperature profile and indicating the different atmospheric regions.

to divide the atmosphere into different regions which are also indicated on figure 1.1. The boundaries between the atmospheric regions correspond to turning points in the temperature profile. Using temperature to classify the atmosphere is useful because many of the dynamic processes in the atmosphere (winds, for example) are driven at least partly by the atmosphere's temperature profile.

The lowest region of the atmoshere, the troposphere, extends from the surface to a height of around 10–15km and is the region we are most familiar with since it is directly measurable. Observable weather occurs in this region which is characterised by an almost constant rate of temperature decline with height. This profile is due

primarily to the convective cooling of the earth's surface which has the effect of heating the gases within the troposphere. The surface itself is heated by solar radiation. A secondary contribution to the profile is the heating caused by the absorption of infrared radiation by so-called 'greenhouse gases' (CO_2, CH_4, H_2O and others). The source of the infrared energy in this case is re-radiation from the earth's surface. The tropopause — a region of almost constant temperature — separates the troposphere from the stratosphere, which spans the altitude range between roughly twenty and fifty kilometres. Throughout the stratospheric region, the temperature increases with height until the stratopause is reached. The ozone layer is found in the stratosphere with the ozone volume mixing ratio reaching a maximum around the thirty five kilometre mark. It is the absorption of solar radiation by ozone which is the primary source of heating in the stratosphere and the region around the stratopause.

Above the stratopause is the mesosphere where the temperature again decreases with height. The mesosphere is the coldest region of the earth's atmosphere; the mesopause can reach temperatures as low as 180K. Radiative considerations like those which explain the temperature profiles of the troposphere and stratosphere do not completely explain the low temperatures encountered in the mesosphere and at the mesopause. Instead, one needs to invoke the action of waves and the results of momentum transfer in order to explain the mesospheric temperature profile which illustrates why a full understanding of these dynamic processes is required to explain even this apparently simple property. Above the mesopause the temperature begins to increase and continues to do so throughout the thermosphere, the uppermost atmospheric region.

1.2 Motivation and thesis overview

The subject of this thesis is the region surrounding the mesopause, namely the upper mesosphere and lower thermosphere. Many inter-related dynamical processes occur in this region with the behaviour, mechanism and significance of many still yet to

be fully understood. It is certainly known that activity in the mesopause region can have significant effects on the climatology of other atmospheric regions and so it is vital that mesospheric properties continue to be studied in order to build a complete understanding of the earth's atmosphere as a whole. This study aimed to add to this knowledge-base.

Many instruments are currently used to probe the upper atmosphere. Radars, lidars, all-sky imagers and photometers complement each other either through observation of different phenomena or different instrumental sensitivities, allowing a more representative picture of the atmosphere to be built up. The study reported in this thesis uses a three field photometer as the primary data source which, when compared to other upper atmospheric sensing equipment, is extraordinarily simple in both hardware requirements and operation. Despite this simplicity the instrument has the potential to make significant mesospheric data contributions, which has been demonstrated in this study. The nature of the photometer is such that it is feasible to have many instuments placed in isolated areas configured for autonomous operation giving greater geographic coverage than is possible with the more involved instruments. It is, however, important to fully understand the limitations and instrumental effects of the methods employed with this and similar equipment, and the exploration of this was also an important aspect of the work reported herein.

Chapter two of this thesis introduces gravity waves, one of the more important dynamical processes affecting the mesopause region. The two primary methods of observing the dynamics of this region, namely through airglow and wind variations, are also discussed along with a brief review of relevant literature to date.

Chapter three describes the equipment used in this mesopheric study, work carried out by the author on this equipment, and discusses a number of operational difficulties encountered during the running of the experiments. A discussion of the development and detail of data analysis methods used for this study follows in chapter four with some aspects of this being directly driven by some of the issues mentioned in chapter three.

Results of the study, their discussion and interpretation are presented in chapters five and six. Chapter five deals with the explicit measurement of gravity wave parameters while chapter six explores the long-term behaviour of the gravity wave field as a whole. Finally, chapter seven summarises the finding of this project and suggests the direction of possible further research.

Throughout this thesis, the uncalibrated optical emission brightness from the photometer has been refered to as 'intensity' in units of 'photon counts per second'. Additionally, when a concise unit was required for clarity, Hertz (Hz) was adopted with an intensity of 1Hz referring to '1 count per second'.

chapter 2

Background and Theory

2.1 Atmospheric airglow

Reports of light present in the night sky (what is now known as 'airglow') started appearing in literature around the end of the nineteenth century although records of polar aurora can be traced back to the first millenium (Chapman 1967). In part this was due to the airglow being much fainter than aurora and nowhere near as spectacular. Adding to the confusion of the time was that a number of spectral features observed in aurora were also present in the airglow. Many theories were put forward to explain the presence of this light, but it was not until 1933 that it was realised that the source was luminescence from within the earth's own atmosphere (Chapman 1967). The term 'airglow' was subsequently employed to describe all such atmospheric emissions. During the following years many features of the airglow spectrum were identified, but a complex infrared feature at 730nm remained unidentified until 1950 when Meinel (1950) showed that it could be attributed to the vibrational-rotational spectra of the OH molecule. This emission is often refered to as being from the Meinel OH bands. By 1961 knowledge of the originating molecules of airglow spectral features and their approximate heights was essentially complete (Chamberlain 1961) with mainly cosmetic improvements being made in later years as instrumentation was improved (see for example Broadfoot & Kendall (1968)). A notable exception was the discovery

in the mid-1990's of a previously undetected faint emission by Evans & Shepherd (1996) using the Wind Imaging Interferometer (WINDII) instrument on board the Upper Atmospheric Research Satellite.

Numerous techniques have been employed over the last century to observe and characterise the airglow, with some predating the realisation that the origin was in fact the earth's own atmosphere. The earliest work carried out in the early 1900's focused on the spectral features of the airglow in part due to a desire to investigate the similarities between the spectra of airglow and aurora. As early as 1915 it was found that the 557.7nm 'auroral' line was also present in airglow. However, numerous differences were also uncovered which made it increasingly likely that the two phenomena were fundamentally different in their excitation mechanism, even if some common molecules were involved.

Following the identification of the Meinel OH bands in the nineteen fifties interest in the airglow shifted somewhat to focus on the emission heights of the various features. The advent of rocket technology throughout the late nineteen fifties and into the nineteen sixties meant that in situ measurements of height profiles could be carried out both by manned and unmanned spacecraft (for example O'Brien 1967, Gulledge et al. 1968, Offermann & Drescher 1973) and such techniques have been continued to the present day. As technology has progressed the reliability of satellite-borne instrumentation has increased, which has allowed longer-term satellite-based studies to be carried out. These have been utilised to provide more spatial and temporal resolution to the knowledge-base of airglow height profiles (Shepherd et al. 1997, Zhang et al. 1998).

2.2 Origin of the airglow

The atmospheric airglow emissions originate from energy level transitions in excited molecules at various heights in the earth's atmosphere. The molecules are generally excited by photochemical reactions during daylight and as such the intensity of airglow

decreases during nighttime periods. However, sufficient energy is absorbed during the day to maintain detectable emissions throughout the night. Molecules giving rise to airglow emissions include sodium, atomic and molecular oxygen and nitrogen. This study concentrates on the OH emission at 730nm and an emission at 557.7nm by OI.

A distinction is made between different types of airglow according to the time of observation; hence we have dayglow, twilight-glow and nightglow. This project is concerned exclusively with nightglow, and thus the term *airglow* is understood to refer to nightglow herein.

2.2.1 OH emission

The OH airglow spectrum is characterised by a number of isolated emission "bands", each of which contain several discrete line emissions. Each "band" corresponds to a transition between two vibrational levels, with the emissions within each band being associated with rotational transitions (Herzburg 1950). Transitions involving all vibrational levels have been observed up to and including the ninth level (Meinel 1950).

The accepted mechanism for OH excitation in the mesosphere was first proposed by Bates & Nicolet (1950) and further developed by Bates & Moiseiwitsch (1956):

$$H + O_3 \rightarrow OH^* + O_2. \tag{2.1}$$

The energy released by reaction 2.1 is 3.34eV which is sufficient to excite ground-state OH to the ninth vibrational level. This explains the absence of evidence of vibrational levels greater than nine in the OH airglow, and is one of the primary reasons that it is considered to be the primary source of vibrationally excited OH (Takahashi & Batista 1981). The dependence of this reaction on O_3 and therefore atomic oxygen means that the unperturbed intensity of the emission is influenced by vertical transport within the atmosphere, although with the time constant being large the intensity variation resulting from these changes over a single night is negligible. Additionally, a further intensity variation of up to a factor of two occurs throughout the night as the OH emission first increases due to a rise in the ozone population

following sunset, and then slowly decreases over the night as the atomic oxygen is depleted. Importantly, the effect from both of these mechanisms is uniform over areas usually associated with instrumental fields of view (typically of the order of 50km × 50km), With a suitable analysis algorithm, this allows such effects to be accounted for with relative ease, as explained in section 4.1.3.

Krassovsky (1971) was notable in his objection to reaction 2.1. He suggested an alternative mechanism involving vibrationally excited O_2:

$$H + O_2^* \rightarrow OH^* + O. \tag{2.2}$$

However, as discussed by Bates & Moiseiwitsch (1956) this reaction is unlikely since it would readily give rise to vibrational levels higher than nine, and these are not observed in the airglow spectrum.

In order to obtain any useful data from airglow observations, the height of the emission must be determined. Traditionally, rocket-borne instruments have been used for in situ measurements of the emission intensity (eg: Rogers et al. 1973, Barker & Waddoups 1967, Takahashi et al. 1996). More recently, satellites such as the Upper Atmospheric Research Satellite (UARS) have been used for this purpose (Evans & Shepherd 1996, Zaragoza et al. 1998). These measurements have lead to the conclusion that the centre of the OH emission is between 85 and 87 kilometers with a full width half maximum (FWHM) of approximately ten kilometres (eg: Rogers et al. 1973, Hecht et al. 1995) and that observations of the OH airglow can therefore be expected to reflect atmospheric conditions at these heights. Recently it has become apparent that there may be significant variation in the height of the OH emission (Plagmann et al. 1998). This situation is complicated by the fact that wind comparisons across different instruments, used as the basis of the Plagmann et al. (1998) study, often show significant variation particularly when a common volume is not present (for example Khattatov et al. 1996). In any case, future progress and developments on this front need to be kept in mind when drawing height-dependent conclusions about the atmosphere from OH observations.

2.2.2 OI emission

The 557.7nm airglow emission from atomic oxygen is known to be caused by an electric dipole transition of excited atomic oxygen (Jacob 1985):

$$O(^1S) \rightarrow O(^1)D + h\nu_{557.7nm}. \tag{2.3}$$

The mechanism for the production of the excited O(^{1}S) state has, however, been the source of considerable deliberation. Chapman (1931) proposed the so-called "Chapman mechanism". First, recombination energy from O_2 is assumed available for transfer to an O(^{3}P) atom in the three body process

$$3O(^3P) \rightarrow O(^1S) + O_2.$$

It was proposed that in addition to reaction 2.3, the O(^{1}S) excited atoms may also be quenched through interactions with O(^{3}P) and O_2:

$$\begin{aligned} O(^1S) + O(^3P) &\rightarrow O(^1D) + O(^3P), \\ O(^1S) + O_2 &\rightarrow O(^3P) + O_2. \end{aligned}$$

For many years this was considered to be the mechanism for the production of the O(^{1}S) state. However, an alternative two stage process — the "Barth transfer mechanism" — was later published by Barth & Carter (1961), consisting of

$$O(^3P) + O(^3P) + M \rightarrow O_2^* + M$$

followed by

$$O_2^* + O(^3P) \rightarrow O(^1S) + O_2.$$

M represents the neutral atmospheric constituents O, O_2 or N_2. The excited oxygen O_2 can be quenched by M or O(^{3}P),

$$\begin{aligned} O_2^* + M &\rightarrow O_2 + M, \\ O_2^* + O(^3P) &\rightarrow O_2 + O(^1D \text{ or } ^3P). \end{aligned}$$

The quenching mechanisms and their associated rate coefficients are important since they regulate the concentration of constituents involved in the Barth mechanism and hence influence the emission intensity and height profile. Following extensive laboratory and rocket experiments and consideration of the slight temperature dependence of the emission (Bates 1981), the Barth transfer mechanism is is now generally accepted as the O(^{1}S) excitation process in the upper mesosphere (McDade et al. 1986). As for the OH emission, the Barth mechanism's dependence on atomic oxygen concentration means that changes in atmospheric vertical transport cause variations in the OI airglow intensity. The associated changes occur over many days, however, with no significant variation occuring over the duration of a single night.

As for the OH emission, the height profile of the 557.7nm emission needs to be known in order to draw meaningful conclusions from observations. Numerous rocket studies at various latitudes (see, for example, Thomas & Young 1981, Melo et al. 1997) and recent satellite-based measurements (for example, Ward et al. 1997) have shown that the 557.7nm OI emission peaks near 95 km with a half-width of approximately 7 km. The recent satellite measurements have shown that there can be variation of the emission height with local time due to dynamical processes, although outside the equatorial region (latitudes between 20S and 20N) the variation is not significant (Angelats i Coll & Forbes 1998).

It is worth noting that in addition to the 557.7nm OI emission near 95km, there is also an OI emission originating in the thermosphere at heights around 250km. While thermospheric conditions near the equator are sufficient to make this secondary emission detectable, it is virtually non-existant at latitudes greater than ten to fifteen degrees (Shepherd et al. 1997).

2.3 Atmospheric gravity waves

The existence of atmospheric gravity waves were first proposed by Hines (1960) to explain numerous wave-like phenomena which had been observed in the atmosphere

with a variety of instruments. These waves arise naturally in the earth's atmosphere as a consequence of the vertical density gradient produced by gravity acting on the atmosphere. This gradient gives rise to a buoyancy force which, together with gravity itself, provides restoring forces which act on parcels of vertically displaced air. If an air parcel is moved a small vertical distance up into a less dense region, gravity will act on that parcel to return it to its original position since it will be heavier than the surrounding atmosphere. The inertia of the returning parcel will cause it to overshoot its original position into a more dense region where the buoyancy force will act to move the parcel up. This gives rise to a harmonic oscillation whose frequency is termed the Brunt-Väisälä frequency N which following Fritts (1984) is defined using

$$N^2(z) = \frac{g}{T}\left[\frac{\partial \overline{T}}{\partial z} + \frac{g}{C_p}\right] = \frac{g}{\overline{\theta}}\frac{\partial \overline{\theta}}{\partial z} \tag{2.4}$$

where z is the height of a coordinate system, g is the acceleration due to gravity, C_p is the specific heat at constant pressure, $\overline{T}$ is the mean temperature and $\overline{\theta}$ is the mean potential temperature. The Brunt-Väisälä frequency is the high-frequency limit of gravity waves. The low frequency limit is dictated by the rotation of the earth and is known as the inertial frequency or equivalently, the Coriolis parameter. It is equal to the vertical component of the earth's rotation vector and is defined as $f = 2\Omega \sin(\phi)$ where Ω is the earth's rotation rate and ϕ is the latitude.

In order to further develop a mathematical description of gravity waves a number of assumptions are prudent. Firstly, if we restrict our discussion to waves with intrinsic frequency ω such that $f \ll \omega \ll N$, we can reduce consideration to motions only in an x–z plane (where x is a horizontal coordinate of a Cartesian system) with a mean horizontal velocity of $\overline{u}(z)$. We then assume that all field variables such as velocity, pressure, temperature and density can be written as the sum of a mean quantity $\overline{\psi}$ and a perturbation about this mean ψ':

$$\psi(x, z, t) = \overline{\psi}(z) + \psi'(x, z, t). \tag{2.5}$$

ψ' is taken as being caused by the passage of a gravity wave giving rise to a single

Fourier component which can be expressed as

$$\psi'(x,z,t) = \psi'(z)e^{\frac{z}{2H}}e^{ik(x-ct)} \tag{2.6}$$

where k and m are the horizontal and vertical wavenumbers respectively, c is the horizontal phase velocity of the motion and H is the atmospheric scale height given by $H = \frac{R\overline{T}}{g}$ with R being the gas constant for dry air. k is related to the horizontal wavelength of the perturbation λ_h by $\lambda_h = \frac{2\pi}{k}$, and similarly for m and the vertical wavelength λ_z: $\lambda_z = \frac{2\pi}{m}$.

With these assumptions the x and z momentum equations, the continuity equation and the adiabatic energy equation can be combined and linearised to obtain the Taylor-Goldstein equation:

$$w'_{zz} = \left[\frac{N^2}{(\overline{u}-c)^2} - \frac{\overline{u}_{zz}}{\overline{u}-c} - k^2 - \frac{\overline{u}_z}{(\overline{u}-c)H} - \frac{1}{4H^2}\right] w' = 0. \tag{2.7}$$

Here w' is the perturbation in vertical velocity and the subscripts z and zz refer to the first and second derivative with respect to z of the associated quantity, respectively. If we further assume that H^2 is constant, that u_{zz} is small and that H is large (which are reasonable giving conditions described above), equation 2.7 can be simplified to

$$w'_{zz} + \left[\frac{N^2}{(\overline{u}-c)^2}\right] w' = 0 \tag{2.8}$$

which can be solved using the Liouville-Green method (also known as the WKBJ method) (see, for example, Bender & Orszag 1978) to yield

$$w'(z) = Am^{\frac{-1}{2}}e^{i\int m dz'} \tag{2.9}$$

where A is an amplitude. On inclusion of the x and t dependence from equation 2.6, this becomes

$$w'(x,z,t) = Am^{\frac{-1}{2}}e^{\frac{z}{2H}}e^{ik(x-ct)}e^{i\int m dz'} \tag{2.10}$$

which can be reduced to the form

$$w'(x,z,t) = Am^{\frac{-1}{2}}e^{\frac{z}{2H}}e^{i(kx+mz-kct)} \tag{2.11}$$

for the case of slowly varying m. Here $m = \frac{N}{\overline{u}-c}$ which describes how the vertical wavenumber m varies with N and $\overline{u}$. The assumption of a slowly varying m gives rise to several other relationships directly from the linearised equations of motion; the continuity equation gives

$$u' = \frac{-mw'}{k} \tag{2.12}$$

and the adiabatic energy equation gives

$$\theta' = \left[\frac{-\theta_z}{ik(\overline{u}-c)}\right] w' \tag{2.13}$$

Of significant interest is the inclusion of the $e^{z/2H}$ term in equation 2.11 which acts to increase the amplitude of the wave as height increases in an environment where density decreases with height. This means that even small perturbations at a wave's source can grow to large amplitudes in the upper atmosphere which is why gravity waves play a major role in the dynamical processes of the upper atmosphere.

Having deduced the nature of the vertical component of the perturbation velocity we can relate other perturbations to w' using the so-called polarisation relations. Of particular interest is

$$u' = -\frac{m}{k}w' \tag{2.14}$$

which relates the horizontal perturbation component to the vertical component w'.

Another important relationship for the description of gravity waves describes how a gravity wave changes as a function of frequency (ω) and is known as the dispersion relation:

$$m^2 = \frac{N^2-\omega^2}{\omega^2-f^2}k^2 - \frac{1}{4H^2} + \frac{\omega^2}{c^2}, \tag{2.15}$$

where c is the local speed of sound. Given assumptions described above this is often simplified to

$$m^2 = \frac{N^2-\omega^2}{\omega^2}k^2 \tag{2.16}$$

although as pointed out by Swenson et al. (2000) this can result in under-estimations of the order of 10% when calculating the vertical wavelength for disturbances with λ_z greater than 20km. Care must therefore be taken when using the dispersion relation

to calculate vertical wavelength and if large vertical wavelengths are expected the full expression should be employed.

Equation 2.16 is sufficient to allow calculation of the group and phase velocities of a gravity wave packet. In this two dimensional consideration the phase velocity is defined as $c_p = \left(\frac{\omega}{k}, \frac{\omega}{m}\right)$ and the group velocity as $c_g = \left(\frac{\partial\omega}{\partial k}, \frac{\partial\omega}{\partial m}\right)$ which, when used with equation 2.16 gives $c_p = \left(\frac{N}{m}, \frac{kN}{m^2}\right)$ and $c_g = \left(\frac{N}{m}, \frac{-kN}{m^2}\right)$. By inspection it can be seen that the z components of the phase and group velocities have opposite signs which shows that a wave with energy propagation upwards will appear to be travelling downwards from the point of view of constant phase contours — one of the more unusual properties of atmospheric gravity waves.

Further consideration of equation 2.16 gives insight into the vertical propagation of gravity waves. Utilising the relation $w = k\left(\overline{u} - c\right)$, this can be rearranged to give

$$m^2 = \frac{N^2}{\left(\overline{u} - c\right)^2} - k^2. \tag{2.17}$$

A so-called turning level for a gravity wave corresponds to the situation where m^2 becomes negative which, by inspection of equation 2.17, can be achieved if N^2 becomes small or $(\overline{u} - c)$ becomes large. The former can occur via changes of temperature with height since N depends on T as per equation 2.4; the latter relies on the wind profile as a function of height. If either these conditions give rise to m approaching 0, the gravity wave phase fronts become more vertical. When m^2 decreases below zero the vertical direction of propagation is reversed resulting in the wave propagating downward with an unchanged horizontal velocity.

Another special case to consider is when m^2 tends to infinity; again inspection of equation 2.17 reveals that this requires $\overline{u}$ to approach c. The phase speed of a wave is usually invariant which leaves only varations in the background wind speed to cause this trend. As a gravity wave approaches a level where the phase speed equals the wind speed the phase fronts become more horizontal and the vertical wavelength decreases, 'compressing' the wave packet and thus dissipating the energy it contains. Such a level is termed a 'critical level' and provides one mechanism for a gravity wave to transfer

momentum to the background wind.

2.4 Gravity wave effects on the atmosphere

Over the four decades since Hines (1960) formulated his interpretation of wave-like phenomena in the atmosphere, the important role that atmospheric gravity waves play on the dynamics of the atmosphere has become increasingly apparent. Gravity waves are known to affect atmospheric circulation by providing momentum and energy transport from one region to another and thus have a profound effect on climatology (see, for example, Holton 1982, Holton 1983). It is fortunate that as a gravity wave passes through the atmosphere it causes changes which can be easily observed from the surface, allowing the passage of the waves to be studied and quantified.

2.4.1 Airglow intensity

As a gravity wave propagates through a region of the atmosphere, the local density and temperature is altered. These perturbations in turn affect the photochemistry of the reactions producing the airglow through changes in rate coefficients and the concentration of the relevant atmospheric species.

In the case of the Barth transfer mechanism (which results in the OI emission as previously discussed), the rate coefficients of the reactions are only weakly dependent on temperature (Rau et al. 1982) and depend mainly on the concentration of the O species itself. The intensity of the OI emission can be expressed as

$$I \propto [O]^3\sqrt{T}, \tag{2.18}$$

where [O] is the concentration of O and T is the local temperature (Tohmatsu & Nagata 1963, Rau et al. 1982). Observation of the intensity variations of the OI 557.7nm airglow will therefore give information regarding the wave parameters of passing gravity waves since the density and temperature vary with the wave's intrinsic properties.

Similarly the intensity of the OH airglow emission can be modulated by a passing gravity wave. The intensity of the OH emission is directly related to the concentration of excited OH and the temperature. As shown by reaction 2.1 the OH concentration is directly related to the concentration of ozone which itself can be related to the concentration of the O and O_2 species. Wave-induced variations of O and O_2 can therefore modulate the OH airglow intensity giving a detectable indication of a passing wave. Recent modelling work of high vibrational band emissions by Swenson & Liu (1998) based on this mechanism gives excellent agreement with observations thereby confirming our present understanding of the interaction of the OH layer with passing gravity waves. However, it should be noted that a zenith-pointing OH photometer (as used in this study) appears to be most sensitive to gravity waves with vertical wavelengths comparable to or larger than the layer thickness (Gardner & Taylor 1998) which introduces an instrumental selection criteria. Conclusions about waves with vertical wavelengths less than the order of ten kilometres can therefore not be made from photometer OH observations in isolation. Care must also be taken that variations due to larger-scale motions such as tides (for example, Ward et al. 1997, Marsh & Skinner 1999, Ward 1999) are acknowledged. However, the larger temporal and spatial scale of the tidal variations are sufficiently different in character to the variations induced by gravity waves that it is possible to exclude the effects of the tides without impacting on the gravity wave data.

2.4.2 Background winds

It is known that irregular variations in wind speed away from the background average (comprising of prevailing winds and slowly varying tidal components) with timescales less than the order of an hour are due almost exclusively to the passage of atmospheric gravity waves (Hines 1974). If gravity waves are present in a given region of the atmosphere, it is therefore possible to detect their passage by measuring the induced variations of atmospheric wind from a mean value.

Other mechanisms (such as tidal and planetary-scale disturbances) can also modulate winds which means that any wind velocity time series is a superposition of these effects. Fortunately these other sources have larger periods than gravity waves and can be trivially filtered out leaving a timeseries whose disturbances can be attributed to passing gravity waves (Vincent 1984).

In order for a gravity wave to influence the background wind, momentum must be transferred. This can be accomplished through a number of dissipative mechanisms including wave breaking, nonlinear interactions between gravity waves and damping by radiative and turbulance processes. Mechanisms behind possible non-linear wave interactions in the atmosphere can be further categorised into resonant and non-resonant groups and were discussed by Yeh & Liu (1981). In such cases a gravity wave can decay and deposit energy into two secondary waves otherwise unrelated to the original via three-wave interactions.

A gravity wave will 'break' when the amplitude grows so large that the perturbations introduced by the wave become irreversible. Convective instabilities then occur causing turbulence which effects a transfer of momentum from the wave to the flow at the point of wave breaking. The scenario of wave breaking was treated in detail by Andrews et al. (1987) and considered specifically in connection with gravity wave observations by Hecht et al. (1995).

The occurrence of the dissipative processes discussed previously give rise to a movement of momentum from one atmospheric region to another, usually referred to as the vertical momentum flux. Because of its importance in driving atmospheric dynamics its direct measurement is often desired in addition to that of the winds themselves. Vincent & Reid (1983) a method of measuring the vertical momentum flux based on Doppler radar measurements which is discussed in section 4.2 on page 86 (see also Reid & Vincent (1987b)). However, as noted by numerous researchers (Vincent & Reid 1983, Reid 1984, Reid & Vincent 1987b, Kudeki & Franke 1998), reliable determination of momentum flux requires long integration times due to the geophysical noise imposed on the measurements by variations in dependent quantities.

2.5 Previous studies

2.5.1 Historical development

Qualatative observations of what are now known as gravity waves date back to the eighteen hundreds when the wave-like structures present in noctilucient clouds were noticed at high latitudes. Quantatative results started to flow in the early to mid nineteen hundreds when Rayleigh (1924, 1935) and others reported short period variations in the intensity of airglow emissions (mainly the 557.7nm OI line).

The emerging radar technology (especially in the years following World War Two) was also seeing similar variations in observations of the D, E and F regions of the ionosphere while studies of meteor trail evolution was also turning up evidence of wave-like motions in the upper atmosphere. Until the nineteen sixties it was thought that turbulence in the upper atmosphere was the primary cause of these observations (Booker 1956); however, in (1960), Hines (1960) put forward his theory of atmospheric gravity waves which, with the benefit of hindsight can now be said to explain most (if not all) of the disturbances reported to that date. When considering the mechanism behind these variations, turbulence was relegated to a minor role (Hines 1974).

Following wide-spread acceptance of Hines's (1960) theory, existing observational methods were adapted to explore the properties of gravity waves. By the seventies it was well established that gravity waves perturb the atmospheric winds and airglow emissions as they propagate through a region (see, for example, Frederick 1979, and references therein). In addition to the airglow intensity, it was also discovered that if it was assumed that the rotational states of the molecules thermalise to the air temperature at the emission height, so-called rotational temperatures could theoretically be derived from the relative intensities of rotational lines within a given vibrational band. This idea was pursued for a variety of different airglow emissions, most notably the OH Meinel system (Merriwether 1975) and oxygen emissions (Weinstock 1978). Spectrometers and photometers were the optical instruments of choice during this period.

One of the major problems with optical-based observations is that owing to the large background signal during daylight hours, data collection is generally limited to hours of darkness. In recent years these difficulties have been overcome somewhat (Chakrabarti 1998, Sridharan et al. 1999) but ground-based observation of airglow during the day is still technically more difficult. Continuous measurements of the airglow are also possible from satellites (Zhang et al. 1998) but such instruments have poor temporal coverage at a given geographic point owing to their orbital trajectory. Airglow measurements from both satellite and ground-based instruments therefore complement each other.

Recently, technological improvements in associated systems have seen the advent of so-called 'airglow imagers' for observing an extended region of the sky (Zhang et al. 1993, Hecht et al. 1994). Such instruments differ from conventional photometers and spectrometers in that airglow intensity can be effectively recorded from many points in the sky simultaneously. This has the advantage removing many of the potential ambiguities of the single-point system by giving a clear picture of the two-dimensional structure of emission layer. Periodic improvements in instrumentation and data analysis now allows unambiguous 2D spectra to be computed (Gardner et al. 1996) shedding great insight into the behaviour of gravity waves in areas such as directionality which was impossible with the simpler instruments used earlier.

Although not directly related to airglow observations it is worth noting that lidar measurements have been found to contain valuable data on the location and width of the OH layer (Brinksma et al. 1998) which adds to such knowledge gained from satellite measurements. An advantage the lidar method has over the satellite instruments and rocket-borne experiments is its temporal coverage in a single location which allows more detailed study of the emission height and processes which affect this. Lidars have also been used to measure gravity waves (Swenson et al. 1995) and the mesospheric temperature (von Zahn & Höffner 1996) providing another tool for probing atmospheric dynamics. Comparison between lidar temperatures and those derived from OH airglow shows good agreement between the rotational temperatures and those

derived from lidar measurements at mesopause heights (She & Lowe 1998).

As mentioned previously the passage of gravity waves can also be observed using radar. Reflections from features of the atmosphere was known as early as the nineteen twenties but systematic investigations of these returns could not proceed before calculation of the returns' ranges was enabled by the development of pulsed radar techniques by Watson-Watts in 1935. Returns from the troposheric region were investigated in the nineteen forties (Friend 1949) and features in the echoes were readily equated with various meteorological effects. However, studies of the mesospheric region (corresponding to the height of the OH and OI airglow discussed previously) were only commenced in the nineteen fifties by Gardner & Pawsey (1953) and Gregory (1956), among others. Irregularities in the wind observed by these radar studies, and other mesospheric measurements of the time lead in part to Hines' development of gravity wave theory.

The task of inferring atmospheric motion from the returns from radar began with the work of Pawsey in the nineteen thirties (Pawsey 1935) which was incorporated into the development of the 'similar fades' technique (Holdsworth 1995). It was soon realised that this method and its assumptions had several serious shortcomings which lead to the development of the 'full correlation analysis' (FCA) by Briggs et al. in (1950). Although not accepted as valid for the E and F regions of the ionosphere (where it was first employed) due to the invalidity of the volume-scattering assumptions made in the analysis at these heights, the FCA technique is widely used when analysing returns from the lower thermosphere down (less than approximately 100km) where this is less of a problem. Recent improvements in the understanding of the behaviour of the FCA (for example Holdsworth 1995) have lead to its acceptance as a reasonable measurement of the wind, at least for heights below 90–95km.

2.5.2 Recent gravity wave research

Over the forty years since gravity waves have been considered, many researchers have contributed to our knowledge of these waves using instruments and techniques outlined

previously. While the early research concentrated on simply observing atmospheric variations (Merriwether 1975, Freund & Jacka 1979) and equating them with the predicted effects of gravity wave theory, recent research has become more systematic in its use of geophysical data to quantify gravity wave activity.

The work of Krassovsky (1972), Frederick (1979) and others in the nineteen seventies conclusively showed that gravity wave activity of scales predicted by theory could cause observable effects in airglow intensity. This meant that airglow could be used as a remote gravity wave sensor so long as the height of the respective emission was known. While work continued on development of optical observational techniques and equipment to extend the coverage of optical observations (for example de Deuge et al. 1994), others used rockets (Barker & Waddoups 1967), balloons and spacecraft (both manned and unmanned) (O'Brien 1967, Gulledge et al. 1968, Offermann & Drescher 1973) in an attempt to identify well-defined height ranges for the more popular airglow emissions including OI and OH. Triangulation between two spatially separated airglow observing instruments has also been used to measure the emission height (Taylor et al. 1995b) with good agreement with other results.

Similarly, radar studies of the atmosphere shifted focus around the late nineteen seventies from simply observing perturbations to using those perturbations to infer gravity wave properties. By 1983 optical and radar observations of gravity waves were becoming common place and this focus remains to the present day. Myrabø et al. (1983) and others reported possible wave parameters from optical observations; Meek et al. (1985) used spaced antenna radar winds to characterise gravity waves while Vincent & Reid (1983) used Doppler methods to achieve a similar end with an MF radar. By the late nineteen eighties, there was considerable suggestion (in agreement with the theory) that gravity waves had a seasonal dependence from both optical (Jacob 1985) and radar (Reid 1986, Reid & Vincent 1987b) data. Seasonal airglow intensity variations have also been observed for several different airglow emissions (Takahashi et al. 1995, Mulligan et al. 1995). Modelling and experimental evidence by Thayaparan et al. (1995) suggested that at least part of the gravity wave variability was

due to nonlinear interactions between atmospheric tides and gravity waves although other modelling work by Hickey et al. (1997) reinforces that the wind field is important when analysing and interpreting wave-driven airglow structures. Gravity wave filtering by the mean winds at lower altitudes (Taylor et al. 1993) and lower frequency motions such as tides (Isler & Fritts 1996, Smith 1996) is also significant, a suggestion reinforced by consistent seasonal mean wind variations being observed in practice (for example, Manson et al. 1991, Nakamura et al. 1996a, Nakamura et al. 1996b, Namboothiri et al. 1999) in general agreement with atmospheric models. There have, however, been studies (Hall et al. 1995) whose direction statistics cannot be explained by filtering, suggesting the possibility of the existence of another season-dependent atmospheric process. Work on perturbation spectra by Qian et al. (1995) suggests that the nature of the wave source may also be significant in determining the properties of the wave field at mesospheric heights.

The advent of low-light television systems (Taylor et al. 1987) gave the first two dimensional view of the airglow across a wide area of the sky although it was the subsequent development of imagers based on charge coupled device (CCD) technology (for example Hecht & Walterscheid 1991) which allowed accurate quantifiable measurements to be made. These measurements have been refined over time from identification of gravity wave activity (Hecht & Walterscheid 1991) to a full two dimensional analysis of wave parameters based on the observations (Hecht et al. 1993, Hecht et al. 1995, Gardner et al. 1996). Using suitable narrow-band filters many imagers are able to observe separate rotational lines allowing determination of the rotational temperature field across the field of view in addition to the emission intensity; doing so results in observation of a geophysical quantity in addition to the simple emission intensity and allows investigation into the atmospheric response to gravity wave passage. While spectrometers and photometers were also able to measure such temperatures for many years, they essentially sample a single point in the sky which gives no direction information for passing waves. Advances in CCD technology have extended observations well into the infrared where the amplitude of intensity variation is larger, thus

producing data with lower environmental noise and a correspondingly higher degree of certainty in the analysis (Frey et al. 2000).

As random access storage has become more accessible it has been feasible in recent years to run imagers for longer periods of time in a single location (Wu & Killeen 1996, Hecht et al. 1997) in much the same way the photometers have been (for example, Giers et al. 1997), which opens the possibility of building up a climatology of gravity wave activity over a year or more and to investigate more fully the seasonal dependence of the wave activity and properties. Such investigations are also possible with radar and seasonal effects have also been seen in such data (Bristow et al. 1996, Manson et al. 1997). The investigation by Manson et al. (1997) also demonstrates a difference in gravity wave activity between latitudes. Long term radar studies (Connor & Avery 1996) have identified the presence of annual variations in gravity wave activity in addition to the seasonal effects observable over shorter timescales.

Intercomparisons between co-located instruments can be extremely powerful since unusual features can be cross-checked and often the data from different observations will complement each other allowing more detailed interpretations to be undertaken. AIDA '89 (Hines 1993, and other papers therein), ALOHA-90 (Gardner 1991), CORN-92 (Hecht et al. 1995) and ALOHA-93 (Taylor & Bishop 1995, and other papers in the same issue) have all contributed to our understanding of gravity wave interaction with the atmosphere by providing a comprehensive description of the atmospheric state during the campaigns. Comparisons between airglow and meteor radar data during the CRISTA/MAHRSI campaign have demonstrated that these two methods of observing gravity wave disturbances give good agreement (Takahashi et al. 1998), and a comparison between ground- and satellite-based airglow instruments confirmed that the intensity observations from the two methods show good agreement (Melo et al. 1999). Smaller scale studies over longer periods have been just as valuable, allowing for example confirmation that seasonal directionality of waves can be related to prevailing winds at mesopause heights (Walterscheid et al. 1999) through comparison of airglow and radar data. Modelling work by Gardner (1998) and Hickey et al. (1998) also

support the suggestion that the properties of gravity waves observed at mesospheric heights depend strongly on the winds at lower heights, an idea suggested by Taylor et al. (1993) based on their observations.

The images obtained from the CCD-based instruments often record striking quasi-monochromatic wavelike structure (for example Taylor et al. 1995) with smaller-scale features superimposed. The exact cause of both the small and large scale features have been the subject of speculation. Hecht et al. (1995) have produced results which support the theory of Fritts et al. (1993) which suggested these 'ripple events' are signatures of gravity waves breaking at or near the airglow emission layer. The quasi-monochromatic disturbances seen in airglow imagers and other measurements have been suggested (Monserrat & Thorpe 1996, Ralph 1997, Walterscheid et al. 1999) to be caused by ducting (Liang et al. 1998). Studies such as those by Taylor & Bishop (1995) which observe wave-like features over a limited height range only add weight to this hypothesis although there is still some disagreement with the suggestion of wave ducting. In this situation a gravity wave is trapped between two turning levels produced by the atmosphere's temperature gradient and, being subject to reflection without loss of energy, can travel long distances from the source while remaining at mesospheric levels.

chapter 3

Equipment

During this research, data were collected from both Buckland Park in South Australia (34°38'S, 138°29′E) and Davis station in Antarctica (68°35′S, 77°58'E). This chapter details the equipment involved and the operational methods used during data collection.

3.1 Buckland Park three field photometer

3.1.1 Physical description

The three field photometer used at Buckland Park is depicted schematically in figure 3.1. The same instrument was previously used for airglow studies by Jacob (1985) prior to its relocation from Mt Torrens (near Adelaide, Australia) to Buckland Park. It was designed to simultaneously observe three different areas of the sky through interference filters selected using a rotating filter wheel.

The objective lens in the roof formed the entrance pupil of the instrument. Light from here passed on to a telecentric lens, which was focused onto the filter wheel plane. Interference filters were used. The telecentric lens was used to ensure that the central axis of a light cone subtended at any one point on the filters was always perpendicular to the filter plane, thus ensuring correct operation of the filters. The mounts for the filters allowed the filters to be tilted slightly to fine-tune their responses

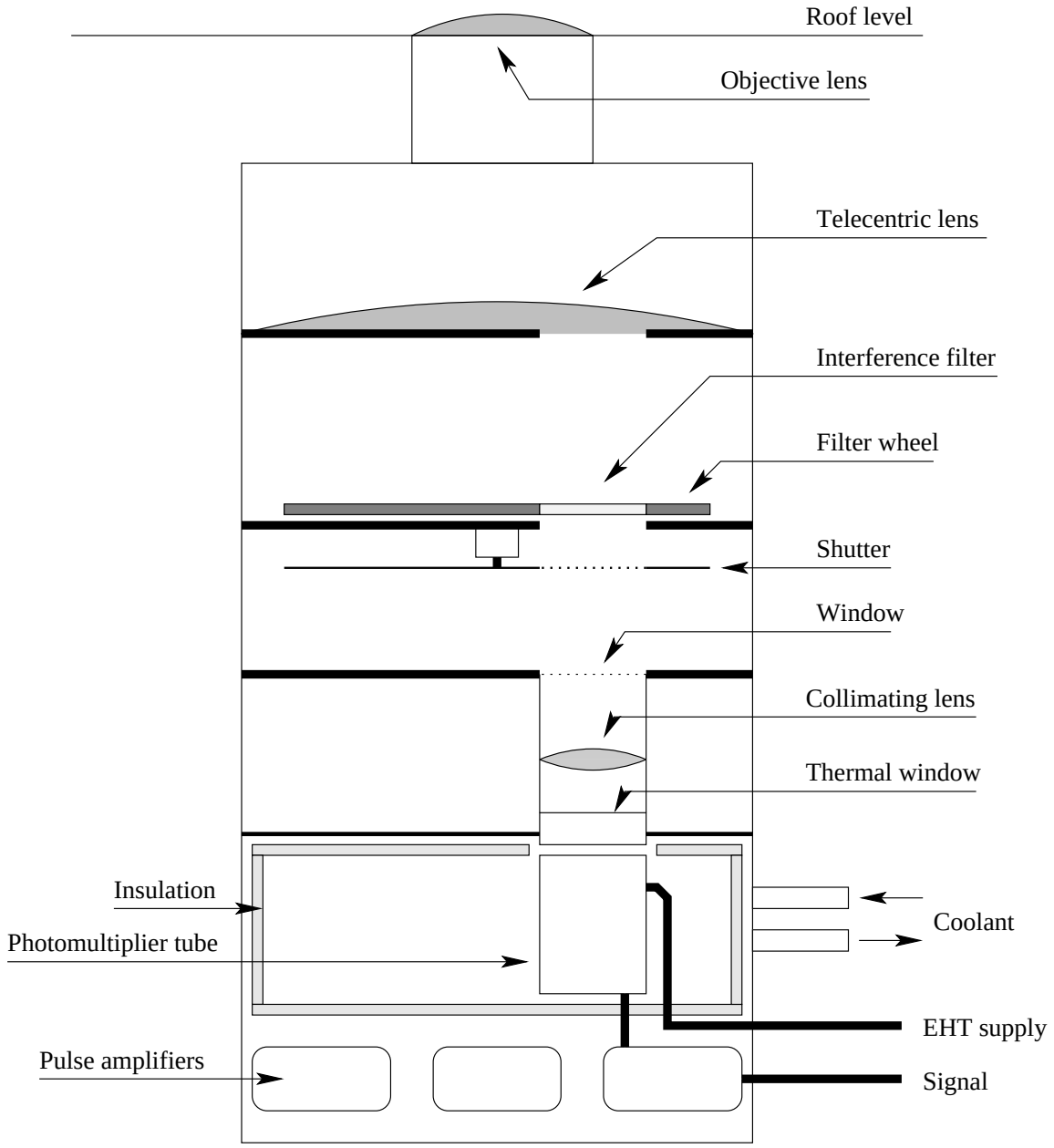

Figure 3.1: Schematic depiction of the three field photometer at Buckland Park. Only one photomultiplier is shown for clarity.

during calibration.

Three photomultiplier tubes (EMI type 9558B/9658) arranged as shown in figure 3.2 formed the instrument's detectors. They were each supplied with nominal 1000V supplies from separate solid state DC-DC converters whose output was set to obtain maximum signal to noise ratio in the respective photomultiplier. There were also 3 separate pulse amplifiers located in the instrument which provided pulse shaping and buffer functions before feeding the signals to the main control electronics. To reduce the dark counts of the photomultiplier tubes, they were cooled to nominally -10°C by circulating ethylene-glycol, cooled with a refrigerated cooler, around the tube enclosures. An insulated chamber and double nitrogen-filled windows isolated the cold components from the room temperature optical assembly and prevented condensation forming on the window of the photomultipliers.

Directly above the photomultiplier entrance windows was an isolation shutter which was opened by activation of a circularly acting soleniod. This was used to protect the tubes from accidental exposure to high light levels and to obtain periodic dark count measurements during the instrument's operation. The shutter was closed in the absence of a drive current to the soleniod giving fail-safe operation in the event of a power failure.

The filter wheel had positions for six separate filters as shown in figure 3.2. Odd numbered filter positions carried broad-band (FWHM $\approx$ 12nm) filters nominally centred at 730.0nm while the even positions had narrow-band (FWHM $\approx$ 3nm) filters nominally centred at 557.7nm. The 730nm filters were used to observe the (8-3) OH band whereas the 558nm filters were optimised to observe the OI line emission at this wavelength. This filter configuration was originally chosen to facilitate an investigation of the vertical propagation of waves betweeen the two emission heights. The filter wheel was rotated by an AC motor which allowed the filters to be moved over the photomultipliers as required. Microswitches were arranged to indicate which filter position was above photomultiplier one.

The action of the optics in the system reversed the positions of the detectors at

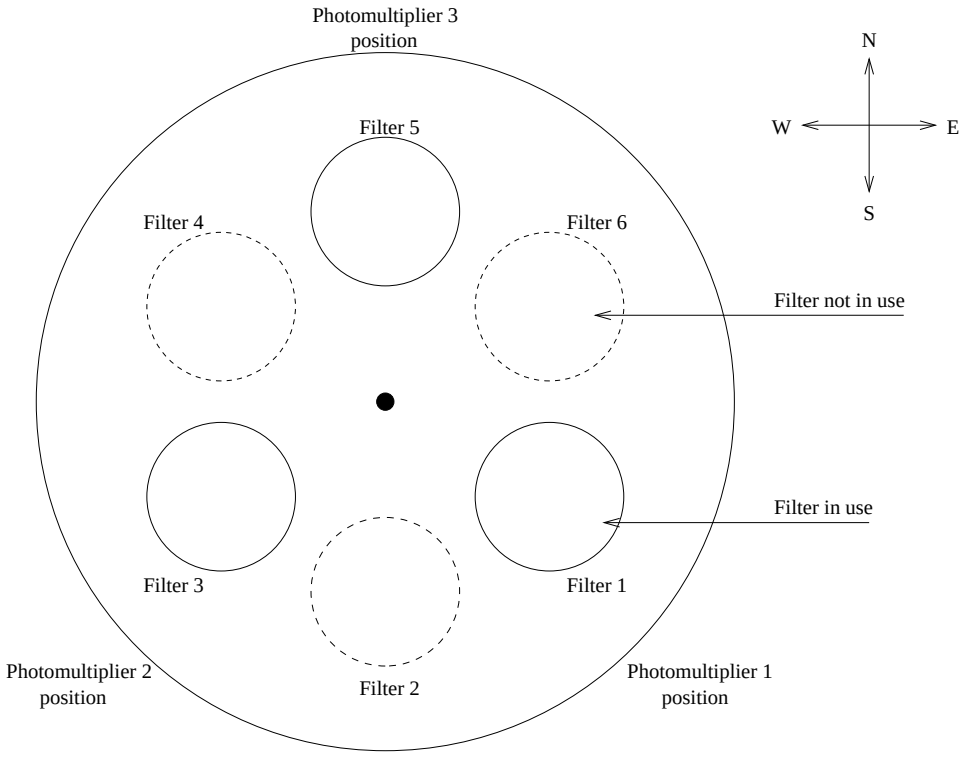

Figure 3.2: Arrangement of filters on the filter wheel showing relative positions of the photomultipliers

the observation height range (that is, 85 to 97km) about the axis of the instrument. Therefore at Buckland Park, photomultiplier position 3 was south of positions 1 and 2, with position 1 west of position 2. At the observation heights of 85km and 97km, the field separation was 12km and 13km respectively while the field of view at these heights was a circle approximately 5km in diameter.

3.1.2 Control system

Since the work of Jacob (1985) the Buckland Park photometer has undergone considerable upgrades to the control electronics and computer control system. The major functional blocks of the control system of the photometer are shown in figure 3.3.

During 1992 the original pulse amplifiers, control system electronics and control computer (a Commodore PET) were upgraded to include improved interface logic under the control of an Olivetti XT Personal Computer running DOS. To facilitate

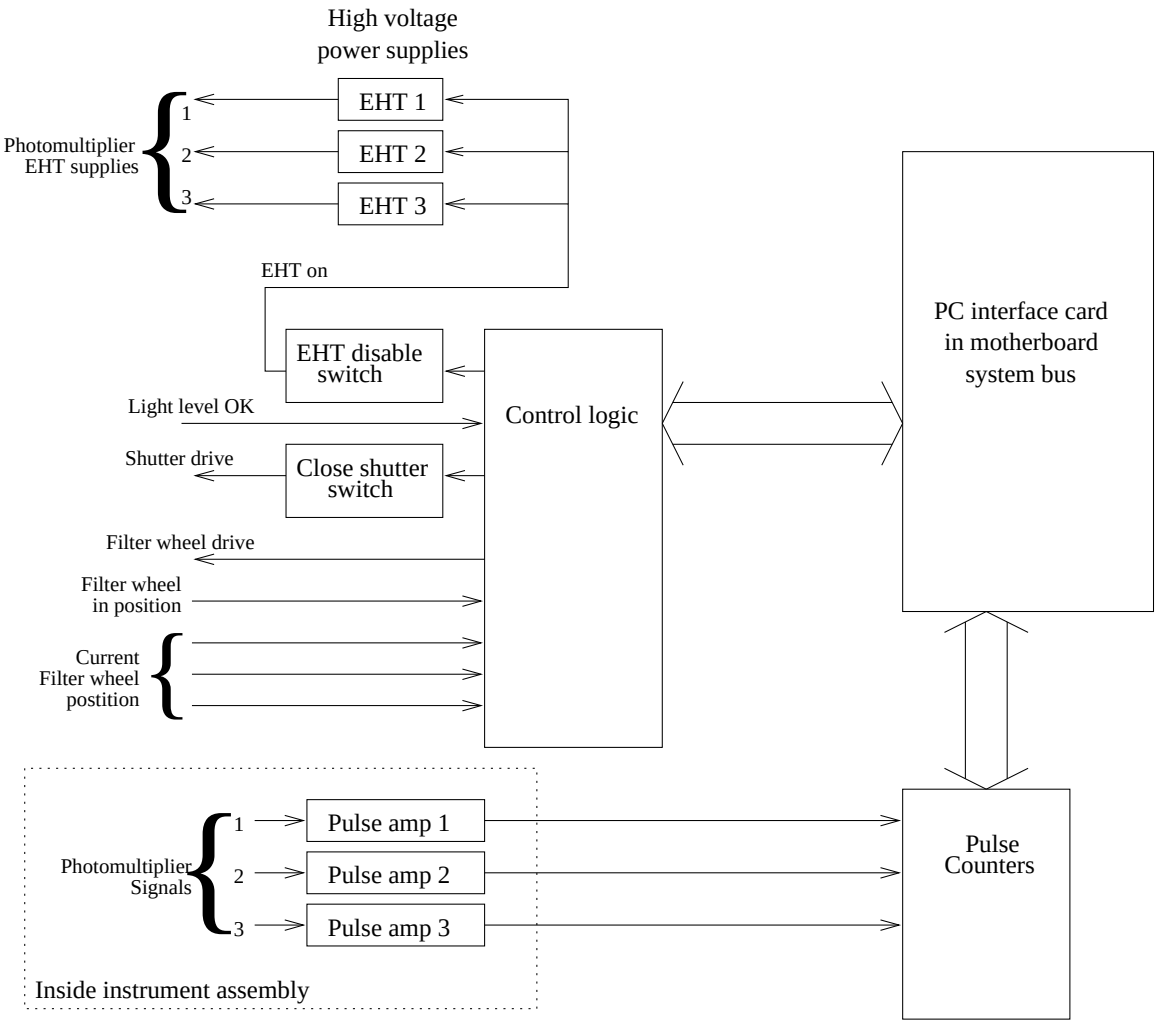

Figure 3.3: System block diagram of the three field photometer

remote operation and data collection, the author replaced the Olivetti with an IBM-PC compatible 80486dx2-66 based machine during 1995 (Woithe 1995). This work also involved rewriting the Turbo Pascal control programs and IO card interface libraries in C. Communication between the PC and the interface electronics was via a PC14 IO card on the ISA bus of the PC. This card provides a number of buffered control lines through two 8255 programmable input/output controllers. This card was connected to the photometer electronics via two 25 way ribbon cables.

The outputs from the three pulse amplifiers/buffers were fed into separate high speed 32 bit counters. Given the expected count rate for the 558nm emission of 600kHz (Jacob 1985) these counters allowed for a maximum observation time of ≈ 7000 seconds (2 hours) before overflow, which was more than enough for this application. The counters were multiplexed onto an 8 bit bus for transfer when requested by the PC. In order to read all three counters, twelve separate 8 bit transfers were required.

The control logic interfaced the signals from the IO card to the three field photometer hardware which allowed the PC to control all aspects of the instrument's operation. Signals from the three binary coded filter wheel position microswitches were passed back to the PC, as is the "in position" indicator (to indicate when a filter was locked in position). The "filter wheel drive" signal triggered a zero-crossing solid state relay which energised the AC filter wheel motor, and the "shutter drive" signal triggered the circular solenoid used to open the shutter. Similarly, the "EHT on" signal allowed the EHT supplies to activate thereby supplying EHT to the photomultiplier tubes.

To reduce the risk of accidental exposure of the photomultipliers during daytime maintenance a number of safety mechanisms were built in. The "EHT disable" and "Close shutter" switches physically prevented the respective signals from reaching the components, thereby stopping the EHT and shutter respectively from being activated. In addition, if excess light was detected by a separate photodiode sensor mounted just above the telecentric lens, the control logic acted to prevent the EHT from being turned on and the shutter being opened.

The control logic included a lightning detector (which took the output from the

photodiode as input) which attempted to protect the photomultipliers from lightning by forcing the shutter closed for fifteen minutes after detection of a nearby flash. Finally, an independent timer switch on the electronic rack's power supply prevented power being applied during the day. This guarded against the possibility of a catastrophic failure of the control PC resulting in the system being turned on during the day.

3.1.3 Instrument operation

An overview of the operational mode of the Buckland park instrument is given in figure 3.4. This control algorithm was implemented as a C program running on the PC under the Linux operating system for the duration of this study.

The start and end times of an acquisition were determined by the rise and set times of the moon and the sun, with the photometer only operating during periods devoid of moonlight and sunlight. These times were calculated using *ephem* (Downey 1992), an astronomical ephemeris program, and provided to the photometer control software in an ASCII file. Given the rise and set times, the control program worked out when it was able to start and at what point acquisition should stop. As a general rule, the system was allowed to function between 'dawn' and 'dusk' whenever the moon was not up.

Each observation comprised an exposure starting either on the minute or 30 seconds past the minute followed by dead time until the next observation. Since writing data to disk took an insignificant time, the majority of the dead time was consumed with the movement of the filter wheel. Until 12 August 1997 the exposure was 22 seconds. However around this time investigation of several anomalies in data files showed that the resulting dead time was not quite sufficient to guarantee the filter wheel enough time to move to its next location. For this reason, exposure was reduced to 20 seconds for all observations taken after this date.

Data were recorded through the 558nm filters (filter wheel position 2) on the half minute and through the 730nm filters (using position 5) on the minute. By always

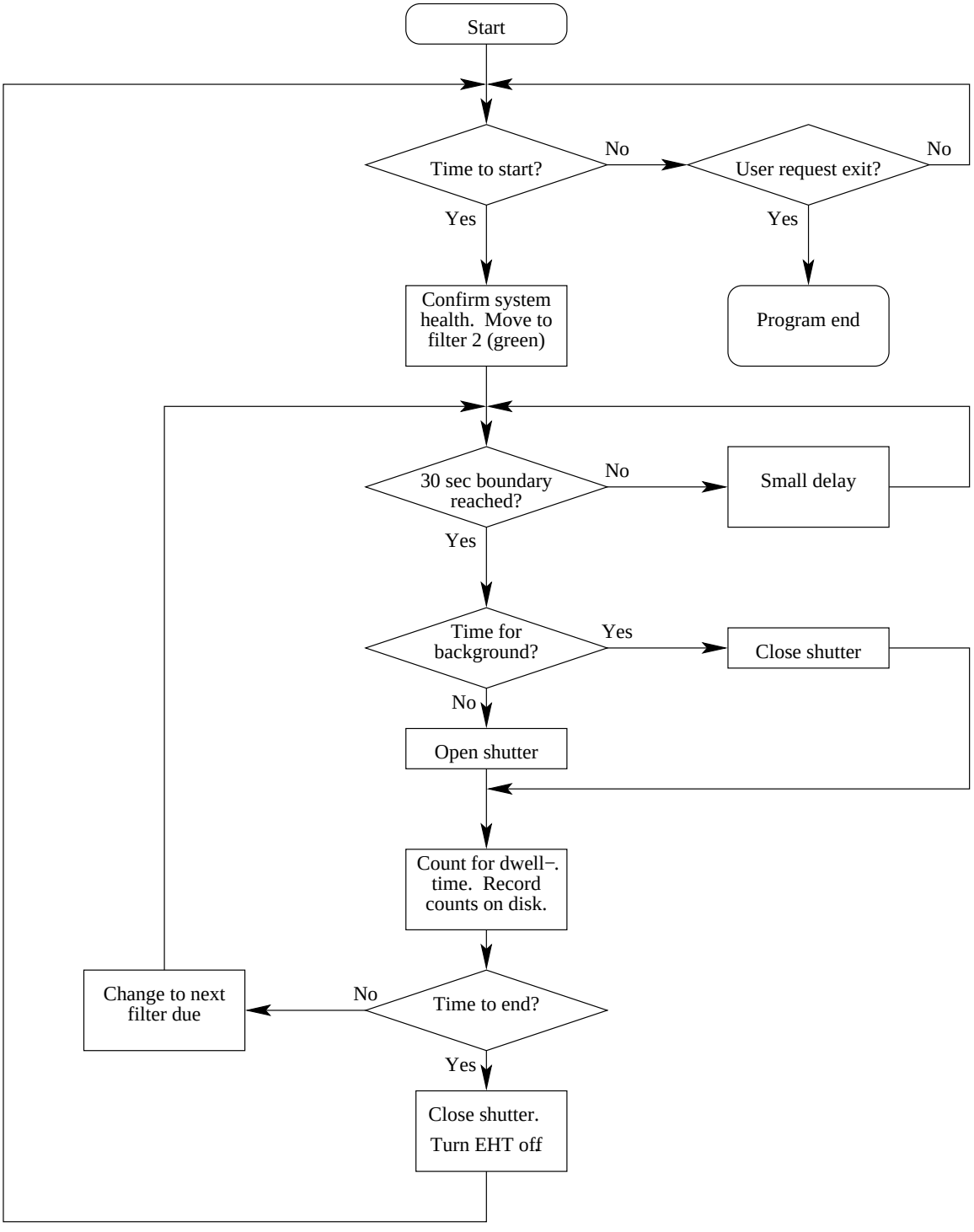

Figure 3.4: System flowchart for control of the photometer

using the the same filter position for observations of a given wavelength, intensity changes due to long-term variations in individual filters' spectral response did not create artificial periodic signals in the time series from given fields. A dark count was recorded every 15 minutes by closing the shutter prior to counting, allowing drifts in photomultiplier noise levels to be accounted for during data analysis.

To simplify the Fourier data analysis it was desirable that each observation of a given colour was evenly spaced in time, or at the very least was separated by integer multiples of the observation period (one minute in this study). Prior to 12 August 1997 this was not guaranteed if the filter wheel did not reach its preset position in time — the observation which was 'missed' (a 558nm exposure for example) would be (wrongly) run at the next half minute instead of the expected 730nm observation. Consequently the software flow control was altered on 12 August 1997 by the author to circumvent this problem.

3.1.4 Operational difficulties

The photometer at Buckland Park was operated by the author for the period 1995 – 2000, during which time a number of hardware related faults developed and needed to be overcome.

When operation commenced in 1995 the refrigeration unit cooling the photomultipliers was known to be slowly failing. The cooling efficiency slowly declined until it was only able to sustain a temperature of ≈5°C during the warm nights of January 1997. (More generally, the temperature would fluctuate between -2°C during the night to 5°C during the day). Consequently the unit was replaced, significantly reducing dark counts (as expected) and retaining the photomultipliers at a more consistent temperature.

The most common fault with the system for the first two years was the reliability of the resistors used in the dynode chains of the photomultipliers. A total of about three months' cumulative downtime occurred between 1995 and 1996 due to a number of resistors going open circuit. The failures were not confined to a single channel.

It is thought that the repeated heating/cooling cycle resulting from the deteriorating cooling unit may have caused expansion stresses in the resistors, giving rise to a premature failure. Since the frequency of resistor failures declined significantly following replacement of the cooler, this seemed a likely explanation.

Reliability of the filter wheel became a problem in late 1997 and into 1998. A number of different problems surfaced at about the same time which took until late 1998 to fully diagnose and rectify owing to their intermittent nature. The problems had varying effects on the data, although fortunately in most cases the data were retrieveable through appropriate processing involving mainly linear interpolation to fill in missing data points. The most frequent problem was traced to the deterioration of an oil seal in the filter wheel motor/gearbox assembly which allowed small amounts of oil to interfere with the friction drive of the filter wheel itself. The loss of friction meant that sometimes insufficient torque was conveyed to the filter wheel preventing it from being released from its locked position and rotating. The effect on the data were easily rectified using interpolation although the intermittent nature of this fault was such that it took nearly twelve months before the hardware problem was observed in action and diagnosed. Concurrent with this problem, the microswitch reliablility declined to a point where reliable indication of the current position was not occurring. This was due to two combined factors: the switches themselves were wearing out, and the metal posts used to activate the switches had worn considerably which meant that the switches were not being depressed enough to ensure a positive signal. Over several months this fault was tackled on three fronts.

- Since the index posts were screwed into the filter wheel, the side used to activate the microswitches was easily changed by adding a washer under the post;
- The microswitches were replaced;
- Progressive changes to the PC software gave it more intelligence when interrogating and interpreting the switch positions.

The combined effect of these three approaches increased the reliablity of the system

significantly. What drew this process out over several months was that any one of these actions appeared to cure the problem at first. After as much as two months however, further attention was clearly necessary.

Even with the improved electronics, random noise spikes of varying magnitudes as observed by Jacob (1985) were still present in the system. The source of these is still unresolved; however they were easily corrected using interpolation, although development of an effective software detector of these spikes did consume considerable time.

The lightning detector circuitry, initially constructed by the author during 1995 (Woithe 1995), gave a number of problems during the early course of the project. The major problem affecting data collection were false triggers, although in situ tests with a photographic flash unit showed that proper triggering in the presence of a flash was also unreliable. A number of improvements were made by the author with the final circuit shown in figure 3.5

Originally the detector circuit was designed to trigger on pulse lengths under 150ms. This was to avoid "lightning" triggers in the presence of long-lasting light. However it became apparent that the (existing) photodiode used for light detection had a very slow reponse time which resulted in pulse lengths of the order of 300ms even though the photoflash time was considerably less than this. To comfortably encompass this, the 1K timing resistor (R1) was changed to 5.6K resulting in a maximum allowed pulse length of about 600ms. It was also observed that the simultaneous operation of the 555C's reset and trigger pins resulted in unreliable triggering; a small delay circuit comprising R4 and C4 was added to the trigger pin to ensure it was operated after the reset. In addition, several pulse stretching circuits (D1/R3/C3 and D2/R6/C7) were added to improve trigger reliablility in the presence of a chain of pulses and to ensure that the 15 minute timer was properly reset on each subsequent lightning event.

The false triggering was a little more difficult to pinpoint. Close correlation with large noise spikes in the data suggested that the cause of these spikes was also the cause of the false lightning triggers. The major problem with these false triggers was

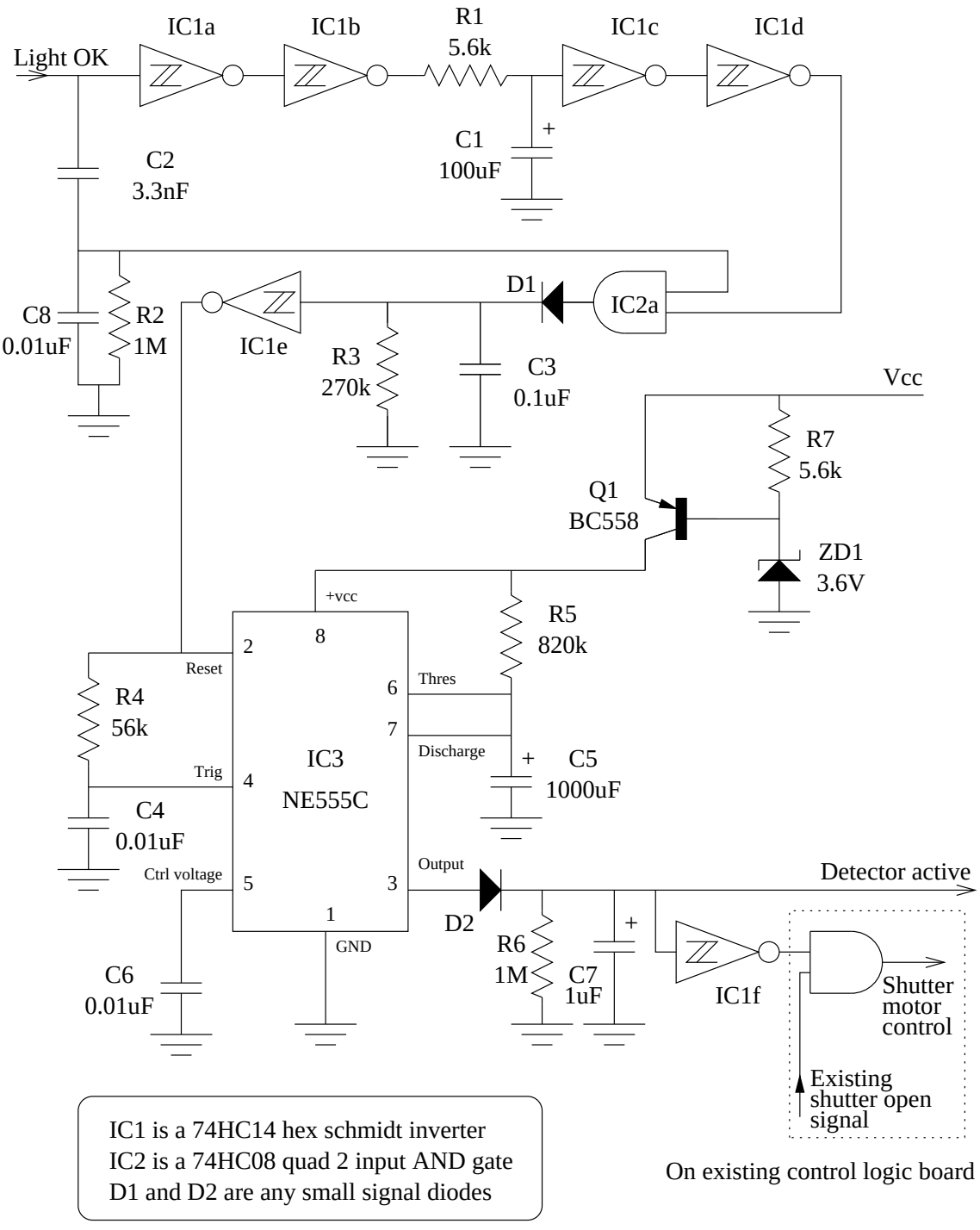

Figure 3.5: Schematic diagram of revised lightning detector

the loss of 15 minutes of data which was a significant outage, especially on the nights of shorter observations. A 0.01μF (C8) was placed between the input and ground to give some protection against extremely short pulses, although the best solution was to identify the source of the original interference. Unfortunately this proved impossible; for this reason, a bypass switch was fitted to allow the detector to be switched out of the circuit at times of low lightning risk.

A final problem with the detector was its initial power-on status; at times it would power up in the 'activated' state which could result in some loss of data if the electronics were powered up less than 15 minutes prior to commencement of observations. This seemed to be caused by the fact that due to current and voltage leakage from the PC interface card through the CMOS chips in the photometer's control electronics, the 555C's power rail remained at 2.5V even when the electronics were off. When the control rack was powered up the lightning detector circuit was already sensitive to noise on the light detector line associated with the powering up of the related circuits. To rectify this, a low voltage cutout consisting of R7, Q1 and ZD1 was added into the 555C's supply line to ensure it remained off until supply reached at least 3.6V.

When dealing with missing or contaminated data within a given night while analysing for gravity wave parameters, interpolation was the predominant method used. It is worth noting that cross-spectral methods described by Scargle (1989), which were utilised in this study for investigating long-term airglow behaviour, could possibly be used to carry out the cross spectral analysis directly on a night's unevenly sampled data. An investigation of the performance of this alternative was not carried out as part of the present study since the effects of the various problems encountered within a single night were not severe enough to introduce significant biases due to the employment of interpolation. The extra complexity involved with Scargle's (1989) method was not deemed justifiable in this situation.

3.2 Davis three field photometer

The Davis three field photometer data used in this study were collected by the various resident physicists present at Davis during the interval of interest (1995 – 1998). While the Davis photometer is based on the same design and philosophies as the Buckland Park model, a number of important differences exist.

3.2.1 Differences from Buckland Park photometer

Like the Buckland Park system, the control system of the Davis photometer has also been considerably upgraded since its construction in 1980 and its use by de Deuge (1990) and de Deuge et al. (1994). In addition, the filter wheel drive has been replaced with a stepper motor to increase reliability of operation at the expense of a slightly longer rotation time. Hall effect devices replaced the mechanical microswitches to provide position information with higher reliability than the original switch-based system.

The arrangement of filters on the filter wheel differed significantly from that at Buckland Park. In addition to single 558nm and 730nm filters, the Davis photometer also carried 428nm and 630nm filters to study auroral and thermospheric emissions respectively. With only one of each filter, a given emission was not observed simultaneously in three fields and in order to analyse the data using cross spectral techniques it was first necessary to process the time series to account for the time difference between observations of a given wavelength in the three fields. This could be done using interpolation or (more appropriately) by introducing a frequency-dependent phase shift to each field's spectrum. The phase shift would correspond to the timeshift required to synchronise the field's time series with whichever field had been chosen as the reference. Mathematically, if field i is chosen as the reference it is necessary to work with all phases relative to the observation grid of field i. Since the phases derived from the Fourier transform of each time series are relative to their respective observation times, a phase correction is needed to make them relative to field i's observation time. If field

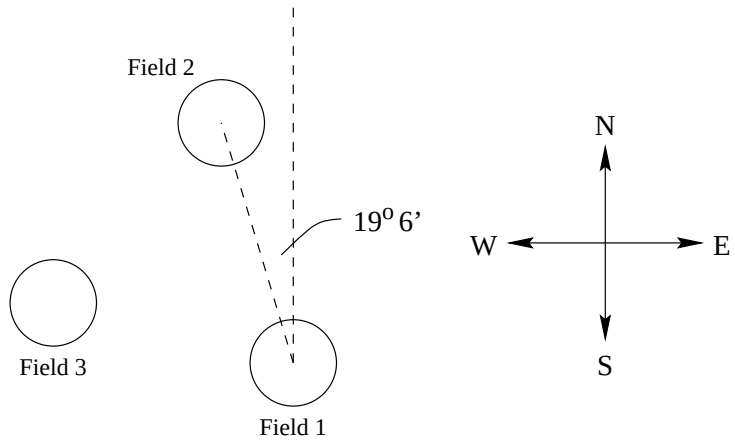

Figure 3.6: Arrangement of fields for the Davis three field photometer system, relative to geographic coordinates on the ground. At the observation heights the field positions have been effectively reflected through the instrument's axis of symmetry as for the Buckland Park instrument.

j observations are separated from those of field i by t seconds such that $\frac{-T}{2} < t < \frac{T}{2}$ for sampling period T, the phase shift required for frequency component f is simply $\phi = -2\pi tf$, which can be trivially applied to field j's data by multiplying the Fourier transform by $\exp i\phi$. Here a positive t indicates field j is observed after field i. Despite the slightly more complex data treatment required, this observational arrangement does give rise to a more comprehensive dataset which can be a distinct advantage, particularly in auroral zones, as it allows uniquely auroral emissions to be observed which can aid in the identification of aurorally contaminated data.

The cooling of the photomultiplier tubes at Davis was accomplished using a heat exchanger placed on the roof of the building housing the photometer. This served to chill the coolant to at least -10°C during times of operation. In addition, the connections between pulse amplifiers, photometer hardware and the control electronics were optically isolated in an attempt to reduce noise spikes due to earth loops.

The final major difference between the two instruments is the orientation of the instrument with respect to magnetic north. Figure 3.6 illustrates the arrangement of field positions relative to geographic north on the ground (L. Symons & J. Innis 1999, [1] private communication).

[1]Both from the Australian Antarctic Division

The computer controlling the Davis photometer was, like the Buckland Park installation, an IBM PC compatible. However, the control software was written 'in house' by the Antarctic Division and is therefore rather different in style from the Buckland Park system. Essentially, though, both systems function similarly.

3.2.2 Instrument operation

As previously mentioned, the three field photometer at Davis had up to six different filters mounted on the filter wheel. During acquisition, the system would expose the photometers for 2.5 seconds and then move the filter wheel to the next position. Including dead time between exposures, each complete cycle of the filter wheel took 40 seconds to finish. As well as sampling more optical emissions, this arrangement also had the advantage that the sampling interval for any one filter was 40 seconds.

The short dwell time — an order of magnitude less than that used at Buckland Park — was feasible due to the increased transfer efficiency of the filters used at Davis which meant that the time series' signal-to-noise ratio was not compromised.

3.3 Buckland Park MF radar

The Buckland Park MF radar was first constructed in the mid sixties (Briggs et al. 1969) and was significantly upgraded between 1989 and 1995 (Reid et al. 1995). The upgrade allowed the radar to function as a true Doppler radar while providing much improved control and data acquisition capabilities.

3.3.1 Hardware

The current configuration of the MF system is described in detail by Vandepeer (1993) and is summarised here. Details are also provided by Reid et al. (1995).

The transmission system is comprised of three independent transitter systems operating at 1.98MHz, made up of ten modules each. A complete module comprises a

phase control module (PCM), a solid state power amplifier (PA) and a filter transmit/receive module (TR). Two of the three transmitter systems used PA modules capable of delivering 2.5kW peak power while the third was populated with higher powered versions capable of 5kW peak power. The PCMs can correct for phase drifts in other areas of the given module and antenna system, and can also introduce a programmable delay to the signal to shift the final output of the respective module by 0 to 360° in 8.5° steps (at 1.98MHz[2]) with respect to a master reference signal delivered to all PCMs. The TR modules allow receiving on the same antenna as transmission if desired and also provide filtering of the square-wave signal from the PCM to retain only the fundamental carrier. In operation the typical duty cycle of the transmitter is 0.2% with a pulse repetition frequency varying from 80Hz during the day to 40Hz at night. The output impedance of each module is less than 10Ω with optimal performance occuring when the module is driving into a pure resistive 50Ω load.

The antenna array is constructed from 178 individual half-wave dipoles arranged as 89 crossed dipoles as illustrated in figure 3.7. The array is orientated 4° west of north which corresponded to the property fence line at the time of construction in 1967. The site itself is nominally flat with a drop of less than two metres towards the south-west corner (Reid 1984). 75Ω coax with an integral number of half wavelengths at 1.98MHz is used to connect each dipole back to the transmitter system, with a balan used to provide matching between the nominal antenna impedance of 28Ω and that of the coax feeder. The length of each dipole is 71.6m long and held about 10m above the ground by wooden poles. In operation, each transmitter module is connected to a group of three 75Ω antenna feeders to provide a nominal 25Ω load for the PA module.

Receiving of the return signal is carried out by receiver modules in a dedicated Radar Data Acquisition System (RDAS). Each module consists of an RF receiver with programmable gain control and a signal processor with 12 bit analog to digital converters (ADC) which provide in phase and quadrature components of the return

[2]The delay is actually achieved using a Newport Microtek 60A-091 programmable delay chip whose step is a 12 ± 2.0 ns giving a total delay of 91 ± 4.5 ns

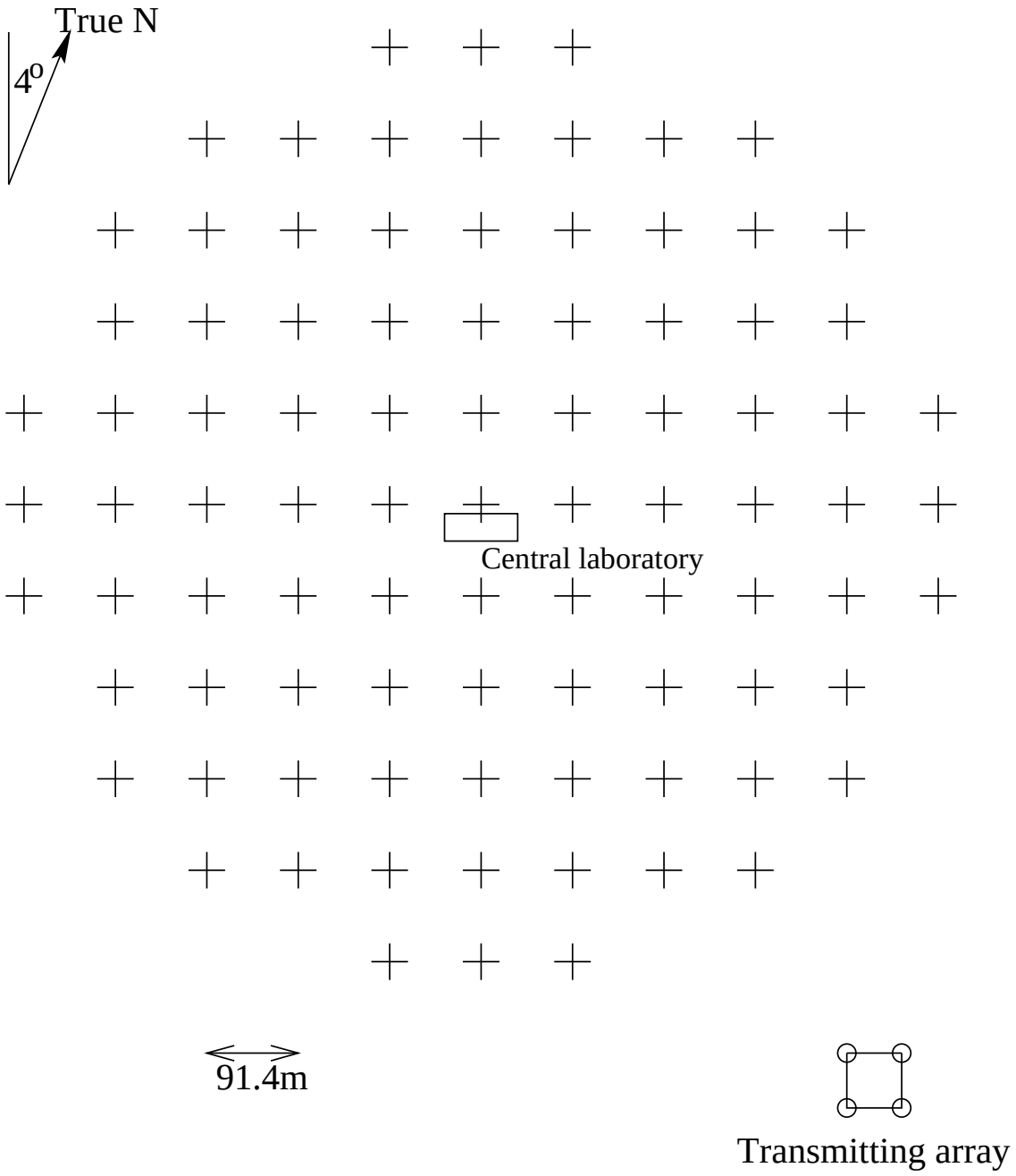

Figure 3.7: The Buckland Park MF antenna array. The separate tranmission array was not utilised for experiments conducted between 1995 and 2000, but may have been used during data collection prior to 1995.

signal with 12 bit resolution. Under software control, the gain control can be adjusted to maximise the dynamic range attainable by the ADCs while preventing saturation in the receivers in the presence of signals whose strength varies by several orders of magnitude, although difficulties with the currently implemented control algorithm meant this feature was not utilised for the current study.

In addition to the receiving functions described previously, the RDAS also makes the data from the receiver modules available for acquisition by an IBM PC compatible computer, and provides a control interface between the PC and the transmitter modules. The RDAS is connected to the PC via a 50 way twisted pair ribbon cable and a National Instruments NI-AT-DIO32F data acqusitition card. Operation of the radar is completely controlled from software running on the PC.

The design of the RDAS hardware mandates that the digitally sampled in-phase and quadrature components from all active receive channels (up to 16) are read at a maximum latency of the order of a millisecond. This imposes a significant real time requirement for the PC acquiring the data if no samples are to be missed. The simplest method of achieving the required latencies was to run DOS (essentially a single task operating system) which could dedicate all CPU cycles to the acquisition program; the program itself was written in C and cross-compiled as a DPMI DOS application under Linux using djgpp with maximum compiler optimisations activated. Because the acquisition PC needs to be dedicated almost exclusively to the radar program it is not possible to arrange reliable remote connectivity since the system is only available to answer requests during times of no acquisition. A second PC (referred to as the 'analysis PC') is therefore utilised to carry out analysis of the digital time series and to provide remote access to the analysed data. The two are connected via a dedicated network with the acquisition PC running 'MS-Client' software allowing drive letter access to the disk on the analysis PC via 'Samba' (Tridgell et al. 1992-2000).

3.3.2 Software improvements

During the course of this study the author undertook a major upgrade of the radar control software [3]. In the form described by Vandepeer (1993) and outlined above, the control software had several limitations:

- control and status observation of the radar was only possible from the radar site,
- only one set of operational parameters could be specified to the system at any one time and these could only be changed by an operator physically present at the radar, and
- some decisions relating to control logic made when the system was initially set up meant that data acquisition was not always taken in intervals of two minutes in the event of unexpected delays.

In order to address these problems the author designed a file-based protocol which allowed the DOS acquisition program, at times when no data were being acquired, to communicate with a 'server' program running on the analysis PC. The server program (which was not constrained to respond only during non-acquisition periods) handled the interfacing between the intermittent file-based protocol and continuous user input provided by a graphical configuration program running under Xwindows. The configuration program, also written by the author, communicated with the server program via TCP sockets using the FTP protocol which allowed configuration of the radar from any machine with TCP access to the analysis PC.

Along with the implementation of the protocol described above, a number of other enhancements and fixes were also applied to the acquisition software by the author as part of this upgrade:

- support for flexible automatic sequencing of multiple experiment configurations was added,
- a number of buffer over-run conditions were fixed,

[3]This work was supported by Atmospheric Radar Systems Pty Ltd

- error handling was improved to facilitate reliable remote control, and
- the source code was verified which rectified several bugs and produced a warning-free compile under the latest djgpp releases.

The resulting improvements to the radar control software increased the overall reliability and consistency of the system and extended the flexibility of its operation.

3.3.3 Spaced antenna operation

Operation of the radar in spaced antenna configuration was simpler than for beam steering work. In this mode, three suitable groups of three dipoles each were selected as receiving antennas for the analysis. Transmission occurred on as many dipole triplets as there were transmitter modules with consideration being given to the creation of a beam with an acceptable polar diagram (for example, Holdsworth 1995). The majority of the spaced antenna results included in this report were collected with ten transmitter modules driving a total of thirty dipoles although results from mid-1999 onwards utilised up to twenty transmitter modules driving sixty dipoles.

Spaced antenna data acquisition involved running the transmitters for 102.4 seconds with an allowance of up to seventeen seconds for data transfer from the acquisition PC to the computer doing the FCA analysis. Data were thus acquired with a sampling period of two minutes.

3.3.4 Doppler beam steering operation

As previously mentioned, each transmission module is connected to a single PCM. A result of this arrangement is that there is complete flexibility when it comes to phasing different antennas — no two antenna triplets necessarily need to be in phase. The ability to arbitrarily program the phases of all transmission antennas relative to each other means that the transmission beam can be steered in any direction (within limits), not just the cardinals and vertical. Given an antenna located distance r from the centre of the array at an angle α to the north, the relative transmit phase $\Delta\Phi$

required to direct a beam at an off-zenith angle of ϕ in a direction θ to the north is given by

$$\Delta\Phi = \frac{2\pi}{\lambda} r \cos(\theta - \alpha) sin(\phi) \tag{3.1}$$

where λ is the operating wavelength of the radar. For the system under consideration, the resulting $\Delta\Phi$ must be rounded to the nearest multiple of 8.5° since this is the quantisation of the phasing system in use at 1.98MHz. When selecting antennas to use care must also be taken to ensure that the polar diagram of the transmission beam is reasonable.

Prior to an acquisition, each PCM was programmed with a delay calculated knowing the antenna's position and the desired beam direction using equation 3.1. For this study, beams in the four cardinal directions 11.6° off-zenith were used in addition to a vertical beam. In order to "steer" the beam on reception, the time series from each receiver were shifted in software by the corresponding $\Delta\Phi$ of the respective antenna, since design constraints prevented such delays being introduced using hardware.

When data collection was carried out with the radar operating in Doppler mode, the beam was directed in the cardinal directions north, south, east and west with a vertical acquisition between each; the resulting radial velocities were then used to allow unambiguous determination of horizontal and vertical wind velocity. The off-zenith angle used was nominally 11.6°. Each acquisition in a given direction lasted 102.4 seconds with approximately seventeen seconds of dead time to allow for data transfer to the analysis PC; an acquisition was therefore taken once every two minutes. This gave a sampling period of 16 minutes for each cardinal direction and 4 minutes for the vertical.

3.3.5 Operational difficulties

Unfortunately, routine collection of Doppler data were not possible over the duration of this project due to a series of incidents involving the MF radar at Buckland Park. Early in January 1998 lightning struck one of the antennas which severely damaged

the RDAS and inflicted minor damage to the control computer and several transmitter modules. This was rectified by May 1998; however, during trial Doppler runs at the start of July and October 1998, further previously unidentified problems were discovered in the transmitters which prevented more than ten modules being used simultaneously. With only ten modules driving thirty antennas the resulting beamwidth was not sufficiently narrow to give reliable Doppler results. By December 1999 work on the transmitters had progressed to allowing the use of up to twenty modules although there were still reliability problems with the second ten.

The Doppler run in October 1998 would have provided sufficient data for a limited optical/Doppler radar study. Unfortunately before the data could be backed up a hard disk failure destroyed all but a few isolated data files. The few surviving files and the limited data from the July 1998 run allowed analysis routines to be written and a proof of concept to be undertaken, but the full intercomparison originally envisaged was not possible.

During the period of downtime in 1998 it was further discovered that many of the MF antennas had drifted significantly from their ideal impedance. While this has marginal effects on the quality of FCA analysis it renders Doppler analysis difficult to impossible. Since the start of 1996 the decrease in the quality of the vertical wind component estimations provided through the routine analysis at Buckland Park was noted, and the discovery of the antenna impedance problems explained this observation. During 1998 and 1999 problems with numerous antennas — including water in cables, weather damage to balans and fallen dipoles – were progressively rectified.

Spaced antenna data were available from the Buckland Park MF radar for significant periods between 1991 and 2000; almost continuous FCA wind data were accessible for 1992–1994, the last half of 1996 through to 1997, and 1999–2000. Due to the problems discussed above, no spaced antenna data were available for significant periods during 1998. Even during the ‘continuous’ periods, short periods of downtime (usually less than a week) did occur resulting from full hard disks and minor hardware

breakdowns. The frequency of the filled hard disks decreased considerably in the latter part of this project due to the commissioning of a fulltime network link to the field site, which made it much easier to keep track of disk usage and to transfer data when appropriate.

3.4 Davis MF radar

Although it was originally intended to use photometer and radar data from Davis to complement that from Buckland Park, practical difficulties outlined elsewhere prevented this from occurring. For reference, details of the MF radar at Davis are included as an appendix.

chapter 4

Data processing and analysis

This project had two main areas of focus: the identification of wave parameters observed in individual nights of airglow data, and the study of the long-term properties of both the airglow and radar data. This chapter outlines the separate processing carried out on each instrument's data before moving on to a description of the long-term analysis.

4.1 Photometer data

As mentioned in a previous chapter, the photometer at Buckland Park developed a number of hardware faults during the course of data collection for this study. In order to deal with this as transparently as possible, it was decided that a data preprocessor should be written which corrected all fixable faults and warned about the presence of those which could not be rectified (like for example, an open circuit dynode resistor). This greatly simplified the analysis programs since they could assume that the data were in a usable form with no missing records, noise spikes and other corruptions. All the complexity for dealing with the numerous faults was isolated into the preprocessor, making it easier to maintain both it and the analysis software.

Once the preprocessor had been run, each data file not affected by an unrecoverable hardware error was visually inspected for quality and presence of cloud. Cloud presence

was typified by a high correlation between the three fields and a noisier overall signal. This allowed compilation of acceptable files of high quality which were to be used for subsequent analysis.

4.1.1 Data preprocessor

Two different types of noise spikes were evident in the data — those many orders of magnitude above the data being recorded, and some roughly 25% above the signal. The "duration" was always a single record; that is, less than twenty seconds. Physical observations suggest that the origin was of a transient nature (such as electrical high current switching noise) although occurrences did not seem to correlate with air conditioners/coolers operating in the instrument's vicinity. A peak detection routine was developed which was capable of reliably sensing both these spike types and correcting for them using linear interpolation.

Dark counts (normally taken every fifteen minutes) were sometimes not correctly recorded. This could be caused either by the shutter failing to shut properly or more commonly a noise spike occurring during an otherwise normal dark count. Interpolation was used to correct for this, using good dark counts either side of the affected one.

At times, peaks with a duration of 2 minutes were observed in a single field at only one wavelength at a given time. An example of such a peak is shown in figure 4.1. They were typically observed at different times in both the 730nm and 558nm time series and there was no detectable correlation between fields or wavelengths. It was not possible to conclusively identify the origin of these although the cause is interesting in its own right. Checks of HV supply voltages and cable integrity suggested that the source was not from the photometer hardware itself. At the same time the nature of the peaks seemed contrary to the behaviour of the airglow layers being observed, and such events have not been observed with other similar instruments or airglow imagers. Dewan & Ricard (1998) describe the observation of a 'mesospheric bore' in OH airglow results from the ALOHA-93 campaign which do give rise to a sharp increase in OH intensity

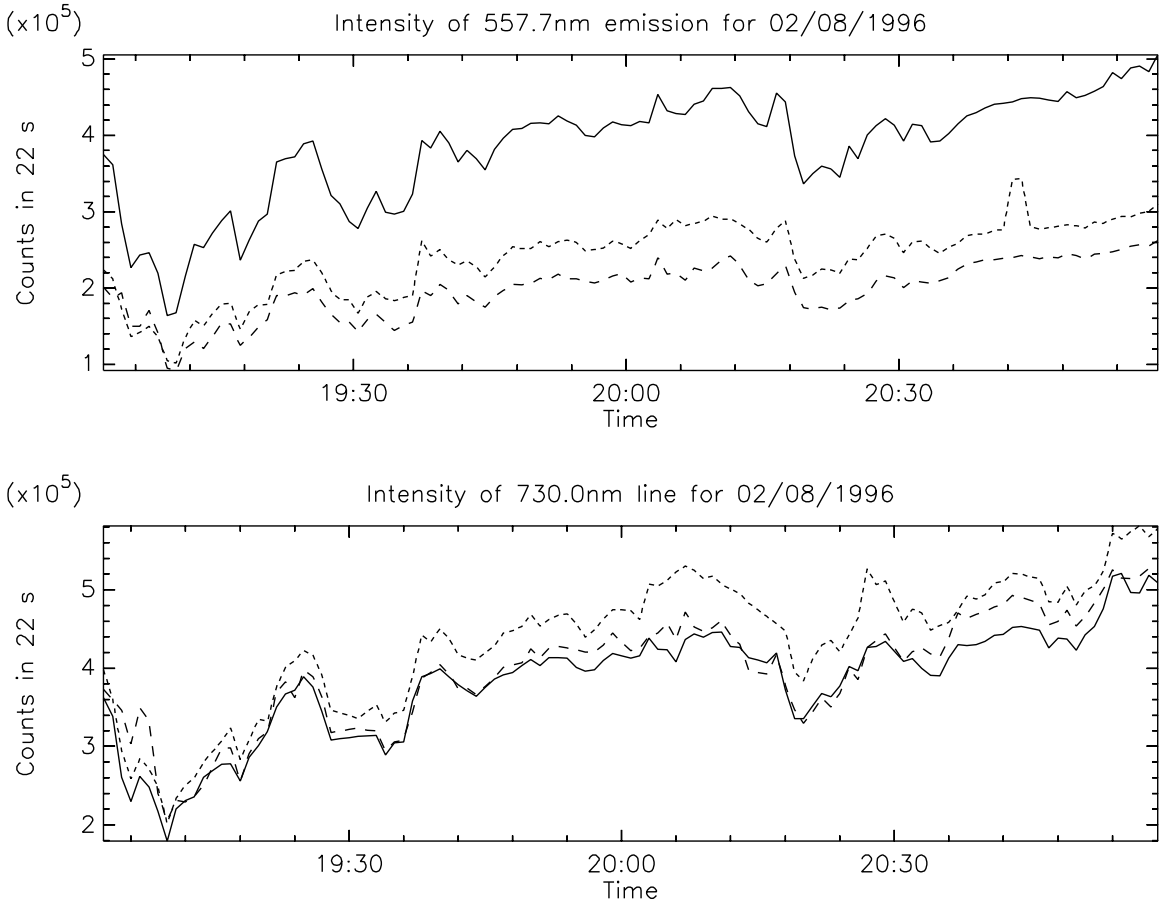

Figure 4.1: Data from 2 August 1996 showing the occurrence of a peak of 2 minutes' duration in field 3 (dotted trace) of the 557.7nm emission near 20:45. (Field 1 is the solid trace and field 2 is the dashed trace.)

but the effect from such a feature lasts for the order of 30 minutes — much shorter than what was observed in this study. The lack of field correlation in the present study also suggests it is not related to the effects described by Dewan & Ricard (1998). In addition, although models suggest lightning can produce mesospheric emissions (Veronis et al. 1999) the observing geometry, enhancement duration and local weather conditions during the present study rule this out as a possibility. It was therefore concluded that some other mechanism was giving rise to these changes and they were therefore removed from the time series using linear interpolation.

A number of hardware faults developed at various times during data collection which had varying effects on the data. The most obvious one was the failure of a resistor in one of the photomultiplier dynode chains. The effect of this was a time

series of zeroes. In this case, the preprocessor simply alerted the operator to the string of zeroes since there was no data available from which to reconstruct the missing field. With only two of the three fields operational, data affected by this fault could only be used for intensity studies since meaningful horizontal wave parameters could not be resolved.

Another hardware fault was ultimately traced to the lightning detector. The same interference which caused the large noise spikes in the time series could also falsely trigger the detector resulting in a loss of data for roughly fifteen minutes. Once again linear interpolation was used to fill the gap in the time series.

During 1997 and 1998, a problem with the filter wheel developed whereby the requested position would not be reached in time for a record to start at the next 30 second boundary. This was ultimately observed to be caused by the wheel not moving at all due to oil leaking from the gearbox onto the drive rotor and causing slippage. Prior to 12 August 1997 such a fault would cause all subsequent acquisitions to be displaced thirty seconds from their proper place, necessitating interpolation to replace them onto their proper time grid. This was not implemented in the preprocessor due to the relatively small number of data files affected up to that date. Following 12 August 1997 the control software was altered such that this synchronisation problem did not occur in the presence of the wheel fault. In the latter case interpolation over just two records was enough to rectify the fault.

Very late in the study (from about the middle of April 2000) evidence of the filter wheel fault reappeared in the raw time series. While cleaning the drive rotor and associated mechanics of oil and metal filings did reduce the occurrence of the fault it did not totally eliminate it. Fortunately the quality of the data used for this study was not adversely affected by the re-emergence of this problem, the cause of which is still the subject of on-going investigations.

4.1.2 Background filter techniques

The primary goal of the background filter was to remove contamination caused by the galactic center of the Milky Way passing through the field of view of the photometer. At Buckland Park, such contamination was mostly confined to OH observations made during the months from May through to September. The contamination showed up as two periods of large amplitude oscillations with period approximately 30 minutes. Generally the first oscillation was about half the amplitude of the second. An example of typical contamination can be seen in figure 4.2(a), where the Milky Way is evident between 11pm and 1am. The exact location of the contamination varied across the night according to the time of year, from 3am in April to 8pm in September. While the shape of the contamination resembled a double Gaussian, the exact form was observed to vary from night to night. This is attributed to differing background noise behaviour, varying lower atmospheric conditions altering the transmission of light, and varying galactic cross sections being transected by the fields.

The Milky Way contamination could not be ignored since its properties meant that the spectral analysis would often identify components of it as valid phase velocities. Since the contamination affected data from over 40% of the year, an effective filter was sought to allow the use of this data without any uncertainty associated with the Milky Way.

A number of alternative filtering approaches were considered as discussed below, with evaluation of all but the first method carried out using a simulated dataset (see figure 4.4). The "Signal" was generated using a noise function whose power spectrum followed a power law of the form $S(\omega) \propto f^{-k}$. A value of $k = \frac{5}{3}$ was chosen to be representative of typical gravity wave spectral slopes as discussed by Vincent (1984). The Milky Way was simulated with a pair of Guassians. Comparison with actual data (from for example, 20 June 1996, as in figure 4.2(a)) showed that the simulated data behaved in a similar way, although observed data did not contain components of period ≈ 1 hour with as high an amplitude. A simulated signal was used to allow comparison

between the original signal and the signal recreated from the contaminated signal. To quantify the differences, a variance value σ was calculated between the filtered and original signals:

$$\begin{aligned} \sigma^2 &= \frac{1}{n-1}\sum_{i=0}^{n-1}(x_i - s_i)^2 \\ \sigma &= \sqrt{\sigma^2} \end{aligned} \tag{4.1}$$

where n was the number of points in the dataset, the set of x_i were the data output from the filter and the set of s_i were the original signal.

The first method was evaluated using data collected on 20 June 1996 as in figure 4.2(a).

4.1.2.1 Subtraction of an average background

This was the most straightforward method trialled. To form the background, a number of clear nights were averaged after shifting the nights to align the Milky Way contamination and normalising to allow for inter-night intensity variation. The normalised average background was then subtracted from the normalised data series of interest. It became clear that all three fields needed different backgrounds since the shape of the contamination did vary significantly between the fields.

While this method did go some way towards reducing the contributions from the Milky Way, the variation in shape from night to night often left a substantial residue after subtraction which was still sufficient to contaminate the cross spectral analysis. An example of the typical behaviour of this filter is shown in figure 4.2. It is worth noting that there was considerable short period activity present in the average background — these features had comparable amplitude to features with similar periods in the signal proper, which is illustrated in figure 4.3. This shows that significant contamination of short period signals can occur with the use of this approach. In addition, application of this filter is unsuitable for nights where no contamination occurs; if this method was to be employed, an effective detector would have to be used to trigger the filter when required.

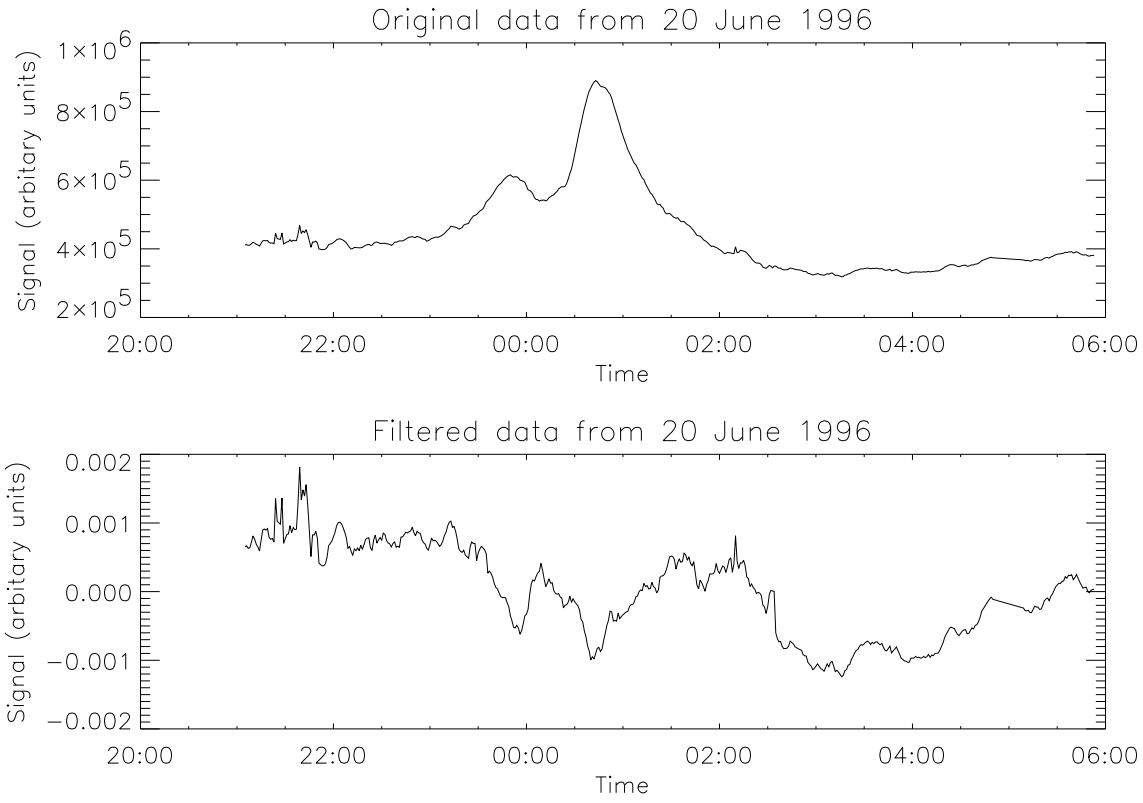

Figure 4.2: (a) (top) Data from 20 June 1996 showing typical Milky Way contamination in the photometer data. (b) (bottom) Performance of the average background subtraction filter method when applied to the data in (a). The average background was computed using the data from 8 obviously clear nights during the period of May to August 1996.

4.1.2.2 Fourier amplitude filter

The Fourier amplitude filter (and all subsequent filter techniques) were evaluated using the simulated data shown in figure 4.4.

This method was observed to be more successful than the subtraction of the average background. To filter the data, each time series was first windowed with a 10% cosine taper at each end to reduce the amplitude of the side lobes in the spectral window and hence increase the reliability of the spectrum (Jenkins & Watts 1968). After being Fourier transformed, components greater than an experimentally determined threshold were zeroed. The time series was then recreated by applying the inverse Fourier transform.

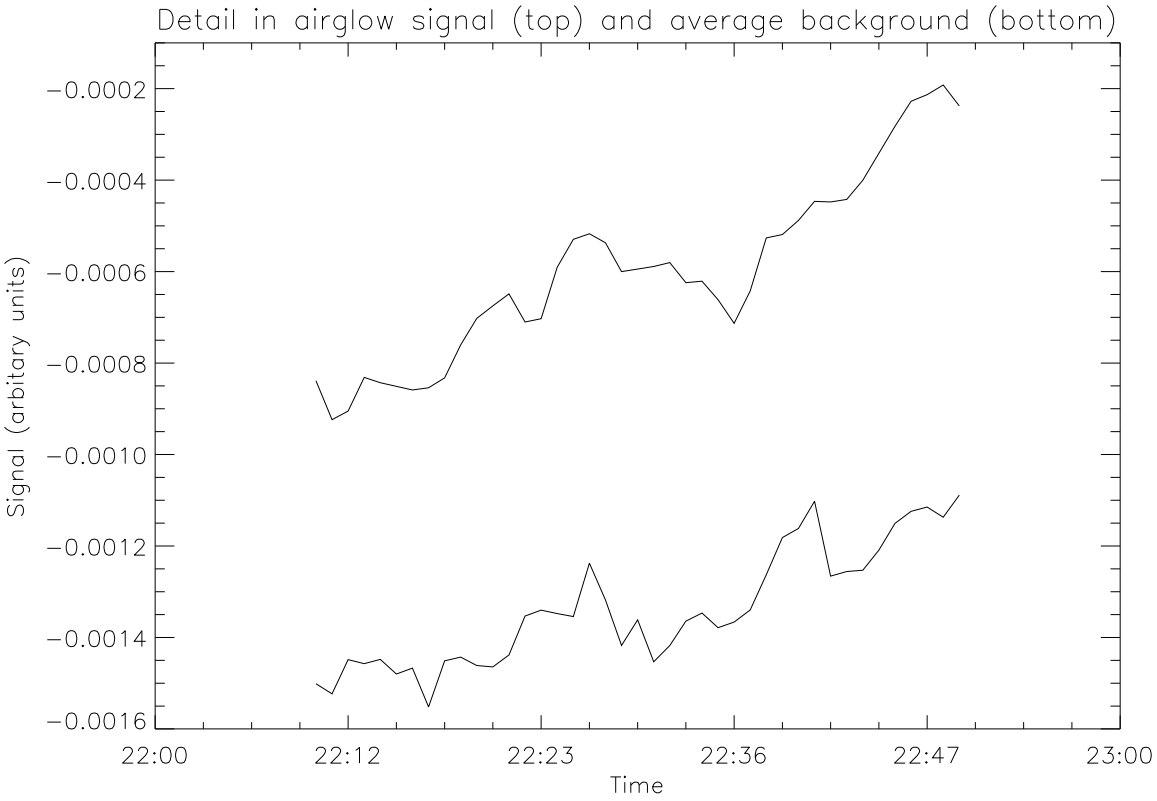

Figure 4.3: A plot on an enlarged Y scale showing the higher frequency detail of an uncontaminated area of the signal (top) and the average background in the same region (bottom). It is clear that significant variations occur with similar amplitude in both, which shows that subtraction of the average background will affect frequencies of interest.

The threshold was determined using model data, and was chosen to give the smallest total absolute deviation between the original and recreated signals. Fifty times the average of the lowest 10 components was deemed the most successful.

Figure 4.5 illustrates the typical performance of this filter method. While the Milky Way is removed, it is clear that long period activity with moderate amplitude is also deleted from the time series. The variance as defined by equation 4.1 was of the order of 2.0×10^4 units^2, where 'units' refers to the arbitrary units of the simulated dataset. For brevity, formal notification of this will be omitted from the variances reported for subsequent filter trials.

It is also evident that this method introduces artifacts of significant amplitude with period the order of 30 minutes. This corresponds to the period of the Milky

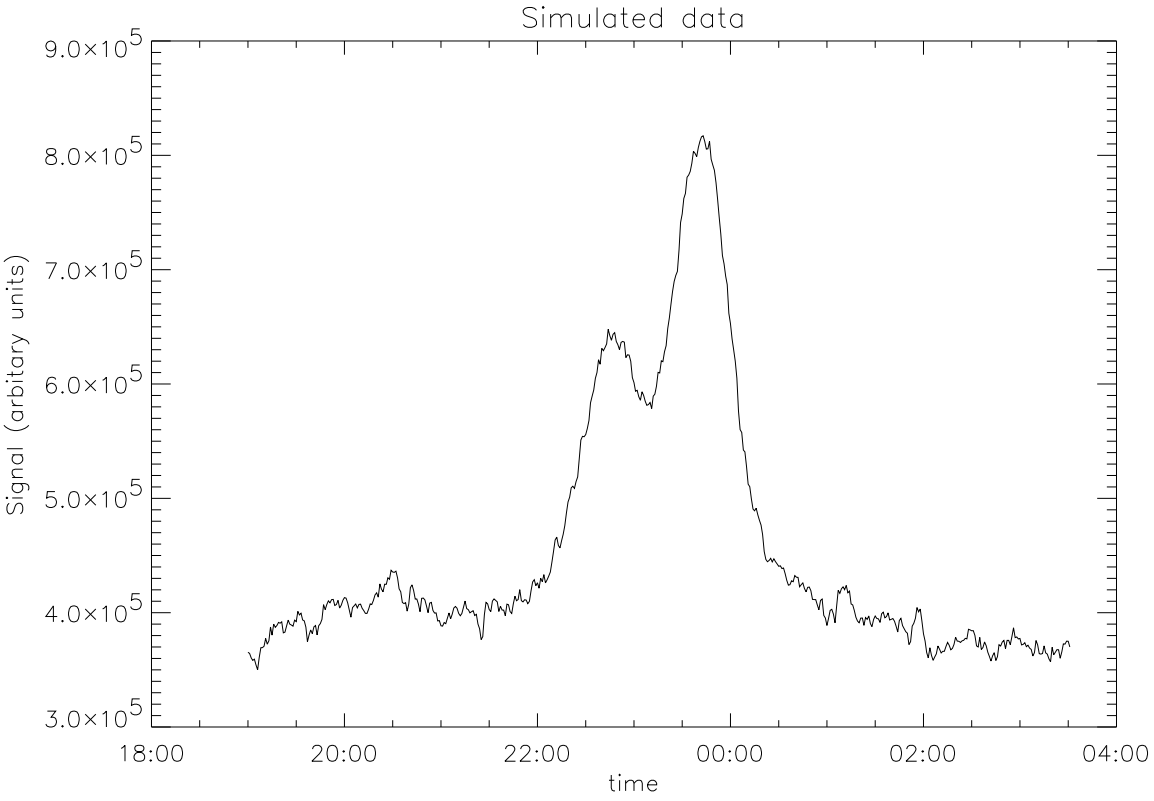

Figure 4.4: Simulated photometer data used to evaluate filter methods

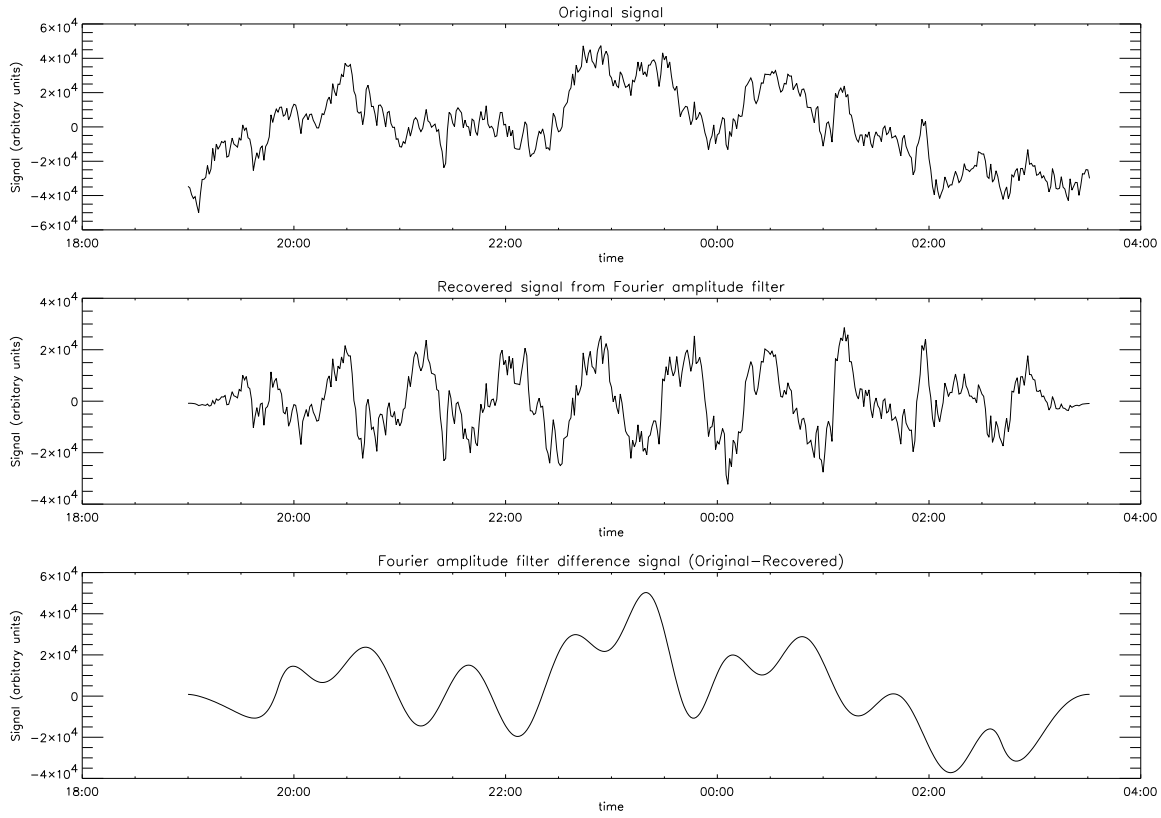

Figure 4.5: Typical performance of the Fourier amplitude filter demonstrated with simulated data. The upper plot shows the simulated signal. The middle plot shows the signal which was recovered using the Fourier amplitude filter, with the difference between the two demonstrated by the lower plot. It is clear that the amplitude of the signal with period approximately 60 minutes has been substantially enhanced through the use of this filter.

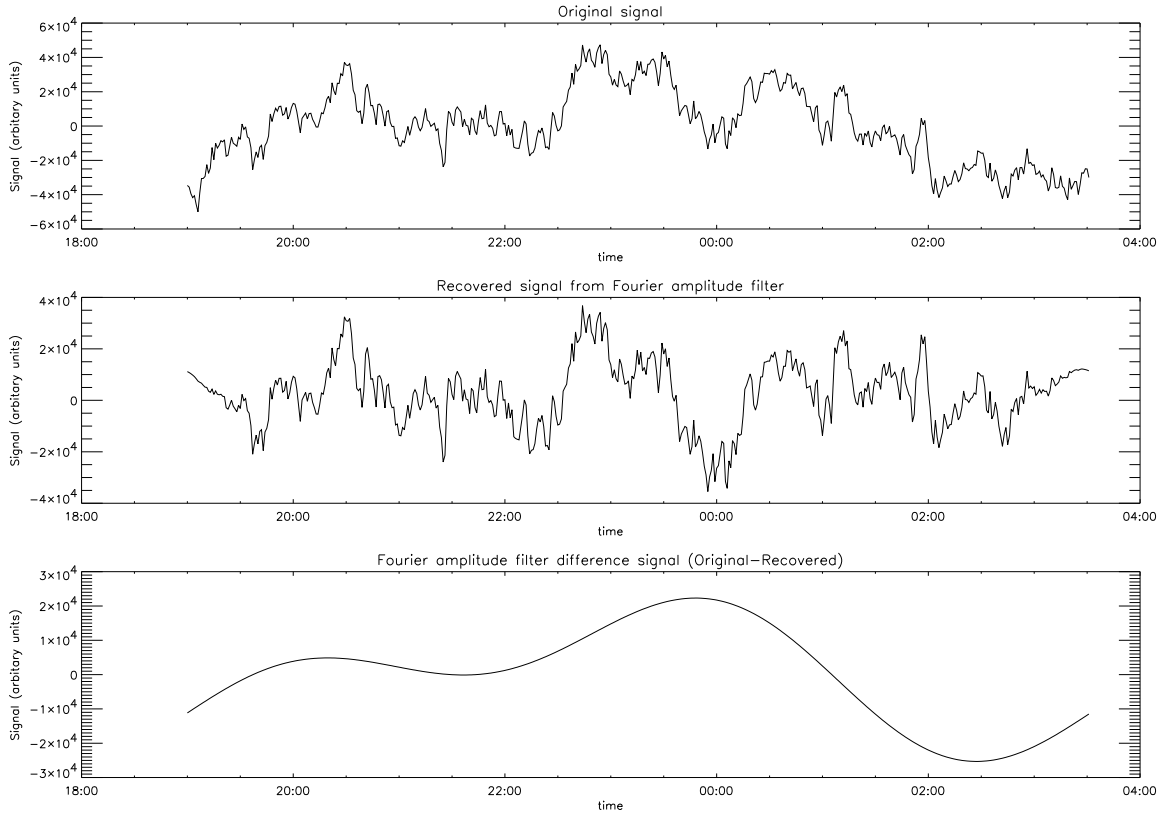

Figure 4.6: Performance of the Fourier amplitude filter when presented with uncontaminated data. Visually the performance is very good, with only long period information adversely affected.

Way contamination and results from the continuous nature of the Fourier components across the time series. The major disadvantage of this method is that activity with similar period(s) to the Milky Way contamination is affected across the entire time series, rather than simply in the originally contaminated region.

Ideally, any filter designed to remove the Milky Way should have no effect on uncontaminated data. The performance of this filter on such data was reasonable, as shown in figure 4.6, with a variance of the order of 1.5×10^4 from the original signal. The signal was the same as used for figure 4.5. While some long period information is lost, there are no substantial artificial periodicities introduced in this case.

4.1.2.3 Fourier phase filter

The assumption behind this method was that Milky Way contamination would be present in all three channels with ideally zero phase observed between fields. That is, it assumes that contamination varies much slower than the airglow intensity, and that the spacial scale is much larger. After windowing with the aforementioned cosine filter, cross spectra between all 3 fields were formed and components with phases less than 0.05 radians were identified as being indistinguishable from zero at the 95% confidence level (Jenkins & Watts 1968). Where such phases were observed in two or more cross spectra, the corresponding components in the Fourier transform of the time series were zeroed, with the time series being recreated by an inverse Fourier transform.

While this method successfully dealt with the background components, it was not able to remove the Milky Way due to the significant phase difference observed between fields. This effect is clearly illustrated in figure 4.7. It could be seen that due to this limitation, the difference between the recovered signal and the original was roughly an order of magnitude larger than for the amplitude based filter, which was reflected by a higher variance of 5.0×10^4. It was observed through experimentation that the choice of the phase threshold did not affect the results over the range 0.01 to 0.1 radians.

Like the amplitude based Fourier filter, the performance of this filter does improve if the data are not contaminated. However, figure 4.8 (and typical variance figures of between 1.5×10^4 and 2.0×10^4) showed that it was not as good as the amplitude based filter: the differences were slightly higher, and significant high frequency information was removed.

4.1.2.4 Wavelet filter method

Unlike Fourier components which extend right across a time series, wavelet components are localised. Since the contamination from the Milky Way was also observed to be generally localised in time, a wavelet based filter was trialled.

Here we follow the development of Chui (1992). We let $\mathbb{R}$ denote the set of real

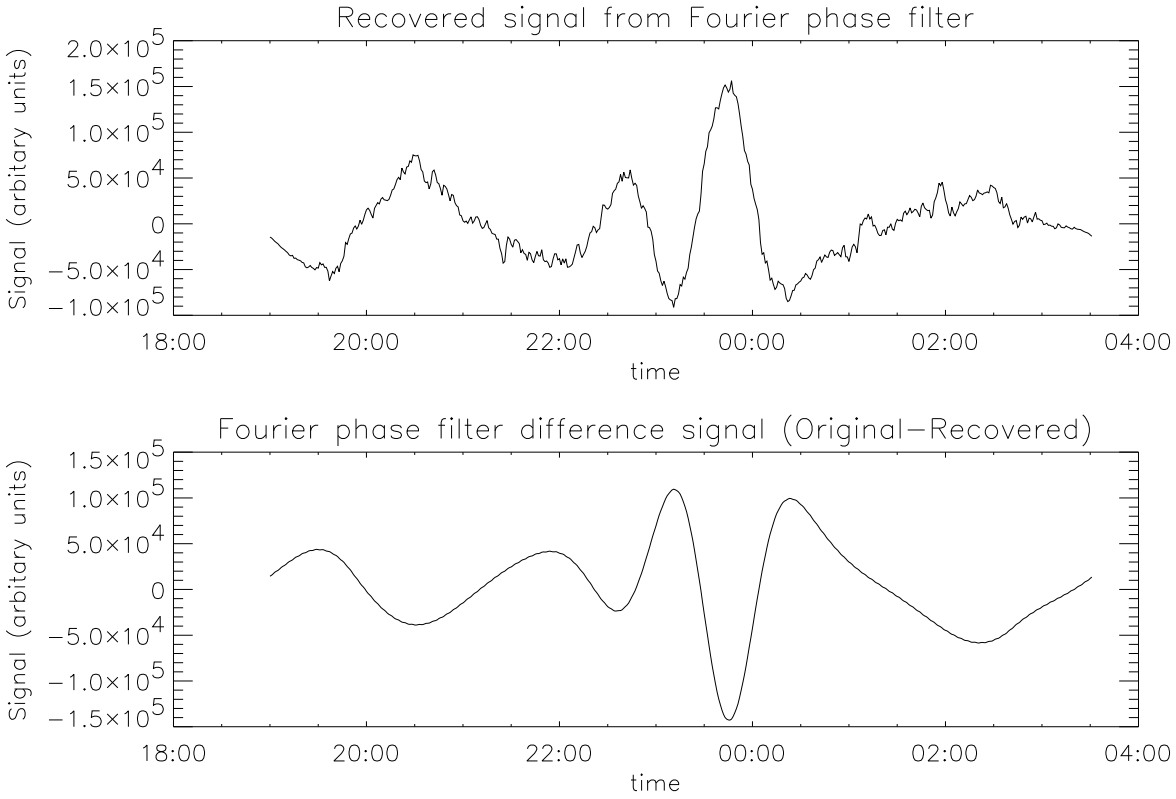

Figure 4.7: Typical performance of the Fourier phase filter. It is clear that substantial traces of the Milky Way remain in the signal.

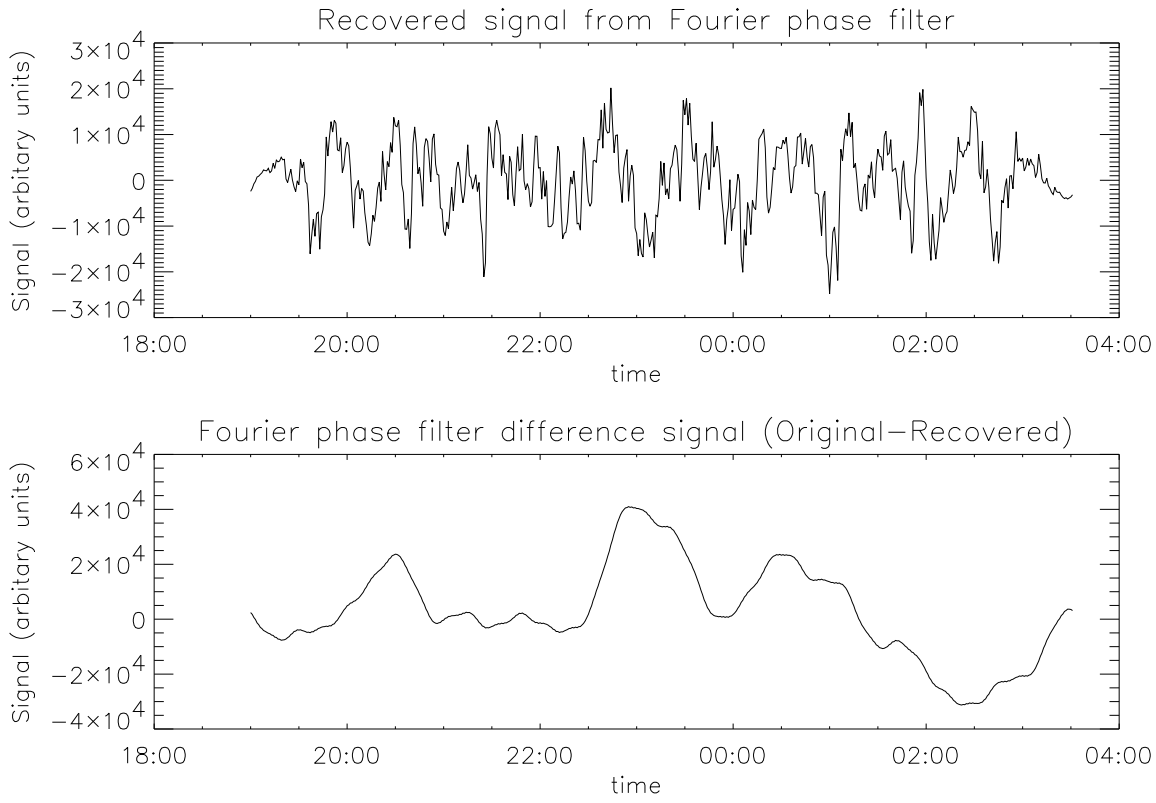

Figure 4.8: Performance of the Fourier phase filter on uncontaminated data

numbers. A wavelet transform involves the mapping of a signal onto the function space defined by the family of functions

$$\psi_{a,b}(x) = |a|^{-1/2}\psi\left(\frac{x-b}{a}\right) \qquad a, b \in \mathbb{R}, a \neq 0 \tag{4.2}$$

generated from the single function $\psi(x)$, where $\psi(x)$ satisfies the so called *admissibiliy condition*

$$C_\psi = \int_{-\infty}^{\infty} \frac{|\Psi(\omega)|^2}{\omega} < \infty. \tag{4.3}$$

$\Psi(\omega)$ is the Fourier transform of $\psi(x)$. With appropriate normalizations, this mapping can be energy preserving. The family of functions $\psi_{a,b}$ are termed *wavelets*. The choice of $\psi(x)$ (the so-called *mother function*) determines the form of the basis functions $\psi_{a,b}$, while the parameters a and b specify the translation and dilation of the mother function. If $\Psi(\omega)$ is continuous, the admissibility condition is equivalent to requiring $\psi(x)$ to have a zero mean with a decay to zero at infinity (although in practice there are no continuity requirements on $\Psi(\omega)$).

When the parameters a and b are made to vary continuously, the resulting wavelet transform is termed the Continuous Wavelet Transform. However, for this analysis the Discrete Wavelet Transform (DWT) was used since the wavelet expansion coefficients can be independent and the computation time is much reduced. As the name suggests, the DWT corresponds to the use of discrete values of a and b. If we first restrict a such that $a > 0$, the admissibility condition of equation 4.3 becomes (Chui 1992)

$$\int_0^\infty \frac{|\Psi(\omega)|^2}{\omega}\, d\omega \;=\; \int_0^\infty \frac{|\Psi(-\omega)|^2}{\omega}\, d\omega \;=\; \frac{1}{2}C_\psi < \infty. \tag{4.4}$$

The values of a and b can then be quantised such that

$$\begin{aligned} a &= 2^{-m}, \\ b &= \frac{n}{2^m} \qquad \text{for } m, n \in \mathbb{Z}, \end{aligned} \tag{4.5}$$

(where $\mathbb{Z}$ is the set of positive integers) so long as further restrictions on $\psi(x)$ (Chui 1992) are observed. For convenience, we now define

$$h_{m,n}(x) \equiv \psi_{a,b}(x) \tag{4.6}$$

for a,b as defined by equation 4.5.

Finally, if independent wavelet expansion coefficients are desired (as for this study), the choice of $h(x)$ is restrained by the orthogonality requirement

$$\int_{-\infty}^{\infty} h_{m,n}(x)h_{p,q}(x)\,dx = A\delta_{np}\delta_{mq}, \tag{4.7}$$

where A is a normalizing factor and m, n, p and q are as defined by equation 4.6.

After Daubechies (Daubechies 1988), the DWT of a function f corresponding to a mother function ψ can be written

$$W_h f(m,n) = \int \overline{h_{m,n}(x)} f(x)\,dx, \tag{4.8}$$

or equivalently

$$W_h f(m,n) = 2^{m/2} \int \overline{\psi(2^m x - n)} f(x)\,dx, \tag{4.9}$$

where $W_h f(m,n)$ are termed the wavelet expansion coefficients. This corresponds to a series of convolutions of the translated and dilated mother wavelet with the data series f.

Given that the admissibility condition (equation 4.4) holds, the wavelet transform is invertible. For the case of orthogonal wavelets, this allows the original signal to be recreated from the wavelet coefficients (Shimomai et al. 1996):

$$f(x) = \sum_m \sum_n h_{n,m} W_h f(n,m) \tag{4.10}$$

The above theory assumes a continuous function $f(x)$. If, however, $f(x)$ is a sampled time series (for example) with N regular samples, the values of m and n can be limited to

$$\begin{aligned} 0 &\leq a = 2^{-m} < N, \\ b &= \frac{k}{2^m} < 1. \end{aligned} \tag{4.11}$$

This demonstrates that for larger scales (larger a, smaller m), the number of wavelets (and hence wavelet expansion coefficients) decreases.

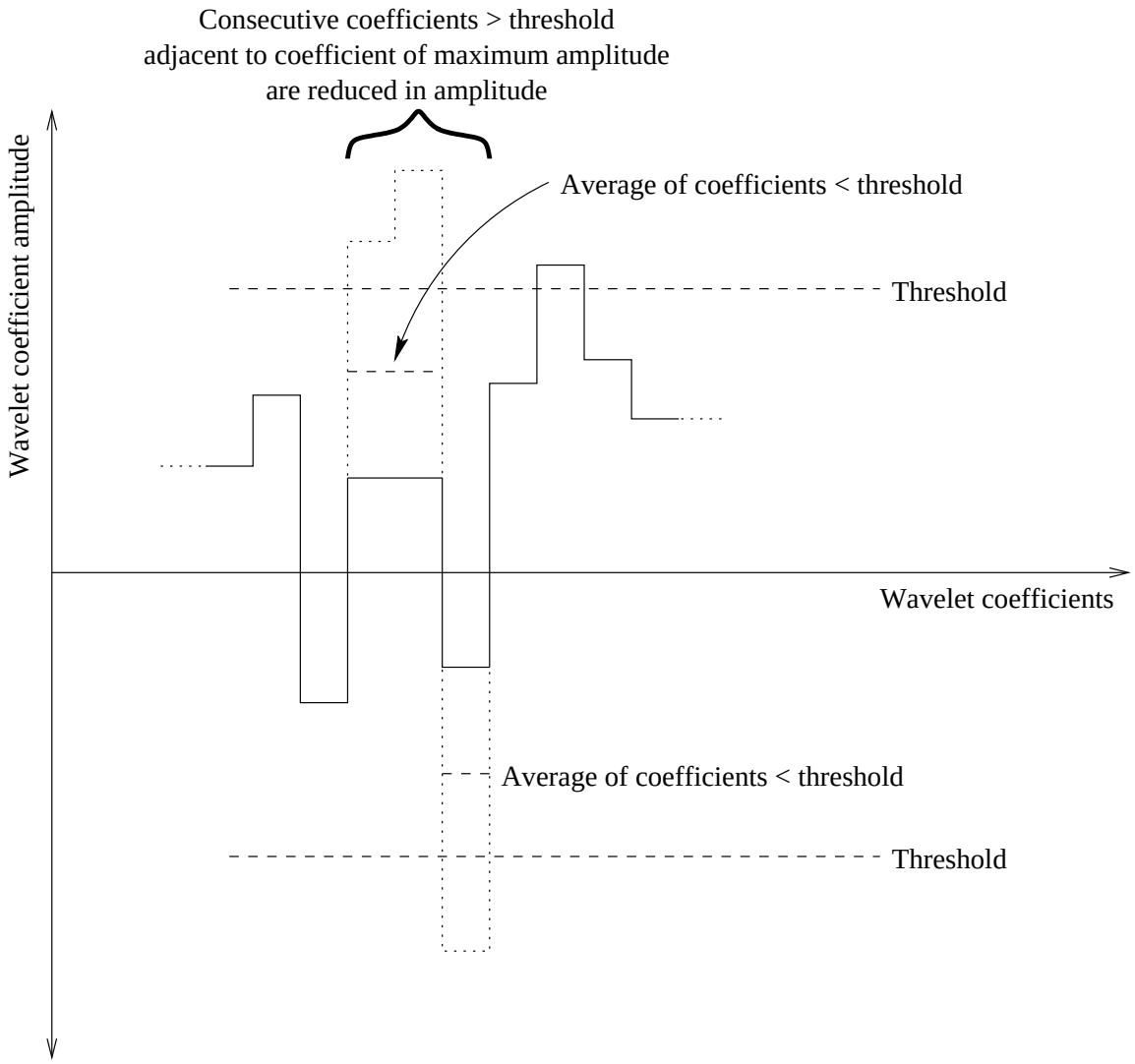

Figure 4.9: Schematic representation of the functionality of the wavelet filter.

For this filter application, the wavelet transform (and its inverse) was calculated using the wavelet transform algorithms as described by Press et al. (1986) and Mallat (1989). Independent wavelet coefficients were desired since they make it much easier to identify large amplitude coefficients with specific features in the original time series. This has obvious advantages when the wavelet transform is being used to filter a time series.

Each time series was treated separately by the filter which is illustrated diagramatically in figure 4.9. The mean of the time series was first subtracted, with the resulting series windowed with a 10% cosine taper to reduce discontinuity effects at

the ends. To increase the reliability of the wavelet coefficients (particularly at the ends of each scale), each end of the time series was then zero padded with at least 64 zeros to a length of the next highest power of 2 (Shimomai et al. 1996). A wavelet transform as described by Press et al. (1986) was then used to generate a series of wavelet coefficents which were subsequently dealt with in 5 blocks. The first block comprised of coeffients 0 to 7, corresponding to the longest period features. These were observed to be the most seriously affected coefficients when the Milky Way was present. The other blocks comprised of coefficients grouped according to decreasing scale: coefficients 8 to 15, 16 to 31, 32 to 64, and 65 onwards respectively. For each block except the last, the component with maximum amplitude was identified. If this was above a predetermined threshold, it was marked. Components were then marked out from the maximum until an amplitude below the threshold was observed. The marked components were considered contaminated, and were replaced with the average of unaffected (that is, unmarked) coefficients within the block, with the sign preserved. If all components were affected, they were set to 10% of the threshold, again preserving the sign. Thresholds were determined experimentally using modelled and real data. Time series were recreated by applying an inverse wavelet transform.

The method was originally developed using the Daubechies-20 wavelet (Daubechies 1988). However, since this wavelet is rather non-localised, artefacts of the filter were observed in data which should have been unaffected by the filter. The Lemarie wavelet as described by Mallat (1989) was applied and was seen to give a much better result. The optimium number of coefficients for this application was determined to be 32; an example of the typical performance of this filter is shown in figure 4.10. Variances as given by equation 4.1 were of the order of 1.5×10^4.

The advantage over the Fourier based methods was that due to the localised nature of wavelets, components with period the order of 30 minutes (the same as the Milky Way contamination) were removed only in the vicinity of the contamination. In principle this would retain any information in these frequency components in areas totally unaffected by the Milky Way. The fine detail of the signal was also not affected.

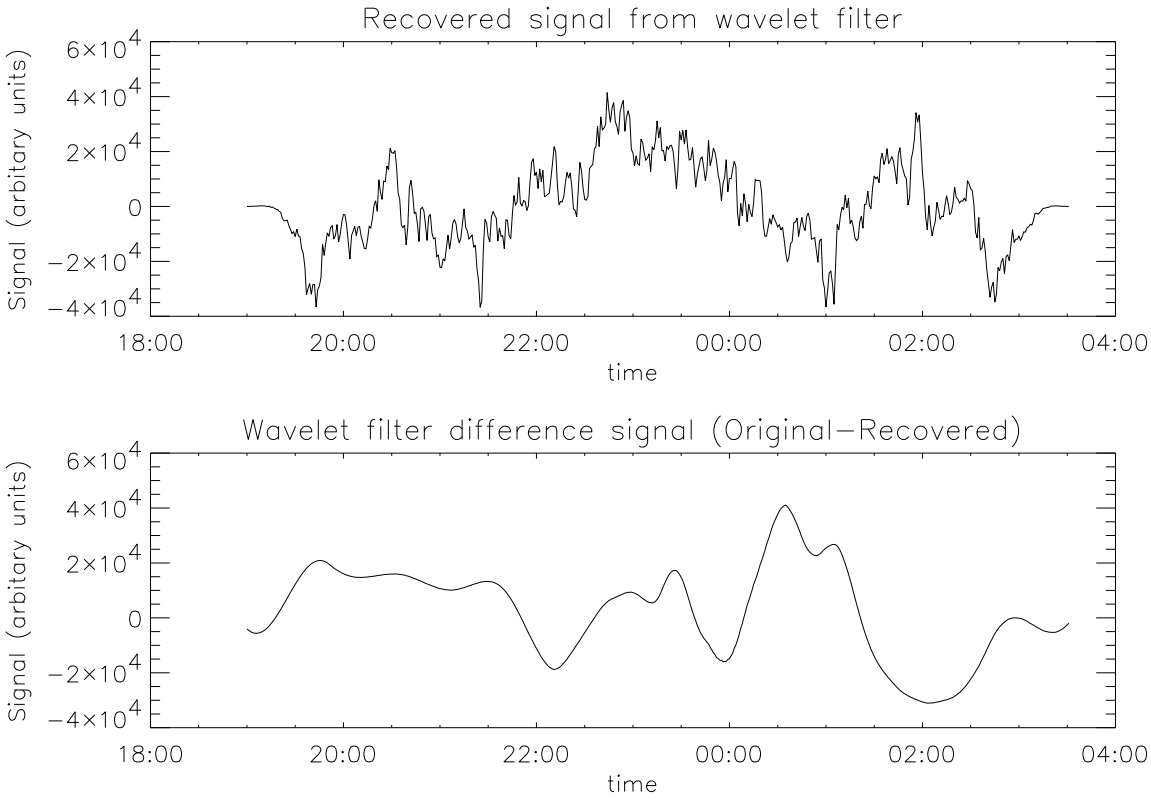

Figure 4.10: Typical performance of the wavelet based filter. The simulated signal is the same as that used for for figure 4.5. The upper plot shows the signal recovered using the wavelet filter, while the difference between this signal and the original is shown below. It is clear that in areas uncontaminated by the Milky Way (that is, the ends) the wavelet filter has had little impact on the signal, in contrast to the Fourier amplitude filter. Of note is the absence of any enhanced amplitudes.

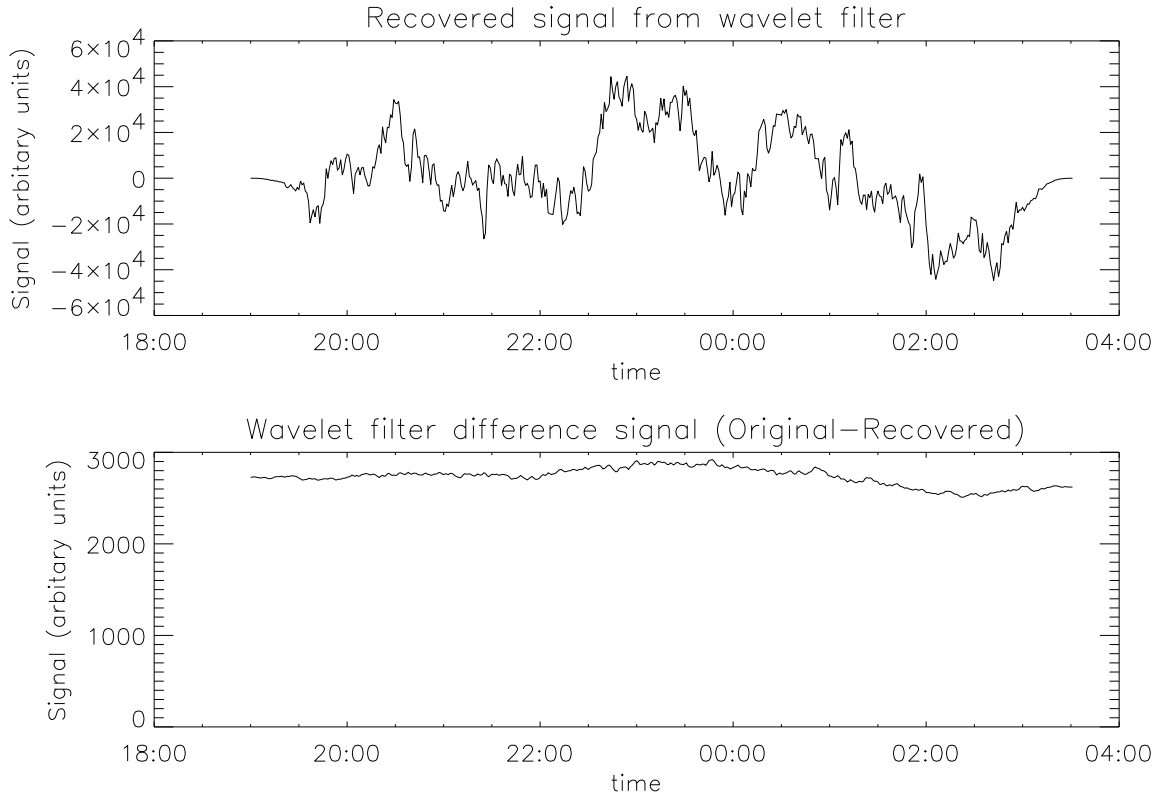

Figure 4.11: Response of the wavelet filter to uncontaminated data. The difference between the recovered signal and the original is insignificant given the magnitude of the signal.

Perhaps not surprisingly, any large amplitude variation in the intensity is removed (or at least affected) by this method. This unfortunately includes tidal period variations. As expected, the greatest effect on the signal occurs in the region of contamination, with only minimal short period ($\lesssim$ 1 hour) effects elsewhere.

When uncontaminated data were provided the wavelet filter did very well, resulting in a mainly DC offset between the input and output of the filter as shown in figure 4.11. This observation was backed up by typical variances from the original signal (equation 4.1) of between 2.5×10^3 and 5.0×10^3 — between five and ten times less than those observed for the Fourier-based filter techniques.

4.1.2.5 Filter method summary

When focused on the analysis of data from individual nights for the purposes of the identification of waves present over that night, the only advantage to the average background method was that it had the potential to preserve long period activity not associated with the Milky Way. However, due to nightly variations in intensity, significant residue still remained after application of this method. The greatest disadvantage of this method, though, was its effect on short-period signals. Since these were the signals of interest in this study, contamination of these at the levels encountered with this method was unacceptable.

It is clear from figure 4.7 that the Fourier phase filter was totally unacceptable for this application due to the large residue. The strength of the method was that it successfully removed background trends. Unfortunately though, the Milky Way does not present itself as a background identical in all fields and it is therefore not effectively filtered with this method.

The effects of the wavelet and Fourier amplitude filters are further illustrated in figures 4.12 and 4.13. These show wavelet transforms of the indicated data using a Daubechies wavelet filter to give a qualitative indication of the frequencies affected by the filters and the time span of the effects. Both figures use the same colour scale to represent wavelet amplitude, which is an indication of amplitude of the periodic components in the signal being analysed. Figure 4.12 deals with contaminated data whereas figure 4.13 illustrates the effects of the filter on uncontaminated data, which gives an indication of how well tuned the filter is for the specific signals being removed. For both figures, the performance of the filter is presented in terms of the data itself and the difference between the recovered signal and the original simulated time series. In the case of the Fourier amplitude filter, an exclusion affecting all data with periods greater than 100 minutes is clear, whereas the wavelet filter affects these periods significantly only at times where the Milky Way was present. Both filter methods performed well when acting on data with no contamination, although the wavelet filter

clearly retained almost the entire spectrum whereas high periods were still affected by the Fourier amplitude filter.

The differences between the recovered and original signals were of similar magnitude for both the wavelet and Fourier amplitude filters when contaminated data were processed. The primary problem with the Fourier amplitude filter was that, as typified in figure 4.5, artificial periodicities of significant amplitude were introduced into the time series. Since the phase of these periodicities was determined by the location of the Milky Way contamination within the time series, they would affect the cross spectral analysis in the same way as the original contamination.

The wavelet method did not introduce significant artificial signals. It is worth noting that long period signals with large amplitudes were affected, especially around the times what Milky Way contamination was present. However, such signals, having periods of the order of three hours and greater, were of marginal interest for the section of this study for which this filter was developed. The method resulted in very little Milky Way residue while not affecting the short period signals, and overall its application was shown to produce the least variance between the original and recovered data. Thus it was determined that for the purposes of identifying waves present in the data from individual nights, the wavelet approach was more workable while producing the least number of undesirable side effects.

4.1.3 Cross spectral analysis

Cross spectral analysis techniques were used on the time series acquired by the photometer to deduce apparent wave parameters of gravity wave induced disturbances in the OH and OI airglow emissions. The methods used are similar to those described by Jacob (1985) and to a certain extent, Giers et al. (1997). Each emission channel (OH at 730nm and OI at 558nm) were treated separately.

The three filtered time series from the photometers were windowed with a 10% cosine taper as before to reduce edge effects (Jenkins & Watts 1968). The prior application of the wavelet filter effectively removed the DC offset component which

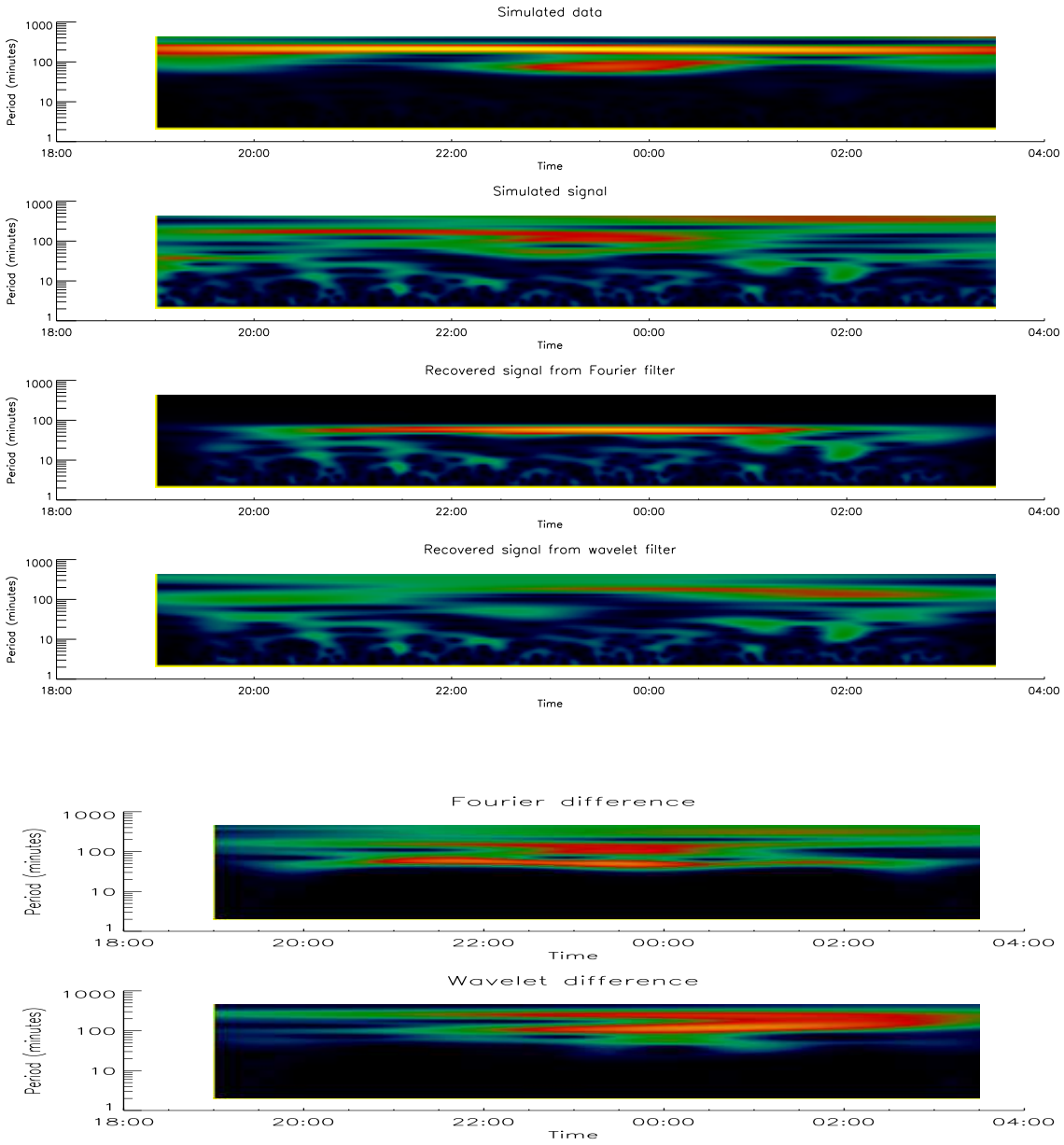

Figure 4.12: The performance of the filters on contaminated data as shown using a wavelet transform. The upper plot shows the simulated data which includes the Milky Way contamination, followed by the simulated signal. The signal recovered by the Fourier amplitude filter and the wavelet filter, and the differences between these and the original simulated signal, complete the figure. All plots use the same colour scale to indicate wavelet amplitude, which is an approximate indication of the amplitude of periodic components in the original time series. Black represents an amplitude of 0 while red indicates the maximum. The units are the same arbitrary units of the simulated data, shown in figure 4.4. The Fourier amplitude filter clearly has a greater effect on periodicities greater than about 60 minutes.

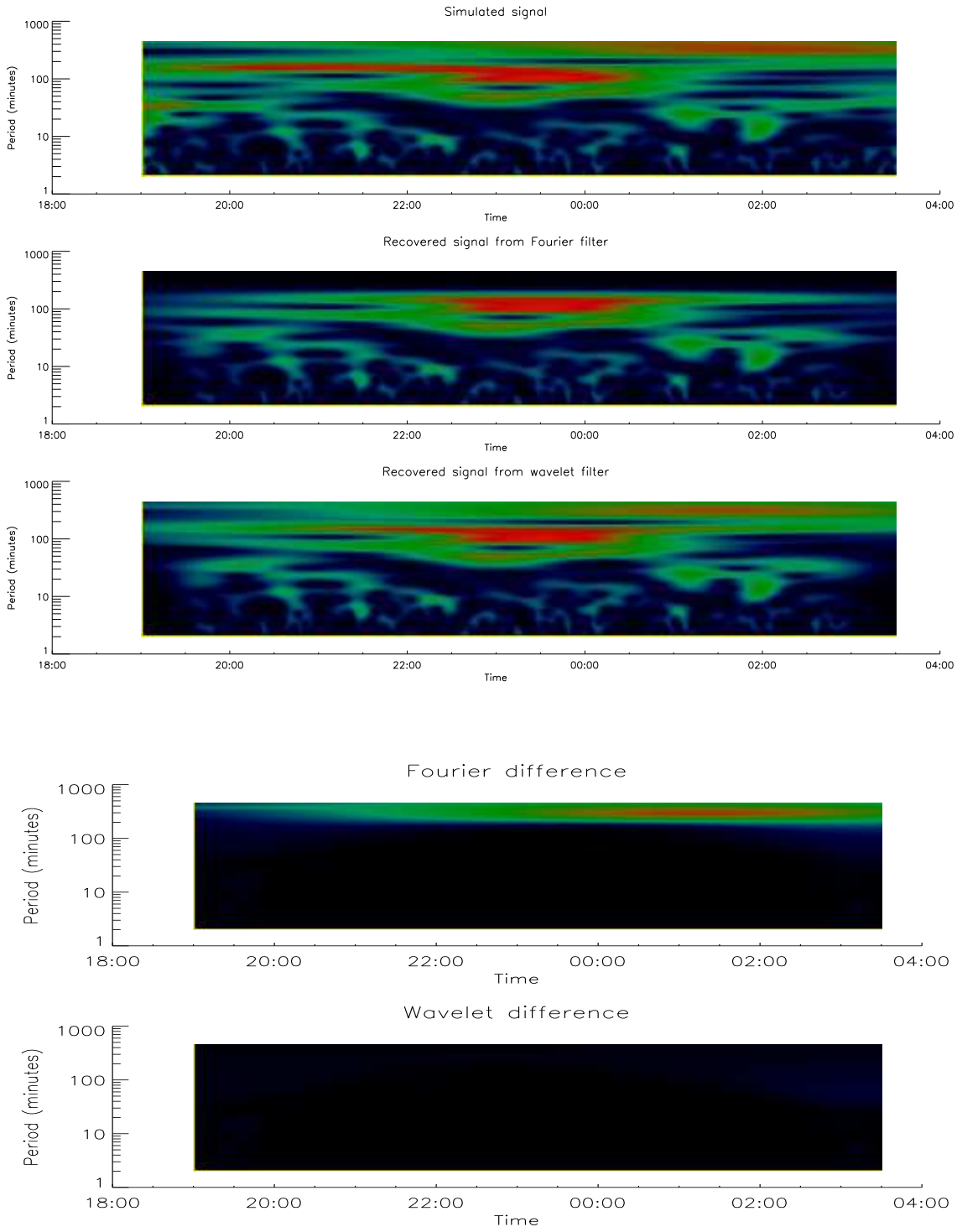

Figure 4.13: As for figure 4.12 but for uncontaminated data rather than data containing Milky Way contamination. The wavelet filter has practically no effect on the signal whereas the Fourier amplitude filter does remove periodicities greater than about 200 minutes.

minimised spectral leakage from the lower frequency components into the higher components. The standard Discrete Fourier transform

$$F_p = \sum_{q=0}^{n-1} f_i e^{-2\pi pqi/n}$$

was applied to the resulting time series using the FFTW library (Frigo & Johnson 1997, Frigo & Johnson 1998). Using the result, three cross spectra

$$X_{pq} = F_p^* F_q$$

were calculated cyclically (that is, X_{12}, X_{23} and X_{31}) using the method of Rayner (1971), where F^* denotes complex conjugation. To increase reliability of the cross spectral components, a three point spectral smoothing was carried out. In addition, the spectra

$$S_p = F_p^* F_p s_i$$

($p = 1, 2, 3$) and coherence-squared statistics

$$\kappa_{pq}^2 = \frac{|\overline{F_p^* F_q}|^2}{|\overline{F_p}|^2 |\overline{F_q}|^2} \tag{4.12}$$

($p, q = 1, 2, 3;\ p \neq q$) were calculated to aid in the determination of the presence of waves in all three fields. s_i is the sampling interval (60 seconds for Buckland Park) and the overbar designates a three point smoothing.

In order to identify the presence of wave-like phenomena in the time series, a number of requirements needed to be met. The amplitude of a given frequency bin in all three spectra was required to exceed a pseudo-background level set at three times the average of the ten highest frequency components. The coherence-squared statistic of the respective cross spectral components was also checked against a threshold corresponding to the 95% confidence limit for the data under consideration (Julian 1974). Similarly, the phase of individual cross spectral components was confirmed above the 95% confidence limit threshold (Rayner 1971). Finally, phase coherence was confirmed across all three cross spectra. When all these requirements were satisfied by a cross

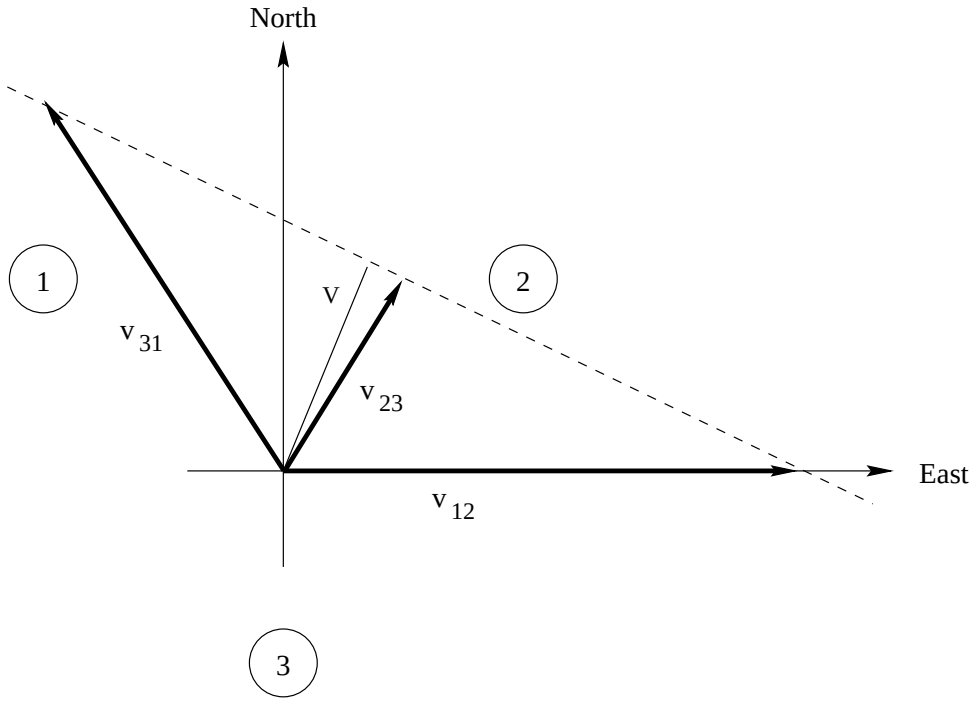

Figure 4.14: Method of calculating phase velocities given three component velocities $\overline{v}_{12}$, $\overline{v}_{23}$ and $\overline{v}_{31}$.

spectral component it was concluded that there was significant wave activity at that frequency over the night's observation duration.

The effect of pre-whitening (Jenkins & Watts 1968, Jacob 1985) was investigated with a wide variety of data. When coupled with the analysis used it was found to have no significant effect on the results produced.

The test for the phase being significantly different from zero as described by Rayner (1971) effectively addressed concerns that intensity variations due to photochemical effects and vertical motion might be detected as waves. Across an area of the emission layer comparable to the photometer's total field of view (approximately 13km $\times$ 13km), such variations were homogeneous. In the case of the three field photometer, this meant that the phase difference observed between any two fields due to this variation were very close to zero, and certainly indistinguishable from zero at the 95% confidence limit. The analysis would therefore reject components affected in this way, and the presence of a wave would not be recorded. In any case, the spectral components at risk were those whose period was comparable to that of the induced intensity variations,

namely periods of the order of six to eight hours. While a tidal study would be greatly concerned with discerning true wave variations with these periods, waves with such periods were of marginal interest in the present gravity wave study, especially given the selection criteria imposed by the limited continous observation time possible on a given night.

Knowing the phase ϕ of the spectral component X_{pq}, the velocity in the direction of the vector from field p to field q could be found using

$$v_{pq} = \frac{-2\pi\nu d}{\phi}$$

where ν is the frequency of the component under consideration and d is the separation of the fields p and q at the observation height. Knowing the relative positions of the fields and v_{pq}, the velocity vector $\overline{v}_{pq}$ in the direction of field q from p could be trivially found. The phase velocity of the associated disturbance was then found from the length of the perpendicular from the origin to the line of best fit of the three velocity vector endpoints $\overline{v}_{pq}$ as shown in figure 4.14.

Since both the north-south and east-west components of $\overline{v}_{pq}$ had equal and finite uncertainties a fitting routine which took this into account was used (Press et al. 1986). The final velocity $\overline{v}$ was calculated knowing the slope of the fit (and therefore θ, the angle of the velocity from north) and the Y-axis (north-south) intercept using

$$\begin{aligned} \overline{v} &= a\cos(\theta) = \frac{a}{\sqrt{b^2+1}}, \\ \theta &= \arctan(-b) \end{aligned} \tag{4.13}$$

where $y = a + bx$ was the fitted line. When fitting lines with slopes greater than 1 and less than -1, the uncertainty in the Y intercept was enhanced, especially when the resulting line was near-vertical. In order to more accurately calculate the velocity in this case, the X and Y axes were reversed with the fit effectively finding the X-axis (east-west) intercept c and the reciprocal of the slope d. The accuracy of the slope did not depend on the fit used which allowed direction θ to be calculated as before. The

expression for the final velocity became

$$\begin{aligned} \overline{v} &= a\sin(\theta) = \frac{-bc}{\sqrt{b^2+1}}, \\ \theta &= \arctan(-b) = \arctan(-d^{-1}). \end{aligned} \tag{4.14}$$

4.1.4 Uncertainty estimations

An estimation of the uncertainties associated with the component velocities v_{pq} followed from Freund & Jacka (1979). Apart from mode of operation, the only significant difference between Freund & Jacka's (1979) instrument and the Buckland Park / Davis model was in the number of fields.

From Bevington (1969), the general form of the variance of a function $f(x_i)$ may be written

$$\sigma^2(f) = \sum_i \left(\frac{\delta f}{\delta x_i}\right)^2 \sigma^2(x_i). \tag{4.15}$$

If the variation in airglow intensity is assumed sinusoidal with period T, the expected number of photons to be recorded in a field m in a second can be represented as a variation of intensity β relative to the average background intensity N_0 given by

$$\langle N_m(t)\rangle = N_0\left[1 + \frac{\beta}{2}\sin\left(\frac{2\pi}{T}\left(t - t_m\right)\right)\right] \tag{4.16}$$

where t_m is the timeshift of the feature seen in field m relative to an arbitrary reference, and β is small compared to N_0. The variance in $N_m(t)$ is therefore, using equation 4.15,

$$\sigma^2(N_m) = \left(\frac{\pi\beta N_0}{T}\right)^2 \cos^2\left(\frac{2\pi}{T}\left(t - t_i\right)\right)\sigma^2(t_m). \tag{4.17}$$

If the feature is observed for time T_L where $\frac{T_L}{T}$ is large or integral, the value of $\left\langle\cos^2\left(\frac{2\pi}{T}\left(t - t_i\right)\right)\right\rangle \approx \frac{1}{2}$. In addition, the N_m quantities are governed by Poisson statistics with the consequence that $\sigma^2(N_m) \approx N_0$. Using these results, equation 4.16 becomes

$$\left\langle\sigma^2(t_m)\right\rangle = \left(\frac{T}{\pi\beta}\right)^2 \frac{2}{N_0 T_L}. \tag{4.18}$$

where the extra factor of T_L accounts for the length of each observation in seconds. It is clear that t_m is related to the phase of field m, ϕ_m, by the simple relation

$$\phi_m = \frac{t_m}{T} \tag{4.19}$$

and therefore that consideration of $\sigma^2(t_m)$ is equivalent to that of $\sigma^2(\phi_m)$ for estimation of uncertainties associated with the phase measurements of the cross spectral technique discussed previously.

Finally, if s is the distance between the fields of view being used to estimate a transit velocity v_m, $v_m = \frac{s}{t_i - t_j}$; since $\sigma^2(t_i) = \sigma^2(t_j)$,

$$\frac{\sigma^2(v_m)}{v_m^2} = \frac{2v_m^2}{s^2}\sigma^2(t_i). \tag{4.20}$$

Thus using equation 4.18, the standard error in the estimate of a transit velocity from field i to j is

$$\frac{\sigma(v_m)}{v_m} = \frac{2v_m T}{\pi\beta s(N_0 T_L)^{1/2}} = \frac{8{\times}10^{-5} v_m T}{\pi s\beta d(\varepsilon\Omega I T_L)^{1/2}}, \tag{4.21}$$

where Ω is the solid angle of the instrument's field of view, d is the entrance pupil diameter, I is the average intensity of the airglow in Rayleighs and ε is the optical efficiency of the photometer. All quantities within this expression are in SI units; distances (s and d) are in metres and times (T and T_L) are in seconds.

With the instrument being considered in this report $s \approx 13$km, $d \approx 20$cm, $\varepsilon \approx 0.02$ and $\Omega \approx 1 \times 10^{-4}$. Assuming $v_m \approx 20\text{ms}^{-1}$, $T \approx 10$min, $\beta \approx 0.1$, $I \approx 50$R and $T_L \approx 60$s, equation 4.21 gives a standard error in each transit velocity magnitude of $\lesssim 10\%$.

Given the uncertainties in the transit velocity components, the line fitting routine estimates the standard error in the fitted parameters as described by Press et al. (1986). The use of the fitting procedure as described in the previous section therefore results in two sets of parameter estimations: $a{\pm}\sigma_a$, $b{\pm}\sigma_b$ and $c{\pm}\sigma_c$, $d{\pm}\sigma_d$. Using equation 4.15 with 4.13 and 4.14 the uncertainties in the magnitude and direction can be found for both cases. When using the standard fit,

$$\sigma(v) \;=\; \sqrt{\frac{\sigma_a^2}{a^2} + \frac{b^2}{b^2+1}\sigma_b^2},$$

$$\sigma(\theta) = \frac{\sigma_b}{1+b^2} \tag{4.22}$$

and when utilising the alternative fitting parameters,

$$\begin{aligned} \sigma(v) &= \sqrt{\frac{\sigma_c^2}{c^2} + \frac{\sigma_b^2}{b^2(b^2+1)^2}}, \\ \sigma(\theta) &= \frac{\sigma_d}{1+d^2}. \end{aligned} \tag{4.23}$$

In practice, phase velocity measurements from Buckland Park showed typical magnitude and direction uncertainties of the order of $\pm 10\%$ and $\pm 30^\circ$ respectively.

4.1.5 Instrumental selection

In addition to the uncertainties associated with the data collection, the effects of the physical setup and operation of the photometer need to be identified. It has been found (Gardner & Taylor 1998) that optical instruments such as photometers and airglow imagers are very insensitive to gravity waves whose vertical wavelength is shorter than the emission layer thickness. This has two main causes, namely that the response of the OH layer's temperature and intensity to these waves is attenuated, and that the presence of more than one half-cycle in the airglow layer means that the wave's effects are partially cancelled from the point of view of a ground-based instrument. Given the generally accepted figures for the OH layer thickness the number of waves detected with a vertical wavelength less than 10km would be expected to be small.

The field spacing at the emission height gives rise to an ambiguity in the horizontal wavelength. Any wave with a horizonal wavelength less than the field spacing (approximately 13km in this study) will effectively be aliased to a longer wavelength by the analysis. It is not possible to directly detect when this has occurred although stringent coherency requirements between the fields should minimise apparent identification of aliased waves.

Sampling interval will affect the highest frequency wave observable in the standard way. Thoughout this study the optical emissions were sampled at 60 second intervals giving a Nyquist cutoff of two minutes. The long dwell time of twenty seconds did not

adversely affect data for waves with period longer than 2 minutes. Its only effect would be to reduce the apparent amplitude of waves with periods shorter than twenty seconds due to partial cancellation on that time scale, thereby helping to prevent unwanted aliasing. In reality, being significantly less than the Brunt-Väisälä period, there is very little wave power at these very short periods making this feature somewhat academic.

4.1.6 Davis photometer data

At the outset of this study it was intended that data from Buckland Park and Davis station be analysed together with the aim of carrying out a comprehensive gravity wave parametric comparison between mid- and high-latitude sites. Following the development of the afore-mentioned filter and preprocessor techniques data from Davis was investigated to gauge the suitablility of these algorithms to this dataset.

It rapidly became apparent that like all high-latitude optical sites, Davis suffered from significant high-level contamination due to auroral activity. As illustrated in the typical time series plot in figure 4.15, the nature of this contamination is vastly different to the Milky Way signal dealt with so effectively by the wavelet-based filter techniques. Whereas the Milky Way gave rise to a slowly varying smooth background signal, auroral effects in the airglow data tend to be very transient in nature. Furthermore, unlike the transient noise observed in the Buckland Park time series, auroral transients occur extremely frequently over the affected regions of the time series making methods developed for the Buckland Park data inappropriate.

Figure 4.16 illustrates thirty minute averaged 730nm intensity data from field one of the three field photometer for all of 1996, a representative dataset showing typical Davis data. While a number of auroral-free nights were available from Davis it was clear that their frequency was not high enough to allow a comparative study to proceed without also being able to utilise some data from nights affected by aurora. An unfortunate consequence of these observations was that a totally new preprocessing system would be required before the Davis data could be utilised in a similar way

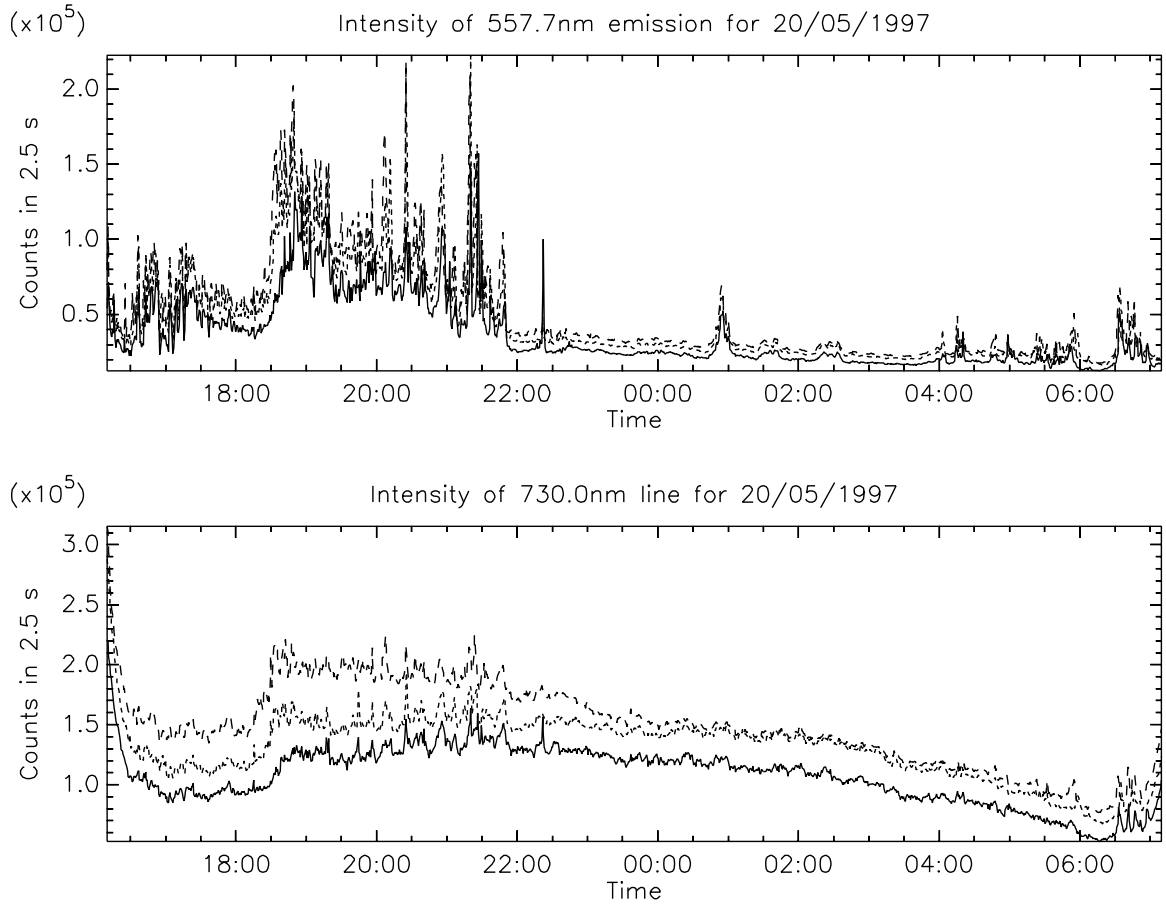

Figure 4.15: Example of typical Davis three field photometer data showing auroral contamination. The most pronounced region of auroral activity is between 18:00 and 22:00, although sporadic activity is clearly visible at other times, namely around 01:00, 04:00 and 06:00. Not surprisingly the contamination affects the 557.7nm data the most since this is an emission produced directly by the aurora.

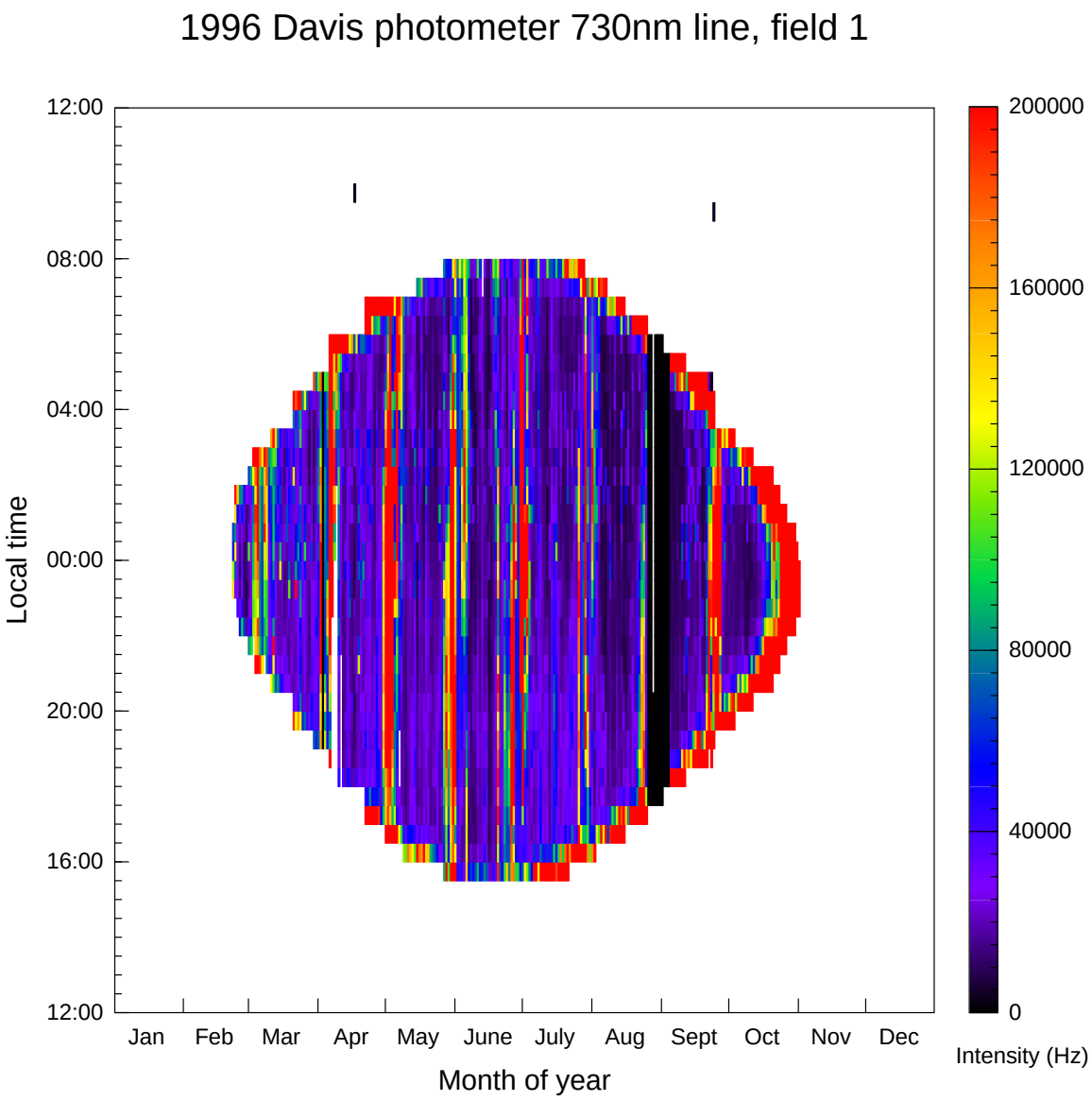

Figure 4.16: An overview of the 730nm airglow intensity recorded at Davis by field 1 of the three field photometer during 1996. The data have been averaged into 30 minute blocks. Throughout the year sporadic peaks can be seen in the data which correspond to times of auroral activity. Often these peaks are isolated and very sharp as illustrated in figure 4.15; the scale of this plot and the averaging itself makes them less obvious than the periods of prolonged intense auroral activity. The bright border seen most clearly during the evenings and mornings in the latter half of the year is caused by light from the fading dusk and approaching dawn, respectively. Isolated data at around 0800 seen in mid April and late September were caused by the instrument starting at these times in error.

envisaged for the Buckland Park data. The decision to drop the inter-latitude comparison aspect of this study was therefore made although it is emphasised that the idea should not be abandoned completely. Other researchers (de Deuge et al. 1994, for example) have successfully applied cross spectral analysis to photometer data partially contaminated by auroral activity through the application of appropriate selection criteria demonstrating that the situation is not impossible. This is discussed in greater detail in section 7.3 on page 199.

4.2 MF radar Doppler analysis

In Doppler mode, the radar measures a velocity component directed radially to the beam by utilising the Doppler shift in the frequency of the return signal. In the presence of a mean wind field (u, v, w), the radial velocity measured by a beam pointing in the direction (θ,ϕ) is (Vandepeer 1993)

$$V_R(R, \theta, \phi) = u \sin(\theta) \sin(\phi) + v \sin(\theta) \cos(\phi) + w \cos(\theta), \tag{4.24}$$

where u, v and w are all functions of R, θ and ϕ. Given two coplanar beams directed at θ and $-\theta$ to the zenith measuring radial velocities V_1 and V_2 respectively, it is therefore possible to resolve the radial velocities into horizontal and vertical components providing the wind field does not change between the regions of observation. That is,

$$\begin{aligned} V_H &= \frac{1}{2\sin(\theta)}(V_1 - V_2), \\ V_V &= \frac{1}{2\cos(\theta)}(V_1 + V_2). \end{aligned} \tag{4.25}$$

V_H is the horizontal velocity component in the direction of the plane containing the two beams, and V_V is the vertical velocity component.

This method of finding velocities is complicated slightly by the fact that the return power backscattered from the atmosphere drops significantly as a function of off-zenith angle, forcing the effective receive beam direction to move back towards the zenith. Unless this effect is accounted for, velocity measurements will be underestimated.

In addition to measurements of the background wind field, gravity wave parameters can also be measured using Doppler radial velocity data. When two coplanar beams are combined with a vertical beam it is possible to unambiguously determine wave properties as discussed by Reid & Vincent (1987a). By forming the cross spectral power of (say) east and westward pointing beams at an off-zenith angle of θ (that is, $\phi = 90°, 270°$), the phase of the cross spectrum $X_{EW} = F_E^* F_W$ can be expressed as

$$\xi = 2kx + \xi', \tag{4.26}$$

where

$$\xi' = \arctan\left[\frac{k(\omega_0^2 - k^2c^2)Bc^2\sin(2\theta)}{(\omega_0^2 - k^2c^2)^2\cos^2(\theta) - k^2c^4m^2\sin^2(\theta)}\right] \tag{4.27}$$

and k is the zonal wavenumber, ω_0 the gravity wave angular frequency, c the speed of sound, θ the off-zenith angle used and m the vertical wavenumber. The constant B is given by $B = \frac{2-\gamma}{2\gamma H}$, where H is the scale height, γ is the ratio of specific heats and $x = R\sin(\theta)\sin(\phi)$.

If coherence is significant in a given frequency interval centred on ω_0 (as defined by the coherence squared statistic given by equation 4.12), equation 4.26 can be used to identify a horizontal wavenumber k by writing m in terms of k using the dispersion relation

$$m^2 = \frac{(N^2 - \omega_0^2)k^2}{\omega_0^2} + \frac{\omega_0^2 - \omega_a^2}{c^2} \tag{4.28}$$

where N is the buoyancy frequency and ω_a the acoustic cutoff angular frequency. However, due to the inherent 2π ambiguity in phase associated with equation 4.26, an associated ambiguity arises in the wavelengths determined from this method. In addition, questions of upward or downward propagation remains unresolved since equation 4.26 is symmetrical in m, the vertical wave number.

Additionally, information about the horizontal direction of propagation is only partially complete since the difference in power returned in the east and west beams $(S_E(\omega_0) - S_W(\omega_0))$ is positive for eastward *downward* propagation; at this stage the vertical propagation direction is unknown.

To resolve these ambiguities, use is made of the vertical beam data in conjunction with one (or both) of the off-zenith beams. Considering the east ($\phi = 90°$) and vertical beam, the phase of the cross spectrum can be written as

$$\xi = kx + \xi', \tag{4.29}$$

where

$$\xi' = \arctan\left[\frac{kBc^2\sin(\theta)}{kc^2m\sin(\theta) + (\omega_0^2 - k^2c^2)\cos(\theta)}\right]. \tag{4.30}$$

The existence of the vertical beam also allows direct measurement of the vertical wavelength and phase velocity (and therefore the vertical propagation direction) by calculating the cross spectra of vertical wind velocities from a range of heights.

Using all this information it is possible to deduce a complete set of gravity wave parameters for the observations. Using the measured vertical propagation direction and the sign of $S_E(\omega_0) - S_W(\omega_0)$, the horizontal propagation direction can be found. Equation 4.26 is then used for frequency components showing significant coherence to obtain a zonal wavenumber (and hence wavelength). Finally, if there is an ambiguity in the horizontal wavenumber and there is significant coherence between the east (say) and vertical beam, equation 4.29 can be used to obtain the true unambiguous horizontal wavelength. The cross spectral phases allow determination of phase velocity in the zonal (east-west) direction.

Analogous equations to 4.26 and 4.29 can be used in the case of three beams pointing north, vertical and south. In this case, meridional (north-south) components of quantities will be determined allowing the full specification of the horizontal wave parameters.

In addition to the gravity wave parameters, the use of the five beam directions as discussed also allows determination of the vertical momentum flux components. As per Reid & Vincent (1987b), the upward flux of zonal momentum can be determined from

$$\overline{u'w'} = \frac{\overline{V_E'^2} - \overline{V_W'^2}}{2\sin(2\theta)} \tag{4.31}$$

and the upward flux of meridional momentum can be similarly calculated using

$$\overline{v'w'} = \frac{\overline{V_N'^2} - \overline{V_S'^2}}{2\sin(2\theta)} \tag{4.32}$$

where $\overline{V_N'^2}$, $\overline{V_S'^2}$, $\overline{V_E'^2}$ and $\overline{V_W'^2}$ are the mean square radial velocities measured in the four cardinally directed beams respectively. As discussed by Reid & Vincent (1987a), lengthy averaging times are required to reduce the random errors in the estimates based on equations 4.31 and 4.32 with a six hour average resulting in an accuracy of approximately 1 m^2s^{-2}. Consequently, any analysis based on these measurements needs to be restricted to time periods of about this magnitude or longer.

4.3 MF radar spaced antenna analysis using FCA

Determination of background wind velocities using the full correlation analysis (FCA) method relies on the measurement of the velocity of the ground diffraction pattern produced by scatterers in the atmosphere. Using correlation techniques between pairs of antennas the velocity of the pattern can be measured, which is twice the background wind velocity.

Following Briggs (1984), the spatial correlation function of the ground diffraction pattern in the ξ-η receiver plane can be approximated by

$$\rho(\xi, \eta) = \rho(A\xi^2 + B\eta^2 + 2H\xi\eta) \tag{4.33}$$

for suitable constants A, B and H. Adding temporal variations into this expression yields

$$\rho(\xi, \eta, \tau) = \rho(A\xi^2 + B\eta^2 + 2H\xi\eta + K\tau^2). \tag{4.34}$$

Inherent in equation 4.34 is an assumption that the spatial and temporal variations in the coherence function are of the same form. Holdsworth (1995) discusses this and shows that for application with MF data at least this is not a crippling assumption.

If this pattern is now allowed to move with respect to the observer (in the ξ-η plane) at horizontal speed (V_x,V_y), the applicable Galilean transformation can be used

to deduce that the spatio-temporal correlation function becomes

$$\rho(\xi,\eta,\tau) = \rho(A(\xi - V_x\tau)^2 + B(\eta - V_y\tau)^2 + 2H(\xi - V_x\tau)(\eta - V_y\tau) + K\tau^2) \quad (4.35)$$

which can be rewritten in the form

$$\rho(\xi,\eta,\tau) = \rho(A\xi^2 + B\eta^2 + C\tau^2 + 2F\xi\eta + 2G\eta\tau + 2H\eta\xi). \quad (4.36)$$

where

$$C = AV_x^2 + BV_y^2 + 2HV_xV_y + K, \quad (4.37)$$

$$F = -(AV_x + HV_y), \quad (4.38)$$

$$G = -(BV_y + HV_x). \quad (4.39)$$

This specifies the correlation function completely in terms of the ellipsoid parameters A,B,C,F, G and H. Equations 4.38 and 4.39 allow calculation of the wind velocity components:

$$V_x = \frac{HG - BF}{AB - H^2}, \quad (4.40)$$

$$V_y = \frac{HF - BF}{AB - H^2}. \quad (4.41)$$

Correcting for the point source effect gives a "true" *wind* velocity of

$$V_t = \frac{1}{2}(V_x, V_y). \quad (4.42)$$

This shows that in order to determine the velocity of the wind from spaced antenna observations, the ellipsoid parameters must be estimated from the observed data.

Consider the situation where a number of receiving antennas are set up at coordinates (ξ_i,η_i) with vectorial displacements between two antennas i and j being r_{ij}. By setting $\frac{\delta\rho}{\delta\tau} = 0$ where ρ is as defined by equation 4.36, the lag corresponding to the maximum of the correlation function between receivers i and j can be found:

$$\tau'_{ij} = -\frac{F}{C}\xi_{ij} - \frac{G}{C}\eta_{ij}. \quad (4.43)$$

Therefore, estimations of $\frac{F}{C}$ and $\frac{G}{C}$ can be determined by finding the maximum in each correlation function and solving a set of linear equations. Least squares fitting

techniques can be employed to deduce the optimum values and error estimates since in general more than two correlation functions will be available.

$\rho(\xi_{ij}, \eta_{ij}, 0)$ is the value of the correlation function at zero lag. If the time shift τ_{ij} where the mean correlation function (that is, the average of all available correlation functions) has this value, then

$$\rho(0, 0, \tau_{ij}) = \rho(\xi_{ij}, \eta_{ij}, 0). \tag{4.44}$$

Again using equation 4.36 this gives the set of equations

$$\rho(C\tau_{ij}^2) = \rho(A\xi_{ij}^2 + B\eta_{ij}^2 + 2H\xi_{ij}\eta_{ij}) \tag{4.45}$$

which leads to the set of simultaneous equations defined by

$$\tau_{ij}^2 = \frac{A}{C}\xi_{ij}^2 + \frac{B}{C}\eta_{ij}^2 + \frac{2H}{C}\xi_{ij}\eta_{ij}. \tag{4.46}$$

By solving this set of equations (again using least squares fitting if more than three correlation functions are available), the coefficients $\frac{A}{C}$, $\frac{B}{C}$ and $\frac{H}{C}$ can be estimated.

At this stage, equations 4.40 and 4.41 can be used to calcalate the velocity of the pattern since the extra factor of C cancels on the right hand side. In other words, if $a \equiv \frac{A}{C}$, $b \equiv \frac{B}{C}$ and similarly for F, G and H,

$$V_x = \frac{hg - bf}{ab - h^2} \text{and} \tag{4.47}$$

$$V_y = \frac{hf - bf}{ab - h^2}. \tag{4.48}$$

The true velocity V_t can then be calculated using equation 4.42.

In order to maintain reliability of the velocity estimates obtained using this method, the data must satisfy a number of criteria. These are discussed in detail by Holdsworth (1995) and Briggs (1984) along with other issues which arise when the above theory is practically applied.

When running in spaced antenna mode the radar's transmitting and receiving beams are directed vertically. It is therefore possible to obtain an estimate of vertical velocity in this configuration by utilising measurements of the Doppler shift in the same

way that radial velocities are determined when operating in Doppler mode. For the Buckland Park MF radar data such estimates have been routinely acquired whenever FCA analysis has been employed.

4.4 Intrinsic wave parameters from optical data

The intrinsic wave parameters are those which would be measured by an observer moving with the medium in which the wave is propagating. In the context of the atmosphere the observer moves with the velocity of the background wind. Observation of airglow variations as in the present study only allows determination of wave parameters relative to the geographically fixed instrumentation. Such parameters are referred to as the 'observed' parameters. In order to deduce the intrinsic parameters, information regarding the background wind is required. For this study the background wind obtained from FCA analysis of MF radar data were used.

Given observed wave phase velocity $v'_p = (v_x, v_y)$, and period T' resulting from the cross spectral analysis described previously and a background wind $v_{bg} = (u, v)$ from radar observations, the respective intrinsic wave parameters can be trivially calculated. The cosine of the angle between the wind vector and the phase velocity was calculated using

$$\alpha = \frac{v_x u + v_y v}{|v_{bg}||v'_p|} \tag{4.49}$$

which allowed calculation of the wind component in the direction of the phase velocity:

$$v_\alpha = \alpha |v_{bg}|. \tag{4.50}$$

The intrinsic period (T), frequency (ν), phase velocity (v_p) and direction (θ) can then be trivially calculated using

$$T = \frac{\lambda}{v'_p - v_\alpha}, \tag{4.51}$$

$$\nu = \frac{1}{T}, \tag{4.52}$$

$$v_p = v'_p - v_\alpha, \tag{4.53}$$

$$\theta = \arctan\left(\frac{v_x}{v_y}\right), \tag{4.54}$$

where λ is the (horizontal) wavelength of the gravity wave in question. The direction of propagation (θ) and wavelength (λ) are invariant. If v_p becomes negative as a result of this calculation it simply indicates that the propagation direction is 180° from θ as a result of the Doppler shift.

4.5 Flux estimation from optical data

Swenson & Liu (1998) have described a method for estimating monochromatic gravity wave vertical flux of horizontal momentum ('momentum flux') and the vertical energy flux from optical OH data providing background wind information is available. [1] Using the model of Swenson & Gardner (1998), the momentum flux at 87km can be expressed as [2]

$$F_{M,87km} = \frac{1.2\times10^5\lambda_z(I'_{OH})^2}{\lambda_x \mathrm{CF}^2(I_{OH})^2}(m^2s^{-2}) \tag{4.55}$$

and the vertical energy flux as

$$F_{E,87km} = \frac{2.3\times10^{-3}\lambda_z^2(I'_{OH})^2}{\lambda_x \mathrm{CF}^2(I_{OH})^2}(Wm^{-2}), \tag{4.56}$$

where I_{OH} is the mean OH airglow intensity, I'_{OH} the perturbation in OH intensity caused by a gravity wave (mean to peak), λ_x and λ_z the intrinsic horizontal and vertical wavelengths respectively and CF the "cancellation factor" for OH. CF can be modelled as (Swenson & Gardner 1998)

$$\mathrm{CF} = 3.5 - (3.5 - 0.01)e^{-0.0055(\lambda'_z-6)^2} \tag{4.57}$$

where λ'_z is the vertical wavelength in kilometres (that is, $\lambda_z = 1000\lambda'_z$). The optical observations from the photometer can directly measure λ_x and the ratio $\frac{I'_{OH}}{I_{OH}}$. With winds determined by the MF radar it is possible to calculate the intrinsic frequency

[1] This technique is refined in section 5.4.2 on page 132.

[2] Swenson & Liu (1998) reported a factor of 6×10^4 in this expression for momentum flux. Independent derivation and comparison with Swenson et al. (1999) seems to indicate that this was in error by a factor of two; the expression quoted here uses the revised constant of 1.2×10^5.

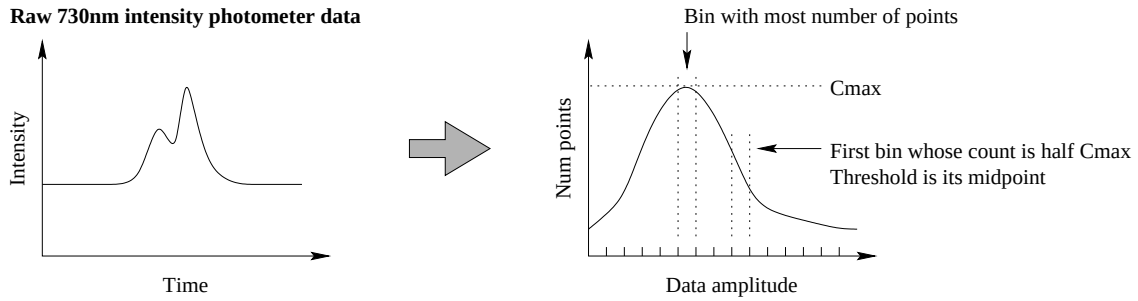

Figure 4.17: Schematic illustration showing method of estimating the intensity of the atmospheric component of the 730nm observations. Bins are sized dynamically such that twenty bins exactly span the data's range; a consequence is that the first and last bin will always have at least one point in them. See text for details.

(equations 4.51 and 4.52) which can be used with the full dispersion relation (equation 2.15) to obtain estimates of λ'_z. Note that the use of the approximate dispersion relation (equation 2.16) for the calculation of λ'_z can give rise to underestimations of the vertical wavelength for waves with λ'_z greater than 20km as per Swenson et al. (2000). This would result in underestimations of energy and momentum flux of the order of 20% and 10% respectively.

The constant factors in equations 4.55 and 4.56 include the square of the Brunt-Väisälä period in the numerator which in this case has been taken as five minutes from the MSIS model atmosphere. If temperature estimates are available in addition to the airglow intensity (as they are in the case of many imagers currently operating) they can be used to dynamically obtain the Brunt-Väisälä period at observation time rather than relying on model values which can routinely differ from experimentally obtained figures by the order of 10% (Swenson et al. 1999).

The ratio $\frac{I'_{OH}}{I_{OH}}$ for a given wave requires a measurement of the average atmospheric contribution to the OH intensity (I_{OH}). Given the need to discount elevated intensities due to the Milky Way when present (which could alter the average intensity by as much as a factor of two), a straight-forward arithmetic average was not appropriate. Instead, a method was derived which relied on the fact that in general the Milky Way would smoothly increase the intensity to a level much higher than unaffected data.

The process is shown schematically in figure 4.17. For each field a histogram

was formed in turn which contained twenty bins spanning the respective field's data amplitude range. The number of datapoints in each bin's range was counted and the bin with the most points was identified. The points counted in this bin would be those clustered around the atmospheric mean since Milky Way points, being somewhat higher, would be contained in bins with higher ranges. Also, because of the amplitude reached by Milky Way signal, the contribution to any one bin is small which means that the bin with the maximum points will refer to uncontaminated data. The first bin higher than this with a count less than half of that of the maximum was then found and a threshold of its midpoint set. All points in the time series less than this threshold were then averaged to arrive at an estimation of the uncontaminated airglow average intensity. Testing with a wide variety of data files showed this method to accurately reflect the atmospheric amplitude mean independent of the presence of the Milky Way.

An estimate of I'_{OH} was slightly more involved since it represents the (average) variation from the mean due to only this wave. To estimate this, use is made of Parsevall's theorem:

$$\text{Total power} \equiv P = \int_{-\infty}^{\infty} |h(t)|^2 \, \mathrm{d}t = \int_{-\infty}^{\infty} |H(f)|^2 \, \mathrm{d}f \tag{4.58}$$

where $h(t)$ is some time series and $H(f)$ is its Fourier transform. The discrete form of this for a time series with N points is

$$P = \sum_{k} |h_k|^2 = \frac{1}{N} \sum_{n=1}^{N} |H_n|^2 \tag{4.59}$$

indicating that the variance contribution from a band of frequencies in a time series can be found by summing the power in those frequencies.

Because the time series from the photometer is real, the power was found by calulating the positive half of the Fouier transform and multiplying by $2N$. The factor of 2 accounts for energy in the negative frequencies; N results from the combination of two factors:

- The Fast Fourier Transform routine used in this study divided the forward transform by N. Equation 4.59 assumes this normalisation has not occurred so we

must undo it by effectively multiplying the transform by N before squaring which is equivalent to a factor of N^2 when applied to the power.

- The $\frac{1}{N}$ term in equation 4.59 acts to reduce the N^2 term to simply N.

The power due to a given frequency bin P_f was then calculated by summing the power components which contributed to that frequency bin.

The amplitude of a given frequency component was obtained from P_f as follows. Consider a signal composed of a single sinesoidal component with frequency f. The time series would thus have the form

$$h(t) = A \sin(2\pi f t) \tag{4.60}$$

where A is the amplitude (mean to peak) and straight-forward application of equation 4.59 over a time series of length l yields

$$P_f = A^2 \sum_{k=1}^{l} \sin^2(2\pi f t_i). \tag{4.61}$$

Writing this in terms of a continuous integral and evaluating gives

$$P_f = \frac{1}{\Delta t} A^2 \int_0^l \sin^2(2\pi f t)\, \mathrm{d}t = \frac{1}{\Delta t} A^2 \left[\frac{l}{2} - \frac{\sin(4\pi f l)}{8\pi f} \right] \tag{4.62}$$

where Δt is the sampling period of the time series. Solving for the amplitude A therefore allows estimation of the amplitude of variations due to the frequency f from that frequency's power value P_f:

$$A = \sqrt{\frac{\Delta t P_f 8\pi f}{4\pi f l - \sin(4\pi f l)}} \tag{4.63}$$

Thus it was possible, given power spectra for the three fields, to estimate I'_{OH} for each field and therefore form the fractional variance $\frac{I'_{OH}}{I_{OH}}$ on a per-field basis. The value of this ratio used in equation 4.55 was the arithmetic average of the three separate ratios since there is no theoretical reason to prefer one over the others.

A somewhat simpler estimation of A can be made by identifying that over a single signal period $T = \frac{1}{f}$, $\sin^2(2\pi f t)$ sums to $\frac{1}{2}\frac{T}{\Delta t}$ and that therefore over a time series of arbitrary length l

$$P_f \approx A^2 \frac{1}{2} \frac{T}{\Delta t} \frac{l}{T} = A^2 \frac{l}{2\Delta t}. \tag{4.64}$$

Numerical experiments showed however that due to the fact that the integral of a sine-squared function is not linear, this estimation introduced significant errors in A especially when l was of the order of the signal's period T. As shown in figure 4.18 the estimate based on equation 4.63 typically gives errors less than the order of one tenth of a percent whereas the error from the simpler method based on equation 4.64 is generally higher by as much as two orders of magnitude.

With the operation of a co-located MF radar producing wind estimations, equation 4.55 could be used to estimate momentum flux carried by gravity waves observed in the photometer data. It was anticipated that when MF Doppler data were available to make another independent measurement of momentum flux, this could be used to verify Swenson & Liu's (1998) theory, but unfortunately owing to difficulties outlined in section 3.3.5 on page 48 this was not achieveable in the timeframe of the current study.

4.6 Long-term analysis

In addition to the short period analysis detailed previously which focuses on the parameters of observed gravity wave events, an investigation of the long-term trends of the airglow and radar data were also undertaken. This utilised the same set of optical intensity and radar wind data as the short period analysis augmented with nights where cloud contamination had little or no effect on the average intensity.

As before, the optical data utilised had been passed through the preprocessor prior to the application of this analysis. Because the wavelet filter effectively removed the mean (and other long-period trends) from each night, it was only used when investigating wave-induced variances relative to each respective night's mean, as discussed later in this section. This limited most of the long-term analysis to the 557.7nm optical data.

The radar data used for this aspect of the study consisted of two minute average winds derived from the FCA analysis. Processing radar wind data in the ways outlined

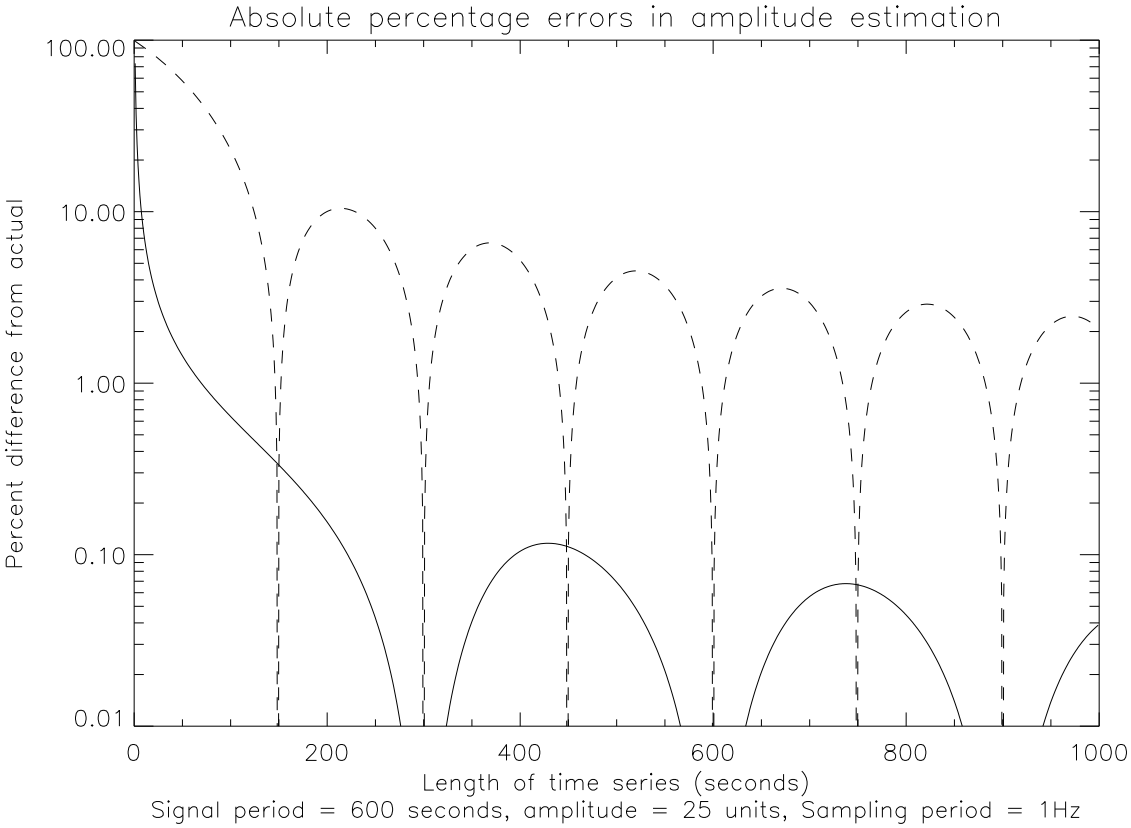

Figure 4.18: Absolute percentage difference between the two alternative methods of estimating a signal's amplitude from a power estimation based on varying time series lengths. Signal period and sampling frequency were chosen as representative of the photometer data. The dotted line shows the error when equation 4.64 is used while the solid line shows the effects when equation 4.63 is used. The difference is typically nearly two orders of magnitude under the conditions typically encountered in photometer data. The actual behaviour of the graphs for time series with length less than the signal period (600 seconds in this case) is somewhat academic since in practice one must observe for at least a signal's period in order to positively identify its presence using cross spectral techniques as employed in this study. The region of practical interest is therefore for time series lengths greater than the signal period.
It should be noted that the error resulting from the use of equation 4.63, while typically better than that from equation 4.64, does depend on the ratio of sampling period (Δt) to signal period (T) with the error being smaller for higher ratios. When the ratio is high more samples are taken each period resulting in a better estimate of the signal's behaviour.

below is somewhat unusual; it has been done this way in the present case to facilitate direct comparison with the optical data, for which this presentation yields a convenient overview. To increase reliability of the wind data and to more accurately represent the average wind present thoughout the emission heights, data were averaged in two blocks, utilising the range bins from 84km to 88km, and 92km to 96km. Because each range bin averaged the winds from its origin to 2km above it, this gave effective coverage from 84km to 90km and 92km to 98km respectively.

For this investigation all available optical and radar data of sufficient quality were loaded into a two dimensional data array which is shown schematically in figure 4.19. Local time was assigned to the Y axis while the X axis indicated the date. Because of the focus on the optical data, the local time axis ran from 1800 hours through to 0600 hours of the following day. The date referred to on the X axis was the date corresponding to the 1800-2359 portion of each nights 'column'. A number of different analyses could optionally be carried out on the data at this point including the calculation of variances relative to a mean over either the whole data set or over each respective night.

To increase statisical reliability, data were then averaged in three hour blocks within each night separately; these blocks ran from 1800–2059, 2100–2359, 0000–0259 and 0300–0559. By not averaging over an entire night a more complete picture of the wind was achieved since it was not subject to cancellation in cases where the wind reversed direction over the observation period. Spectral and harmonic analyses could then be applied to the resulting set of 4 time series to identify periodic variations in four quantities: intensity and variance of optical data, and velocity and variance of the MF wind data.

It should be noted that because of the strong contamination of the 730nm OH data by the Milky Way as discussed previously, the analysis of the intensity and variance relative to the overall mean of the OH emission was omitted since the data affected by the Milky Way would tend to dominate, obscuring effects due to the airglow itself. This contamination as noted previously applied mainly to data thoughout the second

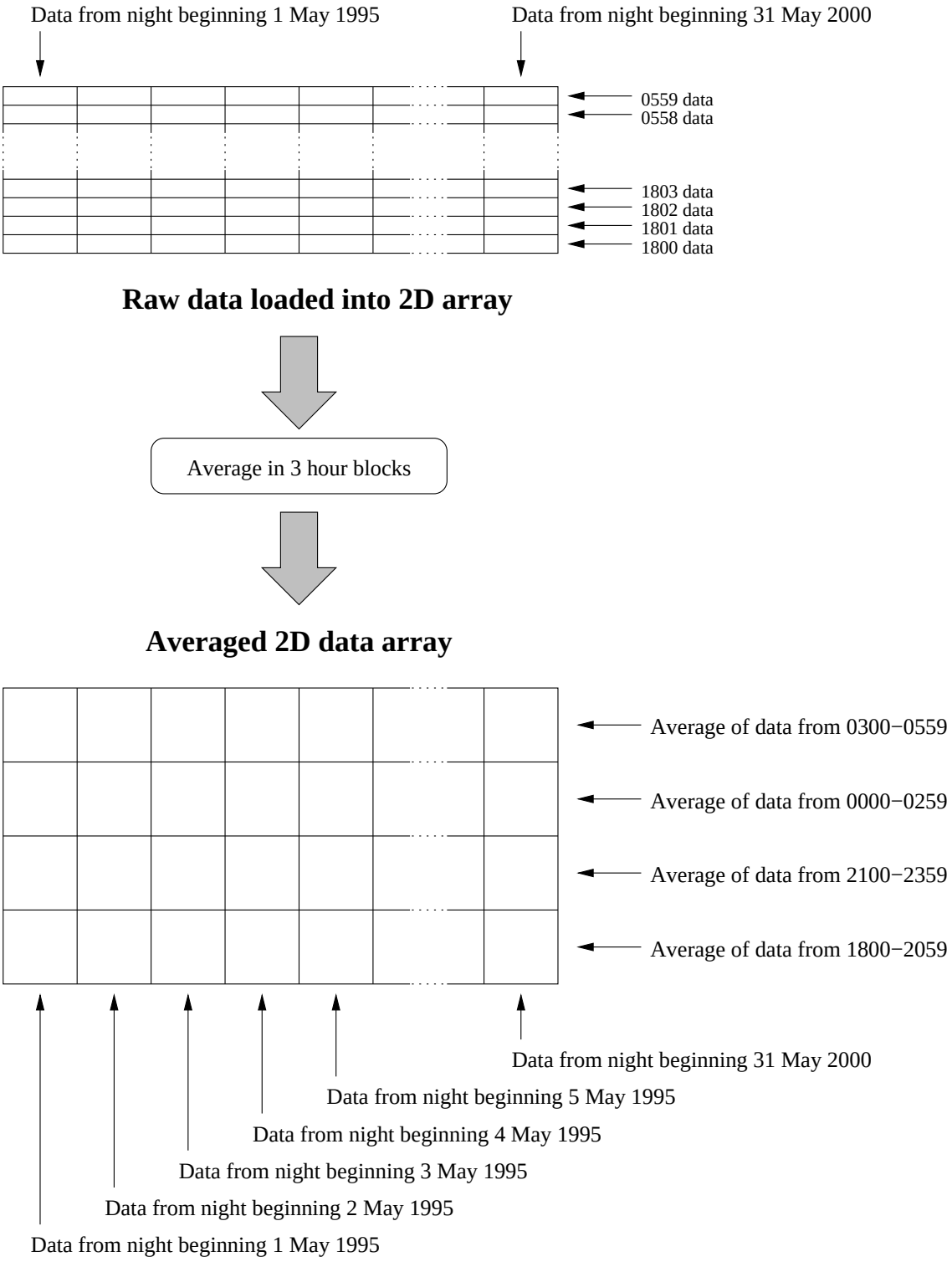

Figure 4.19: Schematic representation of the two dimensional data array used for the long-term analysis and the process used to construct it.

third of each year. However, the aforementioned wavelet filter method enabled reliable variances (relative to each day's respective mean) to be calculated for the OH data. An attempt was made to estimate the OH emission's effective mean and variance on a day by day basis using points with amplitude no greater than 120% of the day's minimum data point. While the results of this method gave reasonable estimations of the mean OH airglow intensity across an entire night there was still considerable uncertainty associated with the resulting variance due mainly to the form of the data itself.

Furthermore, owing to equipment problems with the MF radar at Buckland Park, wind data were not as continuous as the optical data in the interval between 1995 and 2000. For this reason, analysis of the radar data was extended back to 1991 to enable more reliable identification of any long-term trends in the data.

4.6.1 Lomb analysis

Unlike the short period work which involved analysis of essentially continuous data across a given night, the long period analysis had to deal with sparse data. In the case of the optical data from the photometer, gaps in the data were inherent as observations could not be made while the moon was visible. Besides this, both the photometer and radar equipment suffered periods of downtime ranging from days to months as previously discussed. While interpolation could be used to achieve a uniformly sampled data set for spectral analysis via Fourier methods it was felt that it would be better if analysis did not depend on the inclusion of points with no physical meaning. Extensive use of interpolation, especially to the extent required by the data under consideration, often produces spurious power at low frequencies with wavelengths of the same order as the gaps themselves even if the gaps themselves are randomly distributed in the time series.

The Lomb periodogram (sometimes referred to as the Lomb-Scargle method) is an alternative method of spectral estimation, originally conceived by Lomb (1976) and refined by Scargle (1982). Its development came about of a search for suitable

spectral estimations of unevenly spaced data. Press & Rybicki (1989) later deduced a more efficient calculation algorithm based on the Fast Fourier Transform, making the use of this analysis computationally practical even for large datasets. Whereas the FFT weights points on a 'per time interval' basis, the Lomb-Scargle method weights them on a 'per point' basis, evaluating data, sine and cosine components only at times where data have been taken. After Press & Rybicki (1989), given an N element time series $h_i \equiv h(t_i)$ where the t_i are unevenly spaced, the spectral power as a function of angular frequency $\omega \equiv 2\pi f > 0$ can be defined by

$$P_N(\omega) = \frac{1}{2\sigma^2}\left\{\frac{\left[\sum_j \left(h_j - \overline{h}\right)\cos\left(\omega\left(t_j - \tau\right)\right)\right]^2}{\sum_j \cos^2\left(\omega\left(t_j - \tau\right)\right)} + \frac{\left[\sum_j \left(h_j - \overline{h}\right)\sin\left(\omega\left(t_j - \tau\right)\right)\right]^2}{\sum_j \sin^2\left(\omega\left(t_j - \tau\right)\right)}\right\} \tag{4.65}$$

where

$$\begin{aligned} \overline{h} &= \frac{1}{N}\sum_{i=1}^{N} h_i \\ \sigma^2 &= \frac{1}{N-1}\sum_{i=1}^{N}\left(h_i - \overline{h}\right)^2. \end{aligned}$$

τ is defined using

$$\tan\left(2\omega\tau\right) = \frac{\sum_j \sin\left(2\omega t_j\right)}{\sum_j \cos\left(2\omega t_j\right)}$$

The presence of the $\frac{1}{\sigma^2}$ term in this definition of P_N leads to its more complete name, the "normalised Lomb periodogram" as it results in a P_N amplitude independent of the amplitude of the original data.

The lowest frequency resolvable by this method is one whose period T is equal to the timespan of the data; if using FFT calculations, frequencies would be integer multiples of $\frac{1}{T}$. However, in order to accurately determine the height of any spectral peaks to enable reliable statistical interpretation it is usual to 'oversample' the data by some amount (four is often used) resulting in frequencies separated by multiples of (in this case) $\frac{1}{4T}$, so that the spectrum accurately samples peaks whose true centres would otherwise lie between sampled frequencies. It is important to note, however, that each resulting frequency bin is not completely independent.

In addition, the method is not restricted to consideration of frequencies below a Nyquist limit; in any case with unevenly spaced data there is no way to define such a limit in the true sense of the term. Usually an upper frequency limit of $2f_c$ is used, where f_c is the Nyquist frequency one would obtain if the N datapoints were evenly spaced over the same time period. Given knowledge of the sampling theorem it is initially hard to see why such oversampling can yield meaningful results. The key lies in the realisation that f_c effectively gives an *average* sampling interval; by definition there are some points spaced much closer than this and it is from such points that information regarding the finer and higher frequency structure comes.

One useful property of the normalised Lomb periodogram is that it is relatively easy to test the significance of a peak in the spectrum (Lomb 1976). The probability we observe values larger than z in M independent frequencies obtained from a signal comprised only of noise is

$$P = 1 - (1 - e^{-z})^M \tag{4.66}$$

which can be readily rearranged to give

$$z = -\ln\left[1 - (1 - P)^{\frac{1}{M}}\right] \tag{4.67}$$

In other words, any peak in the Lomb periodogram greater than z has a significance level less than P or alternatively, is significant to the $(1 - P)$ confidence level. This makes it straightforward to identify whether a peak is significant or just due to the random noise in the data so long as M can be found. As mentioned, M is the number of *independent* frequencies in the spectral estimation; a complication is that in the general case, the number frequency bins N_f are not independent, so M does not equal N_f. To address this question, Horne & Baliunas (1986) carried out numerous Monte Carlo experiments and found that in almost all cases, M is very close to N. There are only two significant departures from this.

- When data are significantly clumped M decreases, but only by a factor approximating the number of significant clumps present in the original time series.

- If sampling frequencies up to kf_c, M increases by a factor of k.

Given that the accuracy requirements of M are not rigid (Press et al. 1986) it is fairly easy to arrive at a reasonable estimate of M in practice: assuming no significant clumping, $M \approx kN$.

Like Fourier analysis, care does need to be taken in relation to data windowing to prevent undesired spectral leakage induced by side-lobe effects. Numerical experiments have demonstrated that tapering, commonly used for Fourier-based analyses, can also be applied to the unevenly spaced data with the same effect (Scargle 1982).

4.6.2 Cross spectral calculations

In addition to the identification of dominant periodicities it was desired to quantitatively examine the simultaneous presence of these signals in the long-term radar and optical time series. As described above the Lomb periodogram gives only normalised amplitude information, but Hocke (1998) showed that the method can be extended to yield explicit amplitude and phase information as well. [3] If we define constants a and b such that

$$a = \frac{\sqrt{\frac{2}{n}} \sum_{i=1}^{n} y_i \cos\left(\omega\left(t_i - \tau\right)\right)}{\sqrt{\sum_{i=1}^{n} \cos^2\left(\omega\left(t_i - \tau\right)\right)}}$$

and

$$b = \frac{\sqrt{\frac{2}{n}} \sum_{i=1}^{n} y_i \sin\left(\omega\left(t_i - \tau\right)\right)}{\sqrt{\sum_{i=1}^{n} \sin^2\left(\omega\left(t_i - \tau\right)\right)}}$$

then equation 4.65 can be written as

$$P_N\left(\omega\right) = \frac{1}{2\sigma^2}\frac{n}{2}\left(a^2 + b^2\right).$$

The constants a and b are equivalent to those obtained by least-squares fitting of sine waves of the form

$$y_f\left(t_i\right) = a\cos\left(\omega\left(t_i - \tau\right)\right) + b\sin\left(\omega\left(t_i - \tau\right)\right)$$

[3] Other researchers (for example Zhang et al. 1993) had evidently employed this technique earlier.

to the original data. Using trigonometric identities this can be rewritten as

$$y_f(t_i) = A(\omega)\cos[\omega(t_i - \tau) + \phi]$$

where $\phi = \arctan\left(\frac{b}{a}\right)$ and $A(\omega) = \sqrt{a^2 + b^2}$. Because both a and b are explicitly known the ambiguity in the arctan dependency of ϕ is 2π rather than π. The quantity $A(\omega)$ defines the amplitude spectrum and the phase spectrum Φ can be defined as the cosine argument at time $t_i = 0$:

$$\Phi(\omega) = -\omega\tau + \phi. \tag{4.68}$$

Hocke's (1998) work dealt exclusively with the initial Lomb-Scargle algorithm described by Press et al. (1986), pointing out that all necessary variables required by equation 4.68 could be trivially identified or deduced within the code with little impact on the overall speed. In principle similar considerations of the fast algorithm of Press & Rybicki (1989) also allow the amplitude and phase to be calculated using the faster code. While attempts at this were successful at extracting the amplitude spectrum, the phase component appeared to be influenced by the 'extripolation' process in an unidentified (but possibly mathematically definable) way. For this reason the slower algorithm was employed whenever the phase spectrum was required.

The above method allows calculation of the complex spectrum of an unevenly spaced time series. In order to use this to form the cross spectrum of two such time series it was desirable to have spectral estimates occurring at the same frequencies across both. In general this is not guaranteed because the number of frequency bins and the difference between successive bins is a property of the temporal distribution of the original time-domain data. However, since the lowest frequency and the frequency resolution of the spectum is determined only by the temporal span of the data, these properties can be matched across the spectrum of two time series by adding a zero-value data point at the start/end of the time series which starts/ends last/first. This has no significant effect on the spectrum because gaps in the data receive no weighting in the analysis and any windowing function in use will reduce the data to zero at

the ends. The question of the maximum frequency is then determined by the factor k defined in the previous section. The somewhat arbitrary nature of the choice of k means that without loss of generality it is possible to truncate the longer spectrum to match the length of the shorter; a suitable choice of k together with reference to the nominal data sampling time ensures that the resulting spectra contain data at the maximum significant frequency.

Having calculated the complex spectrum of two unevenly spaced time series the cross spectrum between them and the coherence-squared statistic could be formed in the usual way allowing investigation of the relationship between long-term trends observed in the airglow and radar wind data.

chapter 5

Short period gravity wave analysis

In this chapter the results of the gravity wave parameter analysis concentrating on short period activity (periods less than three hours) is presented. The upper limit on period was instrumental in nature, being due to the night-time restriction on the photometer's operation. Optical data from Buckland Park from 1995 through to 2000 were used for this analysis although as previously noted data were not continuous throughout this entire period.

5.1 Acquisition of wave parameters

After applying the data preprocessor, but before analysing for wave parameters, it was first necessary to manually inspect each night's data to identify those nights affected by cloud and exclude them from the analysis. Manual intervention was needed because there was no absolutely definitive way of mathematically identifying cloudy periods given the data available. From experience it was found that clouds would routinely cause one or both of the following effects in the data time series.

- The preprocessed time series contained larger-than-usual amplitude variations which appeared significantly 'rougher' than unaffected data.
- There was a high degree of correlation at zero lag between the time series of the three fields, particularly in the case of data which had been processed using the

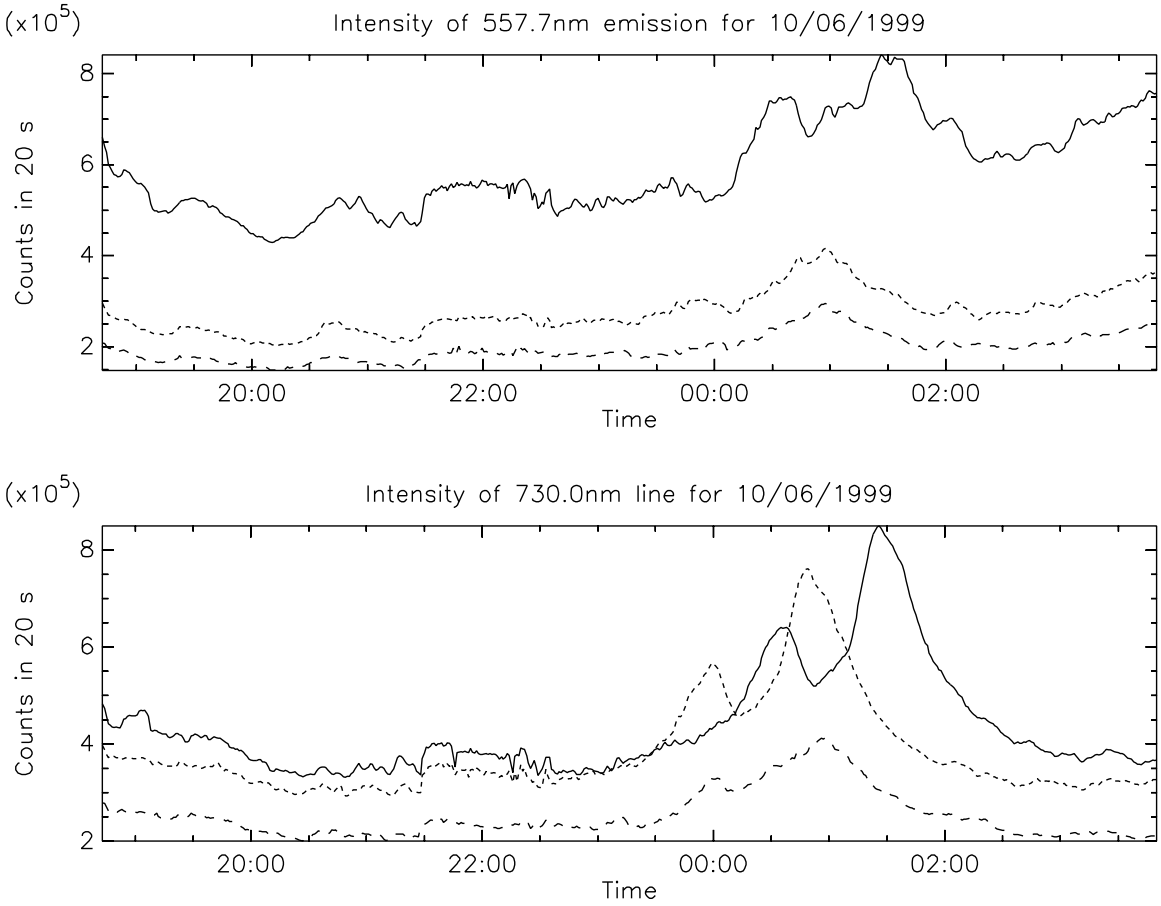

Figure 5.1: Preprocessed photometer data from 10 June 1999 showing the typical appearance of data unaffected by cloudcover.

wavelet filter.

Cloud would more reliably trigger the second of the two effects and the wavelet-filtered data were treated as the definitive cloud indicator. The preprocessed data were used to obtain an overall feel for the nights data, and certainly if the data were smooth there was no need to further investigate for clouds.

Figure 5.1 shows preprocessed data unaffected by cloud, while the data presented in figures 5.2 and 5.3, from the night beginning 23 May 1998 clearly illustrates the two main effects of cloud. The preprocessed time series (figure 5.2) is more uneven than one observes when no cloud is present (figure 5.1) and there are regions (particularly between 02:00 and 03:00) when the data appears to contain high-level noise. When one invokes the wavelet filter (figure 5.3) both channels clearly exhibit a high degree of inter-field correlation at zero lag, confirming suspicions resulting from the observation

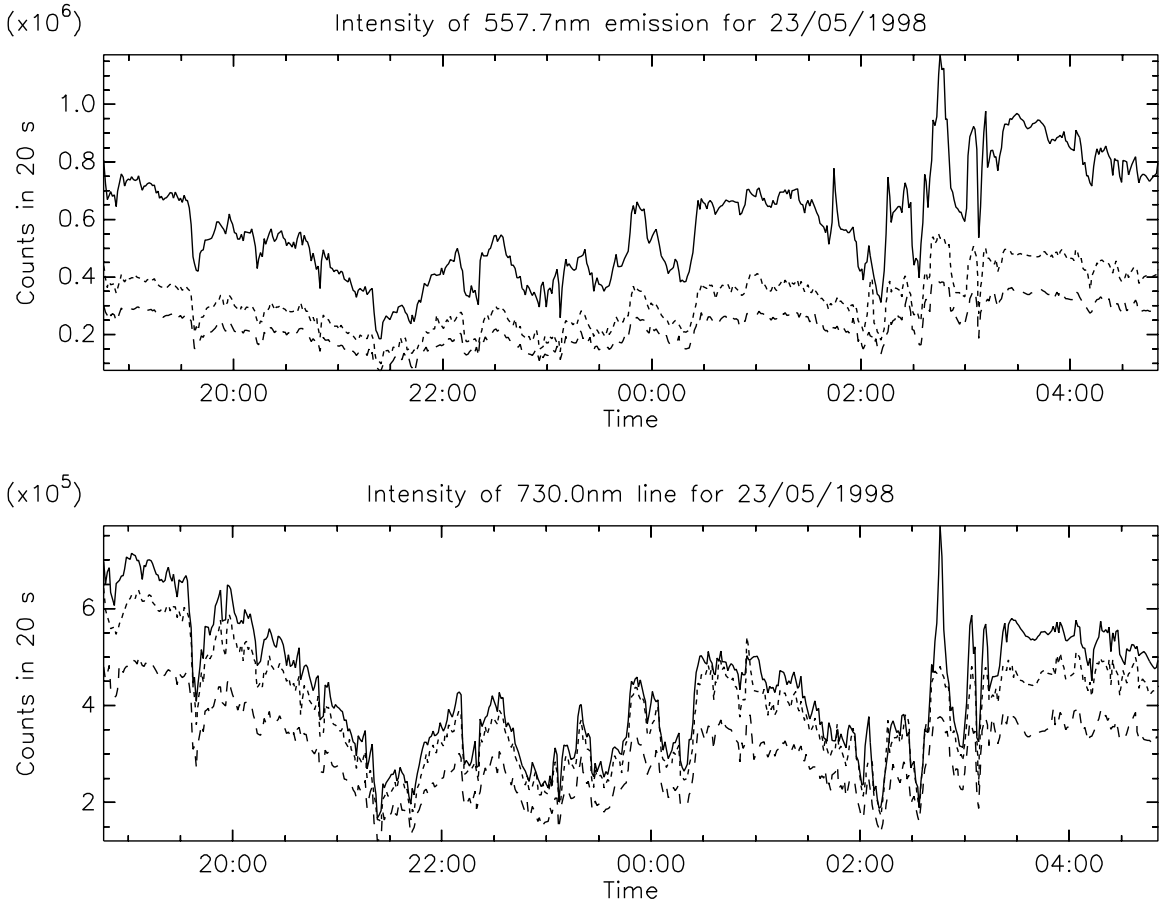

Figure 5.2: Preprocessed data from 23 May 1998 showing the effect of cloud on the photometer time series. Strong effects of cloud can be seen between 02:00 and 03:00, although cloud was present over the entire night.

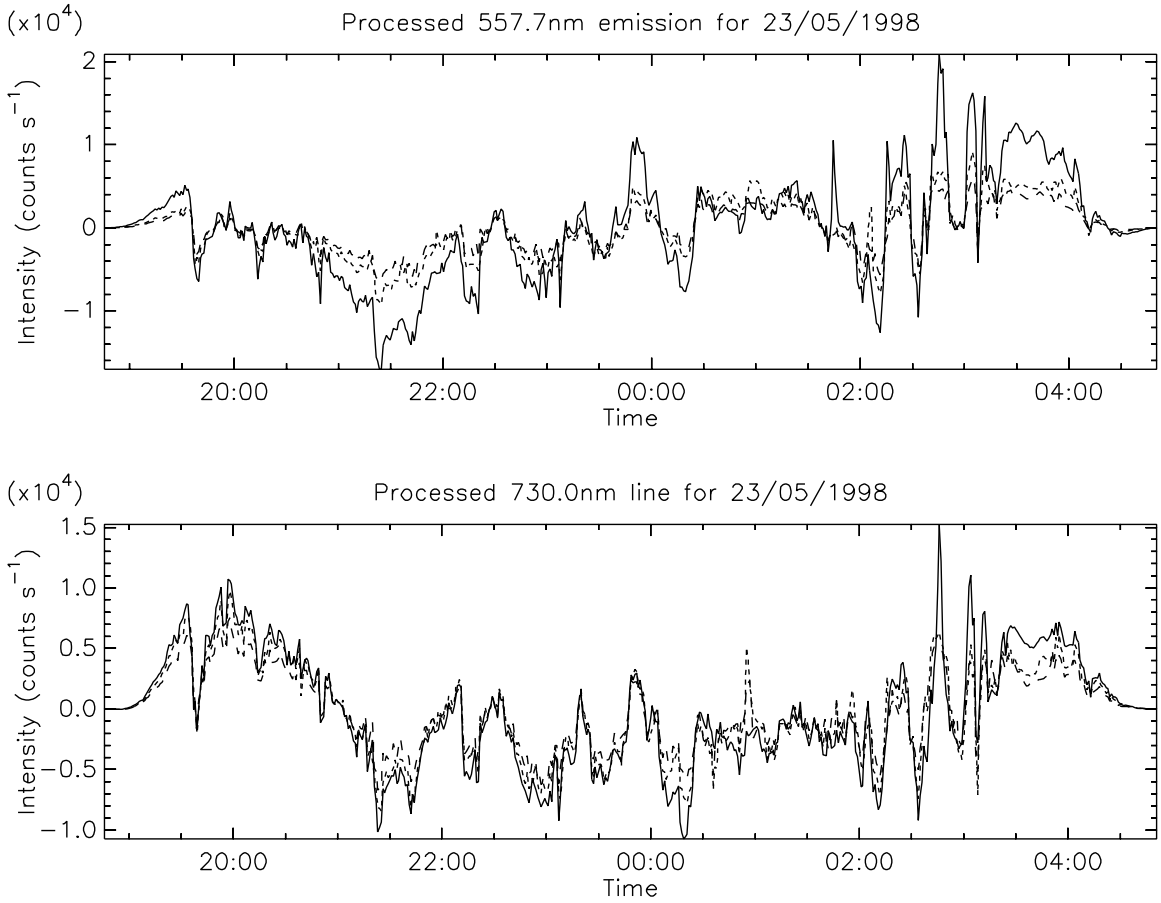

Figure 5.3: Data from 23 May 1998 having passed through the wavelet filter. A high degree of correlation between the three fields, particularly the 730nm channel, is clearly evident. The appearance of such a high inter-field correlation was a reliable indication that thick cloud cover was present.

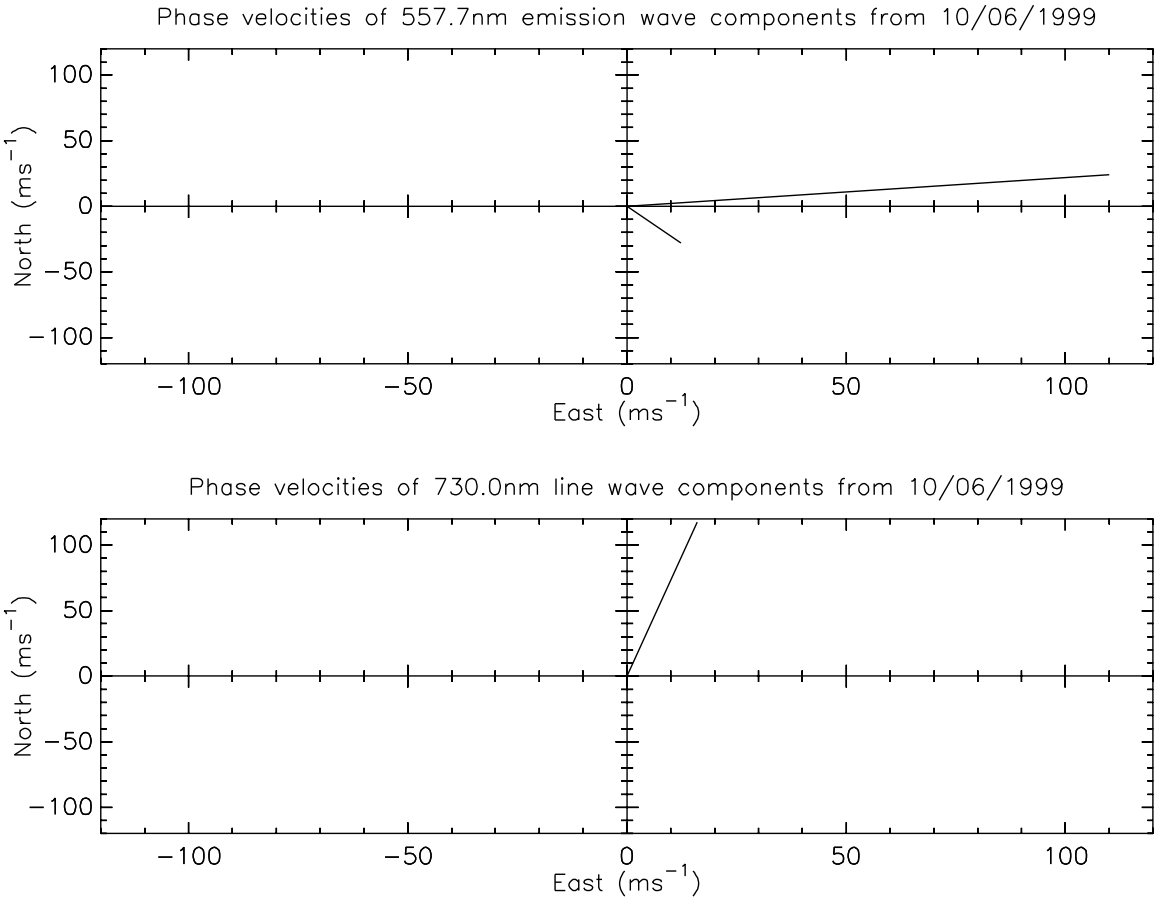

Figure 5.4: Example phase velocity plot from the Buckland Park photometer data. Amplitude uncertainty is typically ±10% while direction uncertainty is of the order of ±20°.

of the preprocessed time series.

Once the list of known good nights had been identified they were processed in turn to yield parameters of gravity wave activity observed thoughout the night. The results were available both as a phase velocity plot and as ascii data containing all wave parameters for later analysis. Figure 5.4 shows typical phase velocities obtained from the analysis; here we see the effect of some wave activity moving towards the east and south-east in the 730nm data, while the 557.7nm data shows activity moving towards the north. Inspection of the wavelet-filtered data for this night (figure 5.5) is instructive: compared to figure 5.3 there is very little visual zero-lag correlation between fields and a timelag between wave-like disturbances in the fields is visible throughout much of the night.

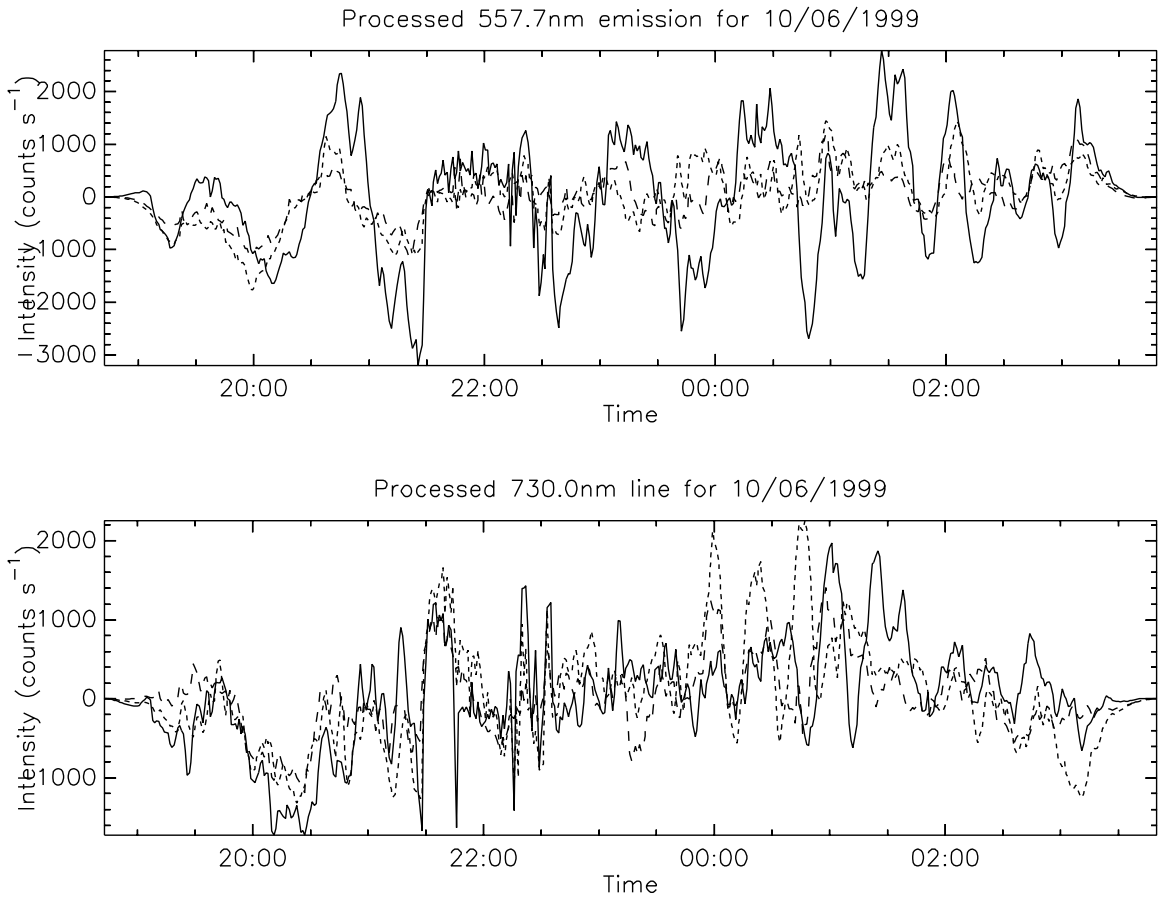

Figure 5.5: Wavelet-filtered data for a cloudless night

Using this procedure on data acquired between 1995 and 2000, around three hundred clear nights were identified containing three to four hundred wave events in each of the two channels (557.7nm and 730nm). Cloud-free nights thus accounted for about 20% of all nights in the five year period, or nearly 50% of the nights when continuous observations could be made for two hours or longer.

5.2 Observed wave parameters

As mentioned in the previous section, routine analysis of data from the clear nights gave rise to a complete set of observed wave parameters: phase velocity, period and wavelength. Parameters except direction for all observed waves are summarised in figure 5.6.

Figure 5.6 contains no out-of-range checks to allow evaluation of the methods used and to verify that a majority of the results make physical sense. A sudden cut-off in phase speed is observed as expected around the speed of sound although the actual value of the cut-off is slightly higher; at least some of the higher phase speeds could be the result of propagation through a background wind. It is also clearly apparent that no waves were observed with wavelengths shorter than approximately 50km which is expected given the field separation at the observation heights being of the same order of magnitude. The effect of the Brunt-Väisälä frequency/period is also clearly visible at the low end of the period range. As for the phase speed case there are a few waves whose parameters take them beyond this cut-off frequency (around four to five minutes at mesospheric heights) and some of these could be due to Doppler shifting by a background wind.

A comparison was made between waves identified in the present study and those published elsewhere. Many of these were summarised by Reid (1986). Figure 5.7 show the relationship of the current 557.7nm and 730nm datasets to previously reported sets while 5.8 summarises both the 557nm and 730nm data. Generally speaking the period and wavelength values span similar ranges to the other datasets, although it is

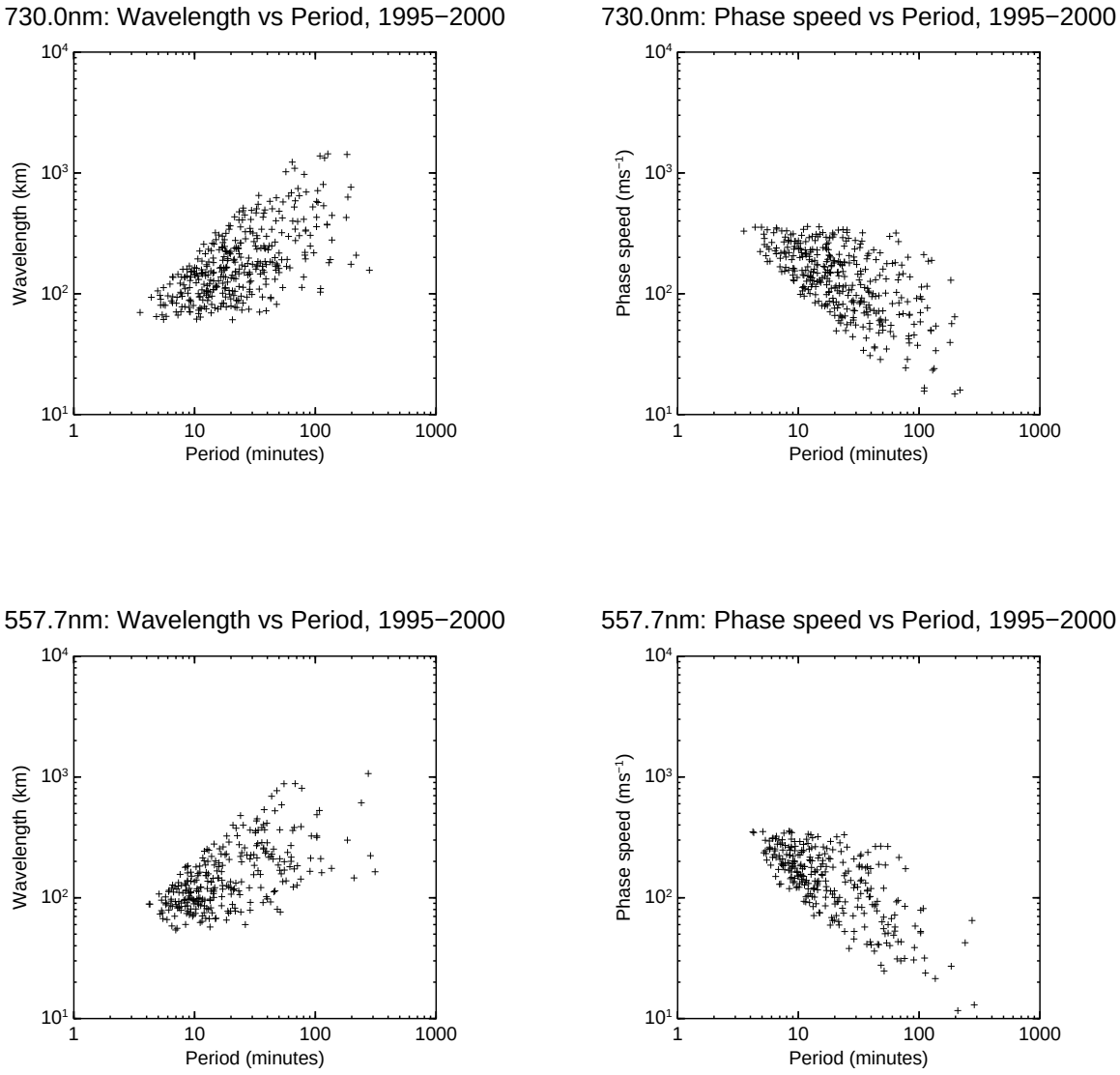

Figure 5.6: Summary of all observed wave parameters from 1995 to 2000. Using a χ^2 fit powerlaw fit, the slope of the wavelength vs period data is 0.45±0.03 for the 730nm observations and 0.41±0.03 for 557.7nm; for phase speed vs period the respective slopes are -0.50±0.03 and -0.58±0.03 respectively. Typical uncertainties are ±10% for phase speed, ±5% for period and ±15% for horizontal wavelength.

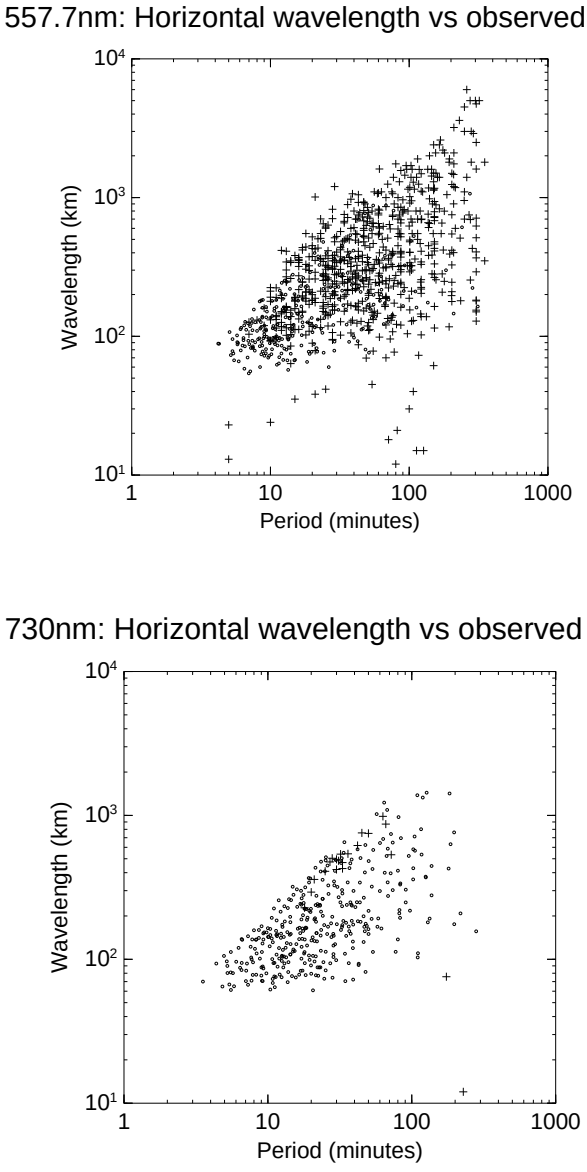

Figure 5.7: Summary of observed wave parameters inferred from optical data reported in the literature (crosses), overlaid with the results of the present study (circles). The upper plot is for 557.7nm observations and includes data from Moreels & Herse (1977), Gavrilov et al. (1978), Freund & Jacka (1979), Armstrong (1982), Gavrilov & Shved (1982), de Deuge et al. (1994) and Fagundes et al. (1995), while the lower plot is for the 730nm emission and includes data from Krassovsky et al. (1977) and Takahashi et al. (1998).

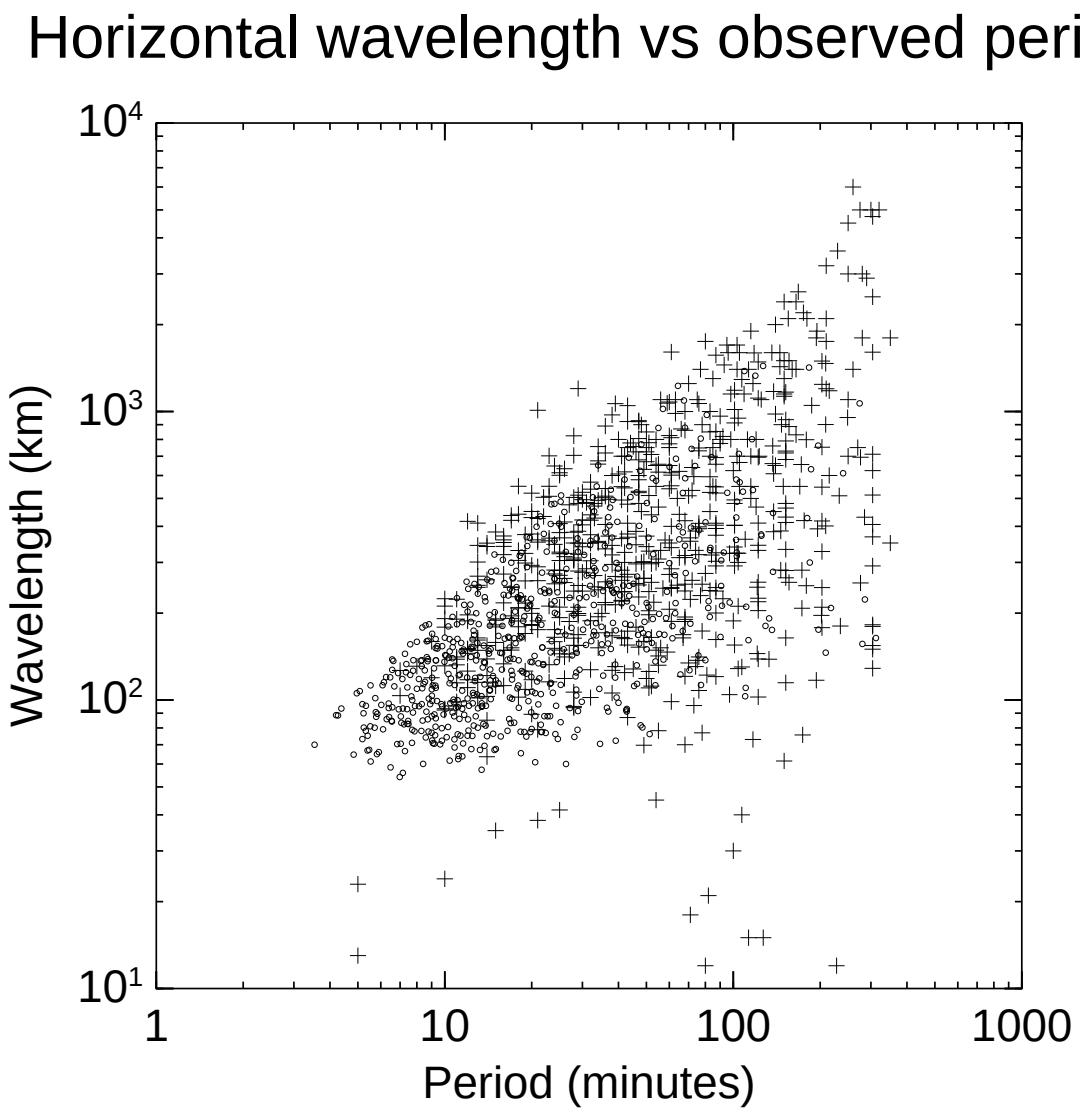

Figure 5.8: Composite plot of data shown in figure 5.7 giving observed wave parameters deduced from both 557.nm and 730nm optical observations. As before, circles represent data from the present study while crosses denote data from the literature.

clear that in the case of the present dataset there are more waves being reported with lower period and wavelength values. One possible explanation for this was that at least some of the studies (for example de Deuge et al. 1994) were conducted in higher latitude sites. Observing at high latitudes results in longer continuous observation times during the winter months which are up to double the maximum observation time possible at the Buckland Park facility, although such studies do have to deal with auroral contamination. The cross-spectral methods applied across entire datasets to identify wave parameters in these studies essentially dealt with an average spectrum for the night, where activity present for only several cycles of period less than the order of the observation length would contribute little to the final spectrum. Conversely, longer datasets are be able to resolve information regarding longer periods more readily than shorter ones. Longer observation times would therefore be expected to be more sensitive to longer-period wave activity, which has been demonstrated by the comparisons presented in figures 5.7 and 5.8.

Gravity wave observations reported in the literature (for example Hall et al. 1995, Wiens et al. 1997) and other studies conducted at Buckland Park (Hecht et al. 1997, Walterscheid et al. 1999) have demonstrated a seasonal dependence particularly in relation to gravity wave directions. For this reason occurrence histograms of gravity wave parameters for summer, autumn, winter and spring were generated and are presented in figures 5.9 to 5.12. The months were assigned to the seasons as shown in table 5.1. The 'autumn' and 'spring' seasons as used in this context are really picking out the equinoctal periods rather than the months traditionally associated with the respective seasons to allow for any changes associated with the changeover between summer and winter atmospheric circulations (Andrews et al. 1987).

A summary of the number of gravity wave observations in each season is given in table 5.2. The reader's attention is drawn to the fact that Buckland Park is in the southern hemisphere, meaning the autumn equinox occurs in March and the spring equinox in September. While the 'per month' statistics indicate the likelihood of a fall-off in coherent gravity wave structure over the March equinox no such conclusion

Season	Included months
Summer	January, February, November, December
Autumn	March, April
Winter	May, June, July, August
Spring	September, October

Table 5.1: Assignment of months to seasons used in seasonal parameter plots

Season	Number of waves		Waves per month	
	558nm	730nm	558nm	730nm
Summer	109	85	27	21
Autumn	51	18	25	9
Winter	141	111	35	27
Spring	48	60	24	30

Table 5.2: Number of gravity wave events observed per season

can be made regarding the September equinoctal period.

The general form of these histograms is certainly in agreement with other similar results in the published literature (Giers et al. 1997, for example). However, whereas many datasets yield little or no horizontal phase speeds greater than 100ms^{-1}, the present results consistently record speeds in excess of 200ms^{-1}. The observed period is clearly limited to less than two hours generally, although isolated examples of long-period activity do exist. This is not highly surprising given the operation of the instrument; as explained earlier maximum observation time per day ranges from between six and ten hours depending on time of year and this is reduced throughout any given month by the moon. The average observation time across all observing nights is of the order of four hours.

5.3 Intrinsic wave parameters

When available, wind data from the Buckland Park MF radar were used to calculate intrinsic wave parameters from the optical observations of the photometer. While this was not always possible for every night of the photometer's operation due to

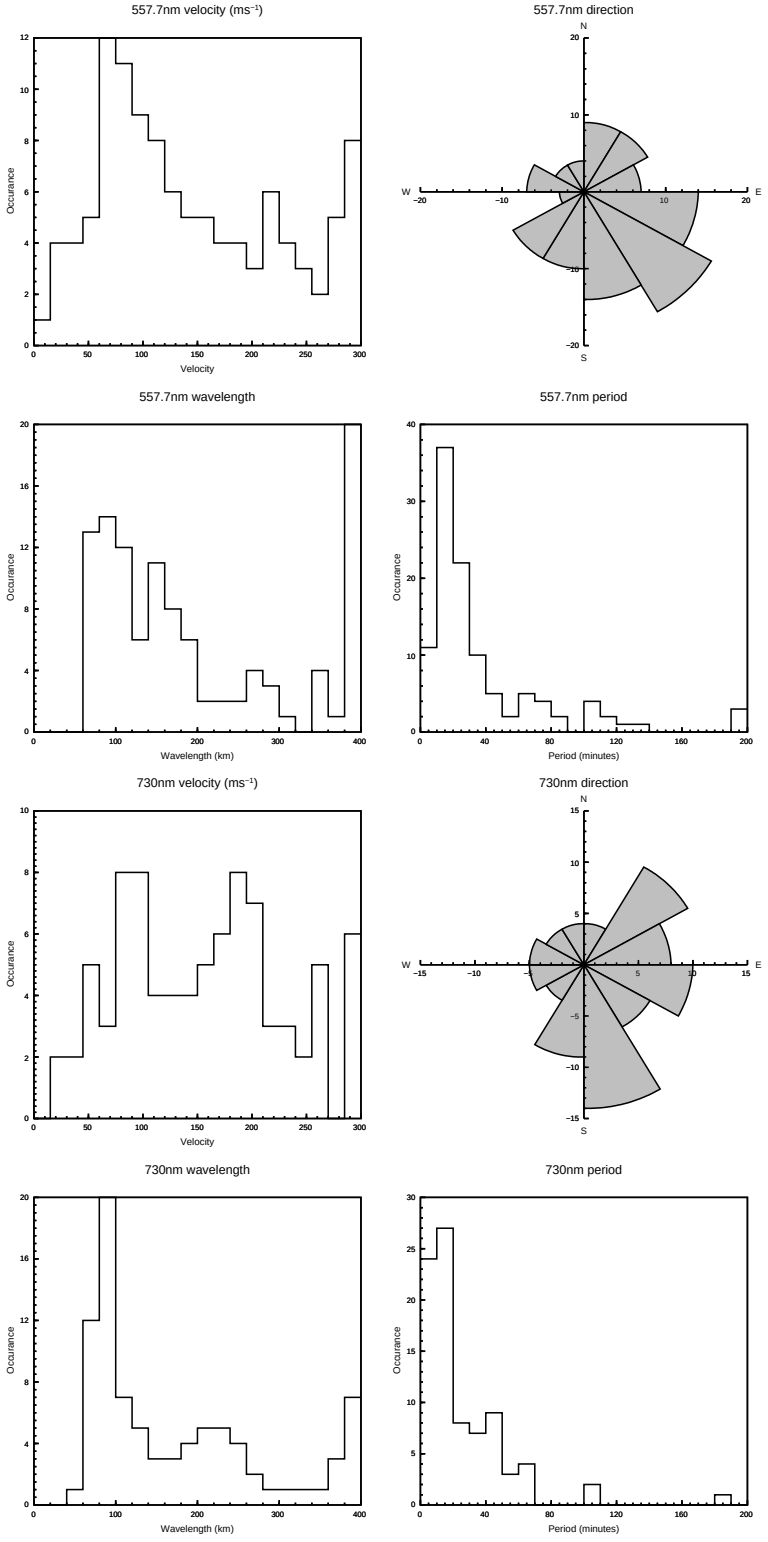

Figure 5.9: Occurrence histograms of parameters from gravity waves observed in summer.

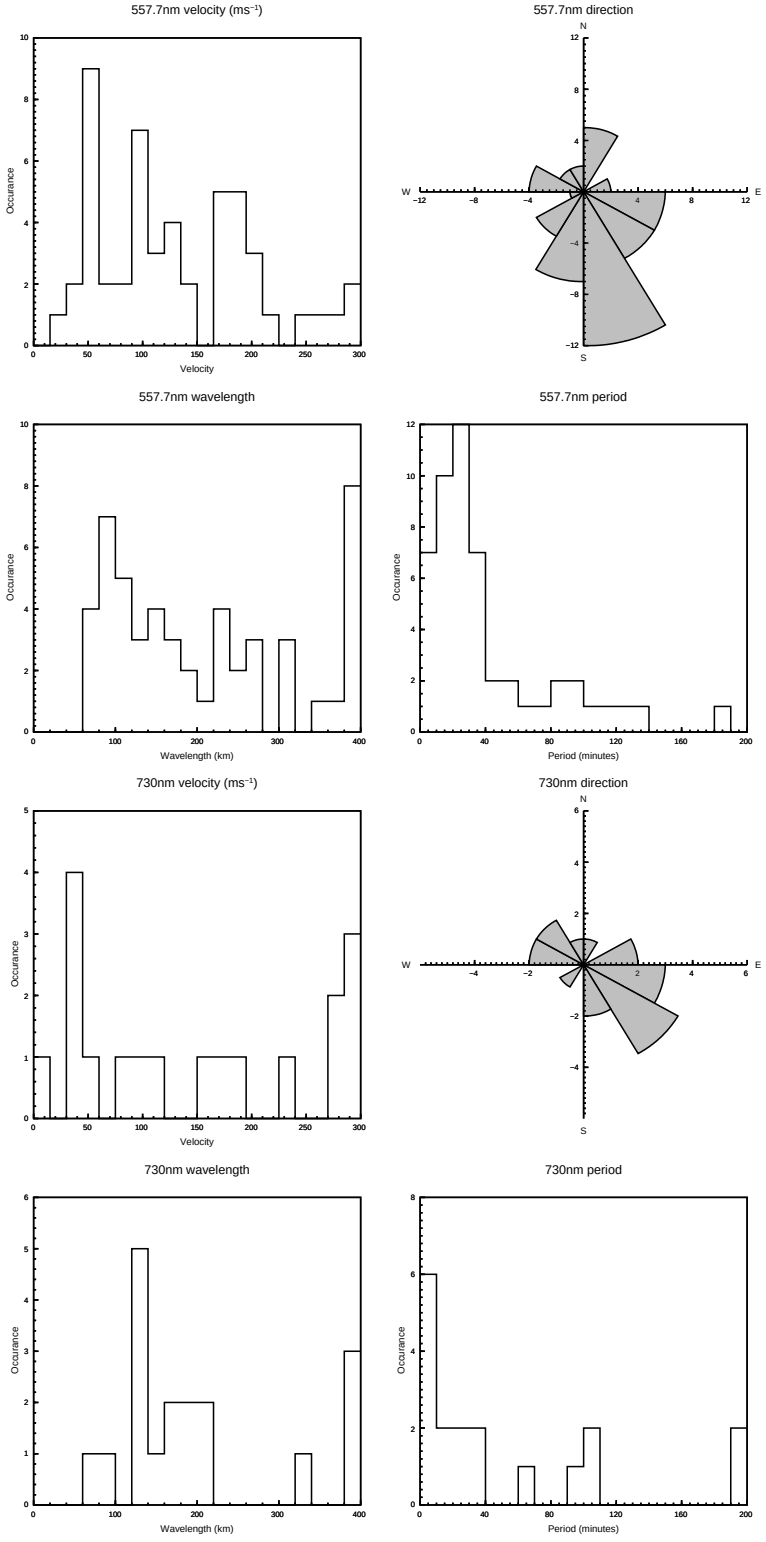

Figure 5.10: Occurrence histograms of parameters from gravity waves observed in autumn.

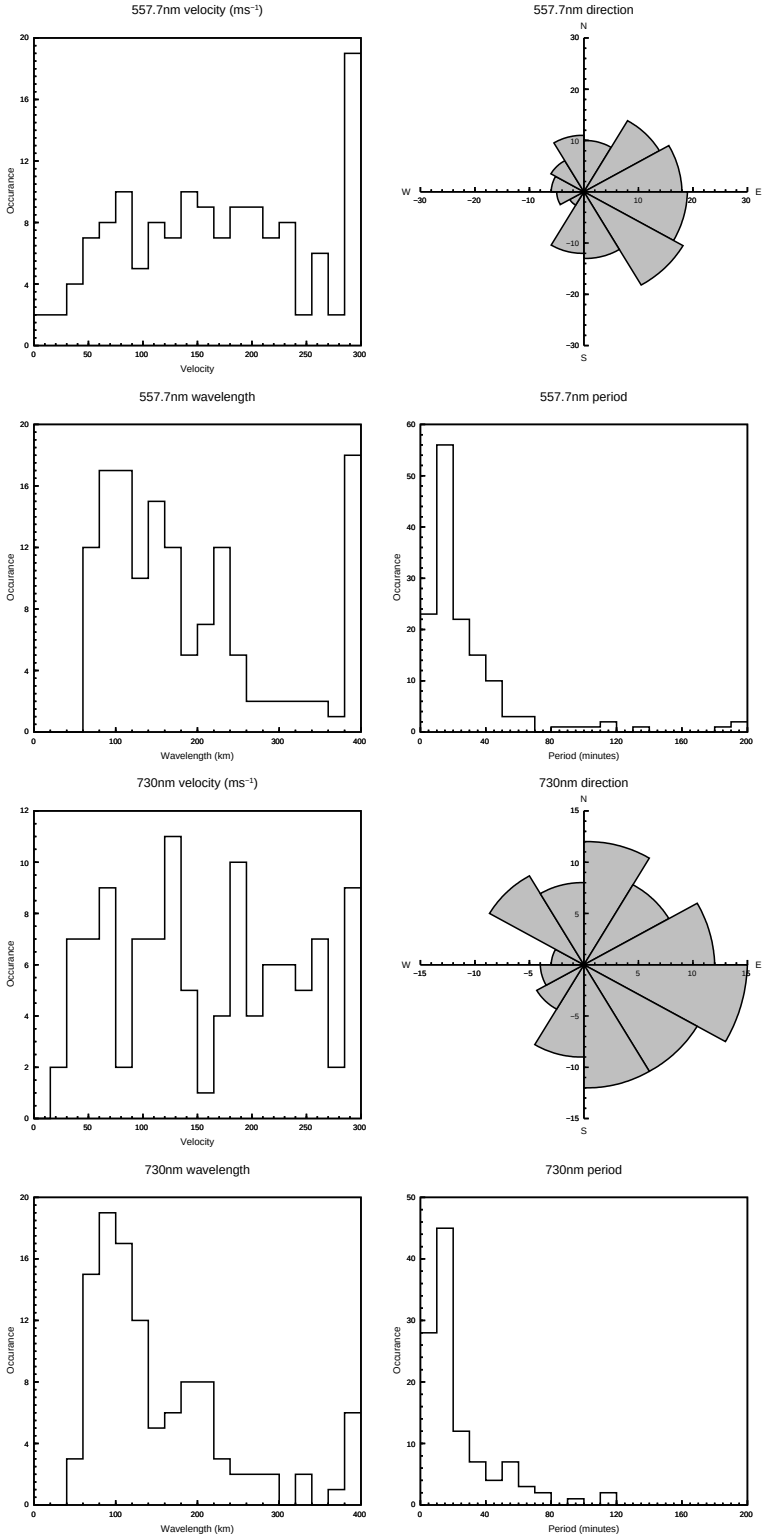

Figure 5.11: Occurrence histograms of parameters from gravity waves observed in winter.

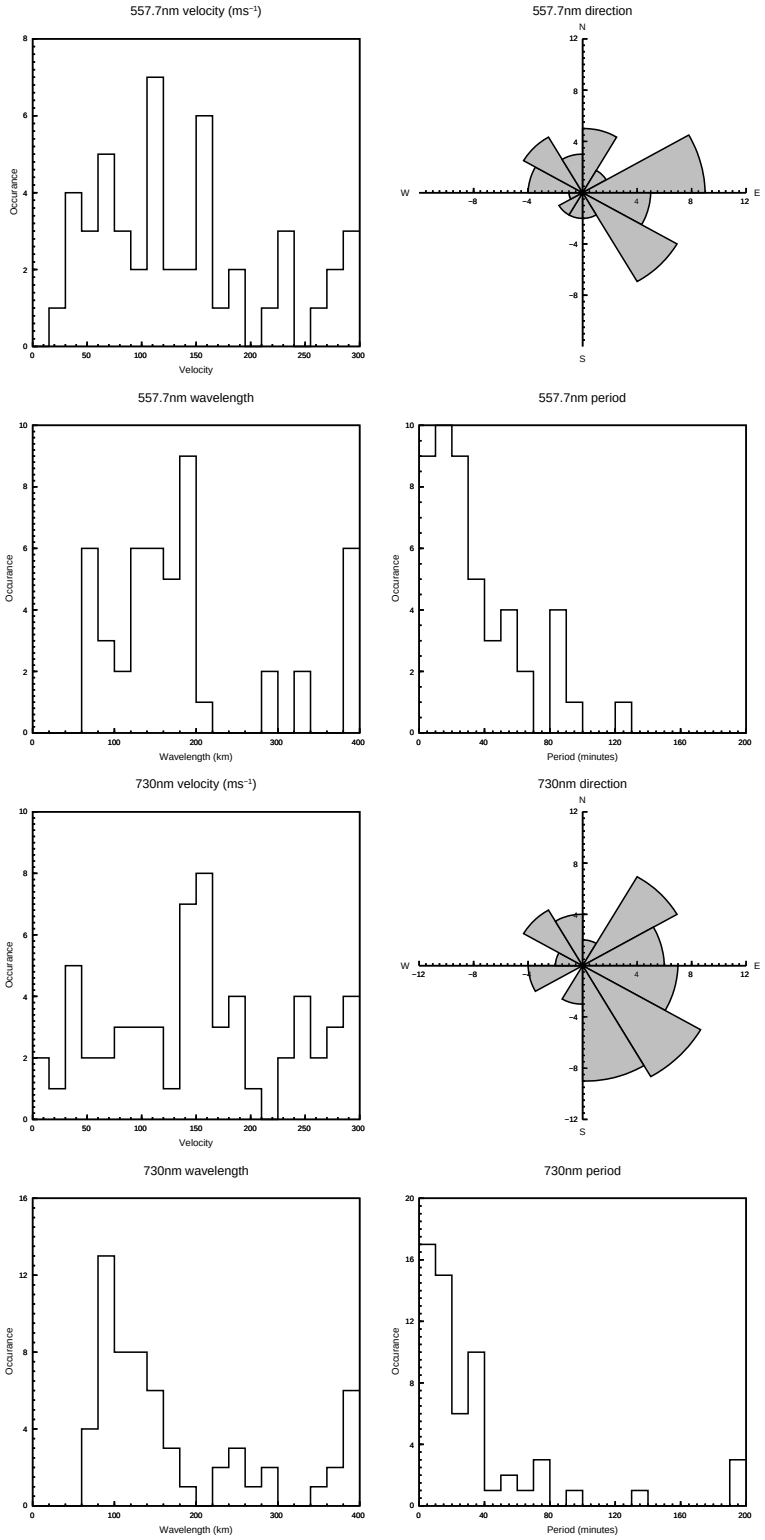

Figure 5.12: Occurrence histograms of parameters from gravity waves observed in spring.

Season	Number of waves		Waves per month	
	558nm	730nm	558nm	730nm
Summer	60	54	15	13
Autumn	32	13	16	7
Winter	83	88	27	22
Spring	26	35	13	17

Table 5.3: Number of gravity wave events observed per season for which background wind data (and hence intrinsic parameters) were available.

equipment problems, the intrinsic parameters of around four hundred waves detected by the photometer were calculable over the period of this study. A summary of these intrinsic parameters is shown in figure 5.13.

As for the observed parameters reported earlier no assumption has been included in the analysis code regarding what the various values should be. Given this the results are pleasing as they are in general within the theoretical limits imposed by gravity wave theory, with only five points lying below the Brunt-Väisälä period. These points were omitted from later analyses.

Figures 5.14 to 5.17 show histograms of the seasonal occurrence of wave parameters. In a wind field horizontal wavelength is invariant, and the direction of the phase velocity — if changed — can only be reversed (that is, shifted by 180°). The occurrence statistics of these respective quantities shown in the figures differ in appearance from the observed case shown earlier mainly because not all the waves detected occurred at times when MF wind data were available. Table 5.3 summarises the number of waves observed across the seasons.

The number of waves with phase speed greater than 250ms^{-1} is relatively lower than in the observed case which could be caused by two effects. Firstly there are fewer waves in this ensemble and it could be that many of those not included due to a lack of concurrent MF data also had the higher speeds. Secondly, the waves concerned could be shifted to a lower intrinsic phase speed by the wind field. A comparison between the observed and intrinsic histograms and the continued (albeit less frequent) presence

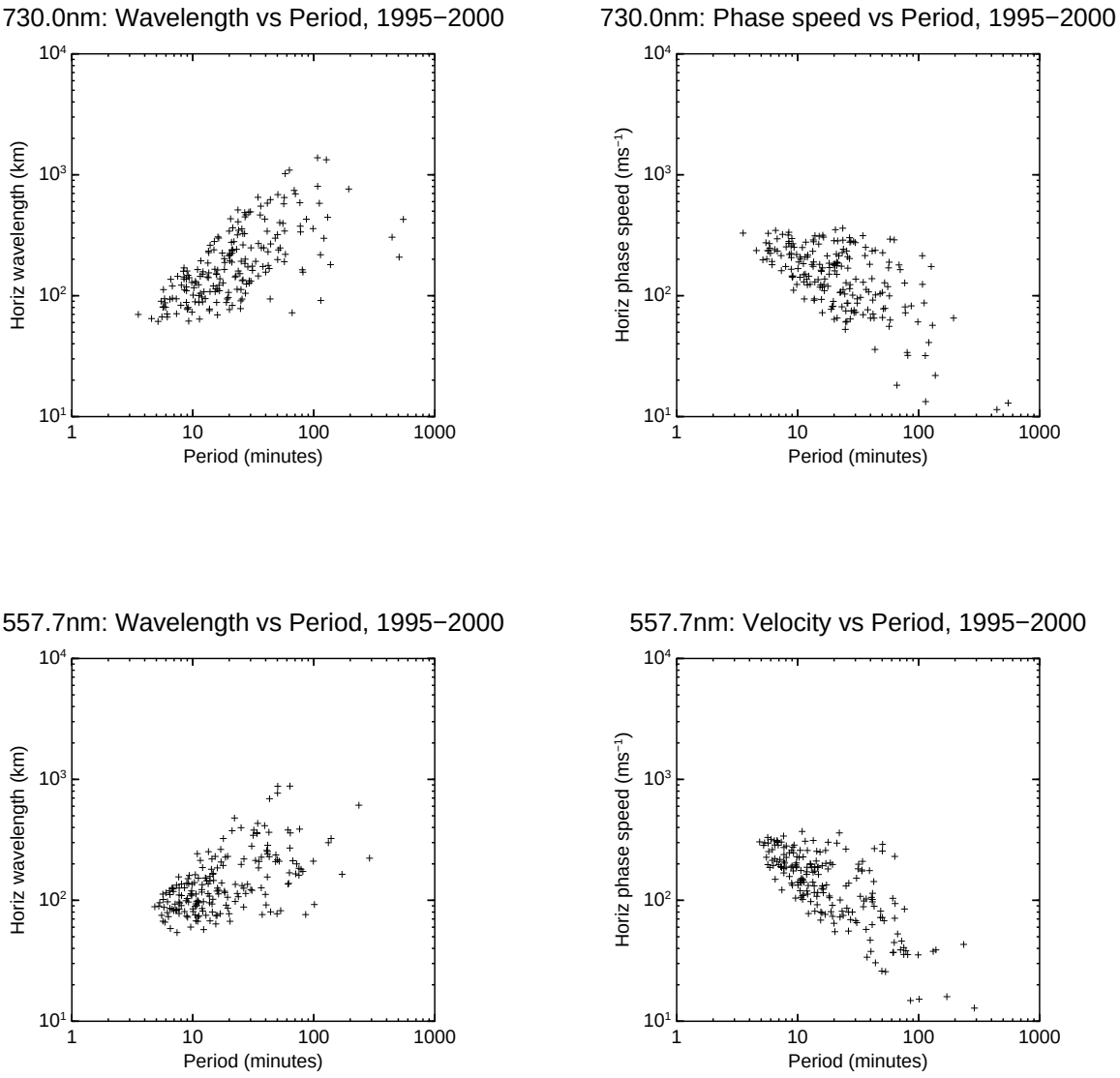

Figure 5.13: Summary of all intrinsic parameters available for gravity waves observed by the photometer. Power-law slopes of the 557.7nm and 730nm wavelength-period graphs, obtained through a χ^2 fit, are 0.46±0.04 and 0.38±0.04 respectively; for the phase speed-period graphs the slopes are -0.50±0.04 and -0.62±0.04. Typical uncertainties are ±15% for phase speed, ±5% for period and ±20% for horizontal wavelength.

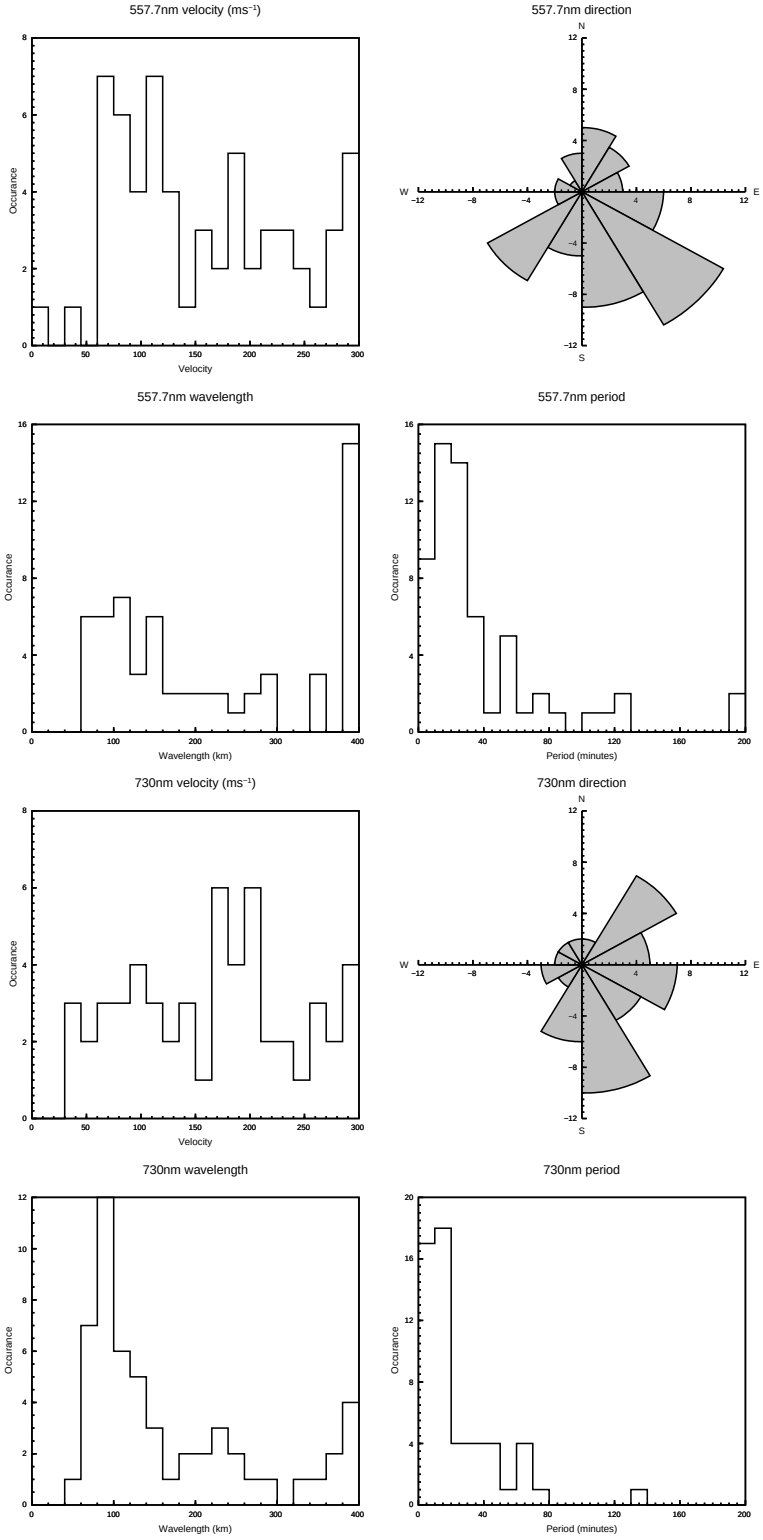

Figure 5.14: Occurrence histograms of intrinsic parameters from gravity waves observed in summer.

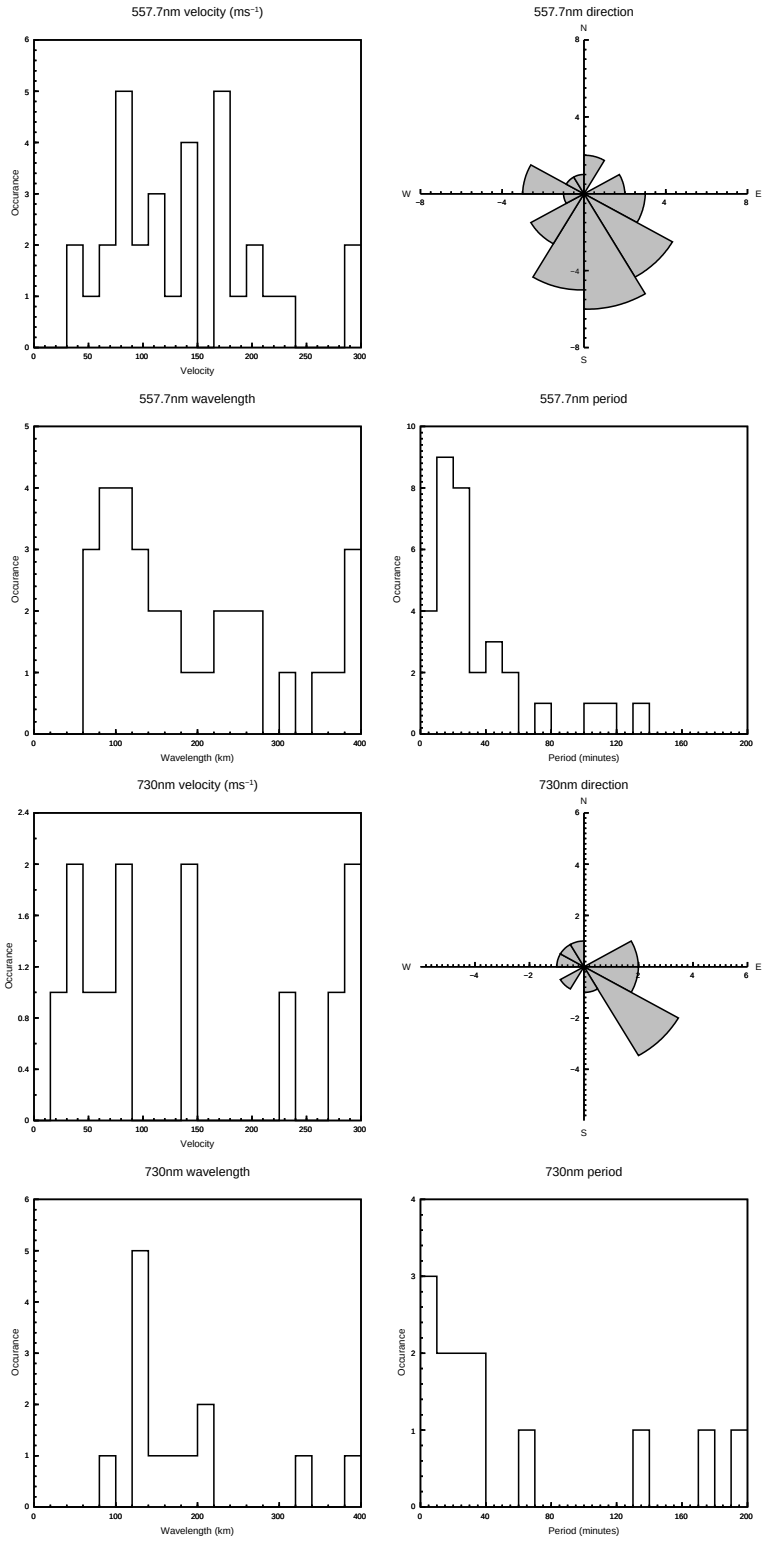

Figure 5.15: Occurrence histograms of intrinsic parameters from gravity waves observed in autumn.

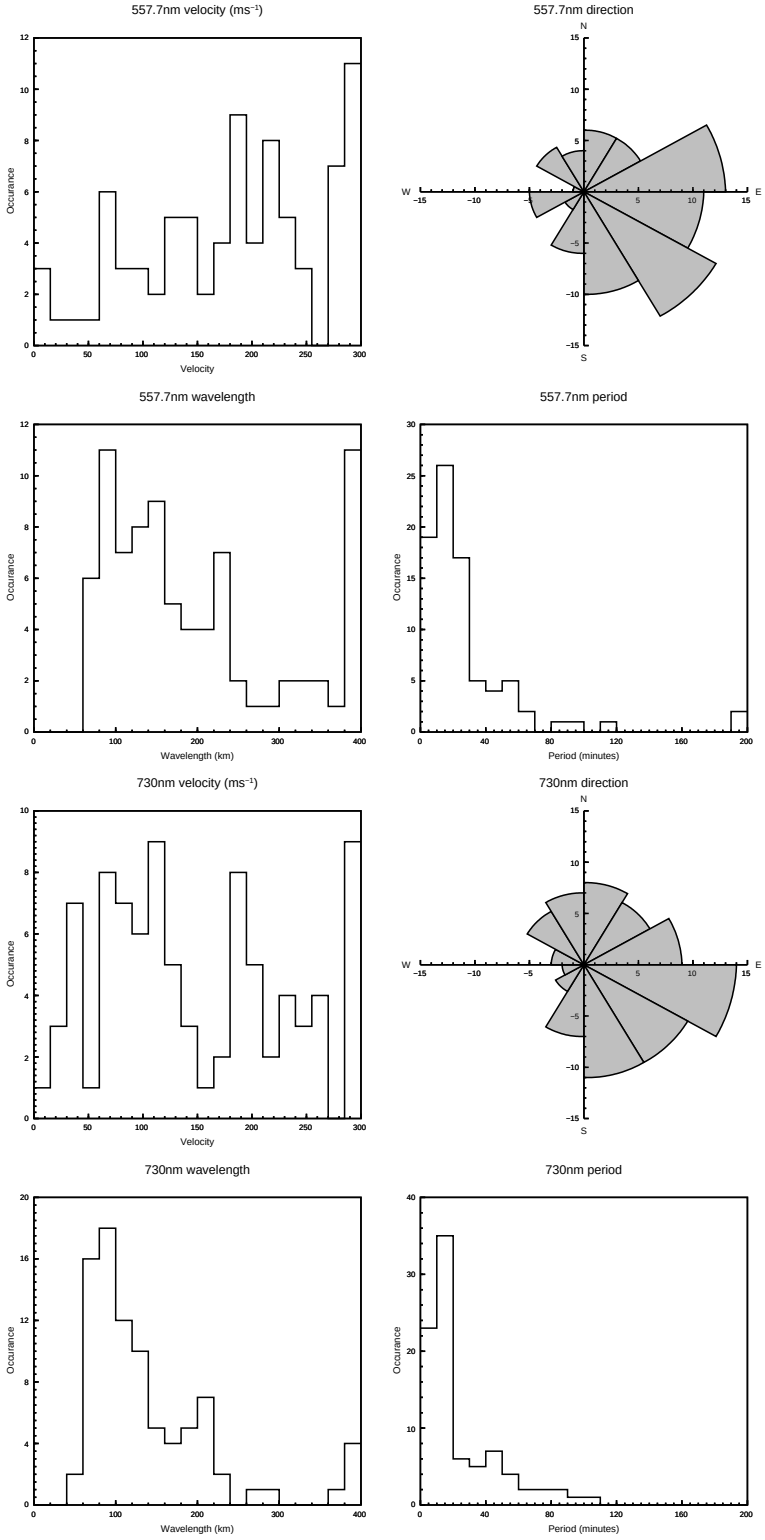

Figure 5.16: Occurrence histograms of intrinsic parameters from gravity waves observed in winter.

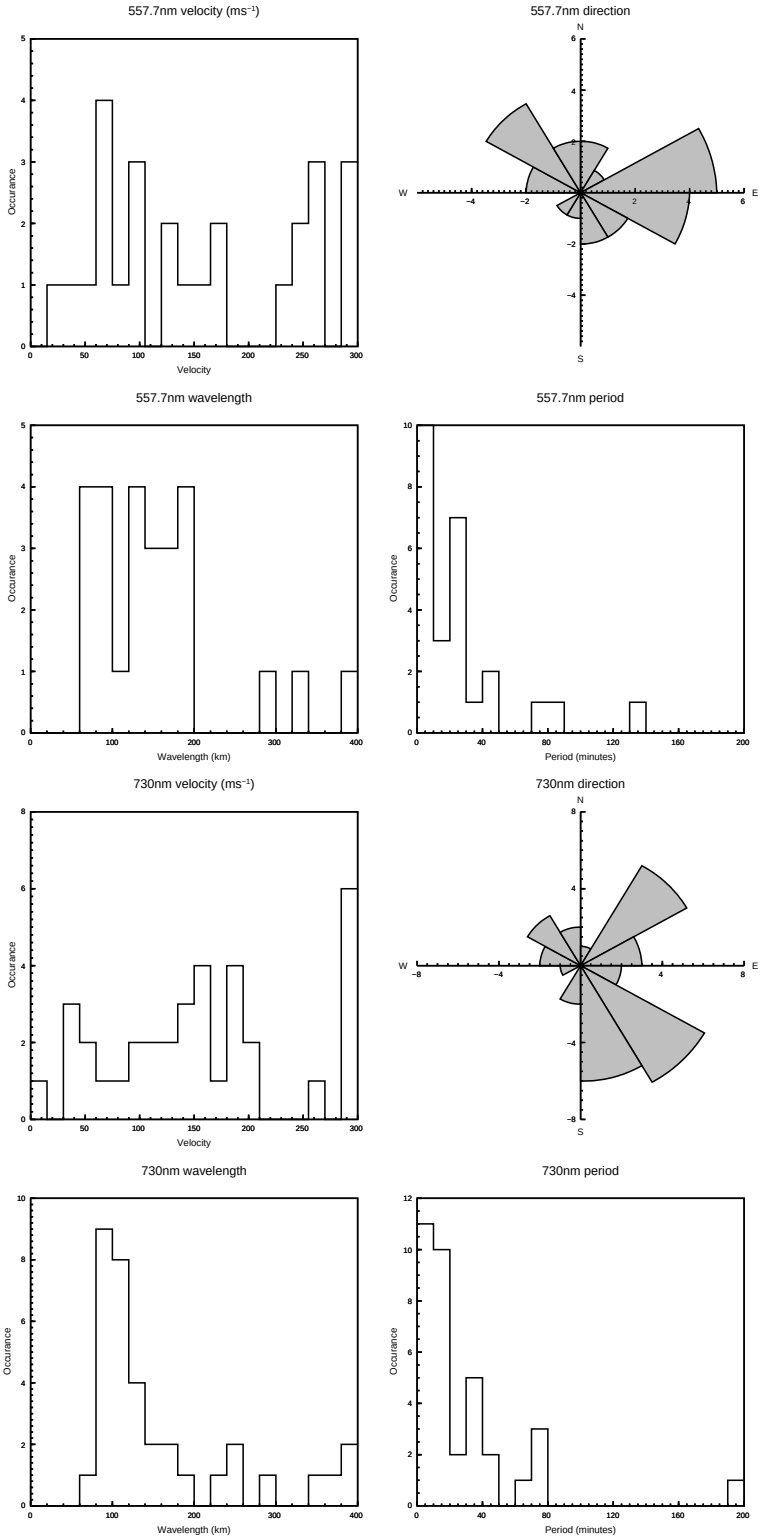

Figure 5.17: Occurrence histograms of intrinsic parameters from gravity waves observed in spring.

of high phase speeds in the intrinsic cases tends to suggest that any decrease which is observed is more due to the first mechanism rather than the second.

The direction histograms derived from both the observed and intrinsic phase velocity show a clear anisotropy throughout the year, although the prevailing direction does shift around from season to season. There are at times noticeable differences between the two observing heights. Generally speaking there is a definitive lack of wave activity propagating towards the west and (to a lesser extent) the north. Earlier studies (Walterscheid et al. 1999) have shown similarly strong directionality of wave activity although the specific behaviour of the directionality in the present study differs from that study. The presence of the winter westward jet in the mesosphere has the potential to explain the lack of westward waves observed in winter as these waves will encounter a critical layer and therefore not propagate to mesopause heights. However in summer when the jet is reversed, eastward wave activity still dominates. Since the jet would be expected to prevent eastward waves propagating from the lower atmosphere into the mesopause region during summer, it therefore seems that the waves being observed may not originate below the jet.

Using a CCD imager at the Buckland Park field station (Walterscheid et al. 1999), many instances were observed where the intensity and temperature of airglow layers were perturbed by strong disturbances propagating through the field of view over a time period of the order of thirty minutes. Similar wave-like structures have been observed in other imager-based studies throughout the world (Swenson et al. 1999, Frey et al. 2000). These disturbances usually persist for about an hour or less at a time and appear to consist predominantly of a single spacial frequency; they are therefore often referred to as 'quasi-monochromatic' (QM) waves. Walterscheid et al. (1999) identified that quasi-monochromatic waves preferentially propagated southward in summer and northward in winter suggesting a shift in tropospheric wave sources from the convection over Northern Australia to unstable weather at high southern latitudes in winter as the most likely cause. The strong eastward waves present in the photometer data at both heights at most times thoughout the year and the lack thereof in Walterscheid

et al.'s (1999) study therefore suggests that the waves detected by the photometer are not from the same population as the QM waves (as defined above) seen in imager data. There is a weak suggestion of varying north-south behaviour in the photometer data mirroring that of the imager study although it is clearly not the dominating effect.

When comparing the present results to other optical gravity wave studies in the literature it is important to note that whereas most recent work has concentrated on so-called 'quasi-monochromatic' (QM) wave features, the photometer data presented here will be less sensitive to QM effects and more sensitive to the total wave field. This comes about because the Fourier-based cross spectral analysis used to detect wave activity by definition more readily detects structures present over an entire observation period (a night in this case) rather than those active over shorter periods. QM waves tend to occur over a limited temporal range (although there are exceptions) and as shown by Walterscheid et al. (1999) there can be considerable differences between the total wave field and QM wave directionality. While one might expect to observe some wave activity of QM origin with the photometer it needs to be realised that a majority of the observed activity is more likely to be from the total wave field and this certainly appears to be the case.

Knowledge of the intrinsic wave parameters (specifically the horizontal wavelength and period) allows the use of the dispersion relation to further test the detected waves for adherence to gravity wave theory. Figure 5.18 shows the result of the application of this relation to obtain estimates of the waves' vertical wavelengths.

The most notable feature of these plots is the rapid fall in the number of waves with vertical wavelengths less than 10km; roughly 95% of all waves have vertical wavelengths greater than 10km. This is the nominal width of the OH and OI emission layers and as discussed by Gardner & Taylor (1998) airglow instruments are necessarily sensitive to waves with vertical wavelengths greater than the order of the emission layer width making the fall-off an expected feature.

It is worth noting that in nearly all cases it was not possible to identify wave signatures in both channels on a given night as being from the same wave. This

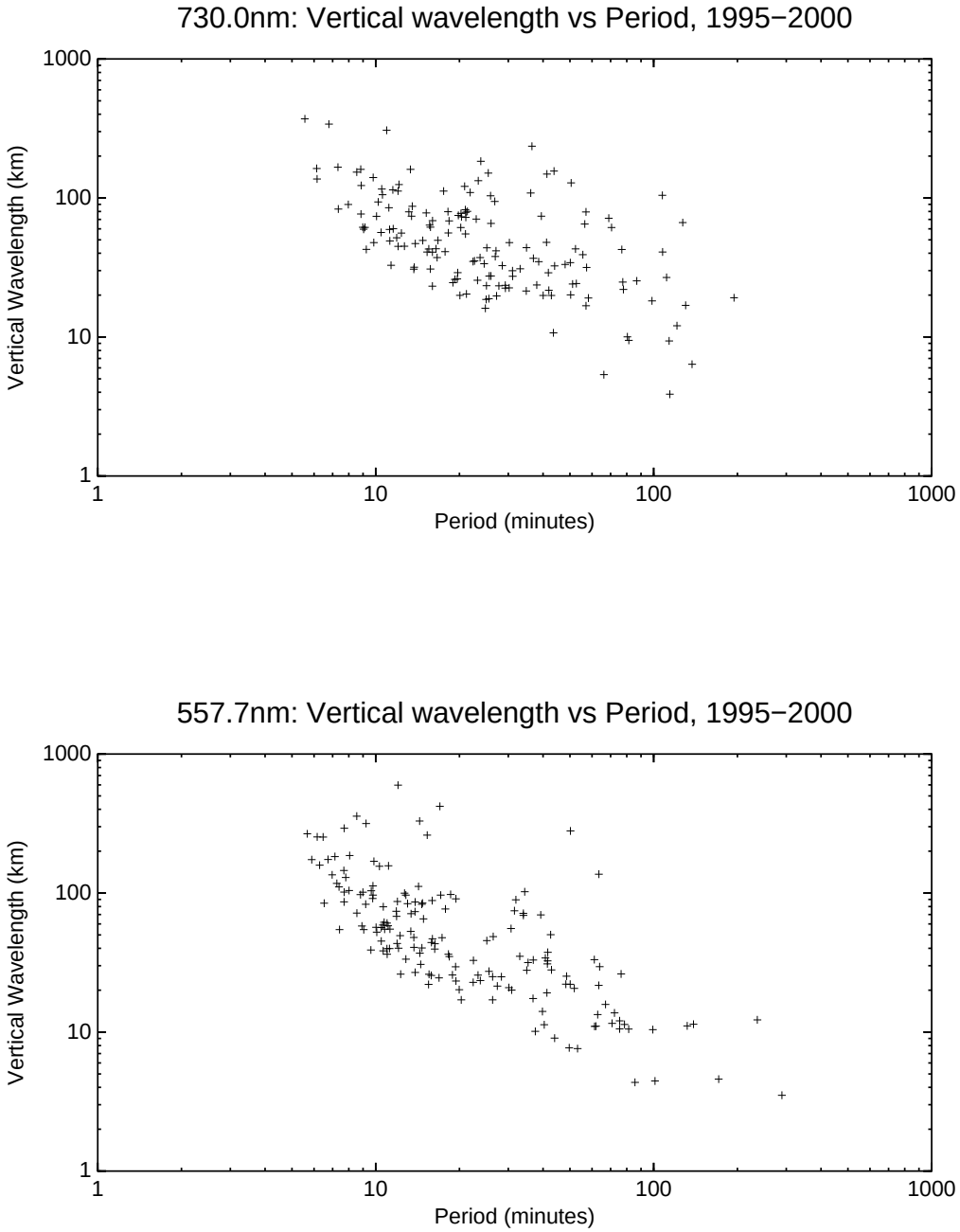

Figure 5.18: Vertical wavelength vs horizontal period for all waves observed at Buckland Park. Uncertainties are typically ±10% for vertical wavelength and ±5% for horizontal period.

strongly suggests that the waves being detected by the photometer at the emission heights are not propagating vertically between the two layers and may in fact be ducted. However, it could also be an effect of the Fourier-based analysis used - if there is a timelag between the wave arriving at the emission heights (as one would expect in the case of a vertically propagating wave) the coherence measured could be low, especially in the case where a wave is not present over an entire night.

5.4 Optical flux estimations

With knowledge of horizontal and vertical wavelengths and the method outlined in section 4.5, estimation of the vertical flux of horizontal momentum and the vertical energy flux carried by the observed waves could be made. The original approach by Swenson & Liu (1998) was first used and found to be deficient for the waves being identified by the photometer. Following the development of an improved procedure which did not include many of the approximations of the original, the fluxes were recalculated and examined in detail. Note that since an analytic expression for the cancellation factor applicable to the OI emission was not available, evaluation of the method was limited to the OH data.

5.4.1 Original Swenson approach

Using the procedure outlined by Swenson & Liu (1998), the momentum flux estimation for each wave identified by the photometer was calculated. These are shown in figure 5.19. Similar calculations have been performed by Swenson et al. (1999) using data obtained from an airglow imager. OH data were collected with a sampling interval of 120 seconds and analysed for monochromatic features. The arithmetic mean of the flux values obtained in the present study was calculated as $4.2 \pm 25 \mathrm{m}^2\mathrm{s}^{-2}$, excluding the two physically unrealistic values greater than $10^3 \mathrm{m}^2\mathrm{s}^{-2}$. Although this average momentum flux value was comparable to the mean magnitude reported by Swenson et al. (1999), inspection showed that the data depicted in figure 5.19 contained many

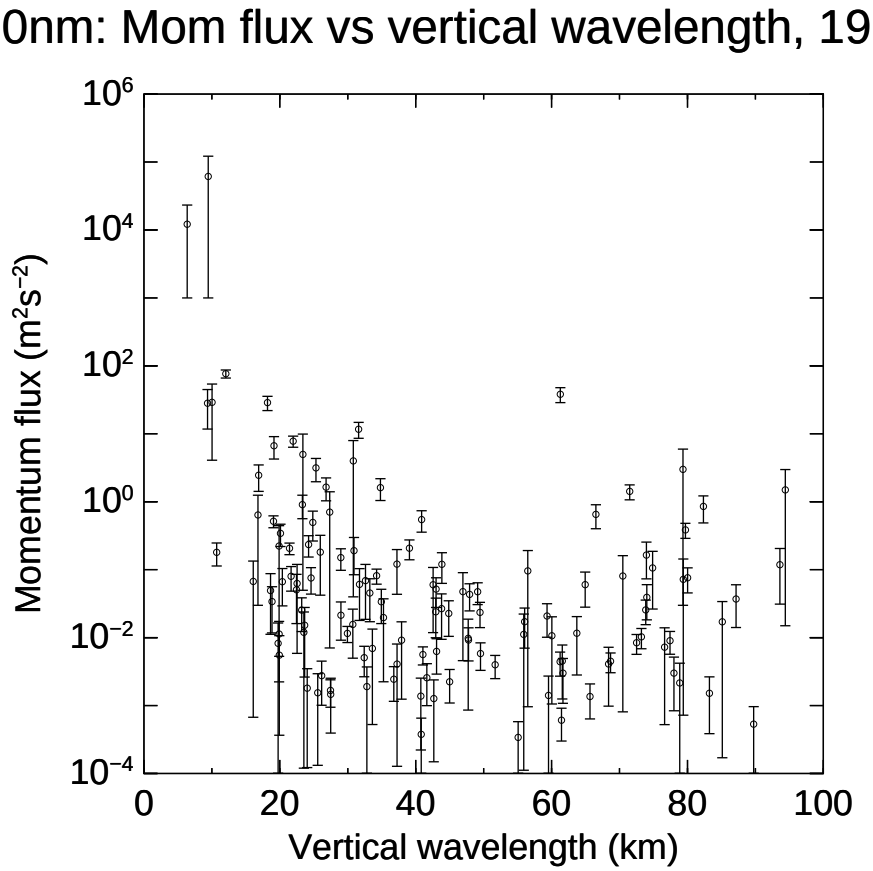

Figure 5.19: Estimations of the vertical flux of horizontal momentum for each gravity wave identified, for which intrinsic parameters and background wind were available. Excluding the two clearly unrealistic values greater than $10^3 \mathrm{m}^2\mathrm{s}^{-2}$, the arithmetic mean of these flux values is $4.2 \mathrm{m}^2\mathrm{s}^{-2}$. The typical uncertainty in the vertical wavelength is of the order of $\pm 10\%$.

momentum flux values less than $1\text{m}^2\text{s}^{-2}$ and some greater than the order of $100\text{m}^2\text{s}^{-2}$ which Swenson et al.'s (1999) results do not appear to contain. The large uncertainty in the average flux of the present results is due the extensive spread of the data which is clearly evident in figure 5.19.

Figure 5.20 summarises the amplitude of the vertical energy flux and the vertical flux of horizontal momentum associated with observed waves; propagation direction of the waves is also indicated. A comparison with the results obtained by Swenson et al. (1999) showed that the current study identified considerably more waves with very low energy and momentum flux values. This was also reflected in lower component mean values when unrealistically high values (that is, energy fluxes greater than 1Wm^{-2} and momentum flux components greater than $1000\text{m}^2\text{s}^{-2}$) were excluded: zonal and meridional energy flux means were -0.07mW^{-2} and -1.77mW^{-2} respectively, while the corresponding component means for momentum flux were -0.03m^{2}s^{-2} and -0.90m^{2}s^{-2} respectively — roughly an order of magnitude lower than those reported by Swenson et al. (1999).

5.4.2 Refinement of method

In order to address the issue of the large number of very small flux values produced, the method used to estimate them was reviewed. When describing the original theory Swenson & Liu (1998) applied a number of approximations which are not completely valid for the current dataset.

- $N^2 \gg \omega^2 \gg f^2$ was assumed, where N is the Brunt–Väisälä frequency, ω is the intrinsic frequency of the wave in question and f is the inertial frequency. While this is reasonable for waves with periods between fifteen minutes and one hour, inspection shows that the current dataset contains many waves well above this interval. An investigation of figure 5.18 shows that waves for which this assumption holds have typical vertical wavelengths less than about 30km, while inspection of flux values corresponding to vertical wavelengths less than

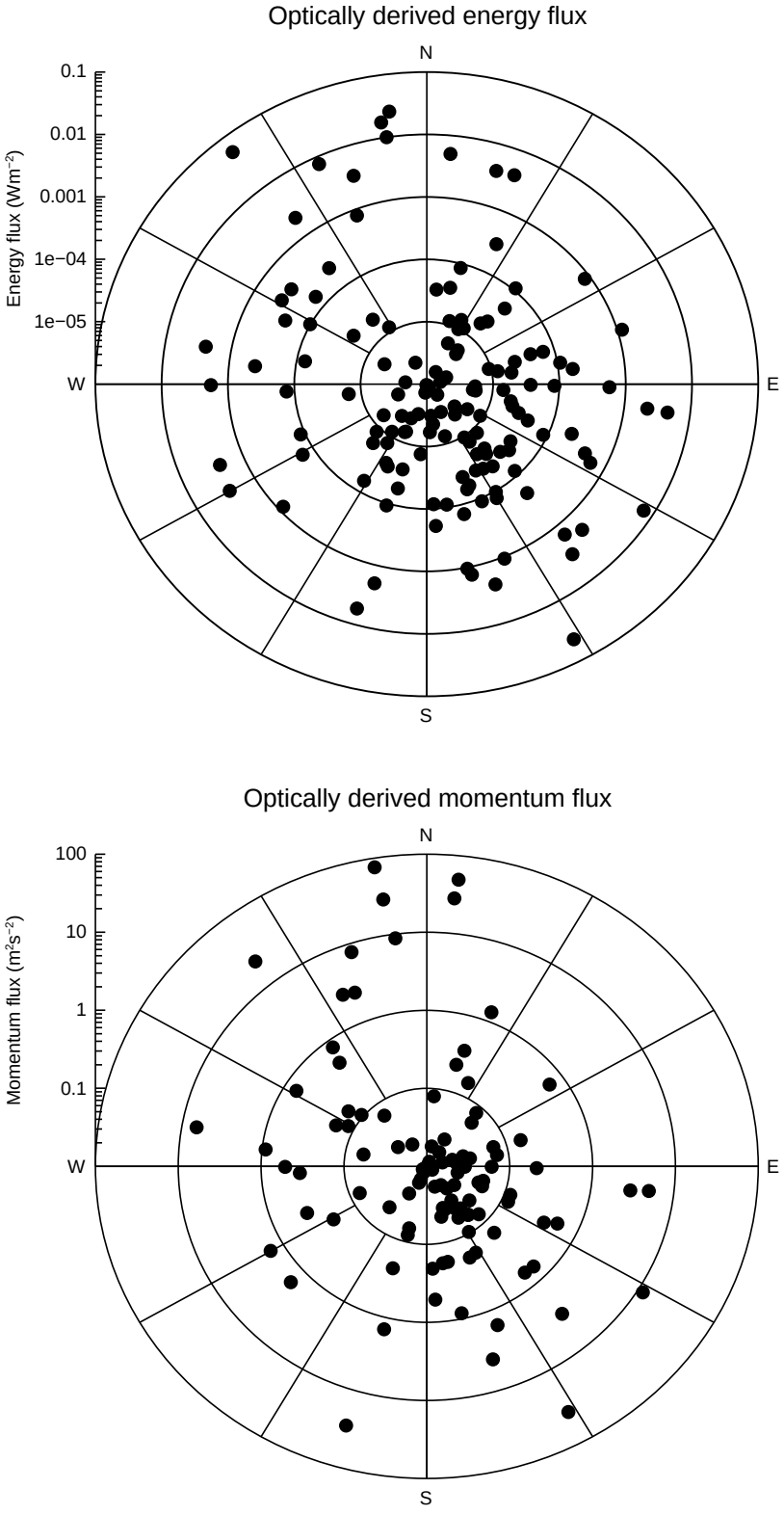

Figure 5.20: Polar plot of vertical energy flux (top) and vertical flux of horizontal momentum (bottom) of all waves observed at Buckland Park. Waves propagate from the origin towards the points indicated.

30km in figure 5.19 reveals flux values closer in average magnitude to those of Swenson et al. (1999). This reinforces the need to address this approximation when studying waves with vertical wavelengths greater than 30km.

- An approximate polarisation expression was used to relate the horizontal and vertical wind perturbations which is again only valid when $N^2 \gg \omega^2 \gg f^2$.

- The method inherently assumes that all waves associated with an intensity perturbation are vertically propagating. This aspect of the present method is common to a similar procedure used to estimate the total flux based on wavenumber spectra (Gardner et al. 1999) and has been strongly emphasised by Fritts (2000) as being a significant problem. It is acknowledged that this is a limitation of this method which must be recalled when interpreting the results.

To address the first two problems the expressions for the energy and momentum fluxes were re-derived. Starting from the expression for energy flux given by Vincent (1984)

$$F_E = -\rho \frac{\omega}{m} \left(\frac{\omega^2 - f^2}{\omega^2 + f^2} \right) \overline{V^2} \tag{5.1}$$

where ρ is the density, m is the vertical wavenumber and $\overline{V^2}$ is the mean square horizontal velocity, and utilising

$$\left| \frac{\rho'}{\rho_0} \right|^2 = \frac{N^2}{g^2} \left(\frac{\omega^2 - f^2}{\omega^2 + f^2} \right) \overline{V^2} \tag{5.2}$$

and

$$\frac{\rho'}{\rho_0} = -\frac{T'}{T} \tag{5.3}$$

where $\frac{\rho'}{\rho_0}$ is the fractional density perturbation and $\frac{T'}{T}$ is the fractional temperature perturbation (Swenson & Liu 1998), the expression for the energy flux magnitude becomes

$$F_E = \rho \frac{\omega}{m} \frac{g^2}{N^2} \left\langle \left(\frac{T'}{T} \right)^2 \right\rangle . \tag{5.4}$$

Here g is the acceleration due to gravity and $\langle\rangle$ denotes an average over a complete wave period. Additionally it can be shown that

$$\frac{w}{m} = \frac{\lambda_z}{\lambda_x} c, \tag{5.5}$$

where λ_x and λ_z are the horizonal and vertical wavelengths respectively, and c is the horizontal phase speed. Using this along with

$$\left\langle \left(\frac{T'}{T}\right)^2 \right\rangle = \frac{1}{2}\frac{1}{\mathrm{CF}^2}\left(\frac{I'_{OH}}{I_{OH}}\right)^2 \tag{5.6}$$

where $\frac{I'_{OH}}{I_{OH}}$ is the fractional OH intensity perturbation and CF is the cancellation factor (Swenson et al. 2000), the energy flux can be written in terms of the wavelengths and the intensity perturbation:

$$F_E = -\rho c \frac{1}{2}\frac{\lambda_z}{\lambda_x}\frac{g^2}{N^2}\frac{1}{\mathrm{CF}^2}\left(\frac{I'_{OH}}{I_{OH}}\right)^2 \tag{5.7}$$

The factor of $\frac{1}{2}$ in equation 5.6 is the result of time averaging the squared sinesoidal temperature perturbation term over a complete period.

The vertical flux of horizontal momentum is defined as

$$F_M = \langle u'w' \rangle \left(1 - \frac{f^2}{\omega^2}\right) \tag{5.8}$$

where u' and w' are the perturbations of horizontal and vertical wind respectively (Fritts 2000). The polarisation relationship

$$w' = \left(\frac{\omega^2 - f^2}{N^2 - \omega^2}\right)\left(\frac{m + i\alpha}{k}\right)u' \tag{5.9}$$

where $\alpha \equiv \frac{1}{2H}$ (Swenson et al. 2000) allows u' to be expressed in terms of w' while

$$\frac{T'}{T} \approx -i\frac{N}{g}\frac{N}{\omega}w' \tag{5.10}$$

relates the fractional temperature perturbation to the vertical wind perturbation (Tsutsumi 1995). Combining these results and utilising equation 5.6 yields

$$F_M = \frac{1}{2}\left(\frac{N^2 - \omega^2}{\omega^2 - f^2}\right)\frac{g^2\omega^2}{N^4}\frac{k}{\sqrt{m^2 + \alpha^2}}\frac{1}{\mathrm{CF}^2}\left(\frac{I'_{OH}}{I_{OH}}\right)^2\left(1 - \frac{f^2}{\omega^2}\right). \tag{5.11}$$

Furthermore, the dispersion relation can be written in the form

$$m^2 = k^2\left(\frac{N^2 - \omega^2}{\omega^2 - f^2}\right) - \alpha^2 \tag{5.12}$$

allowing the expression for F_M to be reduced to

$$F_M = \frac{1}{2}\frac{\sqrt{m^2 + \alpha^2}}{k}\frac{g^2\omega^2}{N^4}\frac{1}{\mathrm{CF}^2}\left(\frac{I'_{OH}}{I_{OH}}\right)^2\left(1 - \frac{f^2}{\omega^2}\right). \tag{5.13}$$

In the limit where $\alpha = 0$ and $N^2 \gg \omega^2 \gg f^2$, equation 5.13 tends to the original expression given by Swenson & Liu (1998) and Swenson et al. (1999) (see equation 4.55 on page 91).

5.4.3 Revised flux estimates

Utilising equations 5.7 and 5.13 the energy and momentum fluxes for waves observed by the 730nm channel of the photometer were recalculated. Figure 5.21 shows a summary of the momentum fluxes as a function of vertical wavelength, while figure 5.22 is a polar plot of the energy and momentum fluxes similar to figure 5.20.

The effect of the revised expressions for energy and momentum flux are clearly visible in figure 5.21: the flux values are higher by several orders of magnitude for waves with vertical wavelengths greater than thirty kilometres. This was expected due to the nature of approximations inherent in the orginal method. Compared with figure 5.19 there are more flux values above $100\text{m}^{-2}\text{s}^{-2}$, although they are no longer confined to low wavelengths and values greater than $1000\text{m}^{-2}\text{s}^{-2}$ are no longer present. Taking into account the large uncertainties associated with the high flux values, about 20% of the values now clearly lie well above $100\text{m}^{-2}\text{s}^{-2}$, a value which is physically unreasonable. Furthermore, momentum fluxes as high as this have not been previously identified in the literature: their plausibility must therefore be questioned. This is reinforced by their arithmetic mean of $130 \pm 200\text{m}^{-2}\text{s}^{-2}$ which is clearly too high by almost an order of magnitude. If consideration is restricted to a range of flux values more consistent with the literature (that is, less than $100\text{m}^{-2}\text{s}^{-2}$) the arithmetic mean becomes $25 \pm 24\text{m}^{-2}\text{s}^{-2}$, although this is still slightly too high compared with most other published values (for example, Reid & Vincent 1987a, Swenson et al. 1999).

When considering the source of these large values, the assumption of vertical propagation should be recalled. Using this method, a wave which is ducted (that is, not propagating vertically at all) will not transport any momentum physically, but this method will still calculate a momentum flux as if it were. High flux values could result.

Another important point to note is that the vertical wavelength reported for some

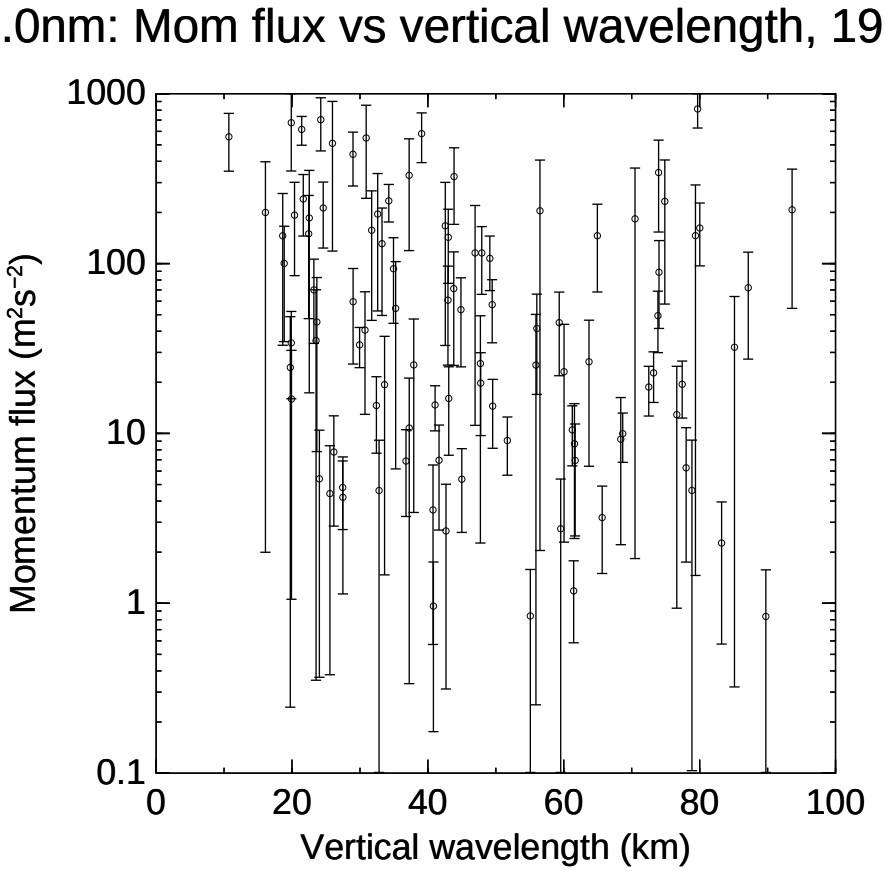

Figure 5.21: Momentum fluxes of waves observed in the 730nm emission calculated without utilising approximate polarisation and dispersion relations. Uncertainties in the vertical wavelength are of the order of $\pm 10\%$. Inspection reveals that fluxes of all waves have been affected. Since $N^2 \gg \omega^2 \gg f^2$ is regarded to hold for waves with vertical wavelengths less than 30km given their intrinsic period (see text), it may not be clear how the approximations can significantly affect fluxes of waves with these vertical wavelengths. It should be recalled that the momentum flux estimation depends not only on vertical wavelength but also on the exponential cancellation factor, which tends to infinity as vertical wavelength approaches zero. Therefore, while the approximations have only a small effect on the calculated vertical wavelength of waves satifying $N^2 \gg \omega^2 \gg f^2$, the resulting change in cancellation factor remains significant since such waves tend to have vertical wavelengths less than 30km. Consequently, the fluxes associated with waves across the entire vertical wavelength range are affected when approximations are removed from the calculation.

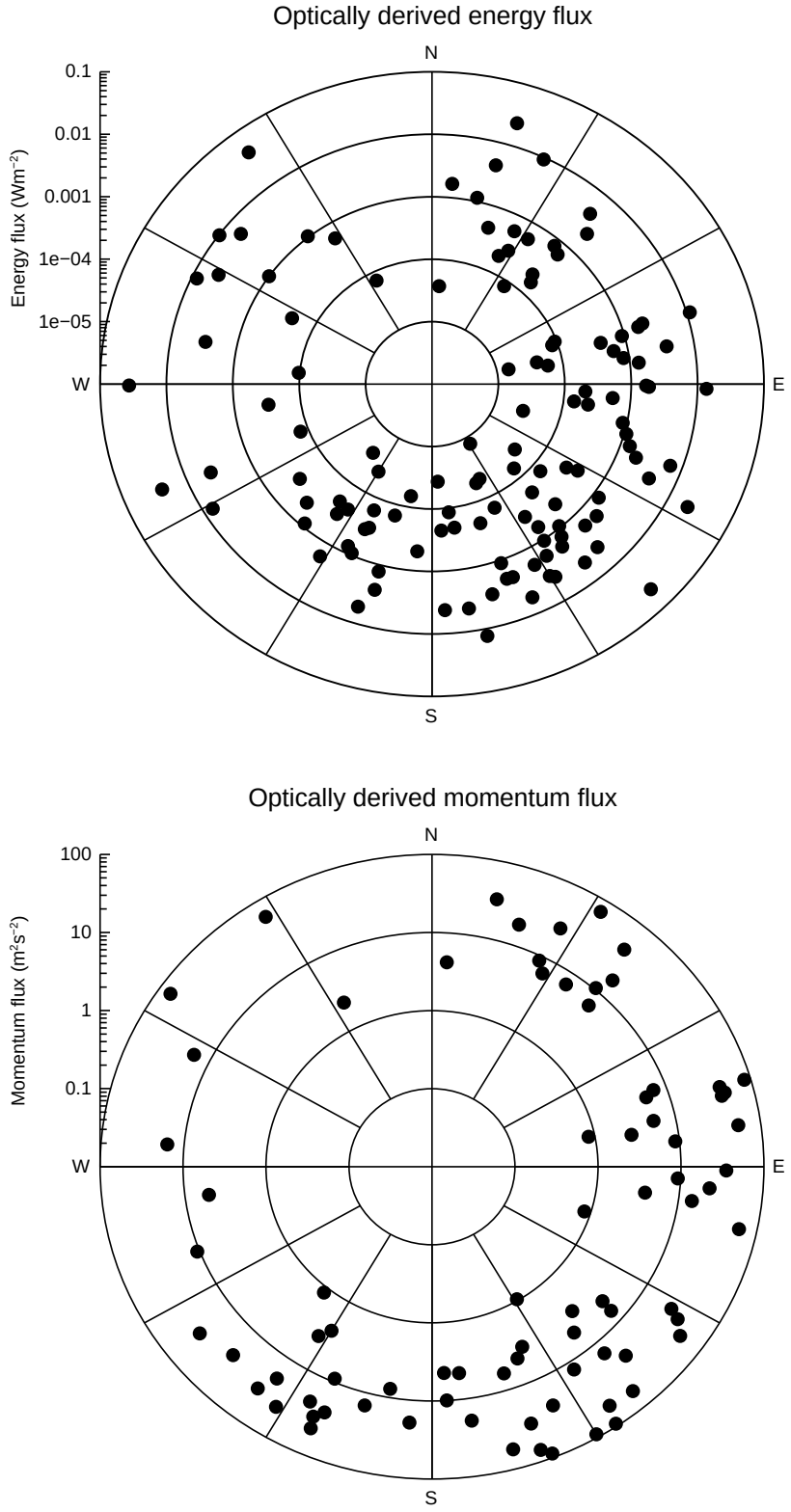

Figure 5.22: Revised polar plot of vertical energy flux (top) and vertical flux of horizontal momentum (bottom) of all waves observed at Buckland Park. As in figure 5.20, waves propagate from the origin towards the points indicated. Estimates shown in this figure use the revised flux equations.

these waves is less than 10km–20km and the analytical expression used for the cancellation factor (CF) as part of the flux calculation has not been validated for wavelengths as low as this. Certainly the analytical expression deviates from the cancellation factor resulting from model calculations and there is a suggestion that the uncertainty in CF at these wavelengths could be greater than 50% (Swenson & Liu 1998). An additional issue is that waves of these wavelengths are not detected reliably by optical instruments due to the vertical wavelengths being of similar order the extent of the emission layer, which introduces further sources of error. These large uncertainties in CF and in the wave parameters themselves have not been included in the error bars of figure 5.21 and could well explain these higher than expected values for low vertical wavelengths.

Higher energy and momentum flux estimates are also evident in figure 5.22 when compared to figure 5.20. Both plots demonstrate an eastward directionality preference although it is arguably clearer in figure 5.22. This is in part due to the points lying away from the centre of the figure where directionality is not clearly visible. Even so, the clarity of a preferential direction is not as obvious as that demonstrated by Swenson et al. (1999), where the south-westward quadrant was almost completely empty. If consideration is restricted to the same flux magnitudes as shown by Swenson et al. (1999) (that is, energy flux amplitudes between 0.1mWm^{-2} and 100mWm^{-2}, and momentum flux amplitudes between $1\text{m}^2\text{s}^{-2}$ and $100\text{m}^2\text{s}^{-2}$ as shown in figure 5.23), the eastward preference remains visible with the north-western quadrant appearing emptier than the other three. In any case the single nearly empty quadrant seen by Swenson et al. (1999) does not occur in the present results, although the limited temporal span of Swenson et al.'s (1999) results could be a factor. Another important point to note is that these two studies could be observing different wave populations; while Swenson et al.'s (1999) study dealt with QM waves observed over five nights, the method used to acquire the results presented herein are likely to be more sensitive to waves present over the whole night.

It is clear when considering the flux and directionality results of the present study,

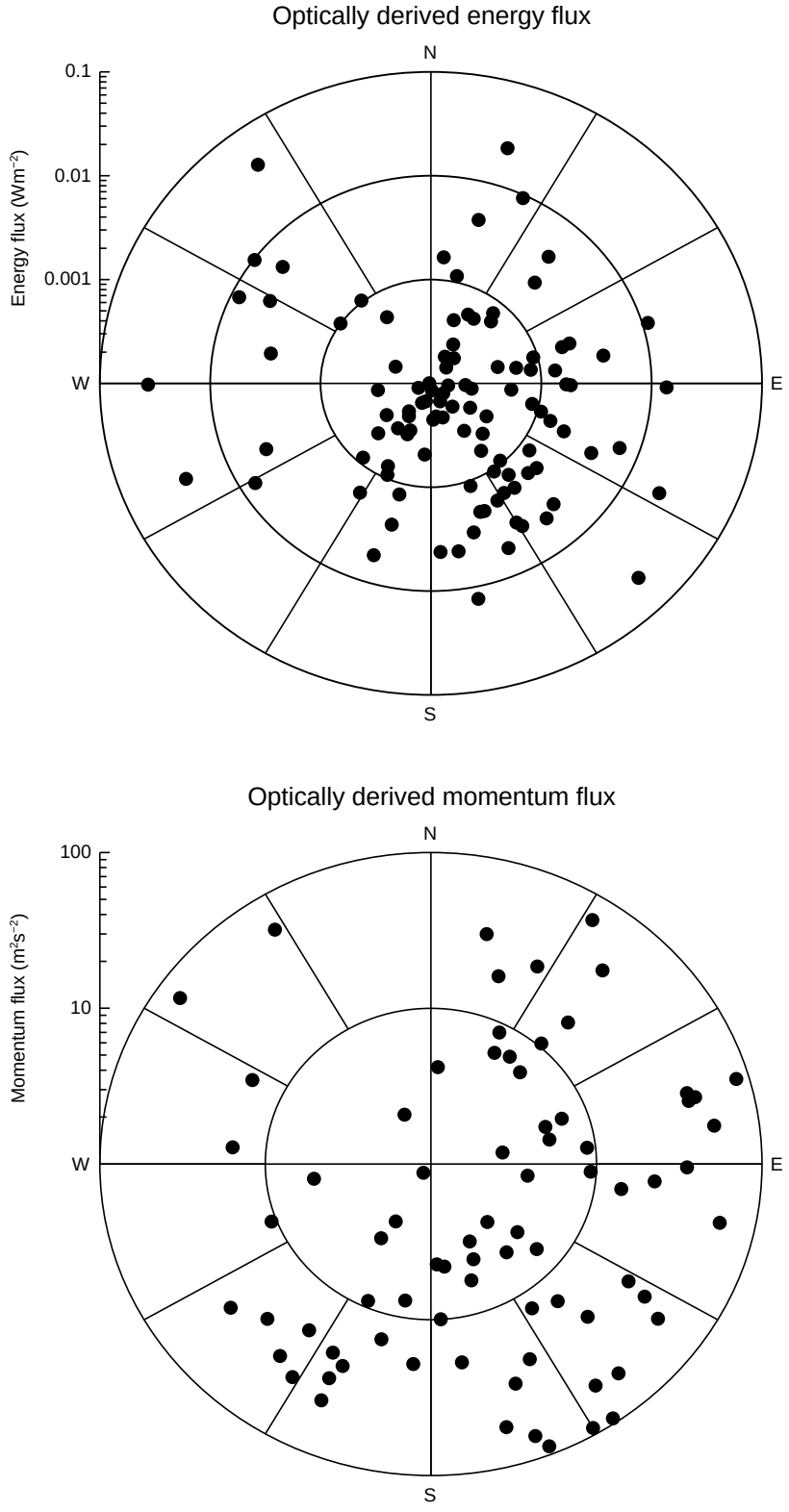

Figure 5.23: Polar plot of vertical energy flux (top) and vertical flux of horizontal momentum (bottom) as for figure 5.22 but restricted to magnitudes greater than $0.1\mathrm{mWm}^{-2}$ and $1\mathrm{m}^2\mathrm{s}^{-2}$ respectively.

that they do not display a directionality trend as strongly as those found in other studies which dealt with QM waves. Studies by Walterscheid et al. (1999) have indicated that the total wave field (which the photometer is inherently more sensitve to) does tend to show weaker directionality than the QM waves, and this is consistent with the present results. It is also worth recalling that few waves detected in either the 557.nm or 730nm data were found to have plausible concurrent signatures in the other optical channel, suggesting that the majority of waves detected by the photometer were not freely propagating between the two layers. This could be caused either by ducting or the presence of a critical layer between the two airglow emission heights preventing downward or upward propagation of a given wave.

To further classify the momentum flux values being calculated, figure 5.24 was generated. The upper plot shows the distribution of momentum flux values using a bin size of $10 m^2 s^{-2}$. The lower plot shows the average momentum flux recorded by waves in each 5km vertical wavelength bin. Although the lower plot of figure 5.24 suggests that higher flux values may result from waves with vertical wavelengths less than 40km and greater than 70km, the large uncertainties encountered across data the prevent a definitive conclusion. With reference to the distribution (the upper plot of figure 5.24), nearly 25% of the fluxes calculated occur in the lowest flux bin ($0–10 m^2 s^{-2}$), and over 50% lie between $0 m^2 s^{-2}$ and $50 m^2 s^{-2}$. Recalling figure 5.21 it can be seen that the vertical wavelength of most of these waves are between 20km and 70km which corresponds with the range observed in other studies (Swenson et al. 1999). It therefore seems reasonable that at least 50% of the waves being identified by the photometer are physically significant and are probably propagating vertically. Determining the origin of the waves giving large flux values and verifying those with lower flux values will require an independent measure of momentum flux such as that provided by the co-located MF radar at Buckland Park. Pursuit of this could provide a valuable insight into any further limitations of the method which may exist, and the reliability of fluxes measured from optical data. On the basis of such a study it may be possible to assign a confidence limit to each wave's flux value on the basis of the probability that the

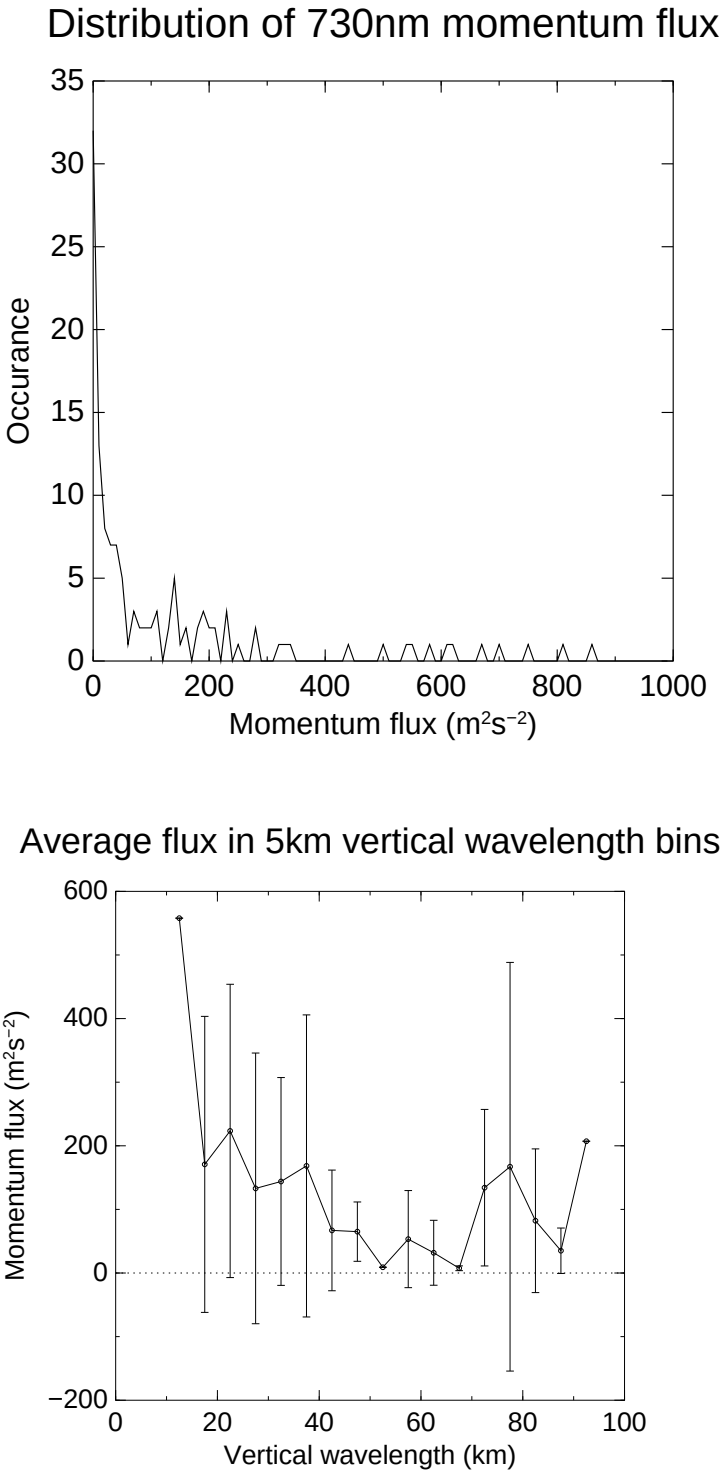

Figure 5.24: Two alternative ways of visualising the fluxes resulting from the revised method. The upper plot shows the distribution of momentum flux values using a bin size of $10\text{m}^2\text{s}^{-2}$, while the lower plot shows the average momentum flux within 5km vertical wavelength bins. The error bars on the lower plot represent the standard deviation of flux values which contributed to each respective bin. The large span of the error bars indicate that waves with large momentum flux values do not have a well defined vertical wavelength range.

flux is real. The existence of additional limitations and the method's reliability must be questioned on the basis of the results presented here.

The seasonal variablility in the vertical flux of horizonal momentum is summarised in figure 5.25 which shows the magnitude of the zonal and meridional components of the momentum flux associated with all waves detected against day of year. It should be noted that this presentation does not specify the waves uniquely since the sign of the components has been neglected and the components themselves are products of two perturbation quantities. For both the zonal and meridional case there is a clear indication that the flux measurements tended to peak in winter and summer, with winter recording the higher overall values. With maxima in summer and winter, the general form of the flux magnitudes is in agreeance with other published work (for example Tsuda et al. 1990, Gavrilov et al. 2000).

5.4.4 Considerations arising from the method

When applying this method to the estimation of fluxes from optical data, there are a number of other issues to be considered. The cancellation factor used to relate intensity perturbations to atmospheric temperature variations as part of the calculation of energy and momentum fluxes is valid so long as the wave under consideration has fully propagated into the OH emission layer. It is possible that occasionally a wave will be observed which does not satisfy this condition; the effect is that the photometer will record a lower total volume intensity than would be associated with the wave if it was affecting the entire OH emission layer and this will result in an underestimation of the fluxes. In the case of waves identified by the photometer in this study, the occurrence of this situation is expected to be low; the coherence requirements across a night would normally mean that any wave detected would have had more than enough time to propagate through the entire emission layer unless a turning level was encountered part way through the layer.

A large number of waves (approximately 20%) were found to have unusually large

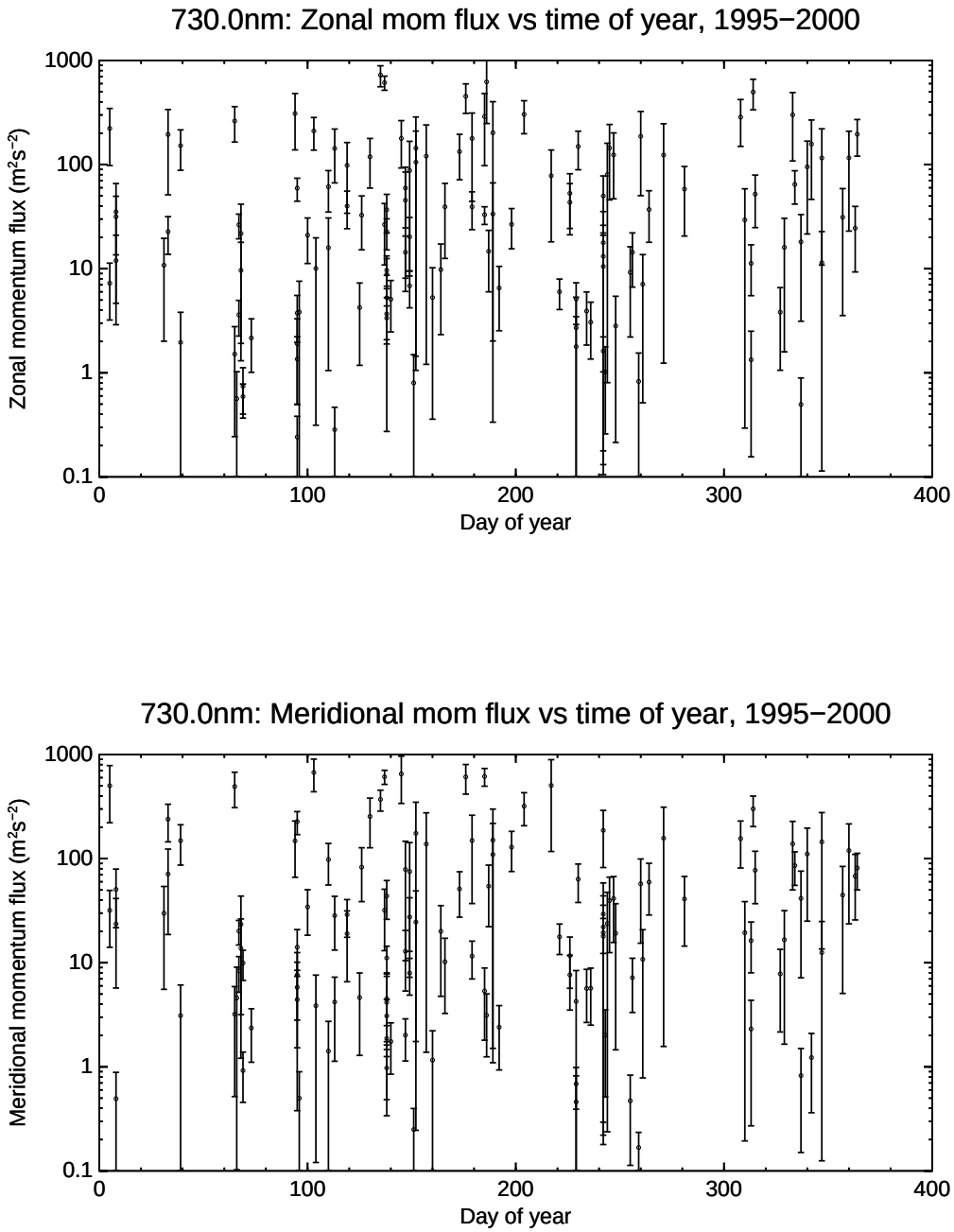

Figure 5.25: The seasonal variation of zonal (top) and meridional (bottom) components of the momentum flux associated with each wave detected by the three field photometer. Contributions from all waves recorded between 1995 and 2000 are included in this figure.

fluxes associated with them. This could indicate that for some waves at least the intensity perturbation amplitudes calculated in this study may be higher than they should be. The algorithms used to estimate the perturbed and unperturbed intensity in the present work may need further attention and possible refinement since any respective underestimation of the perturbed intensity or overestimation of the unperturbed intensity will result in an overestimation of the momentum (and energy) fluxes.

5.5 Summary

Using data obtained from approximately three hundred cloud-free nights between 1995 and 2000 by the three field photometer, a total of around 400 coherent waves were identified in each of the two airglow emissions being observed (557.7nm and 730nm). The development of a wavelet-based filter allowed the use of nights heavily contaminated by the Milky Way. The observed parameters were deduced using cross-spectral techniques, and these were used with wind data from a co-located MF radar to infer intrinsic wave parameters. A strong preference for eastward propagation was seen, although a consistent seasonal variation of other wave parameters was not observed.

The intrinsic wave parameters were used to evaluate a method for obtaining gravity wave momentum and energy flux from optical data. The original method described by Swenson & Liu (1998) was found to be inadequate for the waves identified by the photometer due to a number of assumptions made during its derivation. A refined method was developed which, while giving more realistic flux values in general, resulted in a large number of values (about 20%) which were physically unreasonable. Even with consideration of the limitations of this method raised by Fritts (2000), further research is needed to identify the true nature of these values, especially with reference to photometer data.

chapter 6

Long-term airglow variability

In addition to analysis identifying parameters for specific gravity wave observations, long-term variations in gravity wave activity was also investigated using both the optical and radar data collected at Buckland Park. Whereas the wave parameter study concentrated on the classification of the wave activity observed across nights in isolation, this chapter deals with the general behaviour of the wave field across the entire five year observational period.

6.1 Optical intensity data

In order to get an overview of all available data the intensities from all 557.7nm and 730nm observations were plotted as shown in figures 6.1 and 6.2. The intensity values displayed in these figures are the result of averaging each night into thirty minute blocks and then averaging the respective blocks across adjacent days. A given cross-day average ceased (and a new one started) when a substantial break (more than three days) existed in the observations or the average represented eight days' data.

Figures 6.1 and 6.2 neatly summarise many of the features of the optical data acquired at Buckland Park for this study. The near-sinesoidal variation in start and end times is a direct consequence of the variation in sunrise and set times across a year. The periodic interruptions to data coverage is a result of the moon being up. In

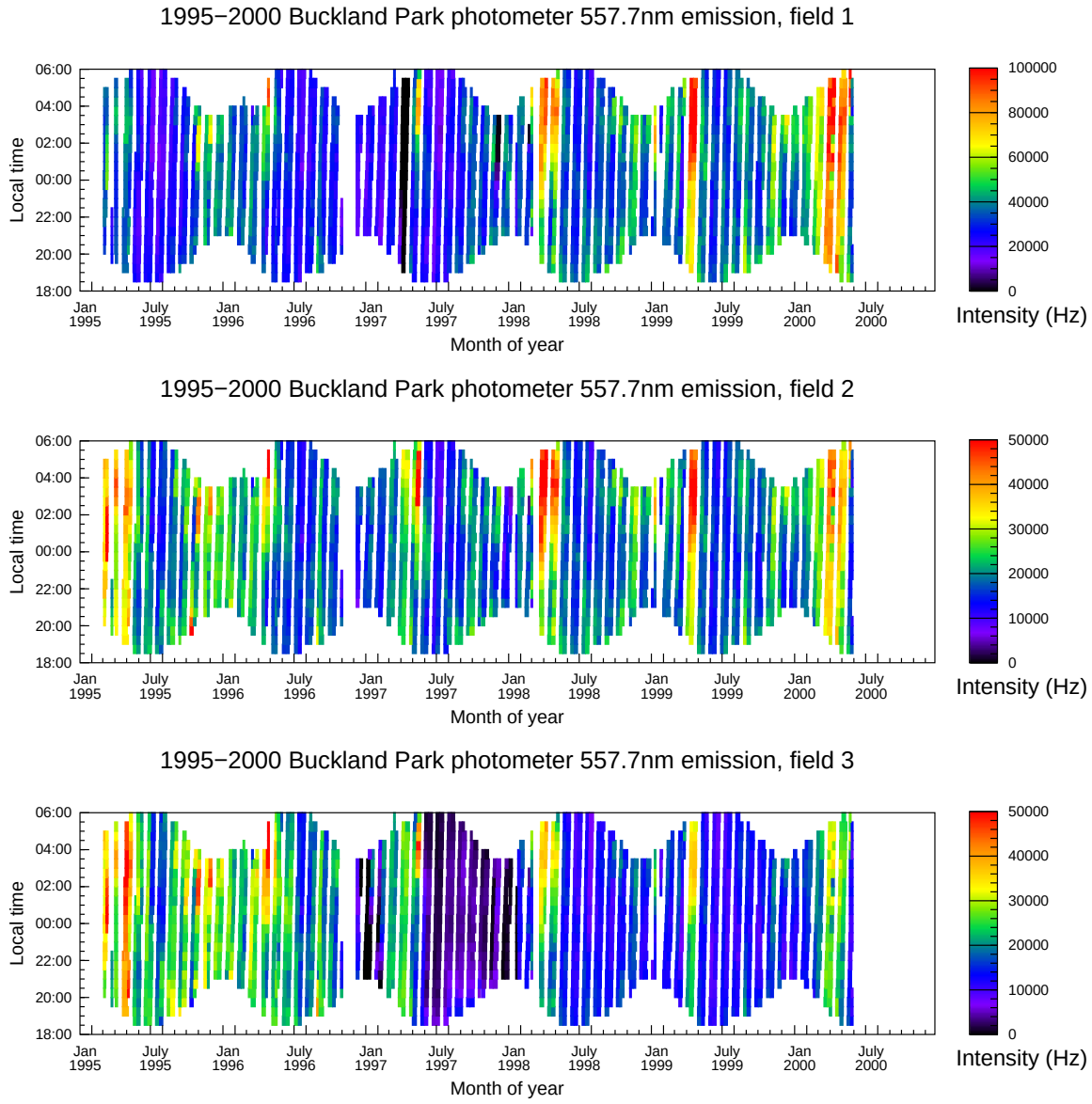

Figure 6.1: Overview of all 557.7nm intensity data recorded at Buckland Park. Data have been averaged in thirty minute blocks and then averaged across adjacent days as described in the text.

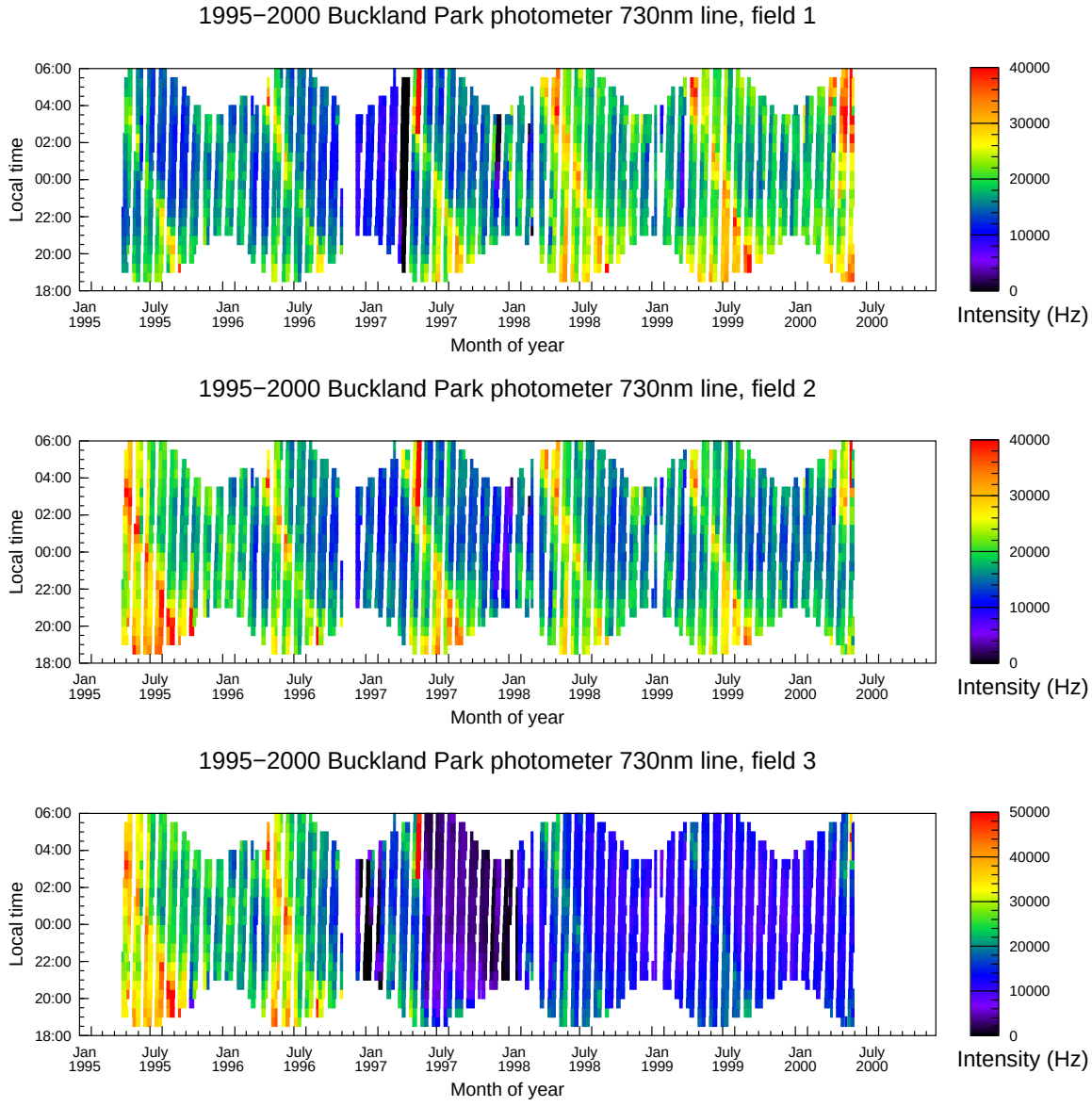

Figure 6.2: Overview of all 730nm intensity data recorded at Buckland Park. Data treatment is the same as for figure 6.1.

any given month the moon's effect was to move the observation start time later and later until no data acquisition was possible. After roughly five days observations could begin again in the evening building up to eventually cover the whole night once again.

Other irregular interruptions in the data series are also evident. The non-uniform coverage of 557.7nm data in March–April 1995 occurred while the instrument was still being set up and fine-tuned. During this time only 557.7nm data was taken — concurrent OH observations commenced in late April 1995. The roughly six week gap around November 1996 and a somewhat smaller interruption between December 1998 and January 1999 were caused by an equipment outage. The significantly lower amplitude recorded in field three mainly during the last half of 1997 was due to a slowly failing photomultiplier tube which was replaced in January 1998 as discussed previously. Other isolated regions of low counts in a single field were caused by dynode resistor failures which were quickly identified and replaced. It is also clearly evident that although the replacement photomultiplier for channel three was adjusted to give a similar signal to noise ratio to the original when it was installed in early 1997 its sensitivity to the emissions being observed was an order of two less than the original.

A strong feature in the 730nm OH data in figure 6.2 is the Milky Way, visible as a bright oblique band running through the data every year. Its influence begins in the morning around April and moves through the night, arriving progressively earlier in the data series over a period of five to six months until finally passing outside the observation times by early September.

The Milky Way's influence on the 557.7nm OI data, although detectable, is not of the same order of magnitude as for the OH data. Of particular interest is that while there appears to be a signature in morning data around April the signal fades considerably to be almost undetectable by June. This is in stark contrast to the 730nm observations where the Milky Way's intensity is fairly consistant. A very weak trace is visible particularly in field three around July 1997 but it clearly has much less influence on the 557.7nm time series than it does on the 730nm data; generally speaking, what Milky Way contamination was present in the OI data had a lower amplitude (relative

to the airglow signal) than in the case of OH data.

At least part of the reason for the stronger Milky Way signal in the 730nm data is to do with the filters in use. For the OH observations, the filters have a full width half maximum (FWHM) of approximately 12nm whereas the FWHM of the 557.7nm filters is only about 3nm. Because of the wider bandwidth there will be more opportunity for background light to be transmitted by the 730nm filters resulting in a lower signal-to-noise ratio. Furthermore, the brightness of the 557.7nm OI emission line is approximately double the integrated brightness of the OH emission across the bandwidth of the filter used (Broadfoot & Kendall 1968) resulting in an inherently higher signal to noise ratio for the green line data.

In order to quantitatively investigate the long term behaviour of the airglow figures 6.3 and 6.4 were produced. In this case data have not been averaged across days but has been binned into three hour blocks running from 1800–2059, 2100–2359, 0000–0259 and 0300–0559 respectively. In addition to giving a closer estimate of the actual average intensity free of most short-period wave-induced fluctuations, the use of three hour averages facilitated the comparison with MF winds as discussed in section 6.5. The choice of a three hour average was also influenced by a desire to have at least two bins present in their entirety across the whole dataset; a choice of three hour bins neatly fulfilled all these requirements. Having multiple bins across a night also meant that when considering the wind in section 6.5, a reversing wind field during the night did not result in an artificial indication of little or no wind across the night.

The effects of the malfunctioning photomultiplier are clearly visible in field three's data in both figures 6.3 and 6.4 in the second half of 1997 as previously discussed. These figures also confirm that the relative effects of the Milky Way are considerably more prevalent in the 730nm data. Inspection shows that the 557.7nm intensity does peak around April of each year which is when the Milky Way is present in the 0300 time bin, although significantly this peak occurs in all four time bins simultaneously. Figure 6.2 clearly illustrated that the Milky Way could influence at most two adjacent three hour bins, and only one most of the time. Furthermore the lack of any coherent

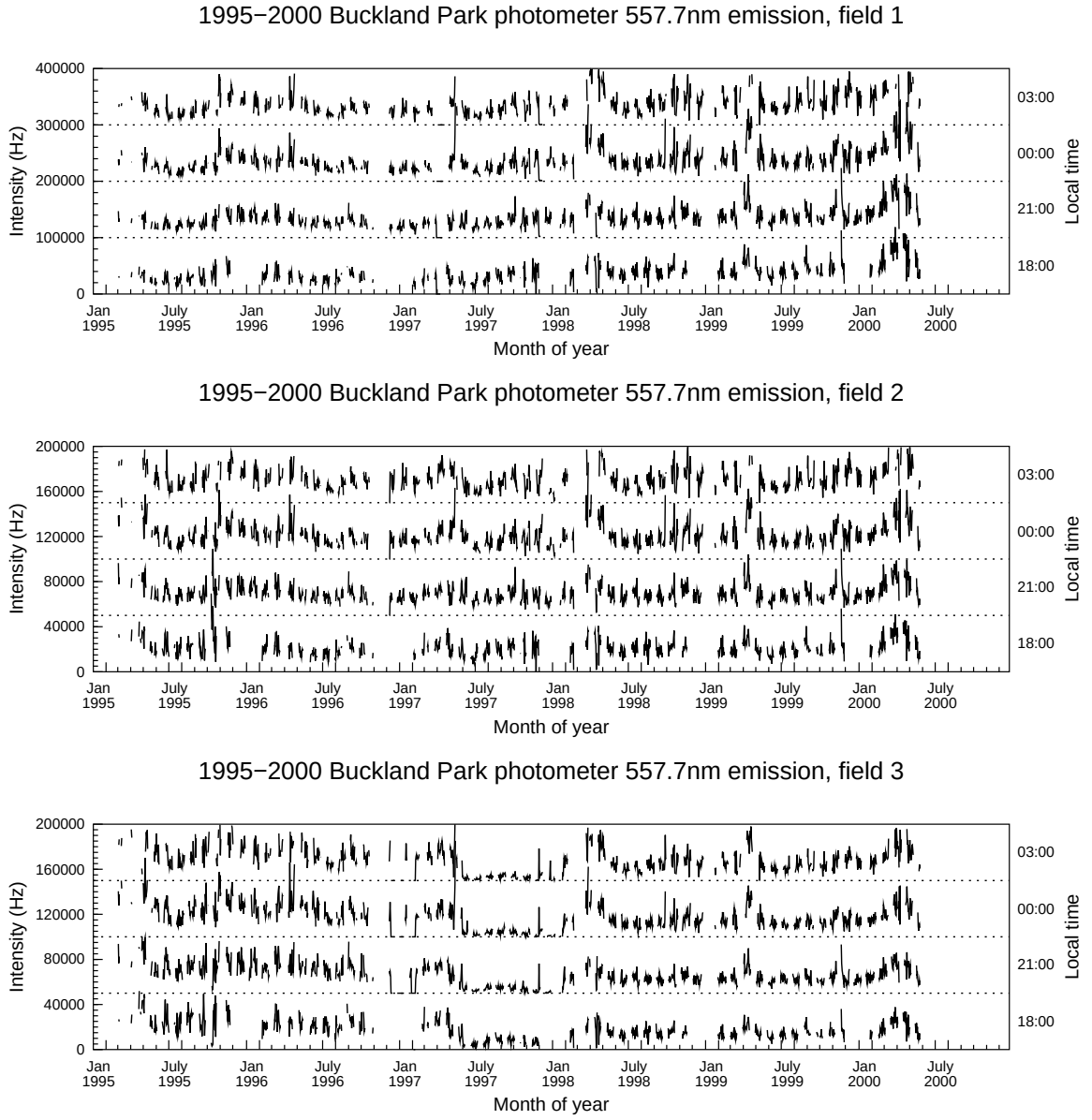

Figure 6.3: Three hour averaged 557.7nm intensity observations from Buckland Park. Aside from the time average, no other binning has been performed.

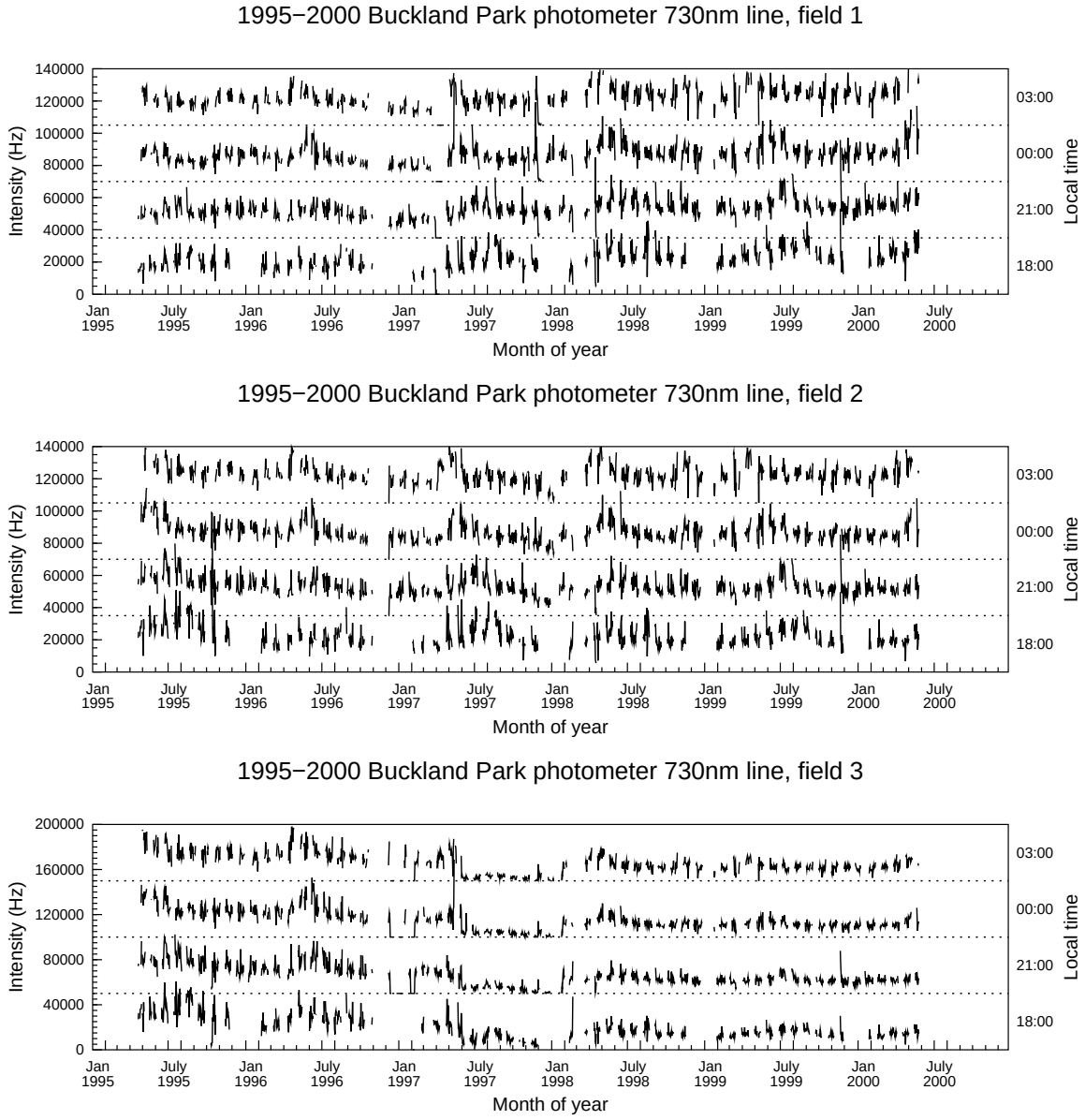

Figure 6.4: Three hour averaged 730nm intensity observations from Buckland Park.

structure moving through the night in the 557.7nm data as the year progresses is additional confirmation what the Milky Way's influence on the 557.7nm data is minimal. A different situation is evident in the 730nm data: a peak in the intensity of the 0300 time bin is found in April but unlike the 557.7nm data it is clear that corresponding peaks in earlier time bins occur later in the year rather than simultaneously. This is particularly clear around July 1999; it is therefore concluded that a significant proportion of the April peak observed in the 0300 OH observation bin is attributable to the Milky Way and that galactic light continues to have a clear influence on the intensity of other time bins in the six months following April. In the OI case the Milky Way possibly contributes to the peak observed in the 0300 time bin; however the concurrency of peaks in all other time bins — which could not be due to the Milky Way — point to the existence of a real geophysical effect.

Turning to figure 6.3, a number of other points are worth noting. Inspection shows that all time bins from all fields are very similar in general appearance which allows instrumental variation to be discounted as a cause of any trends across the five years of observation. It also shows that the extreme time bins (1800 and 0300), although having few points particularly around mid-summer still yield reasonable indications of the intensity as indicated by the more or less complete bins immediately surrounding local midnight. There appears to be an intensity peak occurring from the September equinoctal period extending into early summer, and there is a suggestion that the amplitude of this peak has a significant two-year component given the total absence of the peak in 1996-7 and the somewhat weaker peak in 1998-9 relative to 1999-2000. There is also an indication that the average intensity did tend to increase over the five years of observation suggesting a not-unreasonable link to the 11 year solar cycle which was approaching a maximum during 2000, which is further discussed later in this chapter.

6.1.1 Bright nights

Although not clearly evident in figures 6.1 and 6.2 due to the averaging employed, a number of bright nights were observed over the observation period. Such events comprised of a night (or two consecutive nights) whose average airglow intensity was enhanced by as much as a factor of two compared to other nights immediately surrounding it. The amplitude of perturbations in the intensity, however, did not increase by a similar factor. Nights with increased airglow intensity have been reported in the literature (for example Armstrong 1982) and one explanation for the observations has associated such occurrences with the passage of a gravity wave with large amplitude and long horizontal extent. While such a mechanism might explain some of the effects visible over a single isolated night, it does address those which extend over two or more nights.

Recent analysis of global airglow emission images from the UARS satellite has identified tongues of enhanced airglow emissions which extend outwards from the polar regions to latitudes as low as thirty degrees (J. Kafkalidis 2000,[1] private communication). These features can be present over a given geographic area for several days and show intensity increases of a similar order of magnitude to those seen in this study. The features themselves are thought to be caused by a planetary-scale wave disturbance and the effects on the airglow layers seen by the satellite would explain the photometer data being observed. A detailed comparison between the UARS data and data from the photometer could help in the positive identification of the observed intensity enhancements.

6.1.2 Harmonic analysis

To test the plausibility of these qualitative suggestions, a harmonic analysis was carried out on the 557.7nm OI data shown in figure 6.3 using a Lomb periodogram as discussed in section 4.6.1. The periodogram is shown in figure 6.5. To maintain consistency

[1]From the Space Physics Research Laboratory, University of Michigan

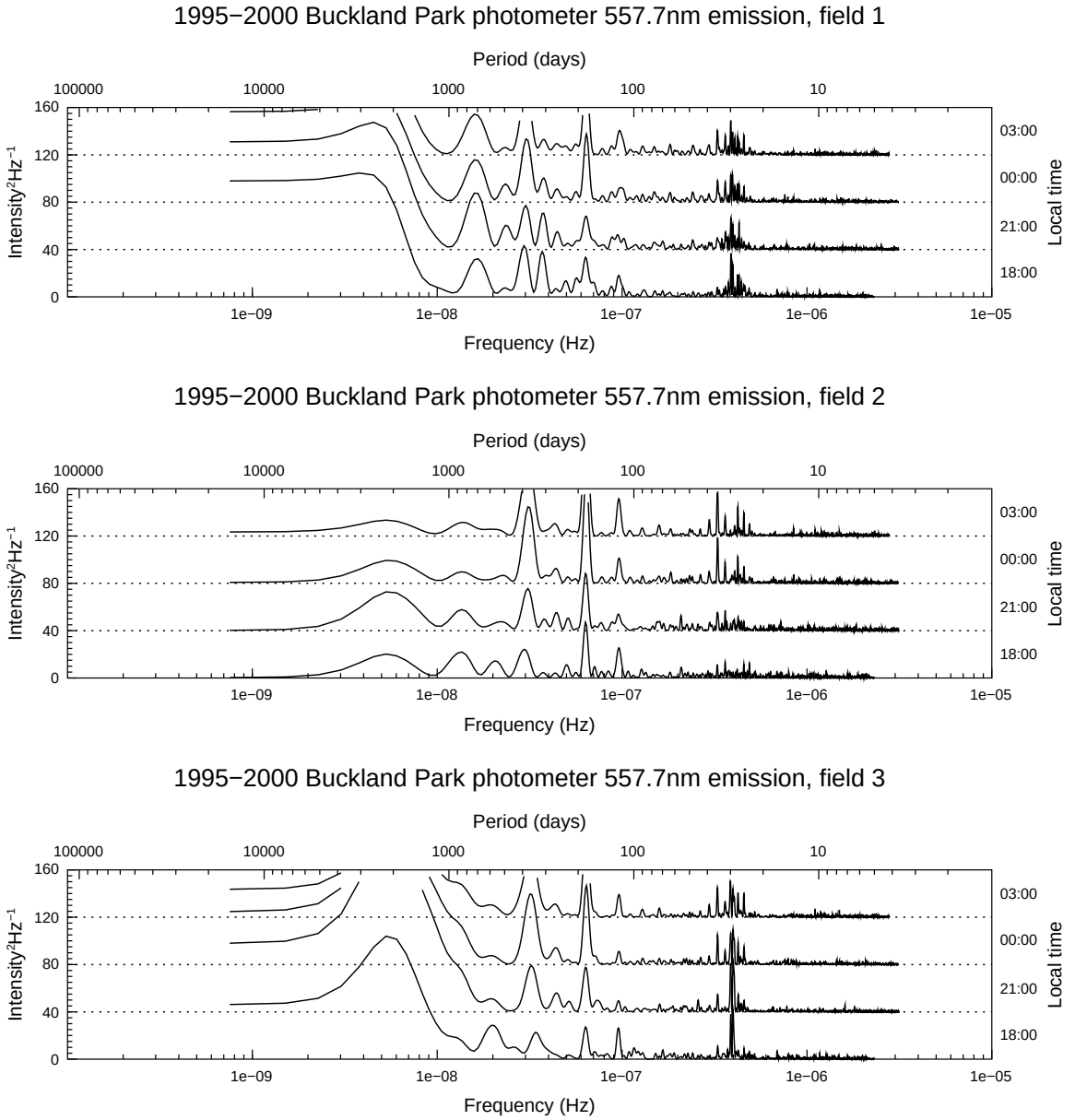

Figure 6.5: Eight times oversampled normalised Lomb periodogram of 557.7nm OI intensity data. The raw periodogram has undergone three point smoothing prior to plotting. The 99% confidence level for this data is the order of 10 Y-axis units.

with other parts of the analysis and to improve the reliability of the estimation the periodogram underwent three point smoothing before being plotted.

Inspection shows significant similarity in the spectral content of all time series investigated which was expected based on the proceding discussion of the optical intensity data. There are clear peaks with a confidence level greater than 99%, present at periods of approximately 100 days, 180 days, 360 days and 700 days with considerable

suggestion of a period between 2000 and 5000 days. There is also marginal suggestion of a component with a period of the order of 70 days, predominantly in field 2.

Narrow sporadic peaks are also evident around the thirty day period, the most obvious possible cause being the near-thirty day periodic appearance of data gaps in the raw dataset caused by the presence of the moon. The amplitude of these peaks is close to the 50% confidence limit, however, and in a dataset of this length apparent signals of this level are expected (Press et al. 1986). In any case, to test the effect of these regular gaps, a simulated dataset was constructed and run through the Lomb analysis. The data were obtained by first generating a separate time series with a flat spectrum for each field, which was copied into the respective field's four three-hour time bins to represent three hour averages. The amplitude of the DC level of this signal was set to 4×10^4 (a typical average observed in actual data). All other Fourier components were assigned an amplitude of 200 with random phase. The gaps created by the moon were simulated by removing data from comparable regions in each of the three fields. By using the same orginal data in each field's time bins the effect of the moon's movement through the night could be investigated since the time series were otherwise identical; the three fields allowed easy investigation of the effects of the moon on several different time series. The result of the Lomb analysis of the simulated data both with and without the moon-induced gaps is plotted as figures 6.6 and 6.7 respectively, with eight times oversampling and a three point smoothing as before.

A comparison between figures 6.6 and 6.7 gives insight into both the behaviour of the Lomb analysis with data of this type and allows evaluation of the typical impact the moon gaps might have on the periodogram. From figure 6.7 we see that although the spectral estimate deviates from the theoretical uniform amplitude, the 'peaks' fall well short of the 99% confidence level. Furthermore, while the effect of the moon in figure 6.6 is noticeable it does not change the general behaviour of the periodogram nor does it introduce significant signatures with periods around thirty days. To a certain extent this was expected as the Lomb method is not meant to be adversely affected by the nature of the gaps in the data. This means, however, that the cause

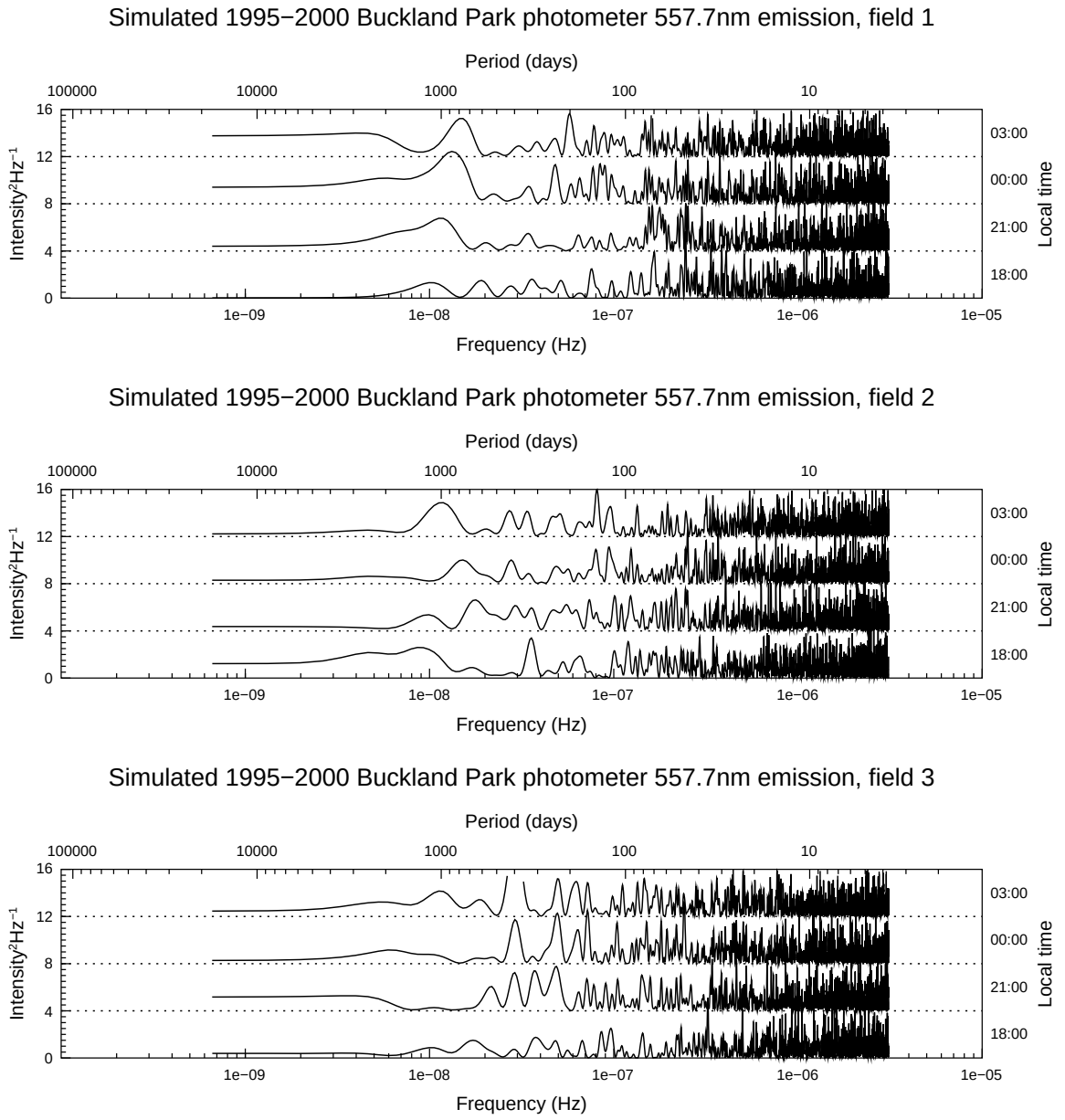

Figure 6.6: Normalised Lomb periodogram of simulated data with moon-induced gaps present. Although there is measurable deviation from the theoretical flat amplitude, the amplitudes of of the deviations are significantly lower than the 99% confidence level.

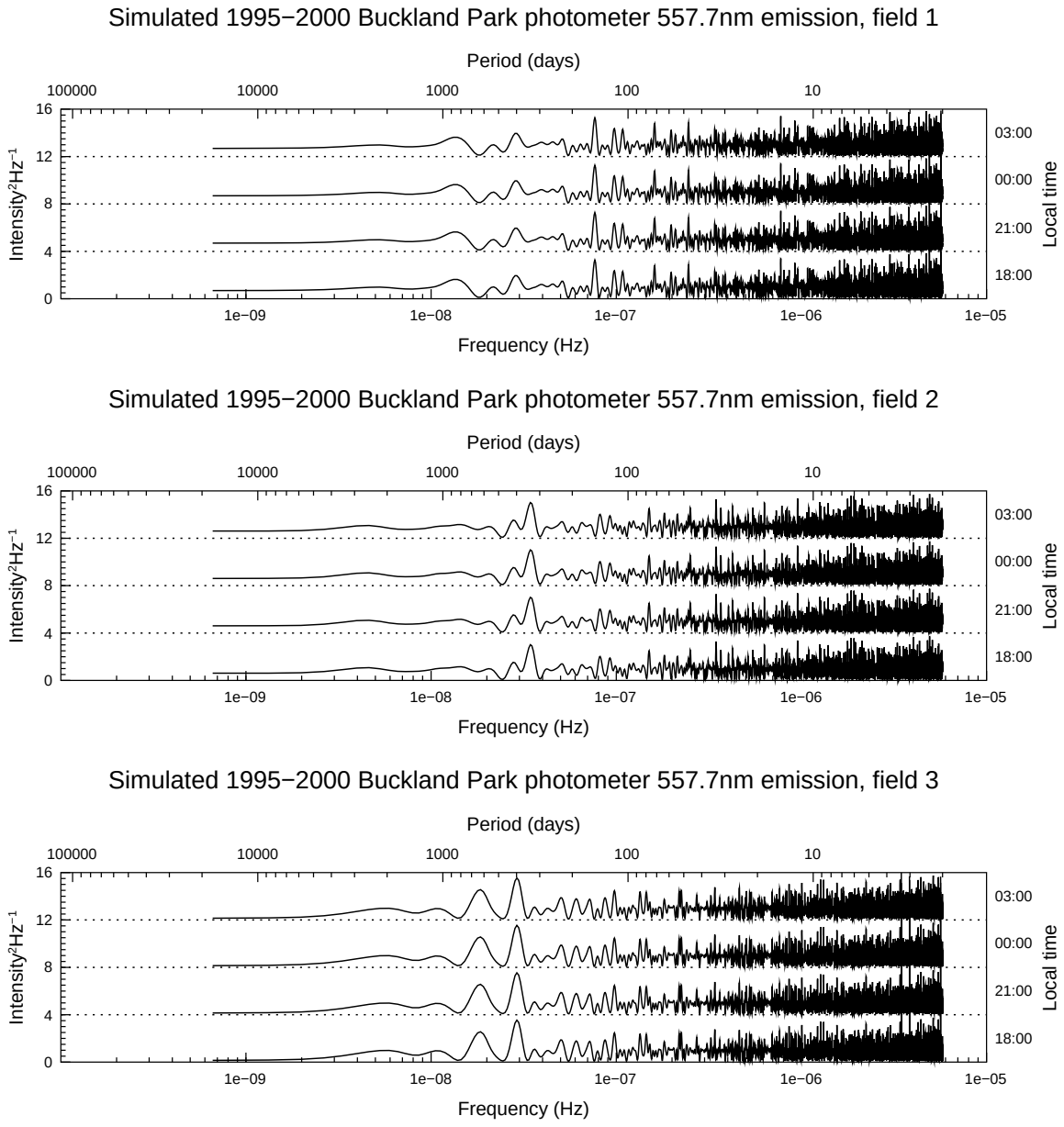

Figure 6.7: Normalised Lomb periodogram of data without moon-induced gaps in the data. Comparison with figure 6.6 illustrates the effect the moon-gaps typically have on photometer data.

of the cluster of signals around a periodicity of thirty days cannot be attributed solely to the windowing effect of the moon-induced data gaps.

The discrete peaks with periods around thirty days might be explained by an effect observed in the data: the airglow, being solar energy driven, is generally brightest during the early part of the evening. After the period of no observations — when the moon is up all night — data collection commences in the early part of the evening, spreading across the night as time progresses. Towards the end of the observation cycle where the moon is once again up for most of the night it is the early part of the evening which is 'lost' first. Averages taken across an entire night might therefore be expected to have a slightly higher average earlier in the cycle. However for data averaged across selected times of the night as in figures 6.3 and 6.5 this effect is not expected since all points in a given time series have contributions only from comparable local times. Thus this mechanism does not apply to the data under consideration.

Another possible source of a periodicity of around thirty days is the 27 day solar rotation; a modulation of the solar radiation intensity could alter the airglow intensity given that the excitation mechanism itself is driven by solar radiation. To investigate this, separate Lomb periodograms of each year were generated to see if a significant signal, present only some of the time, was being obscured through not being present continuously. While some peaks close to a 27 day period were evident they did not have consistent frequency and amplitude across fields, across timebins of the same field or between different years. Further periodograms of data spanning three and six months again showed little consistency; peaks would be present at apparently random times and did not occur at a set frequency. Finally the unaveraged intensity data from figure 6.3 (interpolated over data gaps to allow Fourier analysis) and the corresponding OH data (for completeness) were bandpass filtered with a passband corresponding to periodicities of between 25 and 29 days. As expected, the amplitude of the signal within these periods varied greatly, although no inter-field or inter-timebin correlation was evident. The peak amplitude observed was less than 5% of the average intensity value which is of similar magnitude to the measurement uncertainty.

It is therefore concluded that as observed, the series of discrete peaks with a period around thirty days does not yield any useful geophysical information. The cause of this specific signature is thought to be associated with a beating between sporadic weak signals around this period and the moon-induced periodicity of the data window. When present, the weak signals' amplitude is similar to the noise level in the data, which prevents any further analysis being carried out and significant conclusions from being made.

To confirm that the spectral peaks identified in figure 6.5 were realistic, a χ^2 fit of selected periodic functions was performed on the data. Each timebin was fitted separately. The candidate signals were those with periods of 121 days, 183 days, 365 days, 730 days and 2000 days; these resulted in a minimum χ^2 statistic of the order of 2×10^{11} and gave a visually good fit to the data. Attempting to fit any periods around thirty days did not significantly affect the χ^2 statistic — further evidence that any activity around the thirty day period was sporadic and incoherent. The data with the fit overplotted are shown in figure 6.8. Thus it is concluded that the predominant periods affecting the long-term 557.7nm airglow intensity are a one third year, a one half year, one year, two years and five and a half years. It is thought that the one third year periodicity is an inter-modulation product produced by a non-linear interaction between the one year and one half year periodicities. The results of probable non-linear interactions have been observed in the atmosphere between tides and planetary waves (for example, Beard et al. 1999, Pancheva & Mukhtarov 2000), and between gravity waves themselves as discussed by Yeh & Liu (1981), showing that such processes can certainly occur within the atmosphere.

Semi-annual and annual oscillations in 557.7nm airglow intensity with equinoctal maxima have been observed elsewhere, particularly in equatorial regions (see, for example, Takahashi et al. 1995, and references therein). This contrasts with the intensity behaviour at high latitudes which is characterised by an annual oscillation. The differences are understood to be due to the latitude-dependent variation in vertical transport which affects atomic oxygen concentration (and therefore the intensity of

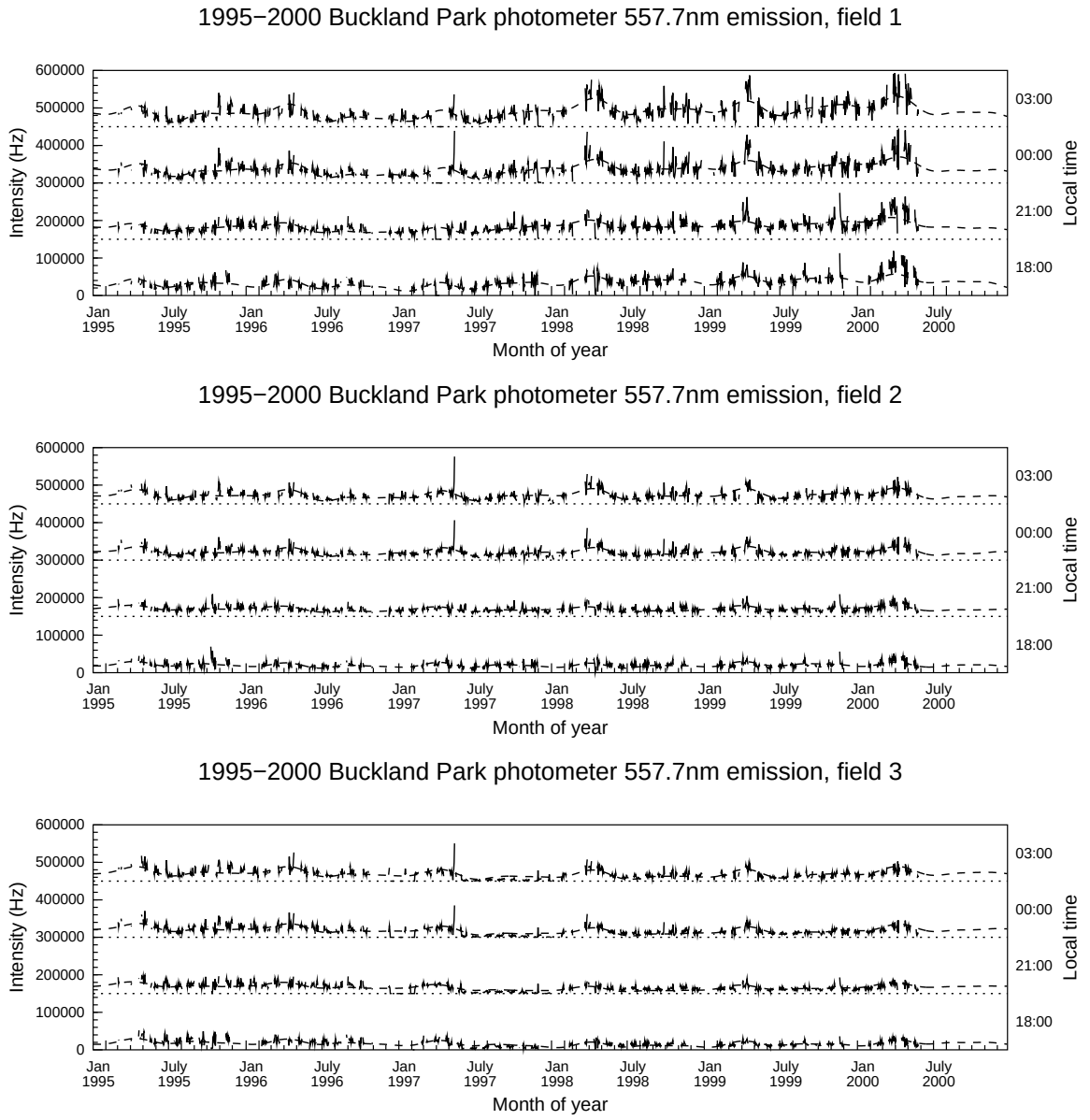

Figure 6.8: Three hourly averaged OI photometer data shown overplotted with a fitted harmonic time series as discussed in the text. The data are the same as shown in figure 6.3. The sharp peak seen in mid-May 1997 corresponds to a series of four consecutive nights (13–16 May) over which the airglow intensity steadily increased. The intensity recorded on 16 May 1997 was the highest recorded during the five year observation period, being a factor of four higher than the mean. The fall-off in intensity from this event was unfortunately not recorded due to the moon preventing significant observations from 17 May onwards. This peak is visible in figure 6.3 although it is not as obvious due to the scale used in that figure.

the 557.7nm emission) over the time scales of these oscillations. The relative amplitude of the semi-annual and annual variations recorded in this study (±50%) matched values observed in equatorial studies, suggesting that any switch from the equatorial cycle to that seen in the lower latitudes occurs at latitudes well beyond 40°, at least in the southern hemisphere.

If there was a cycle greater than 1000 days only in channel three it could be argued that it was due to the drop in sensitivity in 1997 as noted previously. This could give rise to an apparent signal with period of the order of twice the data length (and perhaps harmonics thereof). However, since there is a significant peak present in all three fields it is concluded that the 5.5 year periodicity is real, and is suggested to originate from the eleven year solar cycle. Because this period is essentially equal to the timespan of the data it is not possible to say with certainty whether the real period is half a solar cycle or one complete cycle, or whether a true variation with this period exists at all — a minimum of a five further years' data would be required to remove this ambiguity. However, a comparison between the 10.7cm solar flux (retrieved from the NOAA Solar-Terrestrial Physics division website[2]) and 557.7nm intensity data from figure 6.9 (filtered with a lowpass filter) shows some correlation in the location of the minima and maxima which would be the expected behaviour if intensity was modulated by the solar cycle variation in radiation flux.

A final point to consider in connection with the long period intensity variations concerns itself with a springtime weakening of the OI emission which follows a short-lived increase, as reported by Shepherd et al. (1999). While at first it may appear that such a weakening may permit the thermospheric OI emission to become relatively more significant and provide a possible link between OI intensity and solar activity, the evidence presented here does not support this suggestion. Most importantly, the thermospheric emission from the height region around 250km is very weak at latitudes away from the pole, making it unlikely that significant thermospheric OI signal would be detected in the instrument at Buckland Park. Another consequence of the weak

[2]currently located at *http://www.ngdc.noaa.gov/stp/stp.html*

thermospheric emission is that in the presence of a weakening mesospheric emission, the overall intensity would be expected to decrease. However, over both autumn and spring the photometer consistantly records an intensity increase. Furthermore, this increase generally persists over two months making it unlikely to be related to the short intensity increases noted by Shepherd et al. (1999). It is therefore conluded that long period intensity variations with periods comparable to the solar cycle are unlikely caused by the thermospheric OI airglow emission.

For completeness the three-point smoothed lomb periodogram for OH intensity is shown in figure 6.10. As would be expected, the periodicities for one year and a half year are very strong due mainly to the yearly appearance of the Milky Way in the data. Of interest is the region of this plot for periods greater than 1000 days; although not conclusive, there appears to be significant power occurring around 2000 day periods for most of the three hour blocks suggesting that the 2000 day cycle may also be present in the OH airglow intensity.

6.2 Variance of optical intensity

An investigation of the variance present in the optical data was carried out in much the same way as the intensity study detailed in the previous section as a way to estimate the level of gravity wave activity across the dataset. Within each three hour time interval, two variance calculations were performed. Firstly, the variance for each night relative to the mean of the time interval across the entire dataset was calculated, followed by the variance relative to the respective night's mean, again within the time interval concerned. An advantage of the latter option was that it could be approximated through the use of the wavelet filter before the calculation of the variance since this filter ideally removes the DC component (and the Milky Way if present) leaving a signal relative to the mean intensity due to airglow only. This meant it was possible to utilise the 730nm data in addition to the 557.7nm data for this part of the study.

Figure 6.11 shows the variance of the 557.7nm data across the observation period.

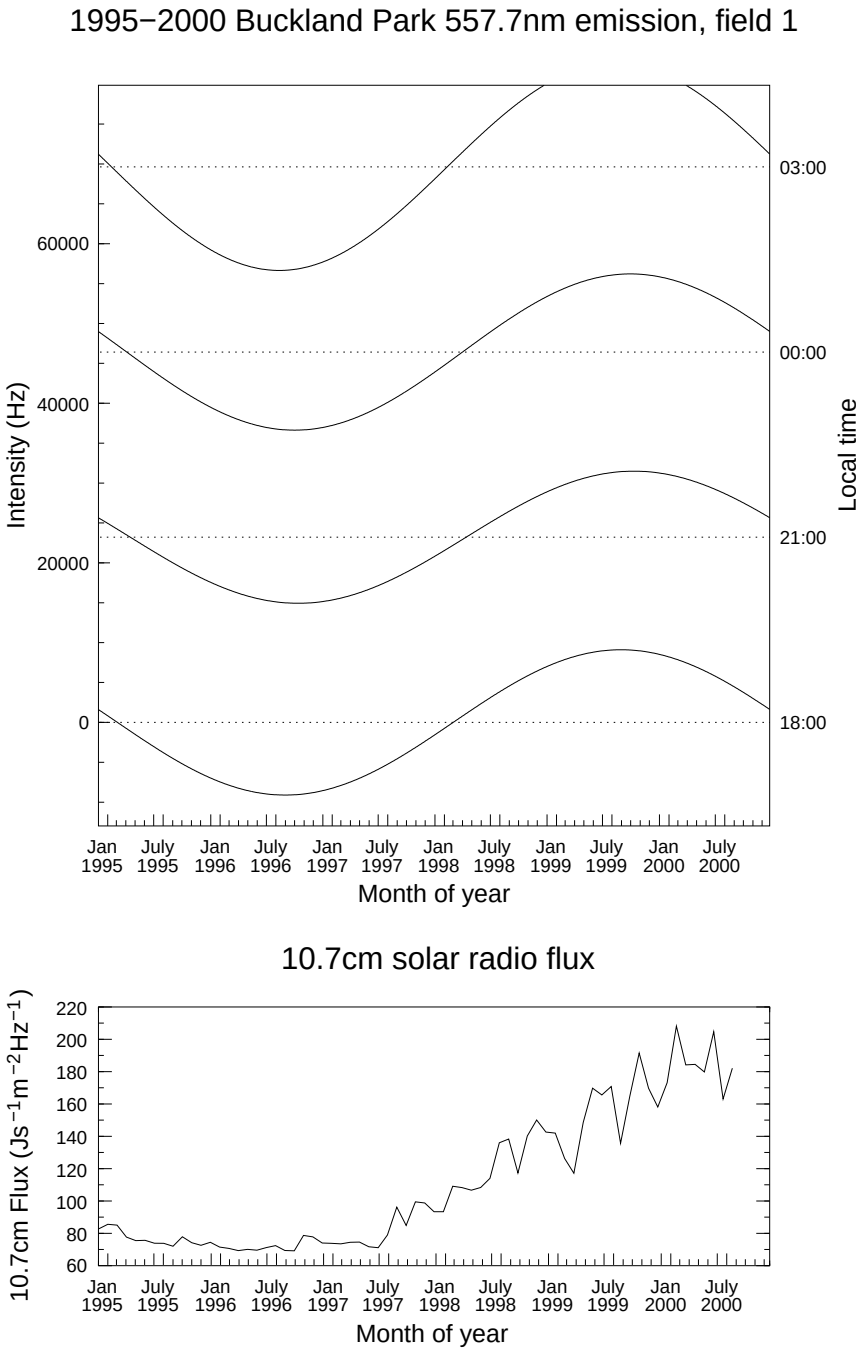

Figure 6.9: A comparison between the observed 10.7cm solar flux and the 557nm airglow intensity from photometer field one. The 10.7cm flux data come from the NOAA website (see text); the photometer intensity data have been lowpass filtered with a cut-off frequency corresponding to a period of 1000 days. Lyman-α data, although arguably more directly relevant to the airglow excitation mechanism, were not available over the period which the 557.7nm data spanned. Of particular interest is the similarity of the four photometer timebins and the correlation of times at which the minima and maxima of the airglow intensity and 10.7cm flux occur. Also note that for minimum χ^2, the phases of an eleven year and five and a half year period were appropriate when individually fitted to the data.

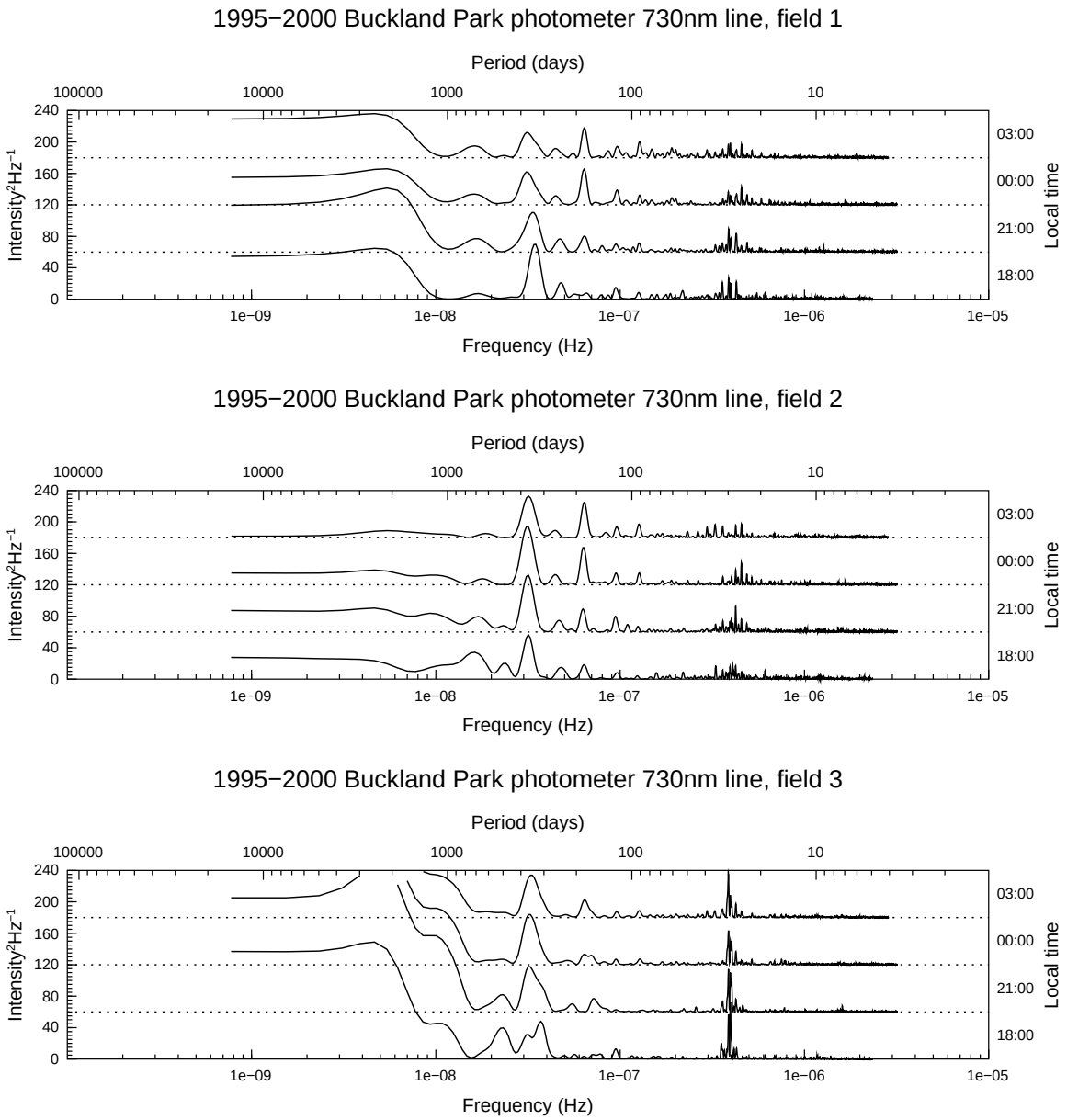

Figure 6.10: Normalised Lomb periodogram of 730nm airglow intensity

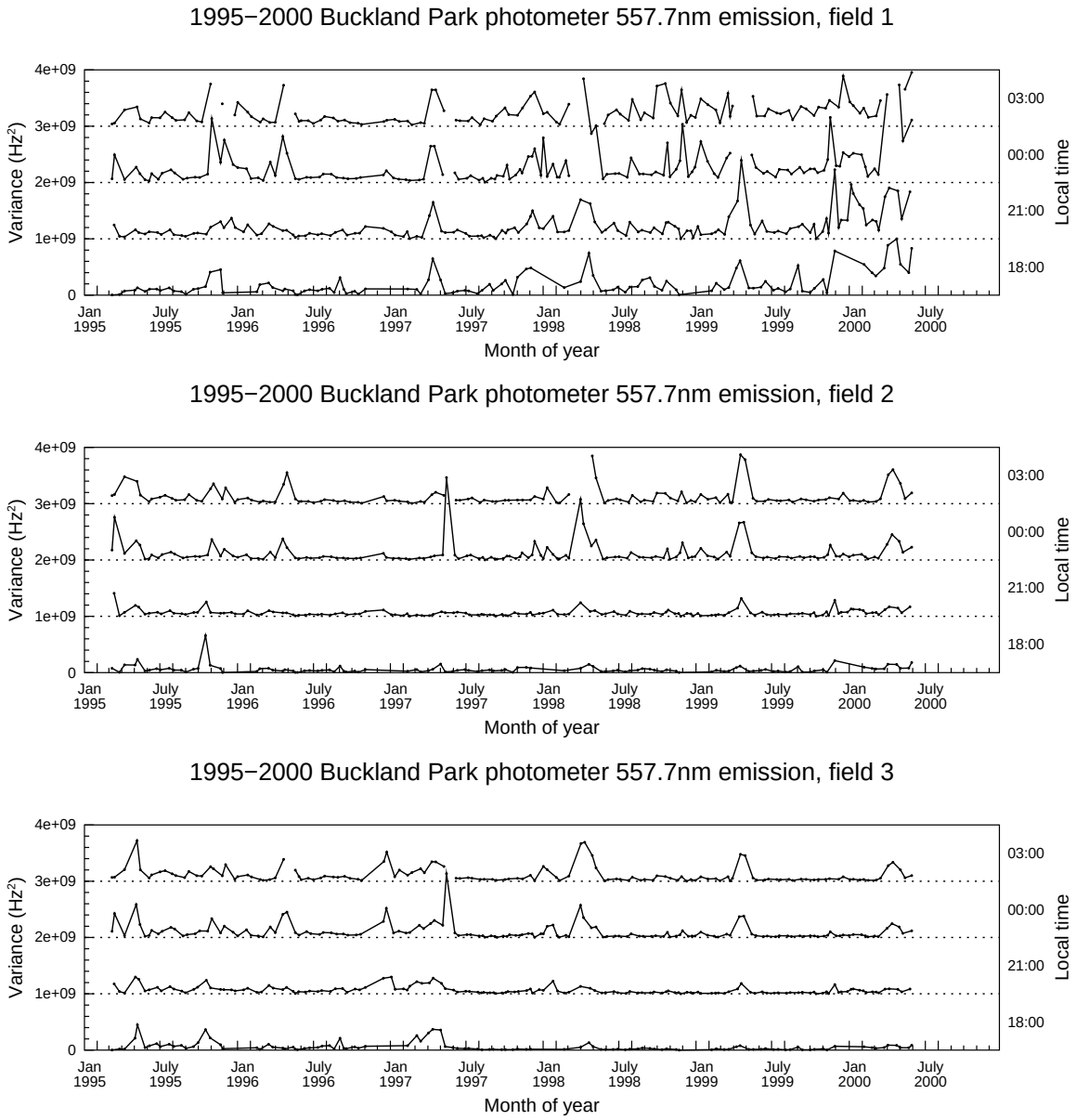

Figure 6.11: Variance of 557.7nm photometer data relative to the overall data mean. To reduce noise in the variance time series an eight day average has been performed.

Because the raw variance data were rather noisy, eight-day averages are shown. Of particular interest are the regular variance peaks occurring in over the autumn equinoctal period, usually between March and April. Smaller peaks are evident over the spring equinox.

The normalised Lomb periodogram for this data is presented in figure 6.12. The Lomb analysis shown was carried out without any eight-day averaging. Unlike the intensity data there is no consistent suggestion of periods beyond one year in the data at hand. The behaviour displayed for long periods (beyond 1000 days) within the variance periodograms may become more defined once further data is available, although at this stage it is not possible to draw any conclusions regarding this region. On the other hand, periods at one year and half a year are still present, with a majority of the power in these periods being due to the equinoctal peaks mentioned above. There is a suggestion of a periodicity at one third of a year although in most cases it lies very close to the 99% confidence limit.

The variance relative to each day's individual mean intensity is shown for both 557.7nm and 730nm in figures 6.13 and 6.14 respectively. A direct comparison between the 557.7nm variance in this case with that in figure 6.11 shows that the peaks are not as pronounced when this 'local variance' is considered which demonstrates that at least some of the apparent activity in the equinoctal periods suggested by figure 6.11 is due more to a long-term drift from the dataset's mean at those times rather than simply to gravity wave fluctuations of increased magnitude. However, even when taken relative to the night's mean there is indication of increased variance around the equinoxes which is not due solely to long-term intensity variations.

Lomb periodograms for the local variance data are displayed in figures 6.15 and 6.16. As expected from the appearance of the time series the spectral peaks are not as pronounced as those in figure 6.12. However in both sets of observations periodicities are still identified which exceed the 99% confidence level. In the 557.7nm case the half-year period is dominant, whereas in the 730nm case it is the one year period which is significant. This appears to be due to the spring equinoctal variance peak

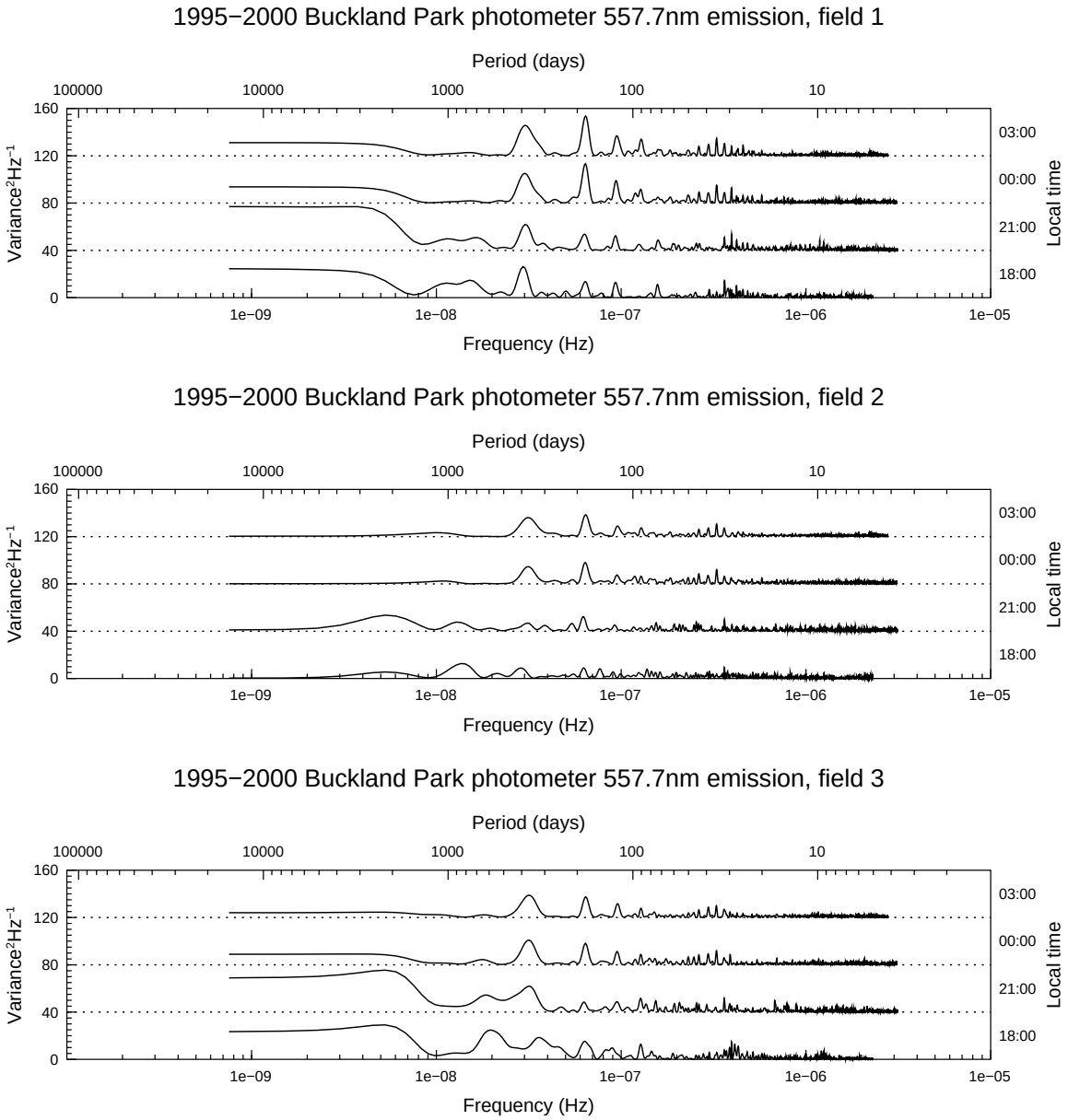

Figure 6.12: Normalised Lomb periodogram of 557.7nm variance data shown in figure 6.11. The eight-day averaging performed to enhance the clarity of figure 6.11 was not performed prior to calculation of the periodogram shown here.

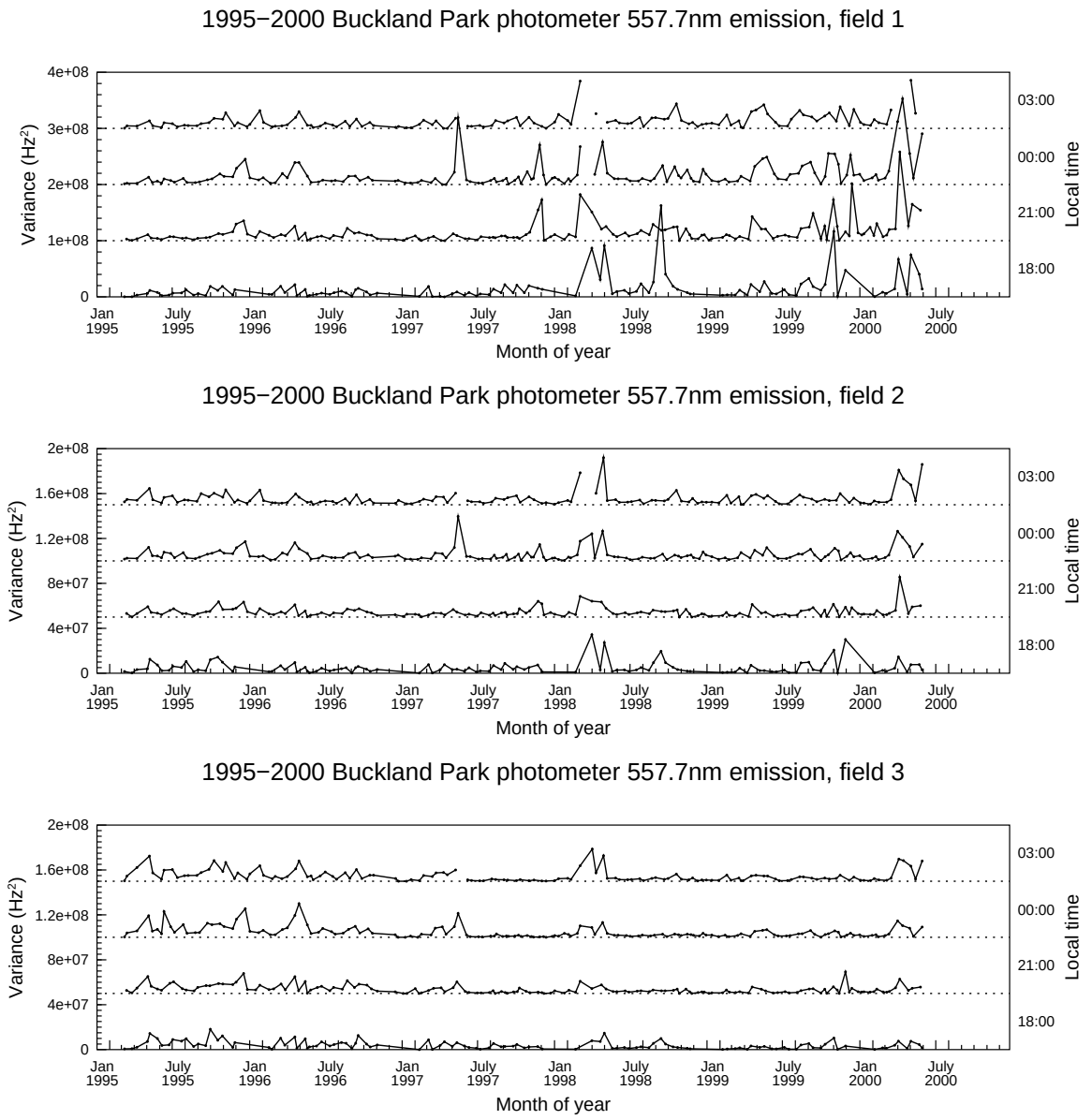

Figure 6.13: 557.7nm variance data from the photometer relative to daily mean intensities. As for other variance plots, data have been averaged across eight days to reduce noise.

being far more prevalent in the OI data than in the OH observations. From the OI results it is clear that the local variance is less sensitive to the activity peaks, so it is not possible to qualify without ambiguity whether the spring peak is truly absent from OH or simply lost in the noise. Given the extremely weak half-year signal though it would seem likely that the OH data does not exhibit the spring variance peak.

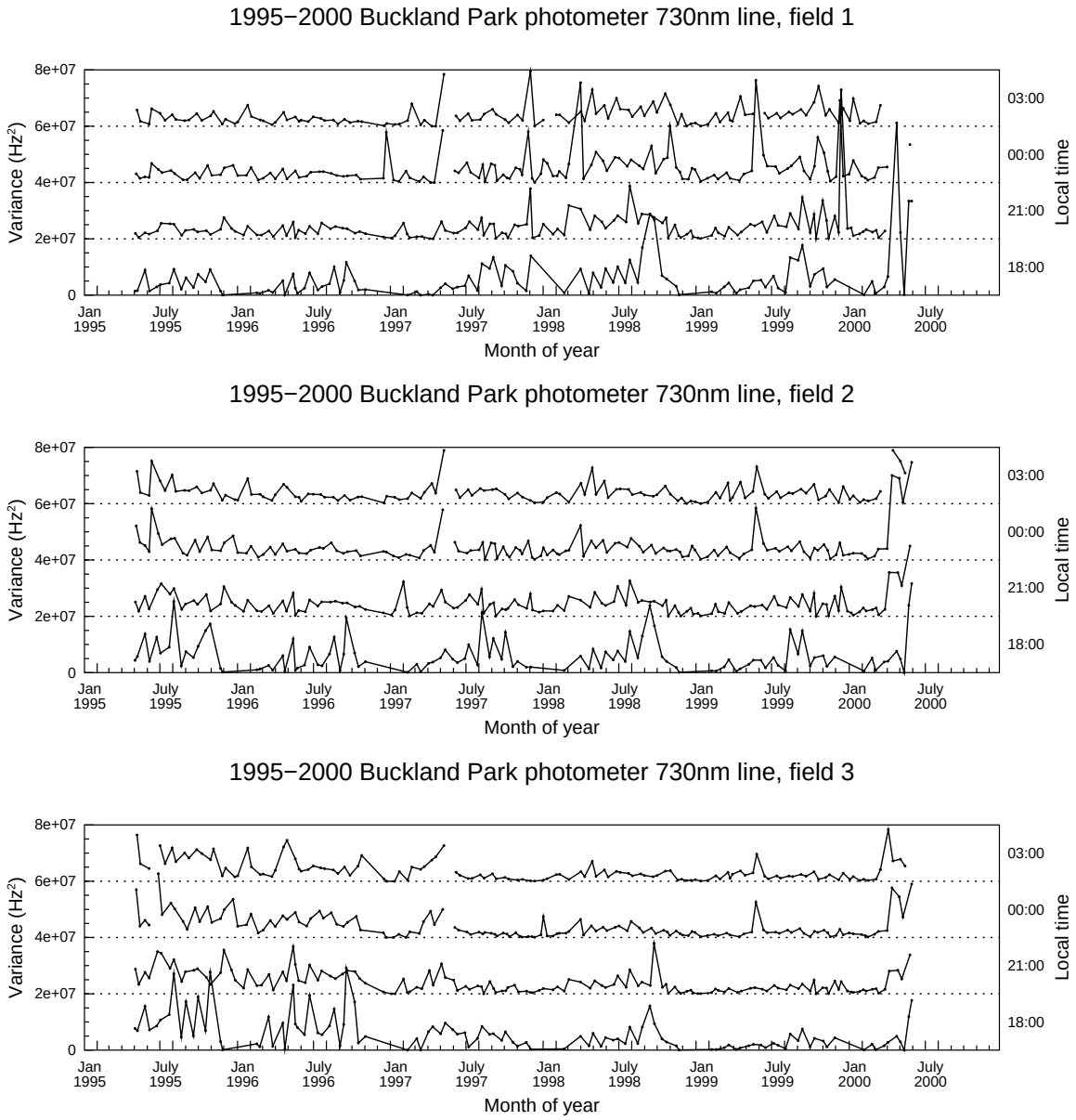

Figure 6.14: 730nm variance data from the photometer relative to daily mean intensities. Eight day averaging has been performed as for figure 6.13.

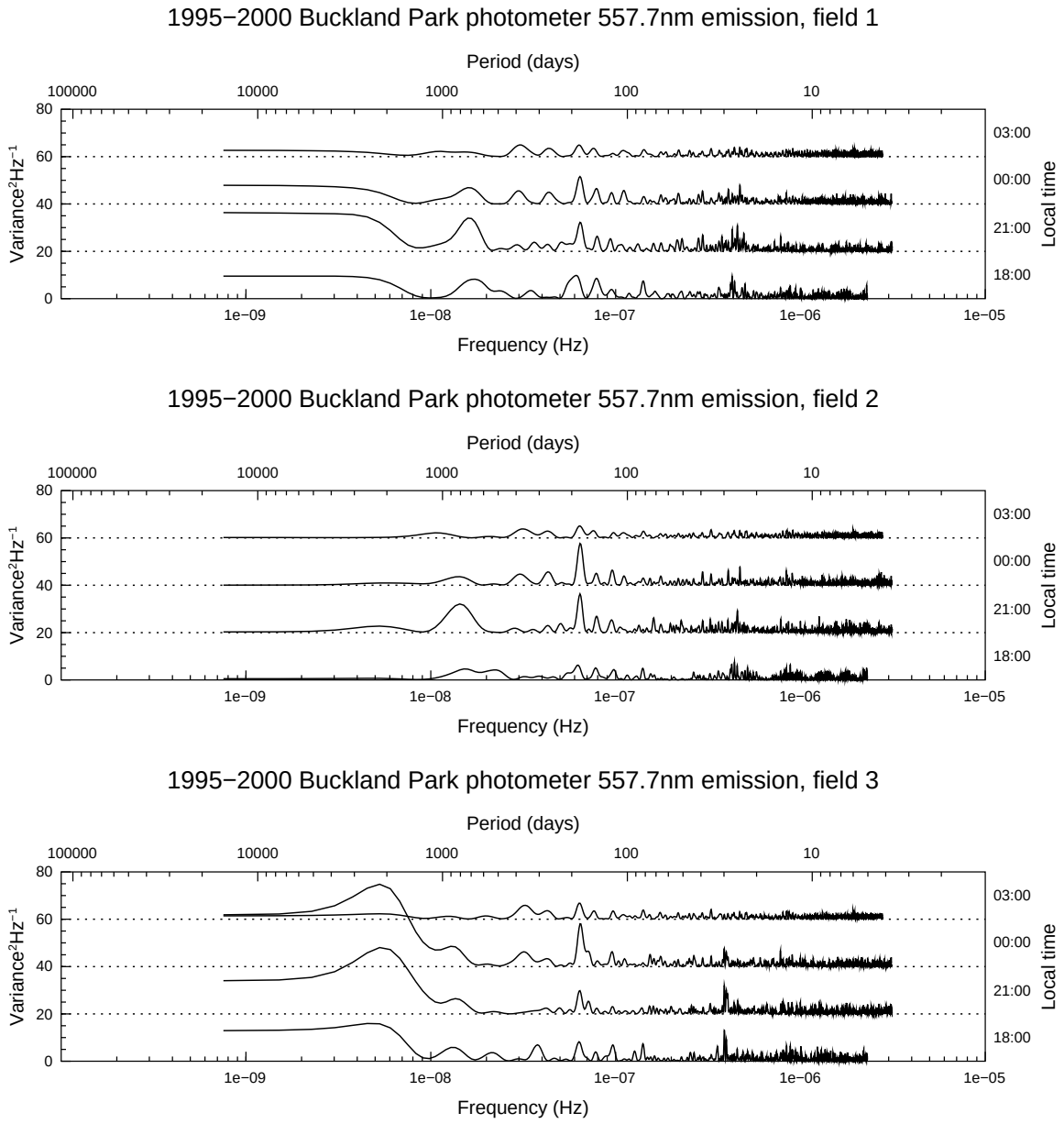

Figure 6.15: Normalised Lomb periodogram of data given in figure 6.13. Three point smoothing has been used as for previous periodograms.

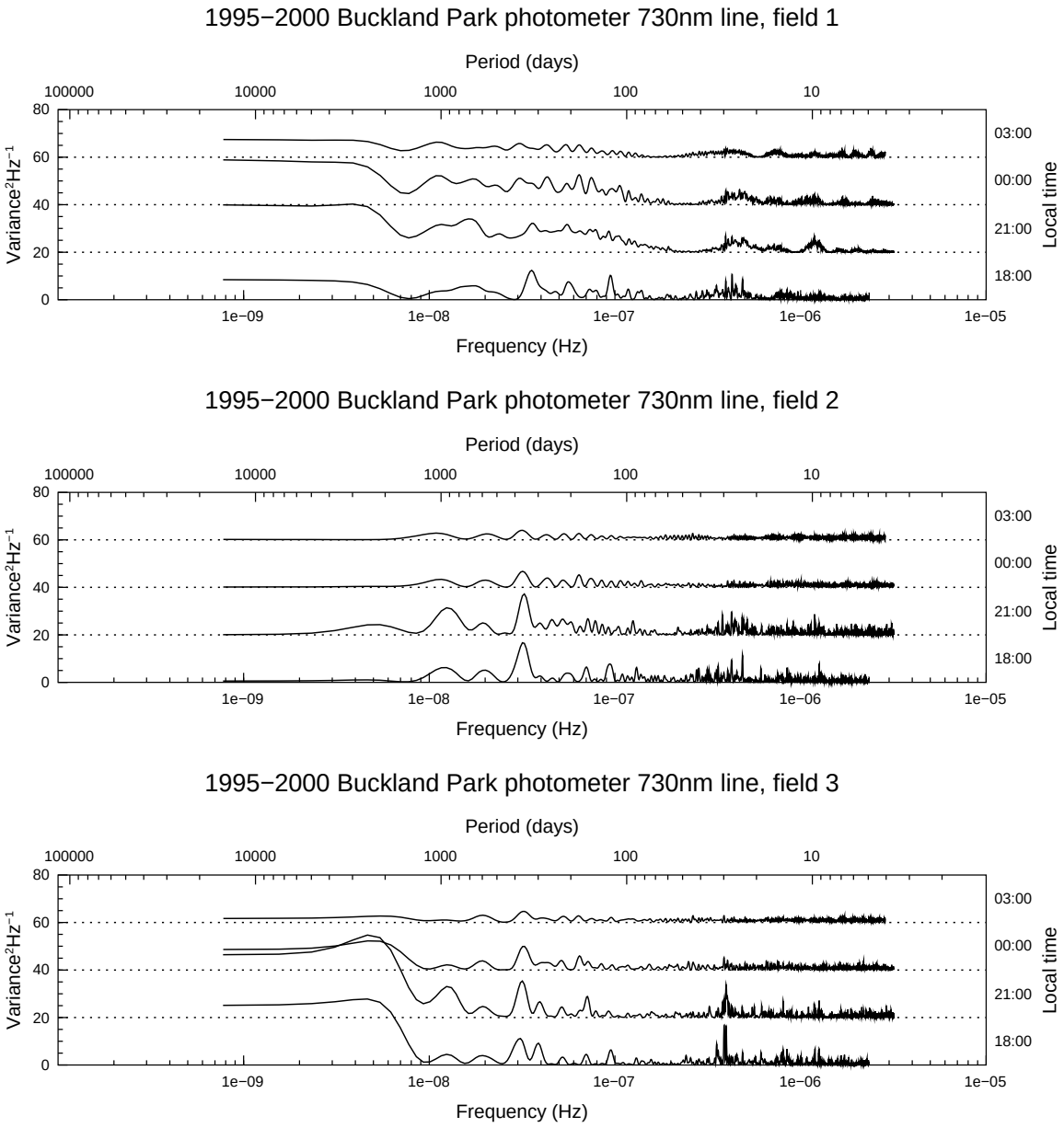

Figure 6.16: Normalised three point smoothed Lomb periodogram of data given in figure 6.14.

6.3 Spectral variations

Given the seasonal variations observed in the photometer variances a logical question is whether these variations are well defined in the frequency domain; in other words whether there was any substantial seasonal variation in the power associated with gravity wave activity of differerent frequencies. To investigate this, all time series from cloud-free nights were filtered using the wavelet-based filter and the spectrum calculated for each field in turn. After amplitude normalisation the spectra from all available years were averaged in blocks of half a month; a series of 24 spectra were then formed by averaging fields one and two within these half-month blocks. Field three was omitted from the average due to extended outages during the data collection. Figure 6.17 shows a typical half-month average spectrum resulting from this analysis.

A notable feature of most of the half-monthly spectra was a distinct downward level shift which affected periods below about five minutes. This is most likely an artefact of the local Brunt-Väisälä frequency; since propagating gravity waves have a high frequency limit defined by the Brunt-Väisälä frequency, the sharp drop in power simply reflects the lack of these waves in this region of the spectrum. Unlike spectra measured by some radar studies (Vincent 1972) the energy-preserving photometer spectra do not exhibit a peak in the region of the Brunt-Väisälä frequency but usually only a simple level shift, although in a small number of cases the drop was more pronounced in the energy-preserving spectra. The absence of a peak is not totally unexpected due to the effective filtering of the optical observations due to the finite layer thickness, which is five to ten times thicker than the range resolution of most radars. An attempt was made to use the location of the power fall-off as an estimate of the Brunt-Väisälä frequency. Assuming an isothermal atmosphere thoughout the emission layer this would allow calculation of temperature, although the accuracy of such an estimate would be limited by the possible Doppler shifting of the apparent Brunt-Väisälä frequency by the background wind. However in practice the location of the shift within the half-month spectra was not consistently identifiable to the accuracy

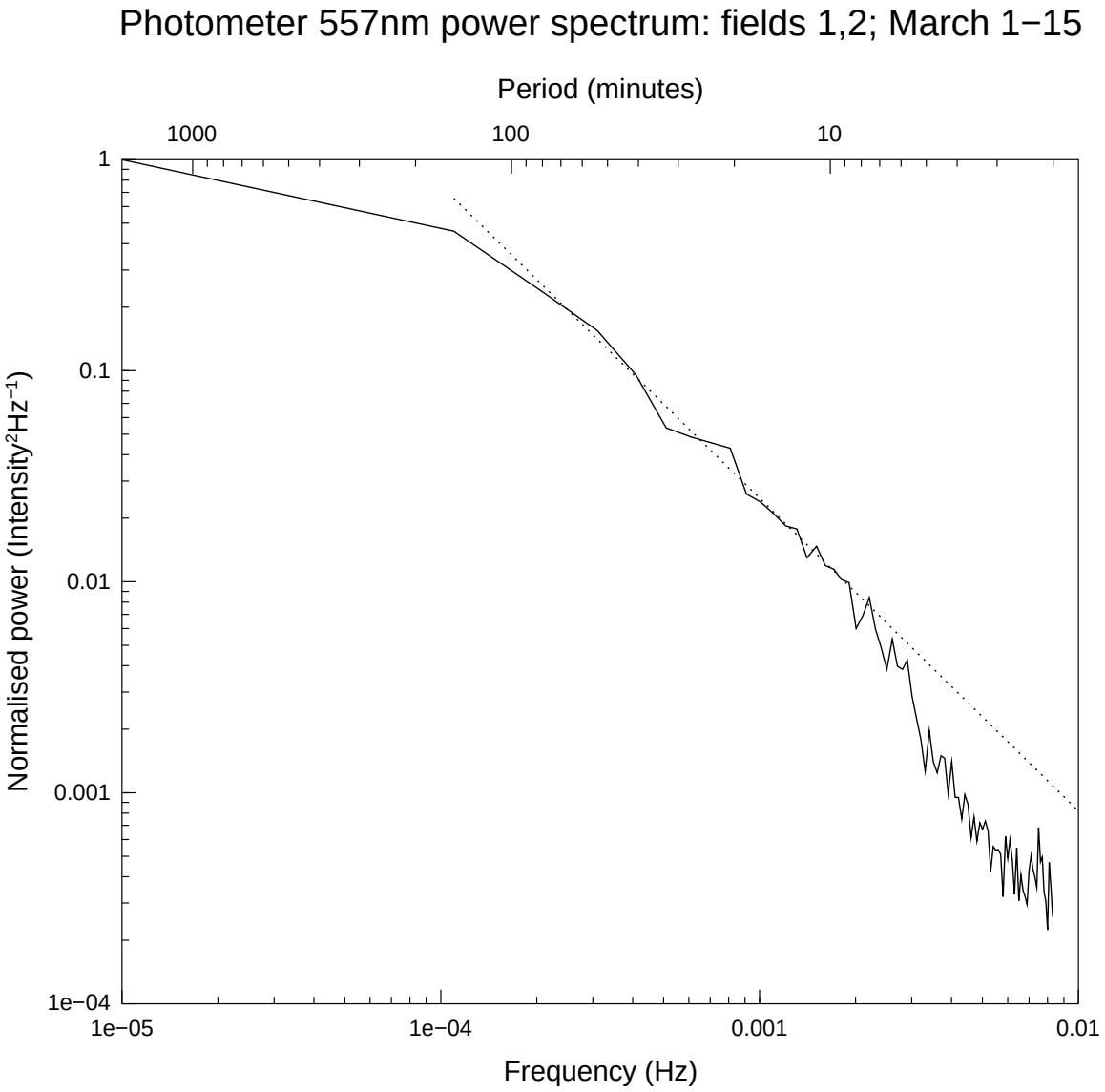

Figure 6.17: The average spectrum of photometer observations recorded between 1 and 15 March. Years represented by this data are 1996 through to 2000. The dotted line represents a least-squares powerlaw fit to the spectrum between periods of eight and two hundred minutes. A notable feature of this spectrum was a distinct downward level shift which affected periods of the order of five minutes and below. See text for details.

required to give a meaningful temperature estimate, probably due to smearing effects of the background wind.

The 24 half-month average spectra were combined to systematically investigate seasonal differences between the spectra such as variations in spectral slope and total variance; this information is summarised in figure 6.18.

By inspection a half-year variation in the power at periods of the order of ten minutes is clearly evident for both the 557.7nm and 730nm observations. The amount of power in higher frequency peaks in summer and winter with a substantial decrease occurring in the equinoctal regions, although the 'minima' of the cycle appear to occur in mid-to-late April and late August — on the winter side of each equinox. Because the spectra have been normalised the variation is not due to a simple level-shifting of the spectrum and further confirmation of this is seen in the total variance where there is no correlation with the variations seen in the main spectral plot. It would be expected therefore that the variation could be seen as a change in the spectral slope with more negative values occurring during the periods of 'minima'; figure 6.18 does appear to support this although the minima in the spectral slope plots are weak. The numerical average of the spectral slopes shown in figure 6.18 is -1.5 ± 0.3 for the 557.7nm data and -1.3 ± 0.4 for the 730nm data.

When comparing this spectral variation with the behaviour identified previously in the optical intensity and variance from the photometer it is seen that the times when there is a lack of power in the higher frequencies corresponds to the times when the intensity and variance of figures 6.11, 6.13 and 6.14 show some form of maximum. The increase in gravity wave activity seen around the equinoxes therefore appear to consist more of periods longer than thirty minutes since there is a substancial power drop in periods shorter than this at those times. On the other hand, activity during winter and summer would seem to contain considerable activity at shorter periods which is lacking at equinoctal times. Furthermore, comparison with the momentum flux results discussed earlier (see page 136 and figure 5.25) shows that the short-period waves give rise to higher momentum flux values, since momentum flux is highest in

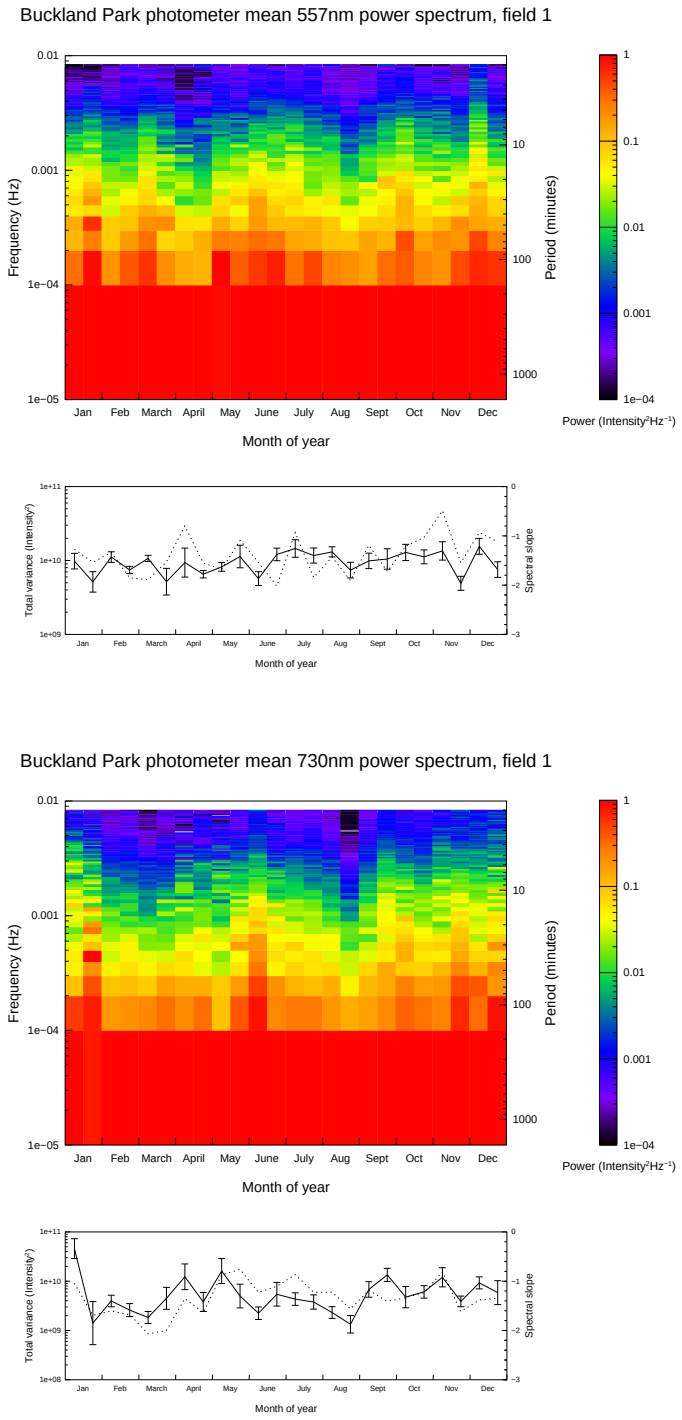

Figure 6.18: Seasonal variation of normalised averaged spectra obtained from the 557.7nm (upper two plots) and 730nm (lower two plots) observations of the photometer at Buckland Park. The second of each group of two plots shows the yearly variation of selected spectral characteristics of the unnormalised spectra, namely the total variance (dotted line) and the spectral slope (solid line). Error bars for the latter indicate the standard deviation for the slope parameter fitted to the spectral data using a χ^2 method.

summer and winter when there is an increase in the short-period activity.

6.4 MF Wind data

To facilitate a comparison between the optical and radar data, the two minute wind records from the MF radar were processed in the same way as the optical data outlined previously. Figures 6.19 and 6.20 show the resulting time series. Eight-day averaging has been employed to reduce the noise present in the data.

The most obvious feature of the 84–88km data is the winter maximum in the zonal component and the summer maximum in the meridional wind. This general trend is present at the higher height as well, although the dynamic range of the data observed is significantly less, as seen in numerous studies. Data from the lower height also displays evidence of a component with period 180 days (half a year).

The vertical velocity component from both MF height ranges shows only a weak suggestion of a maximum during autumn and very little increase over spring, the times of maximum wave activity as detected by the photometer. Signs of an increased vertical component are clearer in the years leading up to 1996. Airglow intensity variations come about due to vertical transport of atmospheric constituents and strong vertical motions would therefore be expected to occur concurrently with significant OH and OI intensity variations. One possible reason for the lack of a significant vertical signature, particularly after January 1996, was a series of equipment problems which adversely affected the vertical component estimations. The estimations of the vertical wind component were made using Doppler techniques which relied on phase information from the radar receivers. Around the beginning of 1996 the antenna array at Buckland Park developed significant problems which adversely affected the phase detected by the receivers. These problems persisted into 1999 and therefore the vertical wind components obtained from 1996 through to the start of 2000 cannot be relied on. The effects of these issues are also clear in the variance of the vertical component as discussed on page 183.

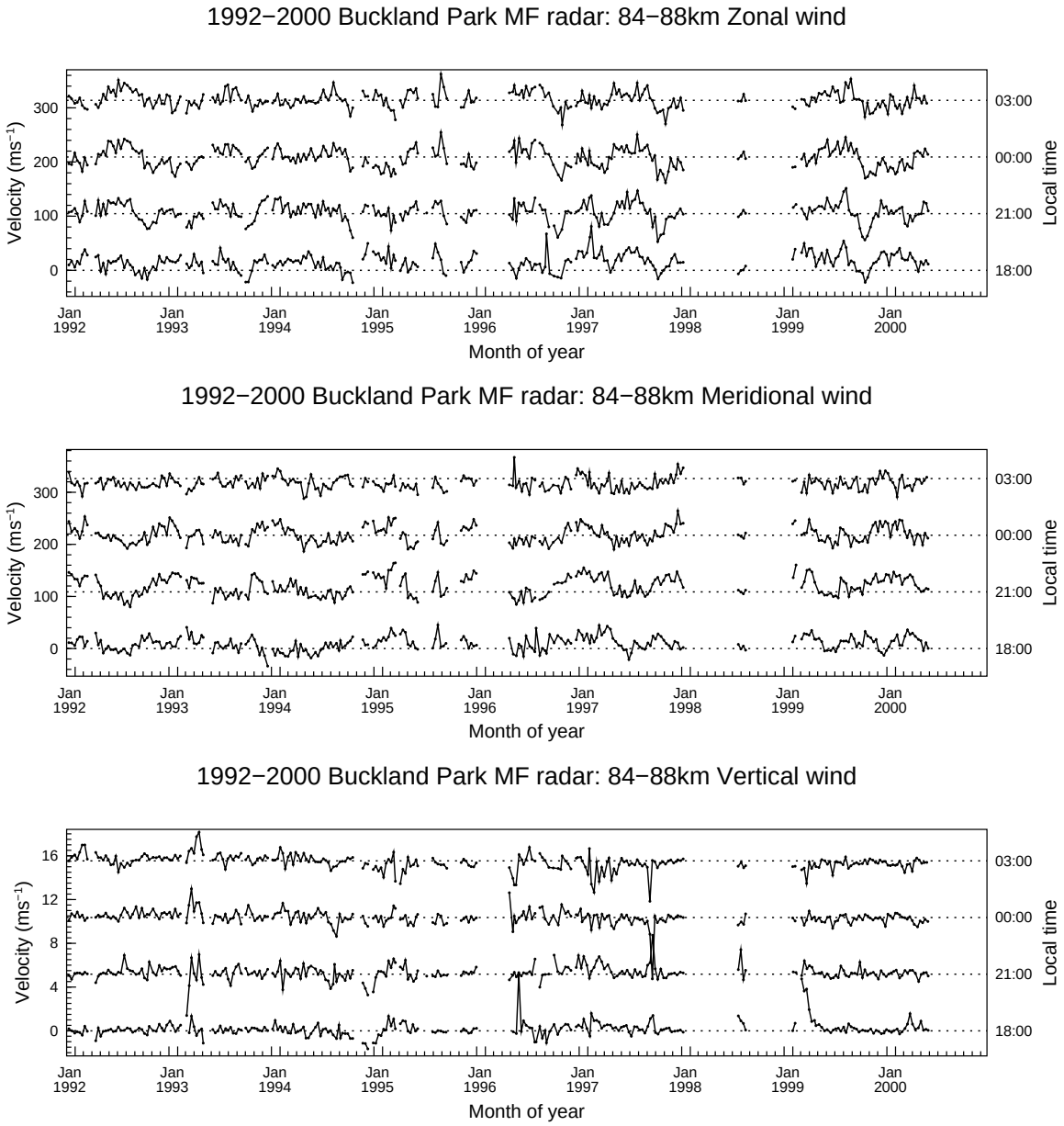

Figure 6.19: Eight-day averaged wind components measured by the Buckland Park MF radar. The data presented here are the average wind in the 2km range bins between 84km and 88km inclusive.

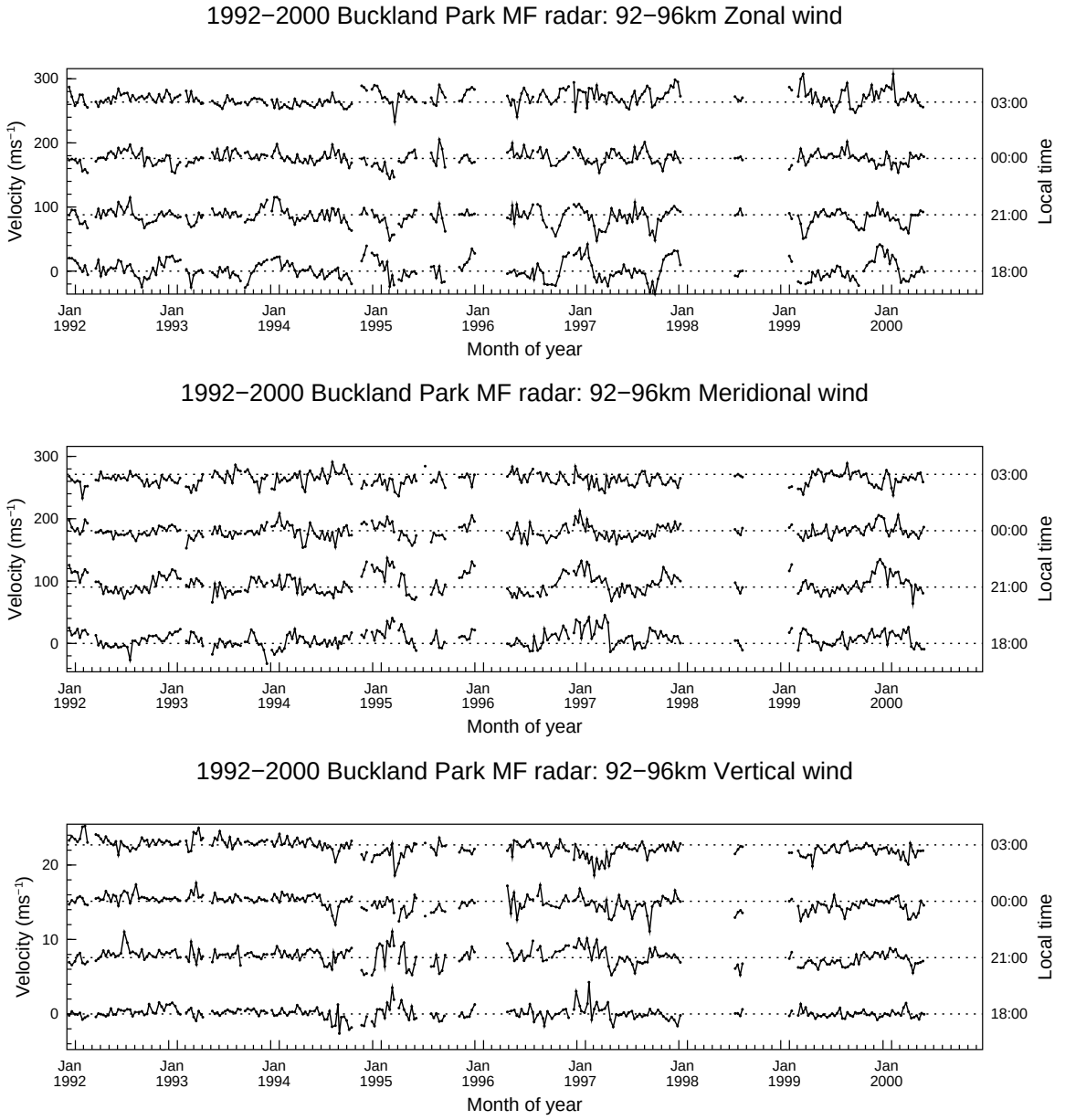

Figure 6.20: Eight-day averaged wind components measured by the Buckland Park MF radar as in figure 6.19 but for range bins between 92km and 96km inclusive.

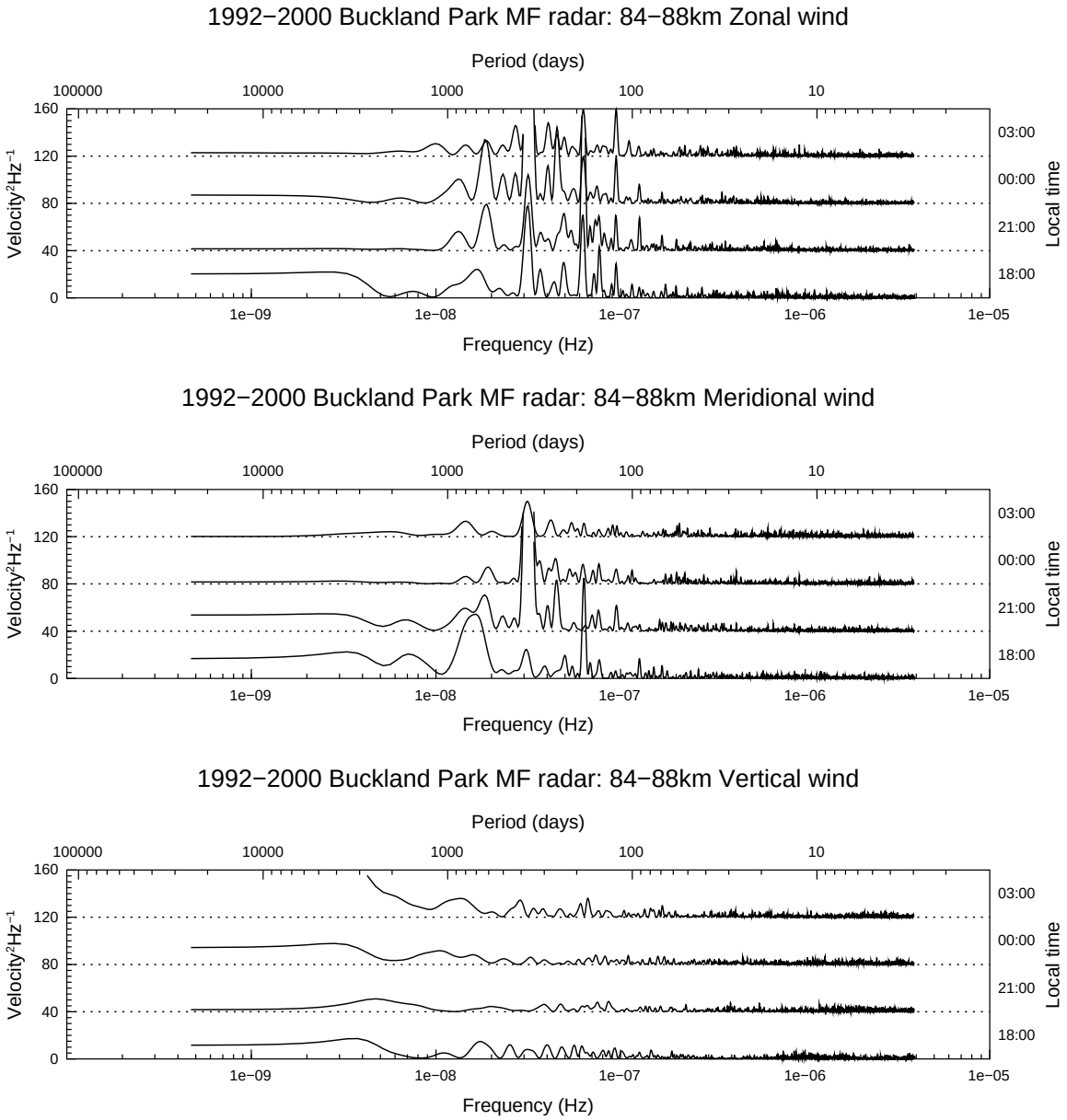

Figure 6.21: Three-point smoothed Lomb periodogram of data shown in figure 6.19.

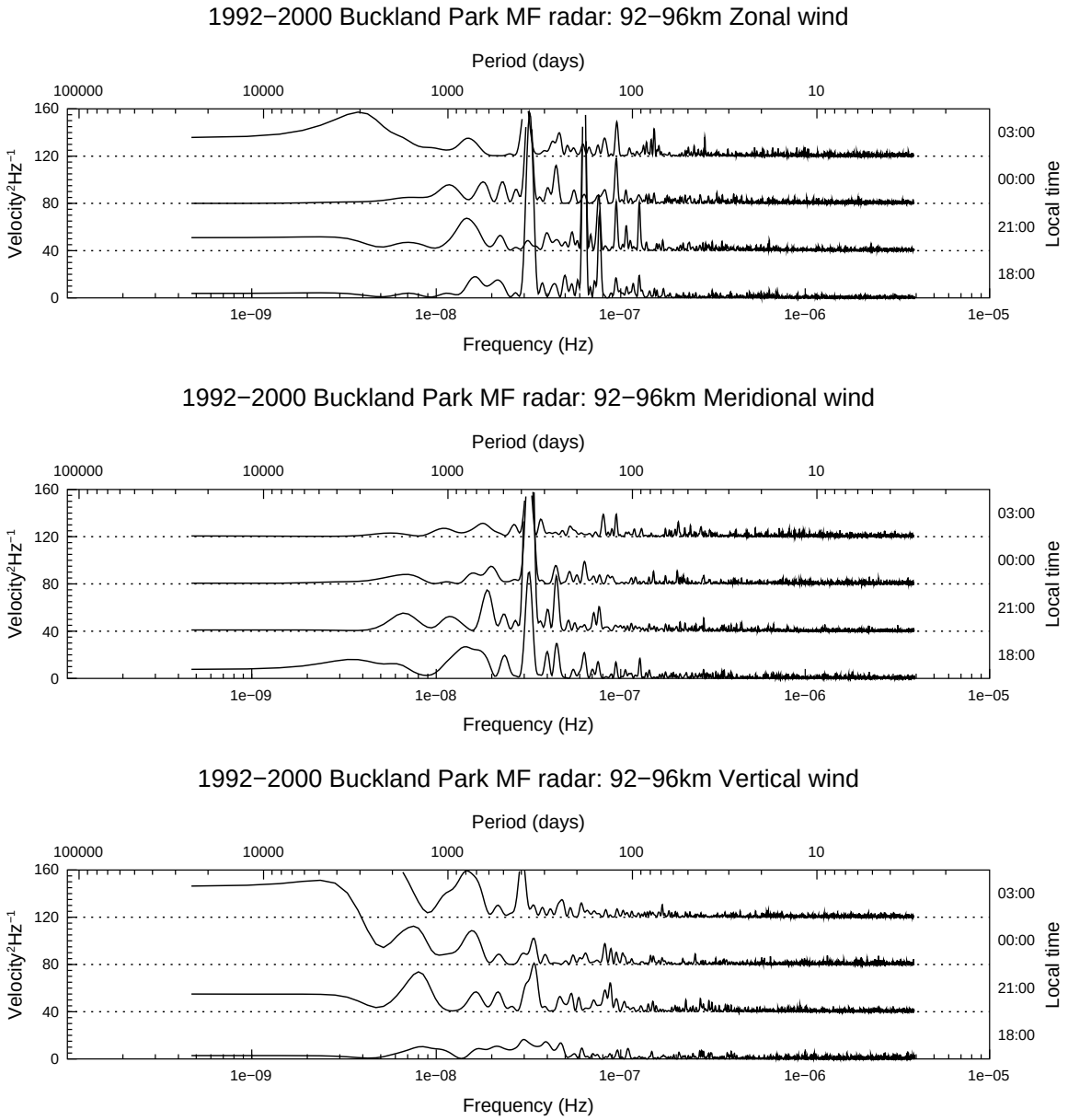

Figure 6.22: Three-point smoothed Lomb periodogram of data shown in figure 6.20.

A Lomb analysis of the unaveraged data used to create figures 6.19 and 6.20 was carried out to quantify the significance of these periodic components, with results shown in figures 6.21 and 6.22 respectively. As would be expected from observation of the time series, both zonal and meridional components at both height ranges have a very significant signal with period of one year. A significant half-year periodic signal is only present in the zonal component of the 84–88km data in all time bins and in the 92–96km data over the first two time bins. Evidence of components with two-year and one-third year periods is also present; again these are strongest in the zonal wind component.

Like variances in airglow intensity, the variance of winds recorded by the MF radar can also give information on the gravity wave activity. The variances were calculated relative to the overall mean in each respective time interval. The plots shown in figures 6.23 and 6.24 show the eight day averaged result for zonal, meridional and estimated vertical components for the two altitude ranges of interest. A first glance clearly shows that variance enhancements are nowhere near as pronounced as they are in the optical data. Even so, both zonal and meridional wind component variances at both height ranges do exhibit a periodic variance increase around the equinoctal periods as observed in the optical data. Significantly the autumn peak appears somewhat earlier than in the optical case; whereas the airglow peak was usually located between March and April, the wind variances appear to peak between January and February. The spring peak appears in a similar location to that in the optical data and likewise is not as strong as the autumn peak.

The relative height of the spring peak compared to the autumn peak is higher in the vertical component, although given the obvious noise in the vertical data (especially in the 84–88km height range), care must be taken that noise peaks are not interpreted as geophysical in nature. The deterioration of the vertical data was the result of problems in the antenna array as previously noted. The variance time series was more severely affected than the vertical component time series itself.

Three-point smoothed Lomb periodograms of the radar variance data are displayed

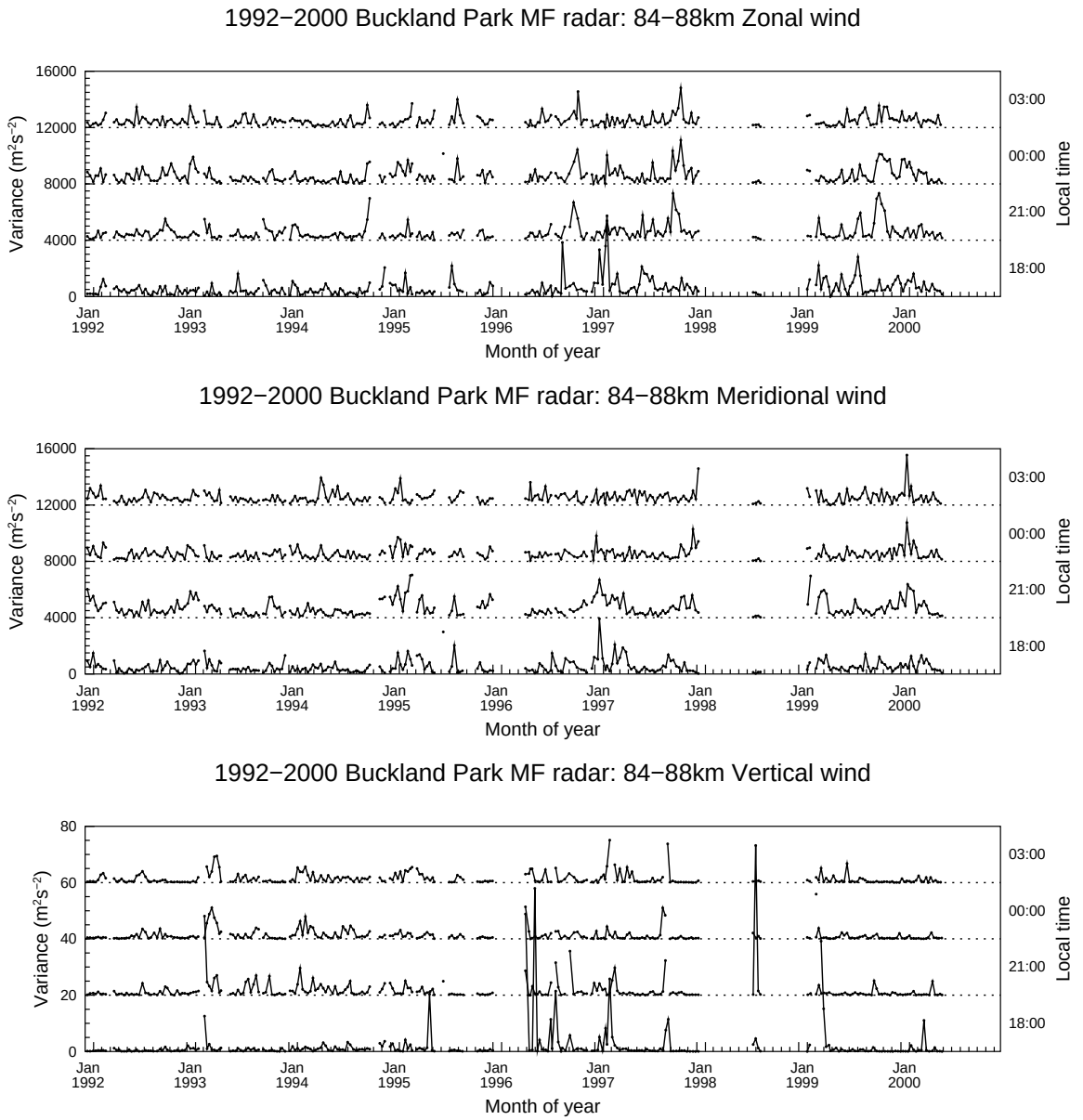

Figure 6.23: Eight-day averaged variance of wind components measured by the Buckland Park MF radar. The data presented here are derived from the average of wind in the 2km range bins between 84km and 88km inclusive. As in figures 6.19 and 6.20 the eight-day averaging was employed to improve the clarity of the plot.

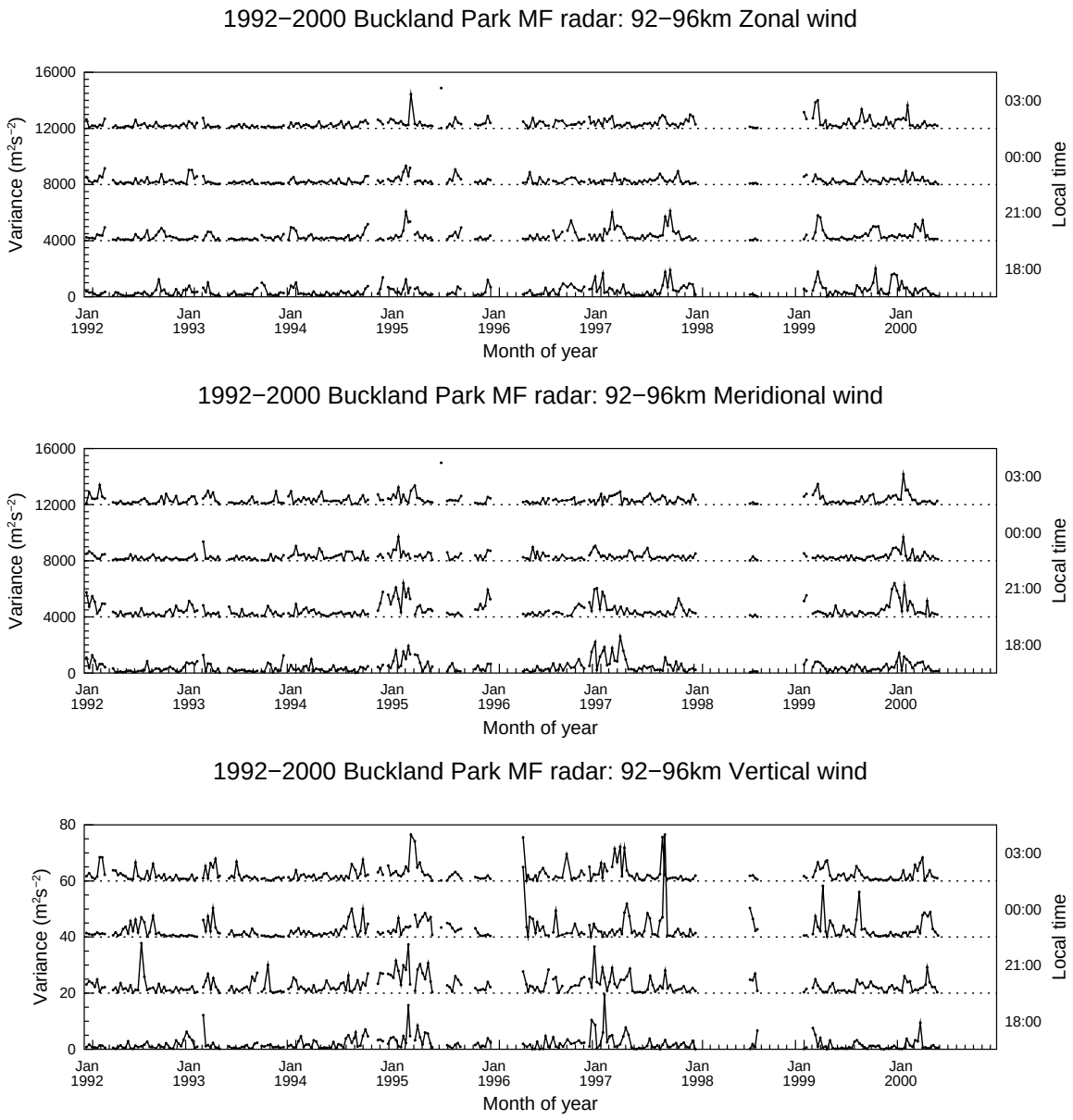

Figure 6.24: Eight-day averaged variance of wind components measured by the Buckland Park MF radar as in figure 6.23 but for range bins between 92km and 96km inclusive.

in figures 6.25 and 6.26. The horizonal 84–88km and 92–96km data show strong peaks at one, two and half year periods as well as a cluster of others at around 200 days and 500 days. The vertical data agrees with this to a certain extent although the peaks are not as strong particularly for periods greater than half a year. The two-year peak is weakest in meridional data at both height ranges. A significant peak with a period around 2000 days occurs in both horizontal 92–96km components whereas in the lower height range it occurs only at certain times, and then only at a much lower (and less than significant) amplitude. The vertical periodogram shows a suggestion of a peak with period between 2000 and 3000 days which, like the similar period seen in the optical data might be associated with the eleven year solar cycle. However, the difficulty with vertical data after 1996 necessitates careful consideration of any apparent feature in the vertical wind. In this case it can be said that such a periodicity might be real but more data are required in order to confirm this beyond doubt.

6.5 Radar–photometer intercomparison

Although the variance time series from the radar and optical data contain significant levels of noise, a comparison between them is informative since both are directly comparable as an indication of the level of wave activity; being from the same height regions of the atmosphere some degree of similarity between the two observations would be expected. By inspection, the spectra obtained from the Lomb analysis of the radar and optical variances have some obvious differences although there are features common to both. Like the optical data, the horizonal 84–88km and 92–96km data show strong peaks at one, two and half year periods. As noted earlier these are accompanied by others clustered around 200 days and 500 days which have an appearance which is reminiscent of the discrete peaks observed in the optical intensity spectra with periods around 30 days and therefore may also be signatures of pseudo-periodic activity.

The strong peaks at one, two and half year periods seen in the wind variances

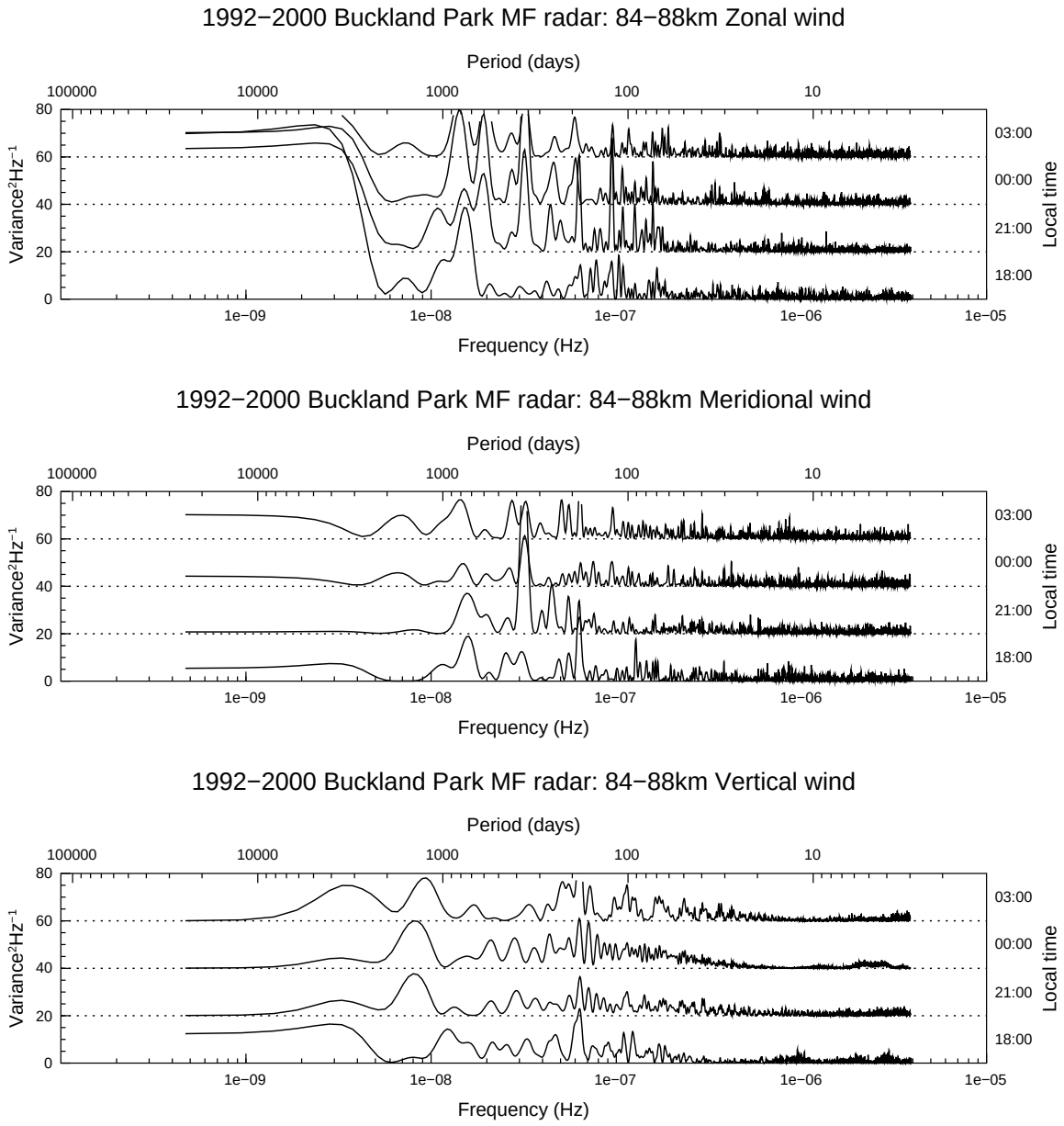

Figure 6.25: Three-point smoothed, normalised Lomb periodogram for MF wind variance data for 84km to 88km as shown in figure 6.23.

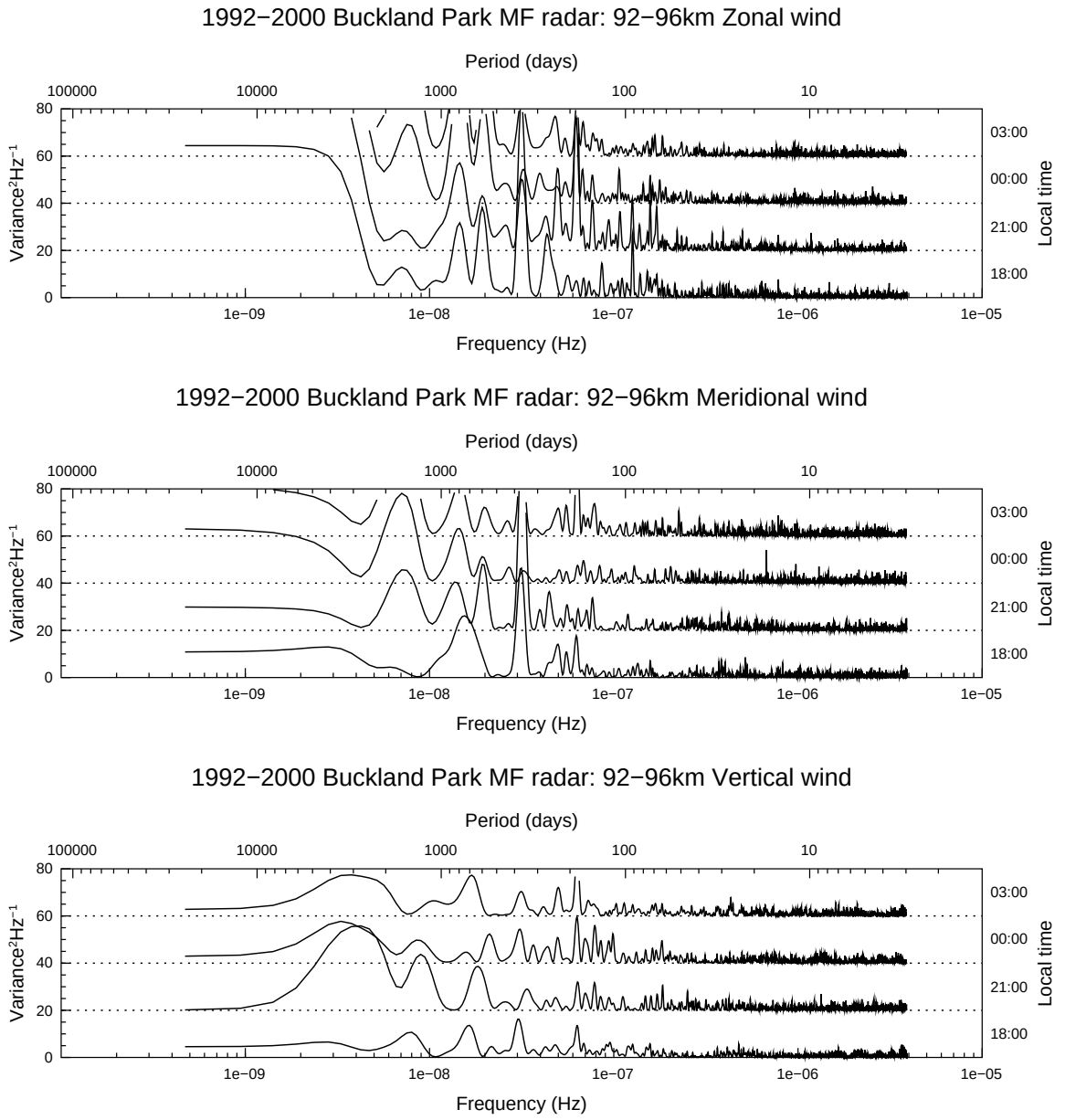

Figure 6.26: Periodogram as for figure 6.25 but utilising data from 92km to 96km from figure 6.24.

correspond to similar peaks observed in the optical variances. It has been well established that gravity wave activity can be deduced from radar wind variances, and the correlation noted in this study therefore confirms that similar conclusions can be validly reached using observations from photometers and spectrometers. The present study had the advantage of being able to utilise three effectively independent photometers which, among other things would lead to the identification of any long-term instrumental variation which might otherwise be attributed to geophysical effects. As an example, this redundancy was useful here in determining that the drop in field three's response in 1997 had no appreciable effect on the spectrum of the long-term signal. An instrument design which incorporated routine calibration capabilities would remove this ambiguity from spectrometer and single-field photometers.

Optical OI intensity data showed a suggestion of a 2000 day (5.5 year) periodicity which is being attributed to solar cycle effects. Such a link was not totally surprising given that the airglow mechanism is excited by solar radiation. Although weak, it was interesting to observe an indication of this signal in the wind data at 92–96km as well, whereas it was almost totally absent from the 84–88km wind data. Unfortunately its presence in the OH optical intensity data cannot be checked thoroughly because of Milky Way contamination, although based on the periodogram of the OH intensity data shown in figure 6.10, it appears more than likely that this periodicity is present at least to some extent. Comparison between the 92–96km wind variance and the 557.7nm airglow periodograms shows that the 2000 day period signal is certainly weakest in the wind data; given that the 2000 day peak is also considerably weaker in the OH data compared to OI data its apparent absence in the 84–88km wind variance may simply be due to an extremely low amplitude. This would not be surprising; if the eleven year solar cycle is behind the periodicity observed in optical data the most obvious mechanism for this is the varying solar energy flux affecting the number of excited molecules — and therefore overall airglow intensity — at mesopause heights. The wind variance is a measure of gravity wave activity and any solar-cycle related effect in the wind data would have to be via an interaction between solar radiation level and

gravity wave generation, an interaction which would be very weak if it existed at all. However, in order to make any conclusive statements regarding this long-term trend a more extensive dataset would be required since the optical data under consideration has a span of only five years. In any case it certainly appears that the airglow is more sensitive to the mechanism causing the 2000 day period than the MF wind data which is what would be expected if it was of solar-cycle origin.

6.5.1 Cross spectral comparisons

To quantify the relationship between the data observed with the photometer and the radar a number of cross-spectral estimations were made following the method outlined in section 4.6.2 on page 102. Because of the relatively large amount of noise in the variances this part of the study was restricted to consideration of wind component magnitudes and photometer intensities. Even so, it became clear from observations of various phase spectra and simulated data that phase estimations could be made no better than $\pm\frac{\pi}{4}$ given the data under consideration.

Photometer field 1 was chosen as representative of the optical data with cross spectra formed between this field and meridional/zonal wind components. The 557.7nm data were compared to average wind data between 92km and 98km (range bins 92km to 96km) while wind data from 84km to 90km (range bins 84km to 88km) were used with the 730nm data. Data from the middle two timebins (2100–2359 and 0000–0259) were used since these times are unaffected by the effects of shorter observation times during summer. A representative cross spectral result is shown in figure 6.27 with tables 6.1 to 6.3 summarising the phases observed for significant periodicities identified previously from the Lomb periodograms of the long-term time series.

Although there was considerable phase noise present, it was usually possible to identify a unique phase for each of the selected periodicities. Generally, phase coherence between the datasets and across local timebins is good, with the phases being in agreement with qualitative obervations noted earlier in this chapter. At times, however, ambiguities in the phase and noisy phase spectra clearly had an affect as

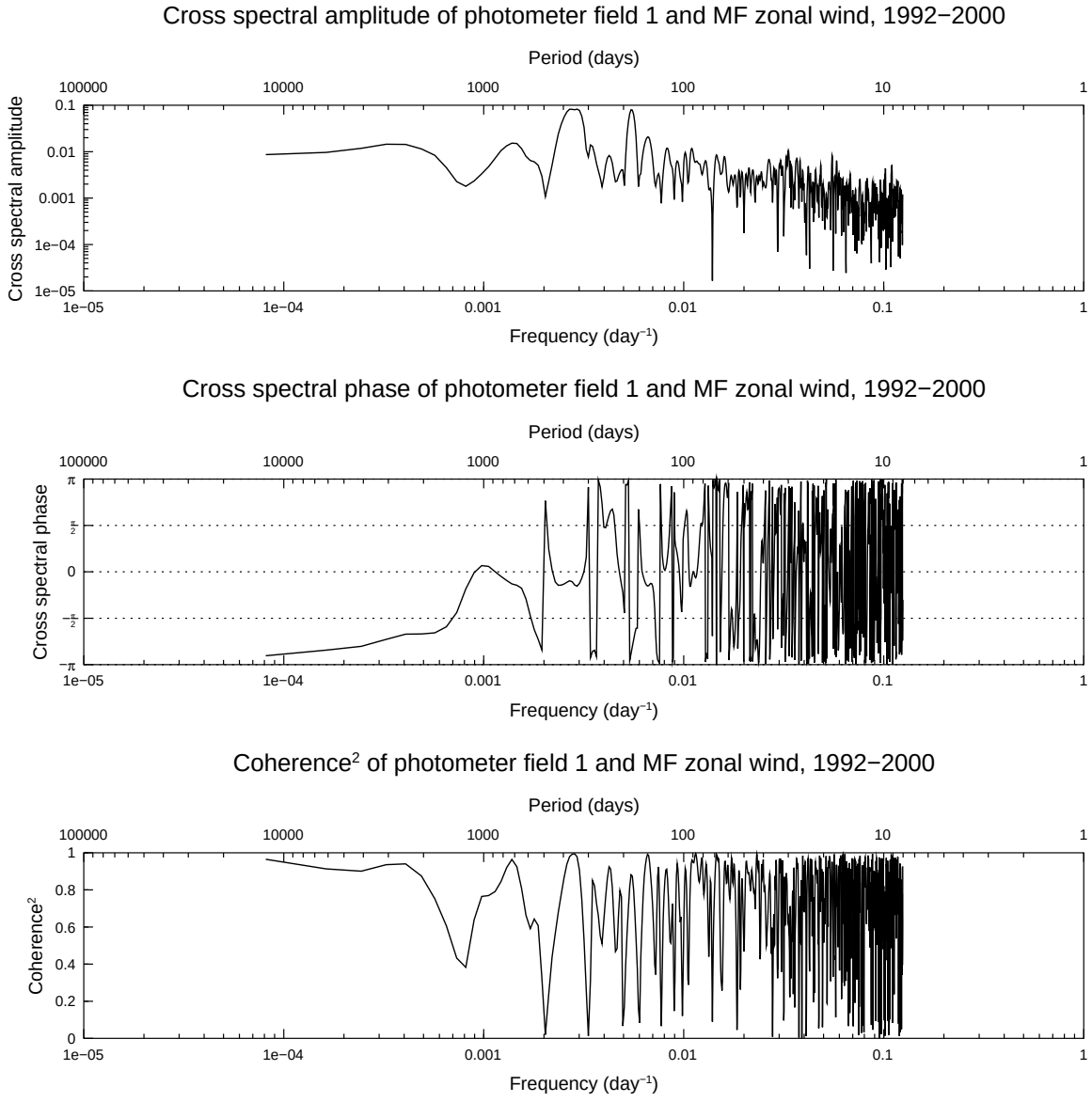

Figure 6.27: Cross spectrum between the 557.7nm intensity observed by field one of the photometer and the average zonal wind observed by the MF radar between 92km and 98km. The time series used were the average of the respective quantities recorded between 2100 and 2359 local time at Buckland Park for each day data were available. Significant peaks can be identified with periods of approximately 720 days, 360 days and 180 days as would be expected based on the previous harmonic analysis.

Period	Zonal/Meridional	558nm/Zonal	558nm/Meridional
720 days	$\frac{-\pi}{2}$, $\pm\pi$	0 , 0	$-\pi$, $-\pi$
360 days	0 , $\frac{-\pi}{2}$	0 , $\frac{\pi}{2}$	$\frac{-\pi}{4}$, 0
180 days	$\pm\pi$, 0	$\frac{-\pi}{2}$, $\frac{-\pi}{2}$	$\frac{\pi}{2}$, $\frac{-\pi}{2}$
120 days	$\frac{\pi}{2}$, $\frac{\pi}{2}$	0 , -	- , -

Table 6.1: Phases of selected periodicities in the cross spectrum between the 557.7nm optical intensity and MF wind components between 92km and 98km. For each cross spectrum, phases are reported for the timebins running from 2100–2359 and 0000–0259 local time, separated by commas. Hyphens indicate a lack of a clearly defined cross spectral peak at the respective period; $\pm\pi$ denotes that in the region of the respective period the phase was changing rapidly between these two values and its true value is therefore in doubt.

Period	Zonal/Meridional	730nm/Zonal	730nm/Meridional
720 days	$\frac{\pi}{4}$, $\frac{\pi}{2}$	$\frac{3\pi}{4}$, $\frac{\pi}{2}$	π , $\pm\pi$
360 days	$\frac{\pi}{4}$, $\frac{\pi}{2}$	$\pm\pi$, $\frac{\pi}{2}$	$\frac{-3\pi}{4}$, $\frac{-3\pi}{4}$
180 days	0 , $\frac{\pi}{2}$	0 , 0	$\frac{-3\pi}{4}$, $\frac{-3\pi}{4}$
120 days	$\frac{\pi}{4}$, $\frac{\pi}{2}$	- , -	- , -

Table 6.2: As for table 6.1 but for 730nm optical data and 84km–88km radar wind components. Due to actions of the Milky Way on the 730nm optical intensity data as outlined in the text, it should be noted that reliability of the results for at least the 360-day period are dominated by the galactic light rather than light of atmospheric origin.

Period	558nm/730nm
720 days	0 , 0
360 days	$\frac{\pi}{2}$, $\frac{3\pi}{4}$
180 days	$\frac{-\pi}{2}$, $\frac{-\pi}{2}$
120 days	$\frac{-\pi}{4}$, $\frac{-\pi}{4}$

Table 6.3: As for table 6.1 but for 557.7nm and 730nm optical data. The Milky Way's adverse influence on the 730nm data should be recalled when considering these figures.

evidenced by inconsistent phases and phase coherence.

6.6 Summary

A Lomb-Scargle analysis of optical intensity data identified significant signals with periodiciteis of two years, one year and one half year which have been linked to seasonal processes. A periodicity identified at one third of a year is thought to be the result of interactions between the one year and one half year signals, while a five and a half year period appears likely to have its origin in the eleven year solar cycle. The variance of the optical intensity showed clear periodicities at two years, one year and half a year. Signatures at other periods were well below even the 50% confidence limit. An equinoctal enhancement in activity was seen, with the autumn enhancement (during March and April) being generally higher than that in spring (September and October).

The long-term behaviour of the spectrum of the variance of optical intensity was studied, and showed a drop in spectral power associated with periodicities less than thirty minutes during autumn and spring. Comparison with summer and winter spectrum suggested that the increase in wave activity observed during the equinoctal periods was concentrated in the longer periods (more than thirty minutes).

Wind data from a colocated MF radar were analysed in a similar way to the optical data. Periods of one year and two years were clearly identified with a somewhat weaker signal at half a year. There was a weak suggestion of a five and a half year signal, although it was not conclusive. Vertical wind velocities, although adversely affected at times due to equipment problems, appeared to maximise concurrently with optical intensity maxima.

A complex extension to the Lomb method allowed cross spectral comparisons to be made between the optical and radar data. In general, the correlation between the periodicities observed qualitatively were found to be statistically significant and have consistent phase relationships.

chapter 7

Conclusions and further work

The work presented in this thesis concerns the analysis of 557.7nm OI and 730nm OH airglow photometer data from Buckland Park with two separate goals in mind: to obtain a climatology of gravity-wave disturbances seen in the airglow layers, and to study the long-term behaviour of the airglow emissions themselves. In doing so a number of data processing techniques were developed which increased the amount of optical data available for use in the analyses. An overview of the major findings and outcomes within these areas is presented in this chapter, followed by suggestions for further work which build on the results of this project.

7.1 Gravity wave analysis

Cross-spectral analysis was successfully employed on a five year optical dataset to obtain parameters for wave activities observed. Interference from the Milky Way was virtually eliminated through the application of a wavelet-based filtering technique which had minimal impact on the time series in regions not originally affected by the Milky Way. Intrinsic wave parameters were deduced using FCA (full correlation analysis) wind data from a co-located MF radar system. In addition, data from the OH (730nm) channel were used to estimate the vertical flux of horizontal momentum associated with each identified wave.

Wave directionality showed clear anisotropies in all seasons, with the preferred direction varying from season to season. Generally there was a distinct lack of waves with northward and westward components which is only partially explainable by the filtering effects of the winter mesospheric jet. Furthermore, the persistence of the eastward waves during summer would not be expected if the waves originated in the lower atmosphere due to filtering by the eastward summer jet. Seasonal variations of other wave parameters (namely horizontal phase speed, horizonal wavelength and period) were not pronounced.

The published procedure for calculating momentum and energy fluxes based on optical data was refined since assumptions made originally proved to be inappropriate for many waves detected by the photometer. Analysis of each previously identified wave event with the revised method resulted in apparently reasonable flux estimates in around 90% of the cases with about 50% being well within limits of other published work. This indicates what while the methodology might be sound in principle, there appears to be issues with its practical application which have not been fully quantified. There are also additional issues which still require attention: the assumption made by the method that all waves are vertically propagating, and the question of whether a more accurate intensity perturbation estimate is required and/or possible. While the latter can be addressed in time, the question of vertical propagation is not so easily dealt with. There is no method whereby optical observations such as those presented can indicate whether a given disturbance is caused by a vertically propagating wave or a ducted wave. Observations at two heights can only show an apparent lack of propagation between the layers which could be due to either ducting or the presence of a critical layer between the two emissions. When analysing optical data for momentum and energy fluxes, this limitation must be acknowledged.

Comparison with other studies and a consideration of the Fourier-based cross-spectral method employed throughout this study suggests that the waves identified by the photometer are most likely to be part of the total wave field rather than the temporally isolated quasi-monochromatic (QM) waves often seen in airglow imager

data. It is therefore expected that differences will arise when comparing wave parameter statistics from the two types of instruments, since different wave populations are being considered.

7.2 Airglow variability

Using three hour average intensities, a time series comprising one point per day was formed using the optical data, spanning the years from April 1995 to May 2000. Similar treatment was afforded to concurrent MF radar data to facilitate comparisons. To investigate periodic behaviour of these time series a Lomb-Scargle analysis was performed, with a complex extension of this allowing calculation of the cross spectrum between optical intensities and radar winds. Because this analysis relied on the optical contribution of the terrestral atmosphere's airglow, only the 557.7nm OI data were used throughout this section due to an inability to successfully remove the Milky Way from the 730nm data while leaving the mean intensity undisturbed. 730nm data were used only when considering variance relative to each night's respective mean. A Lomb-Scargle analysis was chosen due to the discontinuous nature of the data caused by both the moon preventing optical observations when up, and miscellaneous equipment outages.

The Lomb analysis of the optical data identified periods of two years, one year, one half year and one third year with a high degree of certainty in the optical data. In addition, a signal with a period of around 2000 days (5.5 years) was also consistently seen. The one half, one and two year periodicities are thought to be seasonal in nature with the one year and two year signals being dominated by the equinoctal enhancements, while the one third year period is considered to be a product of a non-linear interaction between the one year and one half year signals. The 2000 day period appears to be linked closely to the 11 year solar cycle, although more data are necessary in order to confirm this.

Discrete peaks with period around thirty days were also identified by the Lomb

analysis of the OI data, although their amplitude was no greater than the 50% confidence limit. Modelling with a simulated dataset showed that peaks of this amplitude are not typically caused by the windowing effect of the moon-induced non-observation times. No seasonal or yearly consistency could be identified in this period region, ruling out a significant signal caused by the 27 day solar rotation. It was concluded that these peaks are most likely due to an interaction between a weak signal with amplitude comparable to noise and the sampling effect of the moon. The low level of such a signal (if it exists) makes it impossible to quantify within the confines of the present dataset.

Lomb periodograms of the variance of the OI intensity was used as a measure of overall gravity wave activity. An enhancement in wave activity as inferred from this data is seen in the equinoctal periods although significantly it is missing from some years. Also significant is the suggestion that the spring enhancement was not particularly prevalent in the OH data.

A standard spectral analysis of the optical variance for both OH and OI showed that the equinoctal enhancements in gravity wave activity predominantly occurred at periods greater than thirty minutes. A correlated reduction in the power of shorter period waves was also identified.

A similar Lomb-based analysis of concurrent radar data identified one half year, one year and two year periods in the wind velocity and variance data. No consistent signature of a one third year period was identified, although there may be a weak signal with 2000 day period. Once again, a longer dataset would be required to further pursue the possible existence of the latter signal. Vertical wind estimations do show an increase during equinoctal periods which is expected since the enhancement in airglow intensity seen at these times is associated with increased vertical transport of atmospheric species, particularly atomic oxygen.

Finally, a cross-spectral comparison between the radar winds and the optical intensity data demonstrated that many of the periodic signals identified in the separate time series maintained consistent phases across the instruments and across local time

intervals.

7.3 Further research

The results of this study have highlighted some promising areas of enquiry for further research. Obviously the acquisition of a further five years of optical data at Buckland Park will present the possiblity of more complete evaluation of the existence of links between the eleven year solar cycle and the airglow intensity. Furthermore, introduction of routine Doppler-mode operation of the Buckland Park MF radar will enable direct measurements of the momentum flux to be made with the optical intensity data, enabling a more thorough investigation of the optical momentum flux derivations and the numerous issues raised by the present study.

This study used Fourier-based cross spectral techniques to identify wave signatures, although this has the acknowledged restriction that it is less sensitive to disturbances which persist for only a fraction of the night. A possible way around this restriction is to employ a so-called 'cross-wavelet' method described by Torrence & Compo (1998) and demonstrated by Pancheva & Mukhtarov (2000) which will be, by definition, more sensitive to shorter-lived disturbances. Statistics gathered from such an analysis are likely to give a more complete picture of the perturbations experienced by the airglow layers. In addition, this method could be more sensitive to coherent features in both layers which are displaced temporally which might allow more reliable detection of the vertical properties of the waves being observed. Another alternative would be to divide each night up into three hour blocks and re-analyse with the Fourier-based methods, the shorter time series reducing the masking effects present when a signal is temporally isolated in a much longer time series. A comparison between these two methods could also prove valuable.

As mentioned, an attempt to compare Buckland Park and Davis Station optical data did not proceed due to the unique problems associated with auroral contamination of the latter. However, it should be possible to construct a reliable detection

and exclusion algorithm to deal with this contamination since the Davis instrument includes a filter which reliably detects the presence of auroral activity. The presence of the MF radar at Davis means that a Davis MF/optical dataset could be utilised in a similar way to the Buckland Park set presented herein, resulting in a potentially useful cross-latitude comparison.

As mentioned earlier, concurrent MF Doppler radar operation will give an independent measure of the gravity wave energy and momentum fluxes at the height of the OH airglow layer. Such results could be used to determine whether the optically estimated values are representative of the physical processes. The large number of high flux values calculated in the study, the previously explored limits of the Fourier methods and the lack of agreement between the photometer and imager data do, however, warrant attention. One significant question is whether the waves identified by the photometer are real gravity waves or simply produced within the analysis by the passage of many different waves at various times during the night. If investigations suggest the latter, the physical significance of the detected 'waves' should be determined. The present study indicates that it is likely that at least 50% of the waves detected by the photometer are real. Further work with a co-located imager and the Doppler MF radar, in addition to the exploration of alternative data processing methods could go a long way to fully classifying (and possibly improving) the photometer's observational limits and overall reliability.

The study of the long-term variability of optical and radar data suggested that a number of periodic components may be present with periods below 100 days. With the analysis employed here their significance levels were low but perhaps not so low as to preclude further, more detailed investigation into their origin. A brief investigation was made of signals with periods around thirty days observed in the optical data, but this could not identify any consistent behaviour. However, given the nature of signals seen in the present results with periodicities below 100 days, a more exhaustive, targeted study of these signals may prove valuable in expanding our understanding of the airglow dynamics and the properties of the analysis methods when applied to this

data.

To further enhance the reliability of the Buckland Park optical data, a real-time cloud detector (Clay et al. 1998) should be installed to operate in conjunction with the photometer. This would give an unambigious indication of the cloud-cover and thus a quantitative test for the reliability of the optical data, which could then be used to implement a more autonomous mode of analysis operation.

At various times during the study problems were noticed with the operation various components of the photometer. Although it was usually possible to program the control and analysis software to circumvent these, the time is fast approaching when the causes will have to be addressed rather than the effects. For example, at this time problems with the filter wheel have resurfaced which possibly cannot be dealt with efficiently in software. In order to build on the comprehensive dataset collected over the past five years it is important to continue the instrument's operation and improve its reliability. Possible issues to be addressed are outlined below:

- replacement of the current filter wheel drive mechanism with a directly connected stepper motor;
- replacement of the 'position indicator' microswitches with a Hall-effect mechanism;
- improvement of the shielding of the interconnecting cables between the control electronics and the host computer to try to prevent spurious spikes in the data;
- replacement of field three's photomultiplier tube with a IR-sensitive model similar to those currently in fields one and two; and
- implementation of a controlled temperature environment within the instrument to maintain filter temperature.

With the implementation of these hardware improvements the instrument's effective lifetime should be extended indefinitely. In addition to this, an alteration of the filters in use would extend the usefulness of the data further to include OH rotational

temperature. The 557.7nm filters could be retained as they are to maintain total compatibility with the previous five year dataset, enabling the solar cycle intensity link to be pursued. The 730nm filters could be removed and replaced with two narrow-band filters each centred on a specific vibrational-rotational OH line and a 'background' filter. This would enable temperature measurements to be made and allow a correction for background light in a similar way to that employed by Hecht et al. (1997) and others. A 20 second sampling of the 557.7nm emission every 60 seconds could be retained (again for compatibility with past datasets), followed by approximately 7 second dwell times for each position corresponding to the three new filters. Allowance has been made for a finite filter wheel rotation rate, although the exact timing would be dependent on the performance of the upgraded system. Based on experiences at Buckland Park and Davis, the seven second dwell time should give an adequate signal amplitude. This arrangement would allow each channel to see its own dedicated 557.7nm filter and each of the three new filters in turn every 60 seconds, giving three independent measurements of OI brightness and OH rotational temperature every minute. The instrument would still give gravity wave propagation information at the two emission heights as before, but for the OH emission this would be through OH temperature perturbations rather than via an uncalibrated intensity.

appendix

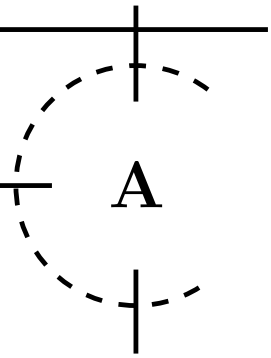

Davis MF radar

The Davis MF radar was recommissioned in 1994 having been moved from Mawson and significantly upgraded after 10 years of operation. Davis station is located in Antarctica at 68°35′S, 77°58'E. Transmission occurs at 1.94MHz. Design and logisitic decisions related to the environment at Davis meant that the system was considerably smaller and simpler than that operating at Buckland Park. Originally it was intended to use data from the photometer and MF radar at Davis to compare with the Buckland Park dataset. However, due to issues raised in the main text this was not possible.

A.1 Hardware

The arrangement of the antennae is shown in figure A.1. Transmission occurred on an array of four half wave dipoles 10m above the ground, arranged in a square with sides approximately 80m long. Opposite elements (sides) were driven in parallel. Either right hand or left hand circular polarization could be selected by appropriate choice of phasing for the two pairs of elements. Reception occurred on three crossed dipole antennae arranged to form an equilateral triangle with 180m sides. The height of the crossed dipole elements ranged from 10m in the centre of the dipole to 2m at the extremities. The system used a pulse repetition frequency of 80Hz with a data set acquisition taking 102.4 seconds — the same as the Buckland Park MF system.

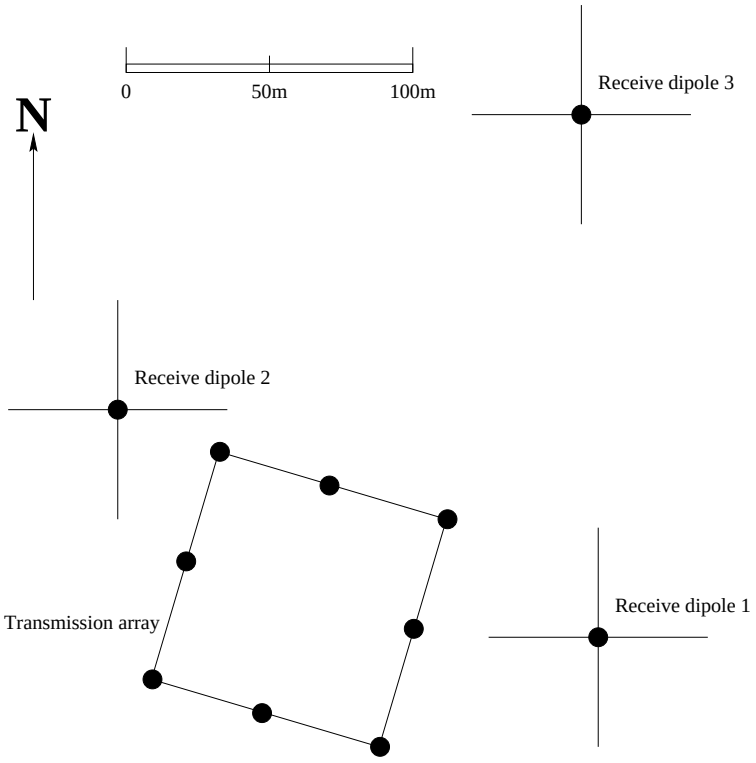

Figure A.1: Davis MF radar antenna arrangement

A.2 Radar operation

As at Buckland Park, the MF radar system at Davis was controlled by an IBM PC compatible, although the actual acquisition software in use was different. The system was simpler than the Buckland Park version owing mainly to the smaller antenna array and the lack of beam steering capabilities. This latter point meant that Doppler measurements could not be carried out by the Davis MF radar and therefore only spaced antenna wind data was available.

appendix

B

Trends of airglow imager observations near Adelaide, Australia

This appendix contains a copy of the paper 'Trends of airglow imager observations near Adelaide, Australia', by J. H. Hecht, R. L. Walterscheid, J. Woithe, L. Campbell, R. A. Vincent and I. M. Reid, published in *Geophysical Research Letters* **24**, 587–590, 1997. Also included is a comment on this paper (*Geophysical Research Letters* **25**, 21–22, 1998) and a subsequent reply.

GEOPHYSICAL RESEARCH LETTERS, VOL. 24, NO. 5, PAGES 587-590, MARCH 1, 1997

Trends of airglow imager observations near Adelaide, Australia

J. H. Hecht, R. L. Walterscheid

The Aerospace Corporation, Los Angeles, California

J. Woithe, L. Campbell, R. A. Vincent, and I. M. Reid

Department of Physics and Mathematical Physics, University of Adelaide, Adelaide, Australia

Abstract. From April, 1995 to January, 1996 a nightglow imager and an airglow photometer were colocated near Adelaide, Australia. The data obtained on more than 50 clear nights revealed seasonal changes in the airglow intensities and temperatures as well as in the gravity wave activity. These temperature data are the first seasonal results from the mid-latitude southern hemisphere mesopause region. The OH Meinel band was observed to have a rotational temperature that was warmer than the O_2 Atmospheric band in the winter. There were also summer solstice maxima and winter solstice minima in the O_2 Atmospheric band and OI(557.7) airglow intensities. The gravity wave activity, seen in the 50 to 80 km horizontal wavelength waves, was generally greatest in the OH Meinel layer and showed a semiannual variation with a strong summer solstice maximum. The relationship between gravity wave activity and airglow intensities disagrees somewhat with models. Compared to previous studies, the data suggest that there may be a difference in the seasonal variability of short and long period gravity waves.

Introduction

Since internal atmospheric gravity waves were first proposed as a significant component in the upper atmosphere [*Hines*, 1960] it has become increasingly apparent that they are not just a theorists toy [*Hines*, 1965] but a key contributor to the dynamics of the upper mesosphere and lower thermosphere [*Holton*, 1983; *Fritts*, 1984]. The techniques for observing gravity waves have become quite sophisticated and include MF radars [*Manson*, 1990], Na lidars [*Gardner et al.*, 1995], large astronomical telescopes [*Ramsay et al.*,1992], CCD airglow imagers [*Taylor et al.*, 1995], and Fourier transform interferometers [*Lowe and Turnbull*, 1995]. In order to understand how gravity waves actually affect the upper atmosphere, longer term studies are needed at many different geographic locations. Unfortunately, only a few studies have been made of the seasonal variability of gravity waves [*e.g. Meek et al.*, 1985; *Tsuda et al.*, 1990; *Senft and Gardner*, 1991; *Collins et al.*, 1996; *Wu and Killeen*, 1996] and only two of these have occurred in the southern hemisphere [*Vincent and Fritts*, 1987; *Vincent*, 1994]. Because different instruments were used (lidars or radars) the seasonal variability has been measured at a variety of vertical wavelengths and/or periods. While there has been agreement that peaks in gravity wave activity occur near the solstice, some studies show a winter maximum while others show a summer maximum. The minima usually appear near the equinoxes.

Airglow instruments, especially imagers, provide another way of measuring gravity wave variability. Recently, *Hecht et al.*, [1994] showed how to measure the 2D horizontal wavelength spectrum of gravity waves perturbing either the OH Meinel (hereafter OHM) nightglow layer, which peaks between 85 and 90 km, or the O_2 Atmospheric (hereafter O2A) nightglow layer, which peaks between 90 and 95 km. Imagers, therefore, can measure the gravity wave variability at various horizontal wavelengths and at different altitudes. Moreover, as models predict that gravity wave activity should affect airglow intensities through changes in eddy diffusion, airglow measurements can provide an insight that is not available from the lidar or radar measurements into the effect of gravity waves on composition [*Garcia and Solomon*, 1985; *LeTexier et al.*, 1987]. This work reports on the results from nine months of airglow imager observations in southern Australia.

Experimental Technique

The Aerospace CCD camera was situated at the Buckland Park Field Station located approximately 40 km north of Adelaide, Australia (35S, 138E) from April, 1995 to the end of January, 1996. This instrument, described in *Hecht et al.*, [1994], operated in an autonomous mode taking data on every night between sunset and sunrise during periods when the moon was no more than one hour above the horizon. Good data were obtained from over 50 clear nights, most of these within one week of new moon. This instrument obtains both spectral and image data.

The spectral data presented here include nightly averages of the OHM and O2A intensities and rotational temperature. Image data were analyzed to obtain the slope and magnitude of the 2D horizontal wave number spectrum for images obtained from either the OHM (6,2) rotational line near 843.0 nm and the portion of the O2A (0,1) band which passes through the instrument's filter centered near 866.0 nm. The general procedure for obtaining these quantities is discussed in *Hecht et al.*, [1994]. However, as further discussed in *Hecht et al.*, [1995] image data need to be properly detrended. The data discussed in this work follow the prescription given in *Hecht et al.*, [1995]. In this work the magnitude at any wavelength bin is defined as the power in that bin in units of $(\delta I/I)^2$ where $\delta I/I$ is the fractional intensity fluctuation.

The Buckland Park Field Station also has, as a permanent facility instrument, the 2 wavelength channel, 3 sky position Buckland Park (BP) photometer system [*Jacob*, 1995]. This system records OI (557.7 nm), hereafter designated as the

Paper number 97GL00128.
0094-8534/97/97GL-00128$05.00

green line, and OHM (8,3) band intensities from 3 positions in the sky. The field of view of the instrument is approximately 3.3 degree and over a one minute period the instrument alternatively observes the OHM and green line simultaneously in the three fields.This paper discusses these data, averaged over the entire night, for the nights recorded by the CCD camera and for a few months before and after that period.

Results and Discussion

Airglow Temperatures

Figure 1 shows the OHM and O2A temperatures derived from the camera data for the clear nights of the campaign. The statistical uncertainty of any temperature data point is less than 1 degree. These are the first measurements of mesopause temperatures in the mid-latitude southern hemisphere. Also shown on these plots are the modelled (TIME-GCM) and the measured (lidar) temperatures at 88 and 94 km and at 41 N latitude for winter and summer solstice and the equinox [*She et al.*,1995]. Based on the modelled plots in *She et al.*, [1995] the 5 degrees difference in absolute latitude is not significant. The *She et al.*, [1995] results show a peaked high altitude, 100 km, mesopause in winter, a broad, 85 to 100 km, mesopause with some structure at the equinox, and a peaked lower altitude, 85, km mesopause in the summer. Our data are qualitatively consistent with this picture except that the O2A data are colder in winter (June) and maybe warmer in summer (December) than the *She et al.*, [1995] data. Thus, the temperature gradients may be steeper for these new data than for the long term average data shown in *She et al.*, [1995].

Airglow Intensities

Figure 2a shows deviations from the mean for the OHM and O2A data from the CCD camera and for the green line

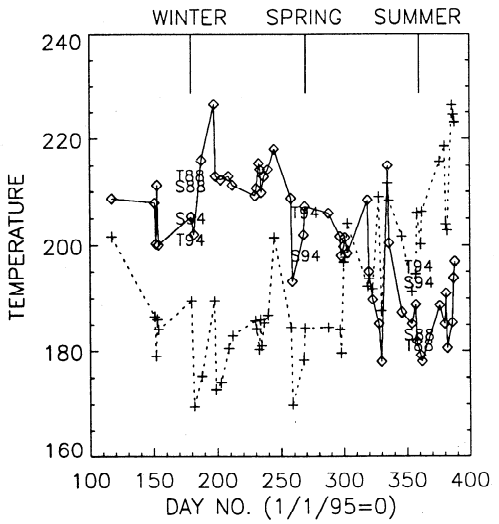

Fig. 1. Temperature versus day number for OHM (solid line with individual nights as diamonds) and O2A (dotted with crosses). Data from *She et al.*, [1995] use the symbols S88, S94, T88, or T94. The S points are lidar data at 88 and 94 km. The T points are model predictions at 88 and 94 km. At the equinox the 88 and 94 km S and T points are the same.

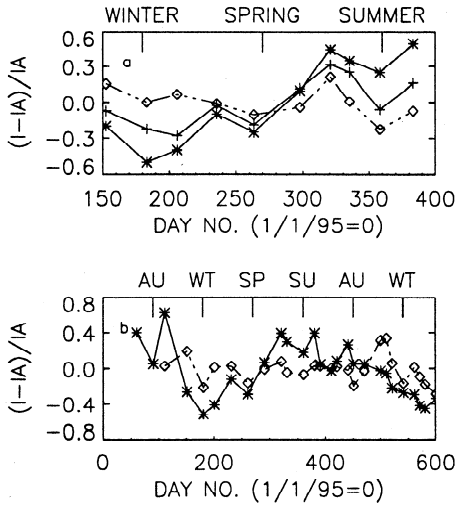

Fig. 2. (a) The deviation of airglow intensity from a mean versus day number for the same period as in Figure 1. The OHM (dashed with diamonds), O2A (solid with crosses), and green line (solid with asterisks) data are grouped as discussed in the text. (b) The deviations of the BP photometer green line (solid line with asterisks) and OHM data (dashed line with diamonds) for the extended data set.

data from the BP photometer. The CCD and BP photometer data points have been grouped and averaged into ten points and are shown from day 150 to day 380 with day 0 being 1/1/95. The single CCD data point at day 100 is not included in these groupings. Figure 2b shows BP green line and OHM data for an extended period from day 61 to day 600.

The data in Figure 2a show an interesting effect. The green line data show the greatest deviation from the mean followed by the O2A data. The OHM data are all within ±20% of the mean. The largest positive excursion for OHM occurs during the same period as the maxima for green line and O2A. The green line data and the O2A data show maxima just before summer solstice and minima just after winter solstice. The extended data in Figure 2b agree with this trend but seem to show a peak in OHM just after the autumn equinox.

Models predicting the seasonal intensity variation for OHM and the green line, due to gravity waves, are discussed in *Le Texier et al*, [1987] and in *Garcia and Solomon*, [1985]. The seasonal predictions of both these models are based on the following reasoning. When gravity wave activity is minimum at the mesopause region, there is a decrease in eddy diffusion, a buildup of atomic oxygen, and a subsequent increase in oxygen related airglow emission intensities. The OHM model predicts seasonal variations of less than 10% except near the equinoxes. In that sense the model is in agreement with our data although the day to day variability of wave activity, including gravity and planetary waves as well as tides, may be, on a short timescale, controlling the OHM intensity more than the climatology involved in the OHM model. For the green line the data show an annual variation with a maximum and minimum at winter and summer solstice, respectively, while the model predicts a semiannual variation with peaks near the equinoxes and minima near the solstices. The predicted

percentage variation in the green line from the mean is close to our data. While some of our observed variations in green line and O2A may be to tidal variations [*Burrage et al.*, 1994] our procedure of taking nightly averages and then averaging over several days should reduce this effect.

2D Horizontal Wave Number Spectrum

Following *Hecht et al.* [1994] and [1995] the spectrum in each image was computed nightly as a function of horizontal wavenumber bins. The wavenumber equal to one included the longest horizontal wavelengths from 50 to 80 km. Because the airglow layer thicknesses are on the order of 6 to 10 km, the vertical wavelengths seen in the imager data are on the order of or greater than 6 km. Therefore, the intrinsic wave periods observed in the imager data are less than $\approx$ 1 hour.

Slope. The nightly results for the absolute value of the slope of each emission are shown in Figures 3a and 3b. The average slope for the whole period for OHM is -2.38 while for O2A it is -2.42. Since the uncertainty in each nightly slope is 0.2 the uncertainty for the average is 0.03. The plots of the two slopes are quite similar. They show slight peaks before and near the September (spring) equinox although the OHM slopes at this period are usually greater than the O2A slopes. Near the December (summer) solstice the O2A slopes are slightly above the OHM slopes. These trends are shown in Figure 3c which plots the ratio of the OHM to O2A slope.

These data are the first to provide a measure of the 2D horizontal wavenumber spectrum in the two airglow layers over an extended period of time. They suggest that on average the same spectral shape is present in both layers. However, during certain periods, such as near the summer solstice of 1995, there were relatively more short horizontal wavelength waves present in the OHM layer compared to the O2A layer.

Magnitude. The average nightly power for the 50 to 80 km horizontal wavelength waves is shown in Figure 4. For both OHM and O2A there is a minimum just before and near

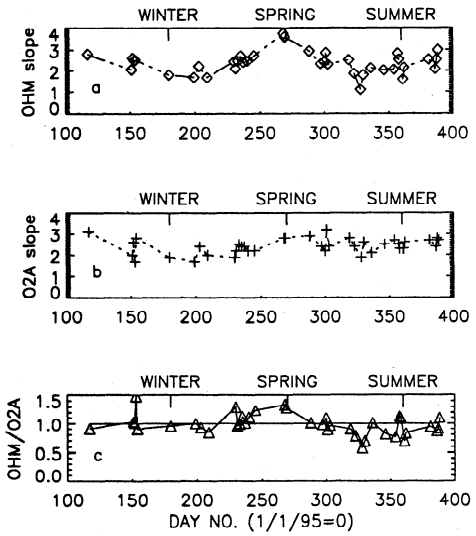

Fig. 3. (a) The absolute value of the log-log slope of the OHM 2D horizontal wave number spectrum versus day number. All slopes are actually negative numbers.(b) same as (a) but for O2A data.(c) the data from (a) divided by the data from (b).

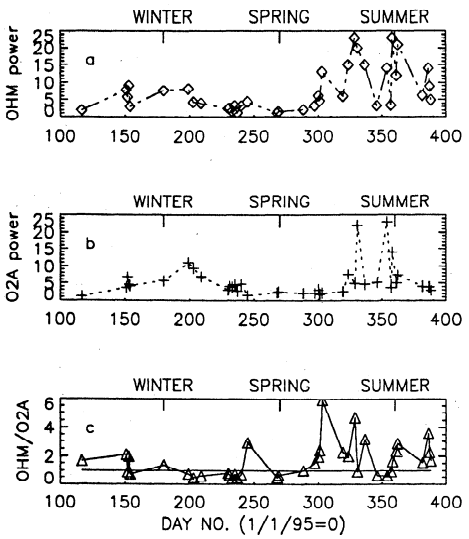

Fig. 4. Same as Figure 3 except the plot is the power in the 50 to 80 km horizontal wavelength interval multiplied by 1E5.

the spring equinox, a strong peak around the summer solstice, and a weaker peak near the winter solstice. Fig. 4c plots a ratio of the OHM to O2A results. This shows that the gravity wave amplitudes increase much more in the OHM layer than in the O2A layer around the summer solstice.

First, these results can be compared to other studies. Both *Senft and Gardner*, [1991] and *Collins et al.*, [1996] show gravity waves of periods around 1 hour peaking in the summer over Illinois. *Wu and Killeen*, [1996] show that the number of nights with short horizontal wavelength monochromatic waves peaks in the summer. Using the MU radar *Tsuda et al.*, [1990] find that gravity waves with periods between 5 minutes and 2 hours peak in the summer. Between the summer maximum and the equinox minimum they find a range of a factor of 4 in the variances induced in the winds by these waves. Other studies, including those at Adelaide [*Vincent and Fritts*, 1987] and at Saskatoon [*e.g. Meek et al.*, 1985] show less variability with gravity wave activity peaking in the winter. However, in those studies the wave periods were between 1 and 24 hours. Thus, there may be a real difference in the seasonal variation of short and long period gravity waves.

Second, these results can be compared to the airglow intensity model predictions, and to our data results for airglow intensities and temperatures. The data indicate that the wave amplitude increase occurs when the mesopause is decreasing in altitude and is becoming broader. Current models do not address this result. However, the models do predict that the airglow intensities should peak when the gravity wave activity is minimum. These data contradict that prediction. In the strictest sense the models relate airglow intensities to breaking gravity waves. Although airglow can be used to indicate the presence of breaking gravity waves [*Hecht et al.*, 1996] an increase in wave activity may or may not indicate an increase in breaking waves. Furthermore, models do not address how tidal or planetary wave variability may be mitigating or enhancing the effect of gravity waves on airglow intensities.

Third, given the complete data set there are three possibilities for the increased wave activity near summer solstice.

One, the waves are breaking in the OHM layer and do not as readily reach the O2A layer. This would explain the increase in waves in the OHM layer but would not agree with the model predictions since the O2A and green line intensities are reaching maxima during this period. Two, there is a deep mesopause located between the OHM and O2A layers causing wave reflection below the O2A and green line layers. Three, wave ducting is occurring preferentially in the OHM layer. These possibilities will be explored in a future paper.

Conclusions

The airglow data reported on in this paper reveal peaks in the seasonal variation of O2A and green line intensities as well as in the gravity wave activity of short period (less than 1 hour), short horizontal wavelength (less than 80 km) waves. The variation in the gravity wave activity, when compared to previous studies, suggests that there may be a real difference in the variability of short and long period gravity waves. The variability of the airglow intensities do not agree with previous models which predict that the oxygen related airglow intensities, at mid latitudes, should peak when gravity wave activity is at a minimum.The data not only indicate that the airglow intensities are at a minimum when the gravity waves are at a minimum but also that the green line data, at least, suggest an annual intensity variation whereas the models predict a semiannual variation. Finally, this work presents the first set of seasonal temperature variations from the mesopause region in the mid latitude southern hemisphere. The O2A temperature data are colder in winter and warmer in summer than the recent results of northern hemisphere studies. The data indicate that the mesopause temperature gradients are steeper than model predictions which could be related to the unusual gravity wave activity found in this study.

Acknowledgments. We thank the staff at Buckland Park Field Station for their support. This work was supported in part by NSF grant ATM 94-15779, by The Aerospace Sponsored Research Program, and by The Australian Research Council.

References

Burrage, M. D., N. Arvin, W. R. Skinner, and P. B. Hays, Observations of the O_2 atmospheric band nightglow by the High Resolution Doppler Imager, *J. Geophys. Res.*, *99*, 15017-15023, 1994.

Collins, R. L, X. Tao, and C. S. Gardner, Gravity wave activity in the upper mesosphere over Urbana, Illinois: lidar observations and analysis of gravity wave propagation models *J. Atmos. Terr. Phys.*, *58*, 1905-1926, 1996.

Fritts, D. C. Gravity wave saturation in the middle atmosphere: A review of theory and observations, *Rev. Geophys. Space Phys.*, *22*, 275-308, 1984.

Garcia, R. R. and S. Solomon, The effect of breaking gravity waves on the dynamics and chemical composition of the mesosphere and lower thermosphere, *J. Geophys. Res.*, *90*, 3850-3868, 1985.

Gardner, C. S., X. Tao, and G. C. Papen, Observations of strong wind shears and temperature enhancements during several sporadic Na events above Haleakala, *Geophys. Res. Lett.*, *22*, 2809-2812, 1995.

Hecht, J. H., S.K. Ramsay Howat, R. L. Walterscheid, and J. R. Isler, Observations of spectra of intensity fluctuations of the OH Meinel nightglow during ALOHA 93, *Geophys. Res. Lett.*, *22*, 2873-2876, 1995.

Hecht, J. H., R. L. Walterscheid, and M. N. Ross, First measurements of the two-dimensional horizontal wave number spectrum from CCD images of the nightglow, *J. Geophys. Res.*, *99*, 11,449-11,460, 1994.

Hecht, J. H., R. L. Walterscheid, D. C. Fritts, J. R. Isler, D. C. Senft, C. S. Gardner, and S. J. Franke, Wave Breaking Signatures in OH Airglow and Sodium Densities and Temperatures, Part I: Airglow Imaging, Na Lidar, and MF Radar Observations, *J. Geophys. Res., in press*, 1996.

Hines, C. O., Internal atmospheric gravity waves at ionospheric heights, *Can. J. Phys.*, *55*, 441-445, 1960.

Hines, C. O., Atmospheric gravity waves: a new toy for the wave theorist, *Radio Sci., 69D*, 375-380, 1965.

Holton, J. R., The influence of gravity wave breaking on the general circulation of the middle atmosphere, *J. Atmos. Sci.*, *40*, 2497-2507, 1983.

Jacob, P.G., "Manifestations of Atmospheric Gravity Waves in the Airglow at 95km", PhD Thesis, *University of Adelaide*, Adelaide, Australia, 1995

LeTexier, H., S. Solomon, and R. R. Garcia, Seasonal variability of the OH Meinel bands, *Planet. Space Sci.*, *35*, 977-989, 1987.

Lowe, R. P. and D. N. Turnbull, Comparison of ALOHA-93, ANLC-93 and ALOHA-90 observations of the hydroxyl rotational temperature and gravity wave activity, *Geophys. Res. Lett*, *22*, 2813-2816, 1995.

Manson, A. H. Gravity wave horizontal and vertical wavelengths: An update of measurements in the mesopause region, *J. Atmos. Sci.*, *47*, 2765-2773, 1990.

Meek, C. E., I. M. Reid, and A. H. Manson, Observations of mesospheric wind velocities 2. Cross sections of power spectral density for 48-8 h, 8-1 h, 1h-10 min over 60-110 km for 1981, *Radio Sci.*,*20*,1383-1402, 1985.

Ramsay, S. K., C. M. Mountain, and T. Geballe, Non-thermal emission in the atmosphere above Mauna Kea, *M.N.R.A.S.*, *259* , 751-760, 1992.

Senft, D. C. and C. S. Gardner, Seasonal variability of gravity wave activity and spectra in the mesopause region at Urbana, *J. Geophys. Res.*, *96*, 17229-17264, 1991,

She, C. Y., J. R. Yu, D. A. Krueger, R.Roble, P. Keckhut, A. Hauchecorne, and M. L. Chanin, Vertical structure of the mid-latitude temperature from stratosphere to mesopause, *Geophys. Res. Lett*, *22*, 377-380, 1995.

Taylor, M. J., M. B. Bishop, and V. Taylor, All-sky measurements of short period waves imaged in the OI(557,7 nm), Na(589.2 nm) and near infrared OH and O_2(0,1) nightglow emissions during the ALOHA-93 campaign, *Geophys. Res. Lett*, *22*,2833-2836, 1995.

Tsuda, T, Y. Murayama, M. Yamamoto, S. Kato, and S. Fukao, Seasonal variation of momentum flux in the mesosphere observed with the MU radar, *Geophys. Res. Lett*, *17*, 725-728, 1990.

Vincent, R. A. Gravity wave motions in the mesosphere and lower thermosphere observed at Mawson, Antarctica, *J. Atmos. Terr. Phys.*, *56*, 593-603, 1994.

Vincent, R. A. and D. C. Fritts, A climatology of gravity wave motions in the mesopause region at Adelaide, Australia, *J. Atmos. Sci*, *44*, 748-760, 1987.

Wu,Q. and T. L. Killeen, Seasonal dependence of mesospheric gravity waves (<100 km) at Peach Mountain Observatory, Michigan *Geophys. Res. Lett.*, *23*, 2211-2214, 1996.

J. H. Hecht and R. L. Walterscheid, The Aerospace Corporation, M2-266, P.O. Box 92957, Los Angeles, CA 90009. (e-mail jim_hecht@qmail2.aero.org)

L. Campbell, I. M. Reid, R. A. Vincent, and J. Woithe, Department of Physics and Mathematical Physics, University of Adelaide, Adelaide, Australia

(Received: November 25,1996; accepted: January 3, 1997)

GEOPHYSICAL RESEARCH LETTERS, VOL. 25, NO. 1, PAGES 21-22, JANUARY 1, 1998

Comment on paper: 'Trends of airglow imager observations near Adelaide, Australia' by J. H. Hecht, R. E. Walterscheid, J. Woithe, L. Campbell, R. A. Vincent, and I. M. Reid

J. Scheer[1], E. R. Reisin[1], P. A. Greet[2], P. L. Dyson[3], R. W. Smith[4], and G. Hernandez[5]

The paper by *Hecht et al.* [1997], hereinafter called HWWCVR, presents results of upper-mesospheric/lower-thermospheric observations performed from April, 1995 to January, 1996 from Buckland Park Field Station (35°S), near Adelaide, Australia. In the abstract, the authors claim to have obtained '*the first seasonal results from the mid-latitude southern hemisphere mesopause region*', regarding (among other parameters) temperatures. Further, this statement is again repeated in the Conclusions: '*Finally, the work presents the first set of seasonal temperature variations from the mesopause region in the mid latitude southern hemisphere*'. The published literature offers much contrary evidence to this claim, and its inclusion would have placed the contribution of the HWWCVR work in its proper context as a confirmation of the earlier investigations.

Papers on southern midlatitude mesopause region seasonal temperature variations have been available in the open literature for nearly 30 years, starting with the work of *Armstrong* [1968] at Camden, Australia, and more recently, the two-year investigation by *Greet and Jacka* [1989] at Mount Torrens (also near Adelaide), Australia. At southern midlatitude locations other than Australia, there has been the report published by *Scheer and Reisin* [1990]. This paper contains results from 32°S in Argentina, for both the OH(6-2) and the O_2(0-1) bands (the same airglow bands employed by HWWCVR), and is based on 54 nights of measurements done in four campaigns from 1984 to 1987. Also it reports the typical (warm winter) mesopause variation for the OH layer, and an unusual, cold-winter, temperature variation at the height of the O_2 emission. In addition, Scheer and Reisin found that OH temperatures were warmer than the O_2 temperatures during winter. In HWWCVR's Figure 1, which shows nocturnal mean rotational temperatures of OH and O_2, a similar and confirming behavior is evident.

With reference to their Figure 1, HWWCVR further state that '*These are the first measurements of mesopause temperatures in the mid-latitude southern hemisphere*', neglecting all earlier work from the midlatitude regions of the Southern Hemisphere, such as Argentina [*Scheer*, 1987, 1995; *Scheer and Reisin*, 1990; *Reisin and Scheer*, 1996] and Australia [*Armstrong*, 1968, 1975; *Greet and Jacka*, 1989; *Hobbs et al.*, 1996]. Reports from other latitude regions of the Southern Hemisphere, including Brasil [*Takahashi et al.*, 1974, 1977, 1994] and Antarctica [*Hernandez et al.*, 1992, 1995; *Greet et al.*, 1994; *Sivjee and Walterscheid*, 1994; *Williams*, 1996] also exist; however, they may not be directly relevant to the primary context of HWWCVR. Temperature data from the SME satellite are also available with complete seasonal coverage between 40°S and 40°N [*Clancy and Rusch*, 1989], albeit limited in local time coverage.

With respect to the observed temperature difference between the OH and the O_2 layers, as shown in Figure 1 of HWWCVR (and comparison with Figure 1 in *Scheer and Reisin* [1990]), it should be remembered that systematic errors due to uncertainties in transition probabilities [see, e.g., *Turnbull and Lowe*, 1989; *Scheer et al.*, 1994] as well as instrumental factors [e.g., *Hecht et al.*, 1995] can easily combine to cause systematic uncertainties of the order of 10K for OH. A similar uncertainty would be expected for O_2 temperatures.

In response to Hecht et al.'s reply, we simply emphasize the direct relevance of papers in the open literature that predate HWWCVR's confirming report and which present seasonal results from the midlatitude southern hemisphere mesopause region.

Acknowledgments. This investigation was partially supported by Consejo Nacional de Investigaciones Científicas y Técnicas, NSF ATM-9300274, the Australian Research Council and Australian Antarctic Science Advisory Committe. One of us (J.S.) also acknowledges financial support by M. Cazanobe de Scheer.

References

Armstrong, E. B., Variations in the width of the OI λ5577 line in the night airglow, *Planet. Space Sci., 16*, 211-229, 1968.

Armstrong, E. B., The influence of a gravity wave on the airglow hydroxyl rotational temperature at night, *J. Atmos. Terr. Phys., 37*, 1585-1591, 1975.

Armstrong, E. B., Irregularities in the 80-100 km region: A photographic approach, *Radio Sci., 21*, 313-318, 1986.

Clancy, R. T., and D. W. Rusch, Climatology and trends of mesospheric (58-90 km) temperatures based upon 1982-1986 SME limb scattering profiles, *J. Geophys. Res., 94*, 3377-3393, 1989.

Greet, P. A., and F. Jacka, Observations of the sodium layer using a Fabry-Perot spectrometer: Twilight temperature variations, *J. Atmos. Terr. Phys., 51*, 91-99, 1989.

Greet, P. A., J. Innis, and P. L. Dyson, High-resolution Fabry-Perot observations of mesospheric OH (6-2) emissions, *Geophys. Res. Lett., 21*, 1153-1156, 1994.

Hecht, J. H., S. K. Ramsay Howat, R. L. Walterscheid, and J. R. Isler, Observations of variations in airglow emissions during ALOHA-93, *Geophys. Res. Lett., 22*, 2817-2820, 1995.

Hecht, J. H., R. E. Walterscheid, J. Woithe, L. Campbell, R. A. Vincent, and I. M. Reid, Trends of airglow imager observations near Adelaide, Australia, *Geophys. Res. Lett., 24*, 587-590, 1997.

Hernandez, G., R. W. Smith, and J. F. Conner, Neutral wind and temperature in the upper mesosphere above South Pole, Antarctica, *Geophys. Res. Lett., 19*, 53-56, 1992.

Hernandez, G., R. W. Smith, and G. J. Fraser, Antarctic high-latitude mesospheric dynamics, *Adv. Space Res., 16*, (5)71-(5)80, 1995.

Hobbs, B. G., I. M. Reid, and P. A. Greet, Mesospheric rotational tem-

[1]Programa Nacional de Radiopropagación, Buenos Aires, Argentina
[2]Australian Antarctic Division, Kingston, Tasmania, Australia
[3]School of Physics, La Trobe University, Bundoora, VIC, Australia
[4]Geophysical Institute, University of Alaska, Fairbanks, Alaska
[5]Graduate Program in Geophysics, University of Washington, Seattle

Paper number 97GL03302.
0094-8534/98/97GL-03302$05.00

peratures determined from the OH(6-2) emission above Adelaide, Australia, *J. Atmos. Terr. Phys., 58*, 1337-1344, 1996.

Reisin, E. R., and J. Scheer, Characteristics of atmospheric waves in the tidal period range derived from zenith observations of O_2(0-1) Atmospheric and OH(6-2) airglow at lower midlatitudes, *J. Geophys. Res., 101*, 21223-21232, 1996.

Scheer, J., Programmable tilting filter spectrometer for studying gravity waves in the upper atmosphere, *Appl. Opt., 26*, 3077-3082, 1987.

Scheer, J., What can be learned from rotational temperatures derived from ground-based airglow observations about the aeronomy of the Southern Hemisphere, *Adv. Space Res., 16*, (5)61-(5)69, 1995.

Scheer, J. and E. R. Reisin, Rotational temperatures for OH and O_2 airglow bands measured simultaneously from El Leoncito (31°48'S), *J. Atmos. Terr. Phys., 52*, 47-57, 1990.

Scheer, J., E. R. Reisin, J. P. Espy, M. Bittner, H. H. Graef, D. Offermann, P. P. Ammosov, and V. M. Ignatyev, Large-scale structures in hydroxyl rotational temperatures during DYANA, *J. Atmos. Terr. Phys., 56*, 1701-1715, 1994.

Sivjee, G. G. and R. L. Walterscheid, Six-hour zonally symmetric tidal oscillations of the winter mesopause over South Pole Station, *Planet. Space Sci., 42*, 447-453, 1994.

Takahashi, H., B. R. Clemesha, and Y. Sahai, Nightglow OH (8-3) band intensities and rotational temperatures at 23°S, *Planet. Space Sci., 22*, 1323-1329, 1974.

Takahashi, H., Y. Sahai, B. R. Clemesha, P. P. Batista, and N. R. Teixeira, Diurnal and seasonal variations of the OH (8-3) airglow band and its correlation with OI 5577Å , *Planet. Space Sci., 25*, 541-547, 1977.

Takahashi, H., B. R. Clemesha, Y. Sahai, and P. P. Batista, Seasonal variations of the mesopause temperature observed at equatorial (4°S) and low (23°S) latitude stations, *Adv. Space Res., 14*, (9)97-(9)100, 1994.

Turnbull, D. N., and R. P. Lowe, New hydroxyl transition probabilities and their importance in airglow studies, *Planet. Space Sci., 37*, 723-738, 1989.

Williams, P. F. B., OH rotational temperatures at Davis, Antarctica, via a scanning spectrometer, *Planet. Space. Sci., 44*, 163-170, 1996.

P. L. Dyson, School of Physics, La Trobe University, Bundoora VIC 3083, Australia (e-mail: p.dyson@latrobe.edu.au)

P. A. Greet, Australian Antarctic Division, Kingston, Tasmania 7053, Australia (e-mail: pene_gre@antdiv.gov.au)

G. Hernandez, Graduate Program in Geophysics, Box 351650, University of Washington, Seattle, WA 98195-1650. (e-mail: hernandez@u.washington.edu)

E. R. Reisin, PRONARP, J. Alvarez 1218, 1414 Buenos Aires, Argentina (e-mail: ereisin@siscor.bibnal.edu.ar)

J. Scheer, PRONARP, J. Alvarez 1218, 1414 Buenos Aires, Argentina (e-mail: jurgen@caerce.edu.ar)

R. W. Smith, Geophysical Institute, University of Alaska, Fairbanks, AK 99775-7320 (e-mail: bblw@geewiz.gi.alaska.edu)

(Received April 18, 1997; revised November 4, 1997;
accepted November 6, 1997.)

GEOPHYSICAL RESEARCH LETTERS, VOL. 25, NO. 1, PAGE 23, JANUARY 1, 1998

Reply

J. H. Hecht, R. L. Walterscheid

The Aerospace Corporation, Los Angeles, California

J. Woithe, L. Campbell, R. A. Vincent, and I. M. Reid

Department of Physics and Mathematical Physics University of Adelaide, Adelaide, Australia

The Comment by Scheer et al. correctly brings to the readers attention previous works which measured temperature variations of emissions originating in the 80 to 100 km altitude region over the mid-latitude southern hemisphere and over season. Nevertheless, because of the predicted 10 km or greater seasonal variation in the altitude of the mesopause, from near 85 km at the summer solstice to near 100 km at the winter solstice [She et al., 1995], we believe that in order to measure seasonal temperature variations of the mesopause region three requirements must be met. First, at least two emissions must be measured, one from below 90 km, such as OH Meinel, and one from well above 90 km such as O_2 Atmospheric or OI(557.7 nm). Second, seasonal temperature variations can only be measured if data are obtained near or around the 3 seasonal periods where variations are predicted; the summer solstice, the winter solstice, and an equinox period [She et al., 1995]. A continuous series of measurements would be preferable so as to determine if the solstice/equinox measurements are representative of seasonal trends or are anomolous. Third the relative uncertainty of the measurements must be low enough so that it is reasonable to expect that such variations would be measured. Models predict temperature variations on the order of 10 K [She et al., 1995]. While the measurements in Hecht et al. [1997a] meet these criteria none of the references cited by Scheer et al. meet all three.

While the Abstract and Conclusions of Hecht et al [1997a] clearly stated that we were referring to the first seasonal measurements of the temperature variation of the mesopause region over the mid-latitude summer hemisphere, the discussion of Fig. 1 inadvertently left out the word seasonal. Because Hecht et al [1997a] addressed the seasonal aspects of our data we did not reference the many previous temperature measurements cited by Scheer et al. We were of course aware of many of these previous southern hemisphere temperature measurements, some of which originated from our group. We did not reference works that took place in Brazil or in the Antarctic since they are outside the scope of Hecht et al. [1997a]. In addition, space limitations in a GRL article do not permit unlimited and unnecessary referencing.

The conclusions of Hecht et al [1997a] with respect to temperature are (a) that there are periods where the temperature gradients exceed the model predictions, and (b) that the O_2 Atmospheric band temperatures are colder in winter and warmer in summer than expected. Scheer et al. imply that these conclusions may be affected by the uncertainties of up to 10 K in the absolute calibration of the OH Meinel and O_2 Atmospheric band temperature data reported on in Hecht et al. [1997a]. While we agree that such an uncertainty is possible, even if the extreme example of a 10 K error occurred this would only serve to shift each entire temperature curve up or down by a fixed amount. Such a shift would not affect the conclusions of Hecht et al [1997a].

However, there are ways of minimizing the absolute calibration errors referred to by Scheer et al. During 1993 the Aerospace imager was operated in Illinois in a manner similar to how it was operated in Australia [Hecht et al., 1997b]. In Illinois, comparisons were made between the OH Meinel and O_2 Atmospheric band temperatures derived from the imager data with those obtained from Na lidar data. The OH Meinel temperatures were within 7 K of the lidar results while the O_2 Atmospheric band temperatures were within 2 K. A 7 K adjustment was applied to the Australia OH temperature data. Thus we believe that the absolute calibration of the Australia temperature data are uncertain by less than 5 K.

Acknowledgments. This work was supported in part by NSF grant ATM 94-15779, by The Aerospace IR&D Program, and by The Australian Research Council.

References

Hecht, J. H., R. L. Walterscheid, J. Woithe, L. Campbell, R. A. Vincent, and I. M. Reid, Trends of airglow imager observations near Adelaide, Australia *Geophys. Res. Lett, 24*, 587-590, 1997a.

Hecht, J. H., R. L. Walterscheid, D. C. Fritts, J. R. Isler, D. C. Senft, C. S. Gardner, and S. J. Franke. Wave breaking signatures in OH airglow and sodium densities and temperatures 1. Airglow imaging, Na lidar, and MF radar observations, *J. Geophys. Res., 102*, 6655-6668, 1997b.

She, C. Y., J. R. Yu, D. A. Krueger, R.Roble, P. Keckhut, A. Hauchecorne, and M. L. Chanin, Vertical structure of the midlatitude temperature from stratosphere to mesopause, *Geophys. Res. Lett, 22*, 377-380, 1995.

J. H. Hecht and R. L. Walterscheid, The Aerospace Corporation, M2-266, P.O. Box 92957, Los Angeles, CA 90009. (e-mail jim_hecht@qmail2.aero.org)

L. Campbell, I. M. Reid, R. A. Vincent, and J. Woithe, Department of Physics and Mathematical Physics, University of Adelaide, Adelaide, Australia

(Received: May 5,1997; accepted: November 6, 1997)

Paper number 97GL03399.
0094-8534/98/97GL-03399$05.00

appendix

C

Analysis and interpretation of quasi-monochromatic gravity waves

This appendix contains a copy of the paper 'Analysis and interpretation of airglow and radar observations of quasi-monochromatic gravity waves in the upper mesosphere and lower thermosphere over Adelaide, Australia (35°S, 138°E)', by R. L. Walterscheid, J. H. Hecht, R. A. Vincent, I. M. Reid, J. Woithe and M. P. Hickey, published in *Journal of Atmospheric and Solar-Terrestrial Physics* **61**, 461–478, 1999.

PERGAMON

Journal of Atmospheric and Solar-Terrestrial Physics 61 (1999) 461–478

Journal of ATMOSPHERIC AND SOLAR-TERRESTRIAL PHYSICS

Analysis and interpretation of airglow and radar observations of quasi-monochromatic gravity waves in the upper mesosphere and lower thermosphere over Adelaide, Australia (35°S, 138°E)

R.L. Walterscheid[a,*], J.H. Hecht[a], R.A. Vincent[b], I.M. Reid[b], J. Woithe[b], M.P. Hickey[c]

[a] *Space and Environment Technology Center, The Aerospace Corporation, Los Angeles, CA, U.S.A.*
[b] *Department of Physics, University of Adelaide, Adelaide, Australia*
[c] *Kinard Laboratory, Department of Physics and Astronomy, Clemson University Clemson, SC, U.S.A.*

Received 3 August 1998; received in revised form 11 November 1998; accepted 1 December 1998

Abstract

Observations of wave-driven fluctuations in emissions from the OH Meinel (OHM) and O_2 Atmospheric band were made with a narrow-band airglow imager located at Adelaide, Australia (35S, 138E) during the period April 1995 to January 1996. Simultaneous wind measurements in the 80–100 km region were made with a co-located MF radar. The directionality of quasi-monochromatic (QM) waves in the mesopause region is found to be highly anisotropic, especially during the solstices. During the summer, small-scale QM waves in the airglow are predominately poleward propagating, while during winter they are predominately equatorward. The directionality inferred from a Stokes analysis applied to the radar data also indicates a strong N–S anisotropy in summer and winter, but whether propagation is from the north or south cannot be determined from the analysis. The directionality of the total wave field (which contains incoherent as well as coherent features) derived from a spectral analysis of the images shows a strong E–W component, whereas, an E–W component is essentially absent for QM waves. The prevalence of QM waves is also strongly seasonally dependent. The prevalence is greatest in the summer and the least in winter and correlates with the height of the mesopause; whether it is above or below the airglow layers. The height of the mesopause is significant because for nominal thermal structures it is associated with a steep gradient in the Brunt-Väisälä frequency that causes the base of a lower thermospheric thermal duct to be located in the vicinity of the mesopause. We interpret the QM waves as waves trapped in the lower thermosphere thermal duct or between the ground and the layer of evanescence above the duct. Zonal winds can deplete the thermal duct by limiting access to the duct or by negating the thermal trapping. Radar measurements of the prevailing zonal wind are consistent with depletion of zonally propagating waves. During winter, meridional winds in the upper mesophere and lower thermosphere are weak and have no significant effect on meridionally propagating waves. However, during summer the winds in the duct region can significantly enhance ducting of southward propagating waves. The observed directionality of the waves can be explained in terms of the prevailing wind at mesopause altitudes and the seasonal variation of distant sources.

1. Introduction

The appearance in airglow images of distinct wave-like features having one to several cycles seems to be a very common occurrence (Gardner and Taylor, 1997; Wu and Killeen, 1996; Swenson et al., 1995, Taylor et al., 1995a b). In accordance with common usage, we refer to these disturbances as quasi-monochromatic (QM) features even when they have as few as one cycle. QM airglow features were observed in ~75% of the all-sky broad-band images of OH Meinel airglow during some periods of a recent study reported by Wu and Killeen (1996). Why

* Corresponding author. Tel.: +1-310-336-7532;
e-mail: richard.walterscheid@aero.org

1364-6826/99/$ - see front matter
PII: S1364-6826(99)00002-4

QM features are so common is still an open question.

The prevalence of QM waves may be in large part an observational bias in favor of waves that have long vertical scales (and do not suffer strong cancellation effects) and have horizontal structure that is well-defined within the field of view (*fov*). We have found that wavenumber spectra of images that contain QM features typically do not show dominant spectral peaks at the observed QM wavelengths. Power is greatest at the longest resolvable scale and decreases with decreasing scale down to the noise floor (Hecht et al., 1994, 1995).

Even though QM features are not dominant they are obvious features of the data and can show up as enhancements in power spectra that have been flattened to remove the overall slope. The nature of these features is of interest. They have short horizontal wavelengths ($\lesssim 100$ km) and they have sufficiently long vertical wavelengths to avoid strong cancellation effects ($\gtrsim 10$ km), or are evanescent.

Waves with long vertical wavelengths are good candidates for ducted waves. Ducted waves are internal waves trapped between two evanescent regions or between an evanescent region and the ground and in the strongest sense exhibit some degree of resonance (Francis, 1973). Nonresonant waves cannot exist as permanent free waves and will decay without continuous forcing. However, trapping favors long-distant propagation whether or not the waves are resonant and we loosely refer to trapped internal waves as ducted. Fairly modest gradients in the background state can cause waves with long vertical wavelengths to be trapped by evanescence. They can be trapped by gradients in the Brunt-Väisälä frequency (N) or by wind shear or by both. Ducts where wave trapping is caused primarily by N gradients are thermal ducts, while ducts where trapping is caused primarily by wind gradients are Doppler ducts (Pitteway and Hines, 1965; Francis, 1973; Richmond, 1978; Schubert and Walterscheid, 1984; Chimonas and Hines, 1986; Wang and Tuan, 1988). A recent study by Isler et al. (1997) argues that Doppler ducting may explain a significant fraction of the QM events seen in all-sky images.

Wind shear can also have the opposite effect: it can diminish the trapping of waves in a thermal duct. Jones (1972) was the first to examine this effect. When there is a wind shear across a thermal duct the winds at the top or bottom of the duct (depending on the sense of the shear) can Doppler shift the wave away from evanescence. If the shear is strong enough, the thermal trapping can be annulled and ducting eliminated altogether.

Wind shear has its maximum effect when it is aligned with the direction of wave propagation. Waves propagating normal to the shear do not feel Doppler effects. Jones found that there is a range of allowed propagation azimuths for ducted waves that depends on the strength of the wind shear. As the shear increases, the range of permitted azimuths decreases. Propagation normal to the shear is always allowed. Similarly, Doppler ducting is azimuth sensitive, being greatest for wave propagation aligned with the flow and nil for propagation normal to the flow. Thus the directionality of ducted waves at a given location can be sensitive to the wind direction.

The purpose of this paper is to present the seasonal observations of small-scale QM waves made at Adelaide, Australia and discuss them in terms of wave sources and propagation, including the ducting concepts introduced above. The organization of the rest of the paper is as follows: in section 2 we discuss wave types and the corresponding domains of dependence for waves observed overhead at mesopause altitudes; in section 3 we present the theory of critically reflected waves; in section 4 we describe the instruments, data and analysis methods; in section 5 we present results; in section 6 we present full wave analysis of some numerical examples; in section 7 we discuss the results; and in section 8 we summarize our conclusions.

2. Waves in the mesopause region

Waves in the mesopause region, as elsewhere, may be internal or external (evanescent). The former may be vertically progressive or vertically standing. Standing waves are trapped waves. The sources of wave generation for ducted waves can be distant compared to the sources for internal waves that propagate freely without trapping.

We first examine the domain of dependence for a point in the mesopause region ignoring refractive effects. Ignoring wind shear and thermal gradients, an internal wave packet seen in an airglow layer at a height Z has traveled a horizontal distance X where X is related to Z by the relation

$$\frac{Z}{X}=\frac{w_g}{u_g}=-\frac{k}{m}\frac{m^2}{m^2+\dfrac{1}{4H^2}} \tag{1}$$

where u_g and w_g are, respectively, the horizontal and vertical group velocities k and m, respectively, are the horizontal and vertical wavenumbers ($k=2\pi/L_x$ and $m=2\pi/L_z$, where L_x and L_z are, respectively, the horizontal and vertical wavelengths). (Note: $m<0$ for upward energy transfer.) The quantity H is the scale height. Equation (1) was obtained from the approximate dispersion relation

$$m^2=\frac{N^2}{\hat{\omega}^2}k^2-k^2-\frac{1}{4H^2} \tag{2a}$$

$$\hat{\omega}=\omega-\mathbf{k}\cdot\bar{\mathbf{u}} \tag{2b}$$

where ω is wave frequency, $\mathbf{k}=(k, m)$, $\bar{\mathbf{u}}$ is the mean wind, and $\hat{\omega}$ is wave intrinsic frequency. There are two categories of waves for which X is very large for fixed Z:

waves for which $m \to 0$ and waves for which $m \to \infty$. The former category includes waves that have high intrinsic frequencies and large horizontal wavenumbers and are subject to strong refractive effects (including ducting) in realistic background atmospheres. In the large m (small wavelength) limit, waves are subject to very strong scale-dependent dissipation and should not propagate into the airglow region. In addition, the airglow response to these waves is suppressed because of strong cancellation effects and these waves should not be evident in airglow observations.

For waves that are more or less typical of internal gravity waves $m^2 \gg 1/4H^2$ and (1) gives

$$X = \frac{L_x}{L_z} Z \tag{3}$$

For L_x/L_z ratios in the range 10–10^2 (typical $\sim$ hour-period waves) and $Z \sim 100$ km, $X \sim 10^3$–10^4 km. Subject to dissipation, the fairly long-period waves can propagate long distances before reaching the mesopause region because the ray paths have shallow slopes. These waves are not representative of the QM waves contained within the *fov* of the airglow images.

Unless they experience strong refraction related to ducting, the observed QM waves should not have traveled great distances. Ignoring refraction, the minimum X for a given Z is obtained by solving $\partial(Z/X)/\partial m = 0$ for m, where Z/X is the slope of the wave-packet trajectory. This gives $m_{X_{\min}} = 1/(2H)$, whence

$$X_{\min} = \frac{L_x}{2\pi} \frac{Z}{H} \tag{4}$$

For typical airglow altitudes $Z \sim 90$ km and $H \sim 7$ km, giving $X_{\min} \sim 2L_x$. For waves resolved in the *fov* of the airglow imager $L_x < \sim 100$ km and $X_{\min} < \sim 200$ km. On the short wavelength side of $m_{X_{\min}}$, observability is limited to waves with vertical wavelengths that are comparable to or greater than the thickness of the emission layers. Equation (3) gives $X < \sim 1000$ km for layer thicknesses $\sim$10 km and $L_x < \sim 100$ km. On the long wavelength side of $m_{X_{\min}}$, observability is limited to waves that can penetrate the region of small N in the upper mesosphere (see below) without undue attenuation by evanescence. Thus, without significant refraction waves seen in the mesopause region overhead should mainly originate in the area $\sim$100–1000 km distant from the observation site.

Also of interest are the evanescent extensions of ducted waves. The lower boundary of the region in the lower thermosphere where thermal ducting can occur is formed in proximity to the mesopause. Figure 1 shows N^2 vs altitude for summer and winter for Adelaide based on the MSIS model (Hedin, 1991). Both profiles show a thick region of large values of N^2 in the lower thermosphere. On the bottom side, values of N^2 increase strongly upwards

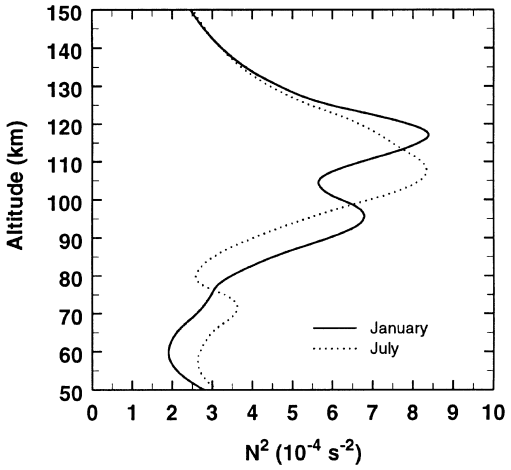

Fig. 1. Brunt–Väisälä frequency squared vs altitude for summer and winter for Adelaide based on the MSIS model (Hedin, 1991).

from a fairly thick layer of comparatively small values of N^2 in the upper mesosphere. The rapid bottom-side increase commences $\sim$85 km in winter and $\sim$10 km lower in summer. The vertical displacement with season roughly matches the vertical displacement of the mesopause; which is located $\sim$5–10 km above the bottom-side of the duct, depending on season.

During the winter months, the mesopause appears to be above the O_2 Atmospheric and OH Meinel (OHM) airglow layers. Nominally, the OHM layer peaks around 87 km and the O_2 Atmospheric layer peaks around 93 km, and both have full widths at half maximum of about 10 km, or less (Hecht et al., 1995). During the summer months, however, the mesopause is at or below 85 km and therefore is located below the centroid of the OHM layer and below essentially the entire O_2 Atmospheric layer (von Zahn et al., 1996). This means that during summer the airglow layers are almost totally (O_2 Atmospheric) or mostly (OHM) within the lower thermospheric thermal duct. During the winter both layers are below the duct.

Waves ducted in the lower thermosphere and strongly attenuated by evanescence below the duct should not have appreciable amplitudes in airglow layers situated well below the duct (e.g., OHM during winter). However, the results we will discuss below indicate that QM features are still common during the winter (though less common than during the summer), suggesting rather weak attenuation. This will be taken up in the section where we discuss critical reflection.

Henceforward, we refer to the region of large N in the lower thermosphere as the LT duct. This terminology will be used to denote the region where thermal ducting

can occur. Whether ducting actually occurs depends on wave properties and winds.

3. Critically reflected waves

In this section we present the theory of critically reflected waves. We consider ducted waves incident from above on an interface that represents the lower boundary of an idealized LT duct (see Fig. 2). The boundary separates two isothermal regions with different values of N. We denote the lower region as region 1 and the upper as region 2. Region 2 is within the duct. The subscripts I and R denote the incident and reflected waves, and T denotes the transmitted wave. The arrows show the direction of energy (group) propagation. In region 2

$$\hat{w}_2 = A_I e^{-im_2 z} + A_R e^{im_2 z} \tag{5}$$

where $w(x,z,t) = \hat{w}\ \exp\ i(\omega t - kx)\ \exp\ (z/2H)$ and w is the vertical velocity, x is the horizontal coordinate, z is the vertical coordinate, and H is the scale height. The boundary between regions 1 and 2 is located at $z = 0$. In region 1

$$\hat{w}_1 = A_T e^{-im_1 z} \tag{6}$$

The interface conditions are the continuity of w and $\mathrm{d}w/\mathrm{d}z$. This gives

$$(m_2^- - m_1^-)A_I = (m_2^+ + m_1^-)A_R \tag{7}$$

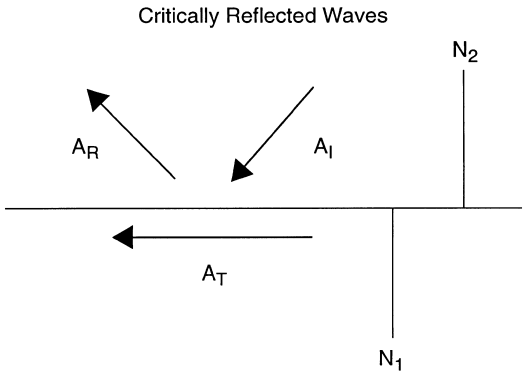

Fig. 2. Schematic for critically reflected waves. The figure shows a wave A_1 incident from above on an interface that represents the lower boundary of a thermal duct. The boundary separates two isothermal regions with different values of Brunt–Väisälä frequency denoted N_1 and N_2 in regions 1 and 2 respectively. Region 2 is within the duct. The symbols I and R denote the incident and reflected waves, and T denotes the transmitted wave. The arrows show the direction of energy (group) propagation.

where $m_i^{\pm} = m_i \mp i\alpha_i$, $\alpha_i = 1/2H_i$ and $i = 1, 2$. Equation (7) gives a reflection coefficient

$$R = \frac{|A_R|^2}{|A_I|^2} = \frac{|m_2 - m_1 + i(\alpha_2 - \alpha_1)|^2}{|m_2 + m_1 - i(\alpha_2 - \alpha_1)|^2}. \tag{8}$$

The reflection coefficient is unity (total reflection) for $m_1^2 \leqslant 0$. The wave is critically reflected when $m_1 = 0$. This occurs when the wave in region 1 is on the boundary of evanescence. (If region 1 is marginally evanescent and finite, near total reflection requires that the region be thick.) Among the waves that are totally reflected at the boundary of the duct, the attenuation of energy density in region 1 is least for critically reflected waves.

The incident wave that generates a critically reflected wave satisfies

$$m_2^2 = \frac{\delta N^2}{\omega^2} k^2 - \delta\left(\frac{1}{4H^2}\right) \tag{9}$$

where $\delta N^2 = N_2^2 - N_1^2$ and similarly for $\delta(1/4H^2)$. The quantity m_2^2 should be large enough for incident waves to fit in the LT duct. For ducts that are not too thick $m_2^2 \approx (N_2^2/\omega^2)k^2$. For critically reflected waves with values of ω and k more or less typical of the observed QM waves $m_2^2 \approx (\delta N^2/\omega^2)k^2$. This implies that if $N^2 \sim \delta N^2$ the waves that may be critically reflected are not too different from the waves that may be ducted. The profiles of N^2 shown in Fig. 1 indicate that a significant population of ducted waves may be close to critical reflection.

If the waves in the duct itself are QM waves, the evanescent extensions would also be QM waves. The greatest observed prevalence of ducted QM features should be in the duct, but QM features should appear in the airglow layers with an occurrence frequency that depends on how far below the duct the airglow layer is situated, and on the population of waves that is not too far from critical reflection.

4. Measurements and data analysis

In this section we describe the instrumentation for the airglow and wind observation, the data and the methods used to obtain the prevalence and directionality of traveling coherent structures in the mesopause region.

4.1. Airglow

The measurements reported on in this paper are from the data set described in Hecht et al. (1997). These measurements were obtained with the Aerospace CCD camera, described in Hecht et al. (1994), which was situated at the Buckland Park Field Station located approximately 40 km north of Adelaide, Australia (35 S, 138E) from April, 1995 to the end of January, 1996. The camera

operated in an autonomous mode taking data every night between sunset and sunrise during periods when the moon was no more than one hour above the horizon. Images of the OH Meinel (8430 Å) emission and the O_2 Atmospheric Band (8660 Å) emission were exposed for 1 min and taken approximately every 7 min during the night. These data were corrected for background contamination, mostly from starlight, by taking an exposure through a filter centered at 8570 Å (Hecht et al., 1994). The fov of the camera is slightly less than 100 by 100 km.

Good, cloud free data were obtained from over 50 clear nights, most of these within one week of new moon. Examination of the data image by image indicated that a total of 1837 O_2 images and 1858 OHM images were sufficiently free of clouds to be useful in the analysis. That is, clouds were not visible on the 8570 Å image and individual stars were seen to propagate in successive images. Clouds would be easily visible on the 8570 Å image due to reflections from man made light sources such as the city lights of nearby Adelaide.

The observed QM waves have characteristics consistent with those of Gardner and Taylor (1998) cited earlier. We found that typically the horizontal wavelengths were a few tens of kilometers while the measured phase speeds were typically $\sim$50–80 ms^{-1}. Observed periods of $\sim$5–20 min were typical.

Using these data, two different methods were used for calculating both the percentage of time waves observed, and their directionality. One method was a simple wave counting technique. First, the image was divided into octants; north (337.5 to 22.5°), northeast (22.5 to 67.5°), east (67.5 to 112.5°), southeast (112.5 to 157.5°), south (157.5 to 202.5°), southwest (202.5 to 247.5°), west (247.5 to 292.5°), and northwest (292.5 to 337.5°). If a discrete feature was seen to propagate between two successive frames it was counted as the presence of a wave on these two frames. The direction toward which the feature was propagating was judged by eye. The number observed was recorded for each of three seasonal periods (around the summer and winter solstices and the spring equinox) and for the entire observation period. The percentage of time waves were present was calculated by dividing the total in each direction by the total number of image frames for each period. These percentages therefore represented the fraction of the time discrete QM features were seen to travel toward a given direction.

The second technique relied on a spectral analysis of the data as discussed in Hecht et al. (1997). The power in any direction was calculated from a Fourier analysis in each image (Hecht et al., 1994, 1995). However, because this analysis is done in wavenumber for each image but not in frequency, there is a 180° ambiguity in the direction of the waves. The power for each image is calculated for four directions: north–south, east–west, southwest–northeast, and southeast–northwest. The first two are calculated from the (1,0) and (0,1) components of the Fourier transformed image. The power in the southwest–northeast direction is the sum of the power in the (1,1), (2,2), (2,1), and (1,2) Fourier components and the power for the southeast–northwest direction is the sum of the $(1,-1)$, $(2,-2)$, $(2,-1)$, and $(1,-2)$. In order to have as much power in the diagonal directions (southwest–northeast, and southeast–northwest) as in the north–south and east–west directions for an isotropic spectrum, the power in the diagonal directions was modified as follows. The 2D power spectrum for these images was observed to fall off as the 2D horizontal wave number raised to the -2.4 power (Hecht et al., 1997). Thus, the 1D power spectrum should fall off as the 1D wave number raised to the -1.4 power. This gives a weighting of 0.67 for each sum defining a diagonal so that if there were no preferred wave directionality on average the power in all four directions would be equal.

4.2. Radar

The radar results were taken with the Buckland Park MF radar operating in the spaced antenna mode. Wind measurements were taken continuously during the period of the imager observations, although equipment malfunctions and modifications to the antenna array meant that observations were not made from mid-September to early November 1995.

At night, winds were measured every 2 km in the 78–98 km height range with a nominal 2-min time resolution. Whether a wind value was recorded at a particular height and time depended on the presence of suitable scattering irregularities so that the effective sampling period was usually greater than 2 min.

In order to obtain information on the directions of wave propagation, the data were analyzed using the so-called Stokes method (Vincent and Fritts, 1987). This method makes use of the fact that gravity waves are transverse oscillations that are polarized such that the horizontal perturbation motions are aligned along the horizontal direction of propagation. The raw data at each height were high-pass filtered to remove periods longer than one hour and the mean square amplitudes for the zonal ($\overline{u'^2}$), meridional ($\overline{v'^2}$) wind components, and their covariance ($\overline{u'v'}$) computed. The Stokes method makes use of the total wave intensity, given by

$$I = \overline{u'^2} + \overline{v'^2} \tag{10}$$

the anisotropy factor

$$D = \overline{u'^2} - \overline{v'^2} \tag{11}$$

and the covariance term,

$$P = 2\overline{u'v'} \tag{12}$$

Waves propagating predominantly in the east–west (north–south) direction will give a D which is positive

(negative). The sign of P provides further information since positive (negative) values imply propagation in the NE/SW (NW/SE) quadrants. More quantitatively, the alignment, φ, of the mean perturbation motions is given by

$$2\varphi = \tan^{-1}(P/D) \tag{13}$$

where φ is measured counterclockwise from east. This also gives the predominant direction of propagation, with an uncertainty of 180°.

The directions were computed for each hour and the results grouped over two height ranges centered on the mean heights of the OHM and O_2 layers. Angular distributions with 30° bin sizes were then constructed for the summer and winter seasons.

5. Results

The data describe the directionality and monochromicity of waves in the upper mesosphere and lower thermosphere. There are three measures of directionality—two based on airglow images and the other on a Stokes analysis of radar data. One analysis of airglow imagery involves a two-dimensional Fourier analysis and gives the directionality of the total wave field (including QM and non-QM features) with a 180° ambiguity. The other analysis involves a visual inspection of images and gives the unambiguous directionality of QM features. Both techniques based on airglow images give directionality information for waves on the scale of the *fov*. The Stokes analysis of radar data gives the directionality of coherent features (not necessarily QM) irrespective of scale size. Each technique gives information on directionality as a function of altitude (emission) and season. Information on monochromicity is obtained from the inspection of the airglow images. This technique gives the frequency of occurrence of QM features that can be discerned in the images as a function of altitude and season.

5.1. Directionality

In this section we discuss the directionality of waves based on airglow and radar observations.

5.1.1. Airglow images

The difference between the two image-based techniques gives an indication of how the directionality of QM features differs from the directionality of the total wave field including coherent and incoherent non-QM features. Figures 3 and 4 are for OHM and show, respectively, the amplitude of the radial wavenumber 1 component (as defined above) of the horizontal wave number spectrum versus azimuth and a histogram of wave occurrence frequency versus azimuth. The results in Fig. 3 are subject to a 180° ambiguity, and for presentation purposes have been reflected so that points that differ by 180° represent the same information. The directions given in Fig. 4 refer to the direction toward which the waves are seen to propagate. Although this convention is destination rather than source oriented and the source of the waves is of greater interest, it is consistent with standard usage. Figures 3 (total wave field) and 4 (QM waves) show a very different directionality for the total wave field and QM waves. The QM wave field shows a much greater tendency for anisotropy (much less zonal propagation) and shows somewhat greater seasonality.

During the solstitial seasons, in particular, there is a very pronounced N–S anisotropy for the QM waves and a very strong seasonality (the designation N–S means north–south propagation with a 180° ambiguity, similarly for E–W). During the summer, QM waves propagate toward directions south of east and west (southpoleward) and in the winter they propagate northward (equatorward). The poleward anisotropy in summer is by far the stronger. By contrast, the total wave field exhibits a high degree of isotropy (subject to the 180° ambiguity) and, in particular, shows a significant E–W component. Whether the waves are all toward the west or all toward the east, or (most likely) something in between is indeterminate. The QM results for the spring equinox show an anisotropy favoring somewhat propagation toward the northeast.

The corresponding results for O_2 Atmospheric are shown in Figs 5 and 6. The results are similar to those shown in Figs 3 and 4. During the solstitial seasons, there is a very pronounced N–S anisotropy for the QM waves with a strong seasonality. During the summer the waves propagate toward directions south of E–W while in the winter they propagate toward directions north of E–W. The poleward anisotropy in summer is stronger. The total wave field shows a much higher degree of isotropy, with a significant E–W component. To the 180° indeterminacy, the total wave field in the O_2 Atmospheric layer is more or less isotropic.

5.1.2. Stokes analysis of radar data

Figures 7 and 8 show the results of the Stokes analysis for the summer and winter seasons. Each figure shows results of wave directionality in polar histogram form for two different altitude ranges (86–88 km and 92–96 km). The data have been normalized to the azimuth bin with the highest frequency of occurrence. The results of the Stokes analysis are ambiguous to 180°. No data were available for the spring season.

The results of the Stokes analysis are consistent with

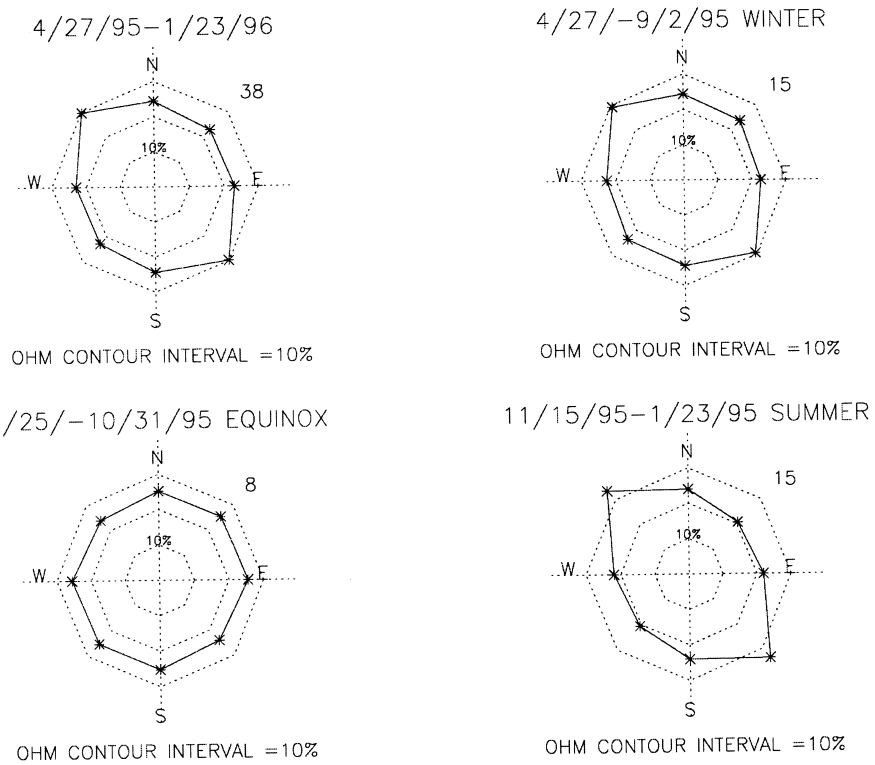

Fig. 3. The amplitude of the radial wavenumber 1 component of the horizontal wave number spectrum vs azimuth for OHM. The amplitude is normalized by the mean emission brightness. The results are subject to a 180° ambiguity and have been reflected so that points that differ by 180° represent the same information.

the results of the wave-counting analysis of QM waves described in the previous section. The direction of wave propagation is predominately N–S during the solstitial seasons. The anisotropy is greater in summer than winter and greater in the higher range of altitude than the lower. The altitude increase in anisotropy is more striking in winter when the lower range of altitudes is near the bottom boundary of the LT duct. In common with the QM results, the Stokes analysis applies to coherent features in the wave field. They differ in that the coherent features in the Stokes analysis do not have to be QM features and the scales of the Stokes analysis are not limited to those scales that can be defined over the *fov* of the airglow imager. However, the similarity in the results suggests that the phenomena described by the airglow QM analysis are closely related to, if not a subset of, the phenomena described by the Stokes analysis.

5.2. Monochromaticity

Figures 4 and 6 also indicate the number and frequency of occurrence of QM waves by season and for the total period of observation. These values are given in the upper right corner of each panel. One should not compare the frequency of occurrence for OHM and O_2 Atmospheric. The noise level is higher for the latter emission and a greater proportion of waves will not be apparent in O_2 Atmospheric images will not be apparent in OHM. In a similar vein, OHM is not noise-free and some weak waves may be obscured as well by noise in the OHM images. Therefore, it is the seasonal variation of the prevalence of QM features in the airglow, rather than the observed occurrence frequencies or their variation with emission layer, that has the greatest significance.

We note a strong seasonal variation for each emission. The greatest prevalence is in the summer solstice period, the least is in the winter solstice period and it is intermediate around the spring equinox. The results of Hecht et al. (1997) are consistent with the summertime mesopause being at or below the centroid altitude of the OHM layer and well below the O_2 Atmospheric airglow layer. Thus both layers are located in the lower thermospheric thermal duct during the summer. The wintertime mesopause is above the OHM layer and this layer, at least, is

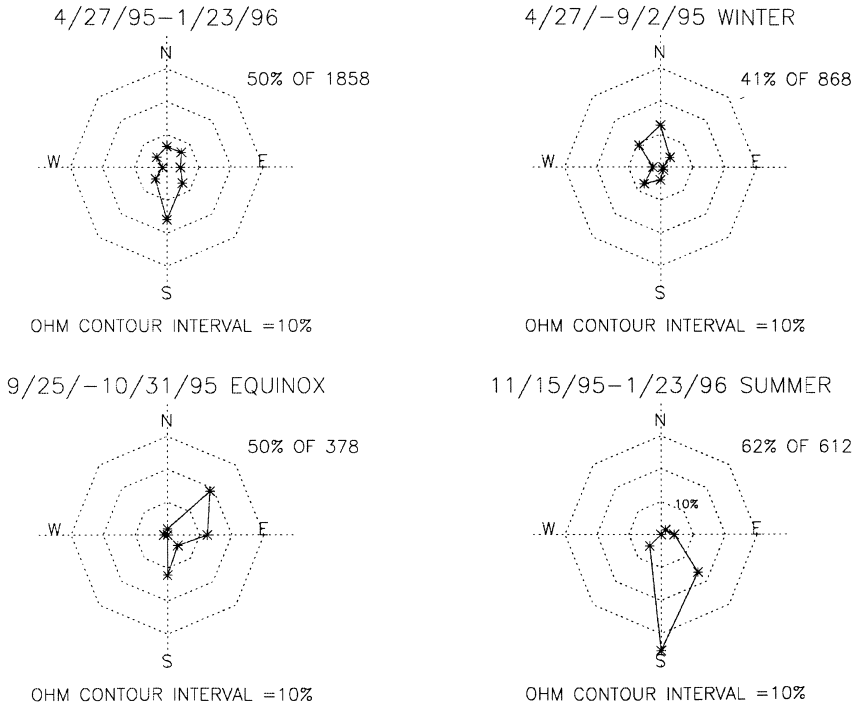

Fig. 4. Polar histogram of occurrence frequency vs azimuth for QM features seen in images of OHM. The directions refer to the directions towards which the waves are seen to propagate.

below the duct. The inferences of Hecht et al. (1997) are consistent with the results of Scheer and Reisin (1990), She et al. (1995) and von Zahn et al. (1996). Thus the frequency of QM waves correlates with the height of the mesopause and whether the waves in the airglow layers are within the lower thermospheric duct, or below it.

The seasonality does not appear to be a consequence of a seasonal variation in the background brightness. Hecht et al. (1997) show the intensities of the airglow as a function of time of year. The OHM brightness is constant to within 20%. There is no obvious summer to winter trend and for some periods the winter intensities are larger than the summer ones. The O_2 Atmospheric airglow is about 20% stronger than average in the summer, near average in the spring, and around 20% less intense in the winter. These trends do not correlate with the frequency of occurrence of the QM features.

For OHM, the day-to-day intensity variations can be much larger than the seasonal trend. Taken together these intensity trends do not support a significant observational bias in the OHM QM results due to seasonal intensity fluctuations. For O_2 Atmospheric there could be some bias, although the change in intensity from winter to spring is the same as the change from spring to summer. A bias could exist if there is some threshold level below which QM features could not be seen. However, since the same trend is seen in the OHM and O_2 Atmospheric data, the existence of such a threshold for the range of brightness levels experienced can be effectively ruled out.

Since the QM waves in OHM in winter are below the lower thermosphere duct they are not likely to have internal structure locally. They may be the evanescent tail of waves ducted in the lower thermosphere or waves ducted between the thermosphere and the ground (Makhlouf et al., 1998) or they may be the extensions of waves that are not too far from critical reflection and thus are minimally attenuated.

6. Full-wave modeling of waves and implications

We have performed numerical simulations of QM waves using a steady-state full-wave model. The simulations were performed for conditions that are more or less representative of the upper mesosphere and lower thermosphere over Adelaide. The model solves the linearized equations of motion for a plane rotating atmosphere subject to dissipation by molecular and eddy viscosity and heat conduction. The model is described in detail in Hickey et al. (1997, 1998). The basic-state tem-

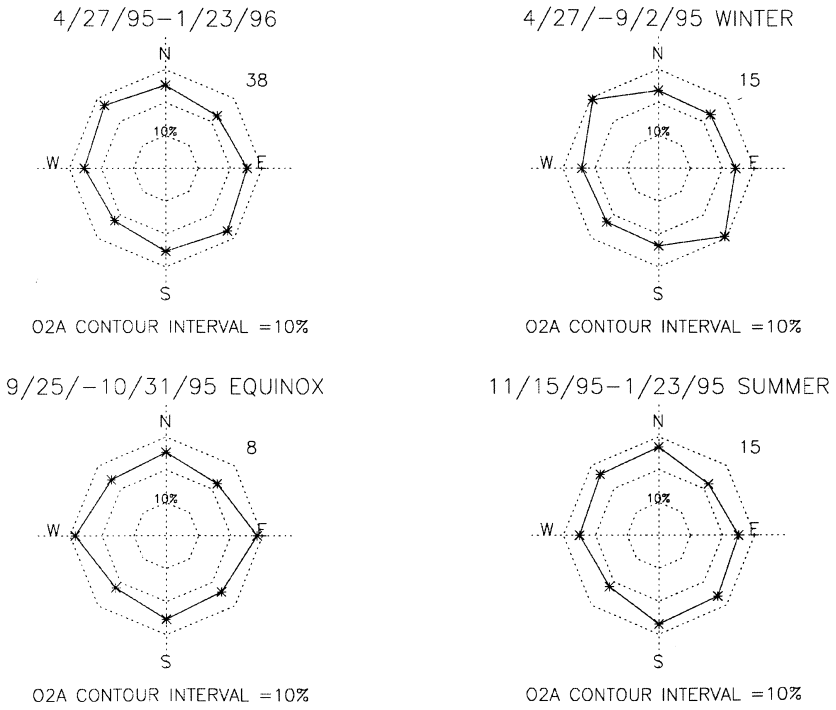

Fig. 5. Same as Fig. 3 except O_2 Atmospheric.

perature profile is defined using the MSIS-90 model (Hedin, 1991) and the winds were obtained by combining the radar-derived winds for Adelaide with the diurnally averaged Horizontal Wind Model (HWM-93) (Hedin, 1996). The radar winds are shown in Figs 9 and 10 for the altitude region 78–98 km for the winter and summer seasons, respectively. The radar winds and the HWM agreed well in the region of overlap. The winds used in the calculation are shown in Fig. 11. In winter, the profile is characterized by strong eastward winds in the mesosphere (with a peak wind of 70 ms^{-1} near 60 km) and fairly weak winds in the lower thermosphere. Compared to winter, the summer profile is characterized by weaker winds in the mesosphere (with a peak westward wind of 55 ms^{-1} near 60 km), but significantly stronger winds in the mesopause region and lower thermosphere, with a broad region of fairly strong westward winds in the LT duct and a shallower region of comparably strong eastward winds near its base. We remark that the simulations based on the basic-state described above do not represent numerical case studies of observed waves over Adelaide, they are meant to illustrate wave and wind effects for conditions more or less representative of the mesopause region over Adelaide.

Results are shown in two sets. The first set is for wave propagation opposite to the prevailing wind in the mesosphere: eastward propagation in summer and westward in winter. Propagation in this sense increases the intrinsic frequency in the mesophere and drives vertical structure toward evanescence, or toward yet stronger evanescence. The second set is for propagation in the direction of the prevailing wind in the mesosphere. Propagation in this sense decreases the intrinsic frequency in the mesophere and drives vertical structure toward vertical propagation, or toward freer propagation (toward smaller vertical wavelengths that are less sensitive to thermal gradients). The results for the first and second sets are shown in Figs 12 and 13, respectively.

Given the parameters of the wave, an approximate WKB vertical wavenumber can be calculated from the dispersion relation. The vertical wavenumber for wind and windless condition is shown for sets 1 and 2 in Fig. 14. The location of the base of the duct is a function of the refractive index, being located approximately where $m^2 = 0$.

All calculations are done for a wave period of 6 min, a horizontal phase speed of 75 ms^{-1} and horizontal wavelength of 27 km. These values are within the range of observed values. Figure 12(a) shows wave amplitude given by the square root of the kinetic energy density (kinetic energy density = mean density × perturbation velocity squared) and (b) shows the phase of the zonal

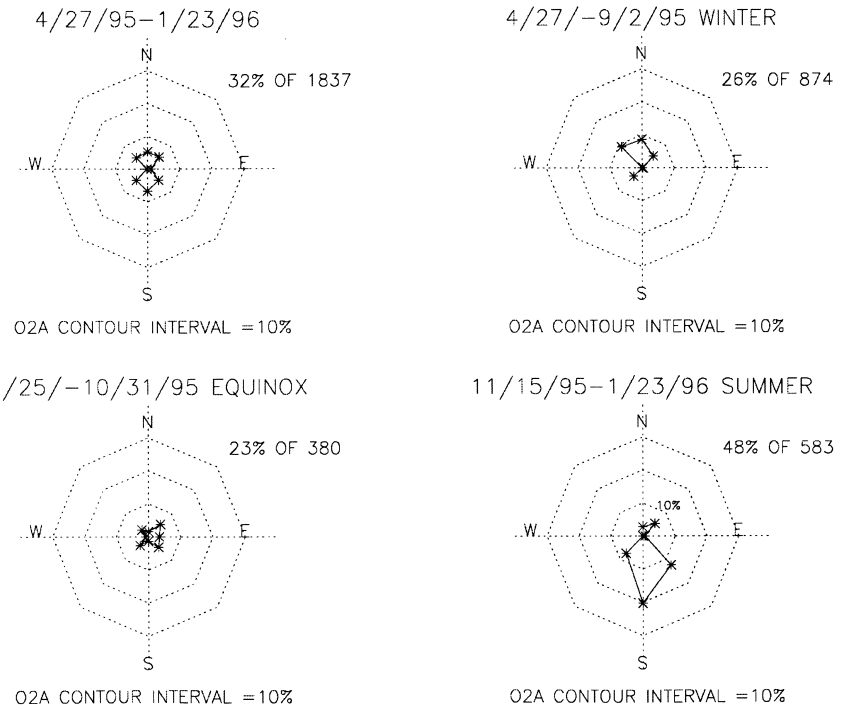

Fig. 6. Same as Fig. 4 except O_2 Atmospheric.

wind perturbation. The actual values of kinetic energy density are arbitrary and were normalized to the same value at 30 km. Four cases are shown: windless January case (solid curve), windless July case (dotted curve), mean-wind January case (dot-dashed curve) and mean-wind July case (dashed curve).

During summer the waves for the windless case show dominant internal standing wave structure between about 90 and 140 km and evanescent structure above and below this range, in agreement with where $m = 0$ (Fig. 14). During winter, the transition between internal and evanescent behavior near the mesopause occurs higher by about 10 km, reflecting the seasonal variation in the mesopause height. The evanescent decay below where $m^2 < 0$ occurs much lower in winter than summer. This downward penetration of the ducted wave is allowed by the fairly small values of m^2 in accordance with the critical reflection arguments given above. Thus, even though the OHM layer is largely below the winter duct, the occurrence of QM waves observed in winter can still be the manifestation of ducted waves. The phase variation during both seasons shows a progressive (untrapped) component in the LT duct. Because evanescence below the mesopause is weaker during winter the duct is leakier and the progressive component is larger.

The zonal winds for set 1 result in a severe reduction of amplitude in the duct. This occurs because the winds shift to m^2 larger negative values in the mesosphere, making the evanescence in this region stronger (Fig. 14a). This means that waves propagating up from below are severely attenuated through the mesosphere.

Figure 13 is the same as Fig. 12 except for set 2 wave propagation: propagation such that Doppler effects shift the waves away from evanescence in the mesosphere. The windless cases are repeated for reference. Relative to the windless case, the wave in summer shows stronger amplitudes and non-evanescent wave structure over a larger range of altitudes. The reason for this is evident in the variation of m^2 (Fig. 14b). For both winter and summer the region of evanescence in the mesosphere is gone.

In summer, the winds have also shifted m^2 away from evanescence on the topside of the duct. The result is much freer access to the lower thermosphere for waves propagating up from below and minimal trapping. This is seen by the phase rotation (as opposed to phase jumps) throughout the LT duct. The ability of the LT duct to support ducted waves in summer is severely diminished by the winds. This is a manifestation of the Jones effect limited to waves propagating eastward.

During winter, the phase behavior indicates that trapping is more effective. However, access to the lower thermosphere is limited by strong dissipation of the wave

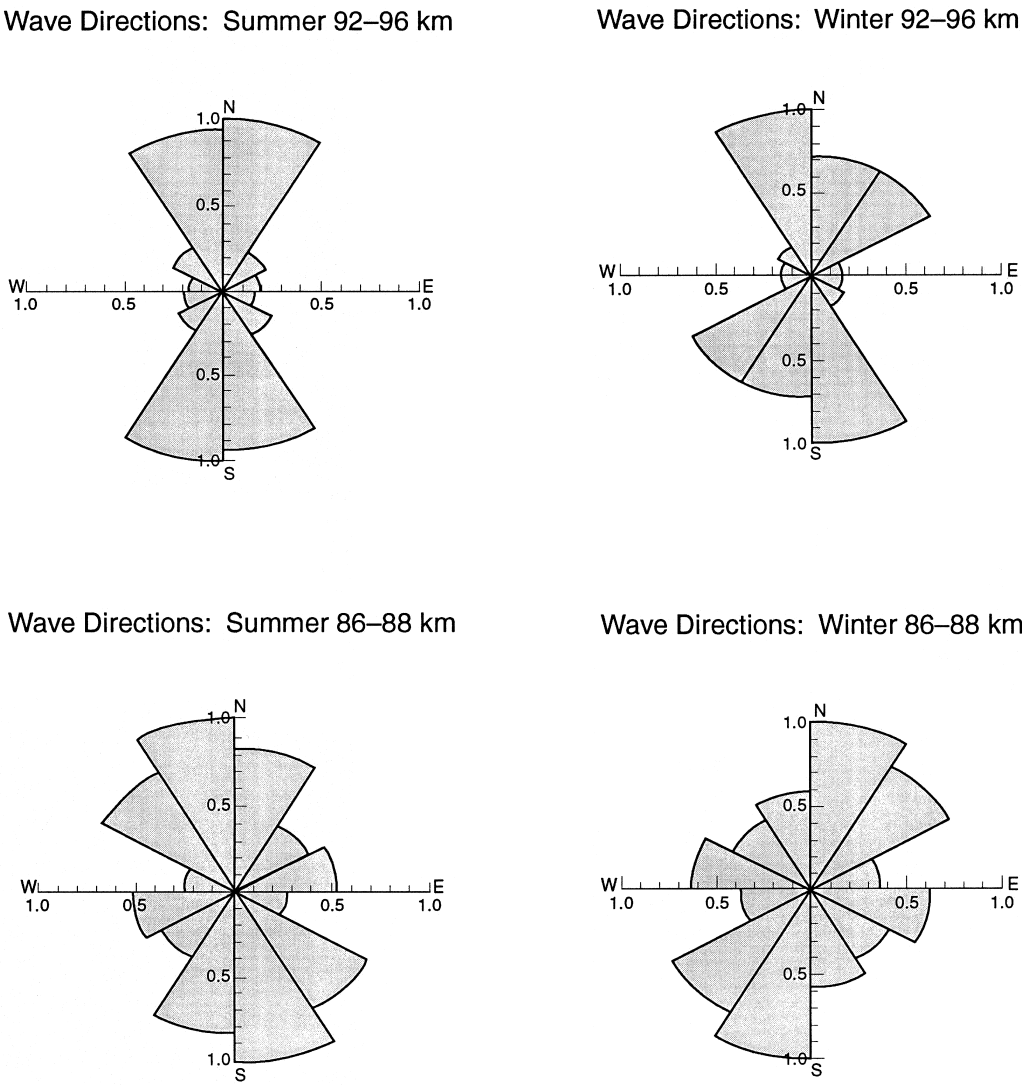

Fig. 7. Polar histogram of occurrence frequency vs azimuth for Stokes analysis for the summer seasons for two different altitude ranges (86–88 km and 92–96 km). The data have been normalized to the azimuth bin with the highest frequency of occurrence. The results are subject to a 180° ambiguity and have been reflected so that points that differ by 180° represent the same information.

Fig. 8. Same as Fig. 7 except winter.

through the mesospheric wind maximum. In this region the wave is Doppler shifted to very small phase speeds (~ 5 ms^{-1}) and very short vertical wavelengths (~ 2 km), with the result that the wave is strongly absorbed by scale-dependent dissipation. Somewhat slower waves would be filtered out by the combination of critical-level and viscous absorption. Wave filtering has been studied extensively by a number of authors (see for example, Taylor et al., 1993; Alexander 1998 and references therein).

The meridional mean radar winds (not shown) corresponding to the zonal winds shown in Figs 9 and 10 are small. In winter, the magnitudes are ~ 2–3 ms^{-1} and rather variable in direction (slightly northward). In summer they are more consistently northward (out of the summer pole) and peaking near 92 km with magnitudes 4–6 ms^{-1}. The HWM shows that in winter the meridional winds remain weak above the region covered by radar. In summer, the winds are 20 ms^{-1} southward at 115 km and about 25 ms^{-1} northward at 140 km, gradually

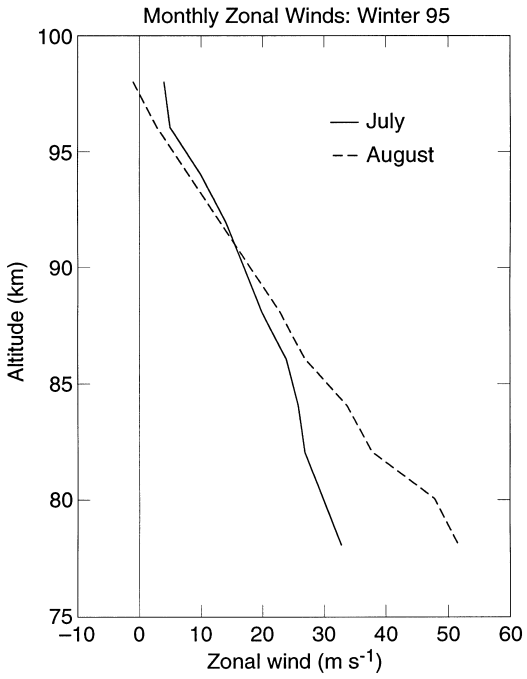

Fig. 9. Prevailing monthly zonal winds for winter 1995 for the altitude region 78–98 km based on radar measurements.

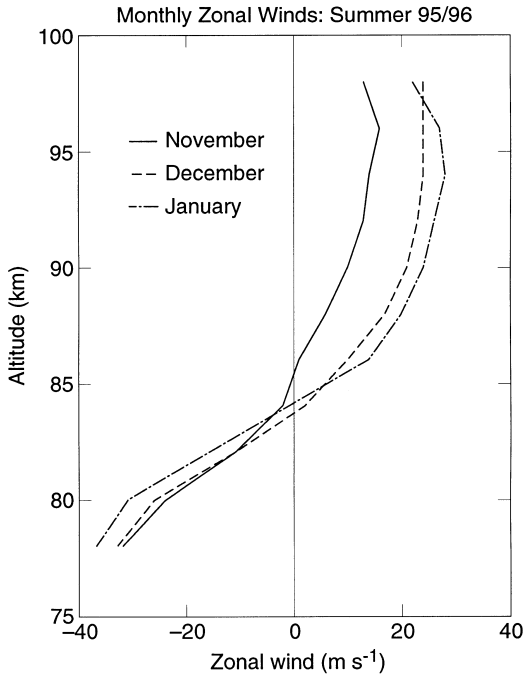

Fig. 10. Same as Fig. 9 except summer 1996.

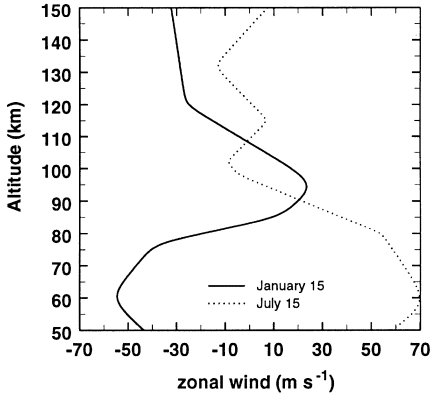

Fig. 11. Prevailing monthly zonal winds for winter 1995 for the altitude region 50–150 km based on the HWM model.

increasing to $\sim 50\ \mathrm{ms}^{-1}$ northward at 300 km. This combination strengthens the summertime duct for southward waves without limiting access to waves coming up from below.

6.1. Implications for ducting of QM waves

The full-wave results serve to indicate thermal and Doppler effects on trapping and filtering in the various atmospheric regions and to indicate the access of small scale waves to the airglow region. However, it should be noted that the results from the full-wave model are for forcing that is nonlocalized in space and time. On the other hand, the QM waves that we observe are localized. Localized waves have a finite residence time in atmospheric layers and, further, may not always self-interfere to give standing-wave behavior even when they are subject to strong reflection.

The prevalence of QM waves in the airglow region is clearly a function of their residence time in the region. A wave confined near the airglow layers has a much better chance of being observed in the airglow overhead than a wave that propagates freely through the region. A prolific local source of waves coupled with free access to the airglow region could populate the airglow region with QM waves. For distant sources, a small-scale wave that propagates freely through the lower thermosphere without reflection has no chance of being observed overhead in the mesopause region. The chances are better for a wave that is trapped in the region between the ground and the layer of evanescence above the LT duct, and best for a wave that is trapped near the airglow layers (e.g., in the LT duct).

The trapping of waves in the LT duct is facilitated by short periods and long horizontal wavelengths. The meridionally propagating QM waves we observe have periods typically ~ 10 min. Using (2) it is straightforward

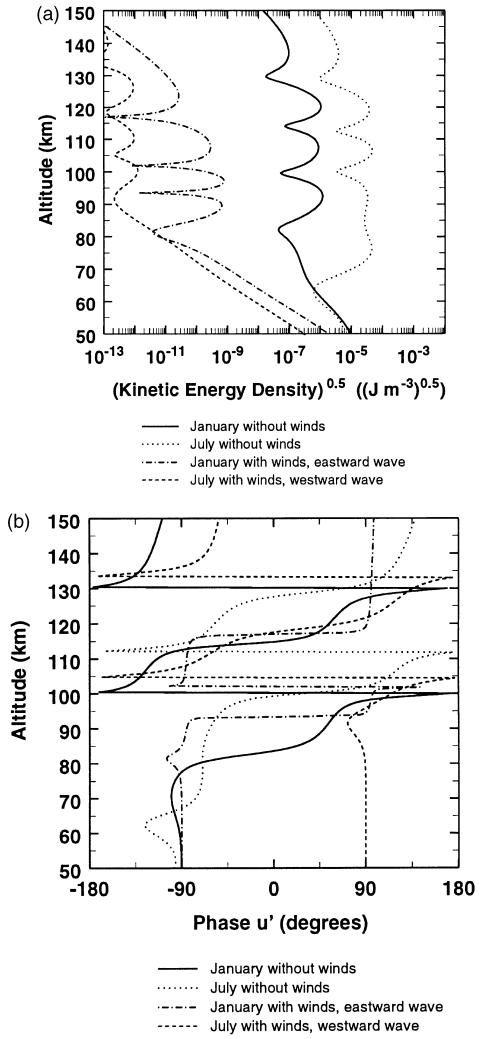

Fig. 12. Zonal wind perturbation amplitude (a) given in terms of the square root of kinetic energy density and phase; (b) for eastward and westward propagating waves with period 6 min and horizontal wavelength 27 km. Four cases are shown: windless January case (solid curve), windless July case (dotted curve), mean-wind January case with eastward propagation (dot-dashed curve) and mean-wind July case with westward propagation (dashed curve).

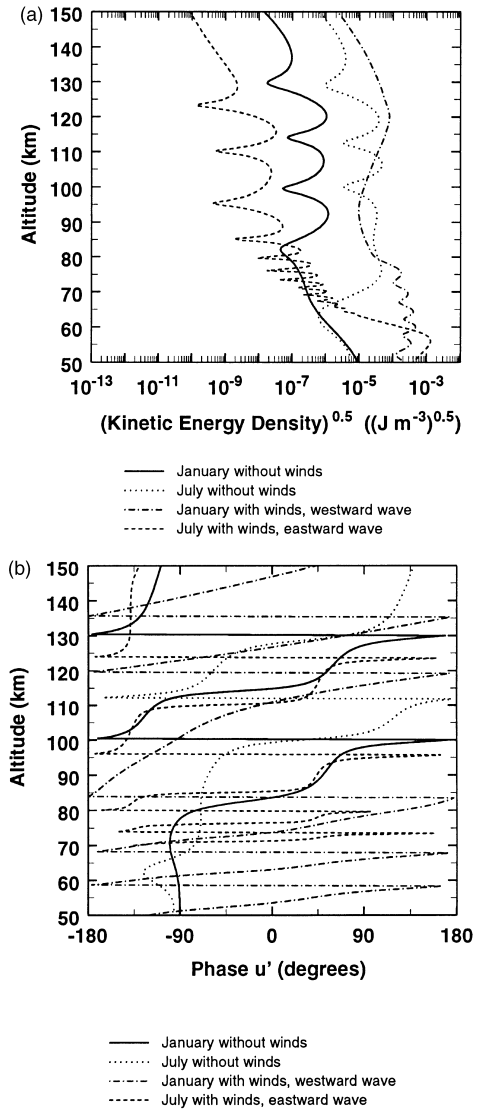

Fig. 13. Same as Fig. 12 except mean-wind January case with westward propagation (dot-dashed curve) and mean-wind July case with eastward propagation (dashed curve).

to show that under windless conditions these periods are near the upper end of the range of waves that may be trapped and seen within the *fov* of the imager. This was confirmed by model calculations for windless conditions. Thus the population of QM waves we observe in winter when meridional winds are weak could include waves trapped between the ground and the region of small values of N above the LT duct (Makhlouf et al., 1998).

In summer, trapping of southward propagating waves is aided by the southward meridional winds in the LT duct and the fairly strong northward winds higher in the thermosphere mentioned earlier. Model simulations with these meridional winds show stronger trapping for southward propagating waves with $\sim$10 min period. This is

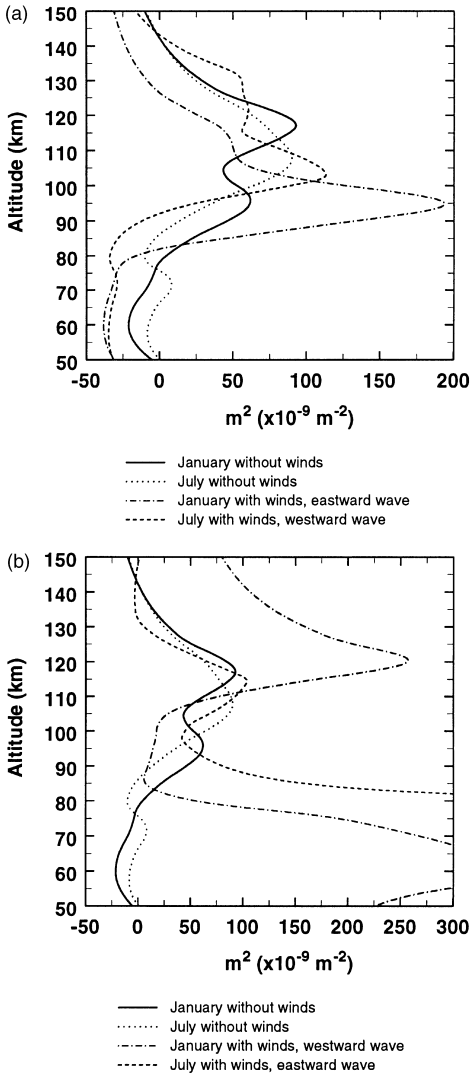

Fig. 14. Refractive index squared vs altitude for waves shown in Figs 12(a) and 13(b).

an example of increased trapping due to the combined effects of Doppler and thermal ducting (Chimonas and Hines, 1986). Thus, the proportion of QM waves that are trapped in the LT duct is likely to be greater in summer than winter.

6.2. Implications for directionality of QM waves

Zonally propagating small-scale waves from distant sources are not likely to be seen above Adelaide during the solstices. When propagation is with the wind, slower waves will suffer absorption in the mesosphere and waves that have free access to the duct will not be trapped. When propagation is against the wind, trapping can occur, but access to the duct is limited by increased evanescence in the upper mesosphere. When small-scale waves have free access to the thermosphere because of the zonal winds, the airglow layers can be populated by locally generated waves. During the summer (see below) there is a paucity of sources nearby. During the winter, the observing limitations for airglow (clear overhead) may help explain the near absence of zonally propagating QM waves. However, the radar has no such limitation. The radar observations show a dominance of N–S propagation, but do show a greater degree of E–W propagation at OHM altitudes for winter than is reflected in the airglow observations. Overall, windless conditions appear more favorable than solstitial zonal winds for the occurrence of distantly generated small-scale waves over Adelaide. In winter, the meridional winds are weak and propagation resembles windless conditions. In summer the meridional winds strengthen the trapping of southward propagating waves. We believe that this helps explain the strong summer and winter anisotropy in favor of N–S propagating QM waves, i.e., waves propagating approximately normal to the strong prevailing zonal winds in the upper mesosphere and lower thermosphere.

As mentioned, the absorption of zonally propagating waves in the zonal winds below the airglow layers plays a role in explaining the N–S anisotropy in QM waves. However, some waves are too fast to suffer critical-level and viscous absorption. Moreover, the total wave field (Fig. 3) does not show the extreme filtering of E–W propagating waves seen in QM waves, and we do not believe that this filtering alone can produce the strong N–S QM anisotropy. The effects of winds in diminishing thermal trapping and strengthening evanescent attenuation in the upper mesosphere also play a role.

The reversal of the direction of propagation from poleward in the summer to equatorward in the winter is not explained by zonal wind effects; wave propagation in either direction is insensitive to the zonal wind. The summer to winter reversal is most likely explained in terms of the seasonal variation in the location of sources of ducted waves.

It might be argued that apart from wave filtering the location of the sources alone might explain the directionality. However, this does not explain the difference between the directionality of the total field and QM features. There is a significant source of E–W waves for the total wave field and it seems likely that there would also be a source for E-W QM waves. There is a significant E–W component during the spring when climatologically the zonal winds are weak (Hedin, 1996). The fact that QM E–W waves are virtually absent during periods of strong zonal winds argues that the effects of the zonal wind on wave reflection in the upper mesosphere are significant.

6.3. Implications for seasonality of wave occurrence frequency

The wintertime OHM layer is not in the duct, yet the occurrence frequency of QM waves seen in the OHM airglow is still far from nil, being only about one third less frequent in winter. The wintertime QM waves are plausibly evanescent extensions of waves in the lower thermospheric duct. We suggest that a large fraction of the ducted waves are not too far from critical reflection and are only weakly attenuated by evanescence between the duct and the airglow layers. This possibility is made viable by (8), our numerical simulations and the fact that a significant population of trapped QM waves should be near critical reflection.

7. Discussion

The directionality of QM waves in the mesopause region is highly anisotropic, especially during the solstices, and highly seasonally dependent. During the summer QM waves in the airglow are predominately poleward propagating, while during winter they are predominately equatorward. The directionality inferred from the Stokes analysis also indicates a strong N–S anisotropy in summer and winter, but whether the direction is from the north or south cannot be determined from the analysis. The total wave field, which contains the incoherent continuum as well as coherent features, shows a different directionality. Most notably, the total wave directionality derived from spectral analysis of the images shows a strong E–W component, whereas, an E–W component is essentially absent for QM waves. The Stokes analysis also shows a significant E–W component in winter

The occurrence frequency of QM is also strongly seasonally dependent, being greatest in summer, least in winter and intermediate in springtime. The occurrence frequency correlates with the height of the mesopause and whether it is above or below the airglow layers. The height of the mesopause is significant because for nominal mesopause structures it is associated with a steep gradient in the N frequency that causes the base of the LT duct to be located in the vicinity of the mesopause. During the summer, the mesopause is low and is located below the OHM layer, while during the winter it is above or near the O_2 Atmospheric layer. Thus, during summer the QM waves are in the duct, while during winter they are below.

7.1. Wave sources

The most prolific source of wave generation north of Adelaide during the summer is apt to be the extensive region of deep cumulus convection over northern Australia $\sim$2500 km to the north associated with the southpoleward displacement of the inter-tropical convergence zone (ITCZ). There is little activity over southern and central Australia during the summer. During the winter the most prolific source of waves is apt to be regions of unsettled weather in high southern latitudes over and near Antarctica. This is consistent with the results of Allen and Vincent (1995) who found that the seasonal variation of stratospheric wave energy density has a low-latitude summer maximum and a middle-latitude winter maximum. They show the stronger wave activity over the northern parts of Australia associated with the monsoon. As Alexander (1998) notes, this kind of seasonal variation cannot be accounted for by filtering effects and appears to be source (i.e., convection) related. We rule out significant local sources for the observed QM waves during the solstices. While wind effects could explain a N–S anisotropy for waves generated fairly nearby, we are aware of no nearby sources that would also plausibly explain the extreme change from strongly poleward propagation in summer to equatorward in winter.

7.2. Wave ducting

We interpret the observed QM waves as ducted (trapped) waves. First, the waves that we observe are in the frequency and horizontal wavenumber regime of waves that are most readily ducted by thermal structure: those with short horizontal wavelengths and short periods. Second, the waves are observed in and near the LT thermal duct. Third, the prevalence of the waves correlates with whether they are in the duct or below it (however, this is complicated by the seasonal variation in sources). Also, the anisotropy as measured by the Stokes analysis increases toward the center of the duct. The increase is much greater in winter, when the lower of the two altitude ranges considered was close to the bottom boundary of the duct.

Fourth, and perhaps most significantly, the observed prevalence and directionality of small-scale QM disturbances at mesopause altitudes, especially during summer, is hard to explain without some wave guiding related to ducting. For QM waves to be seen in the observations over Adelaide, the source region would have to be in the domain of dependence of the mesopause region over Adelaide. As mentioned, the observed anisotropy and seasonality of wave directionality are difficult to reconcile in terms of local sources. On the other hand, without strong refractive effects the convective summertime source, in particular, is not within the domain of dependence (see (1)–(4) and the accompanying discussion). Overly strong refraction would deny access to the mesopause altogether. Insufficiently strong refraction would cause the waves to propagate through the mesopause region before they reached Adelaide. Long-distance propagation with access to the mesosphere over

Adelaide strongly suggests the influence of wave trapping and guidance related to ducting.

In traveling from the source to the point of observation, waves are subject to attenuation by geometric spreading into three dimensions and by dispersion and dissipation. It is difficult to understand how small-scale QM waves excited at large distances could arrive at Adelaide with significant amplitudes without strong forcing and strong trapping, and perhaps some degree of tuning. Most meteorological variability capable of wave generation is on time and space scales much longer than those of small-scale short-period QM waves. However, the convective summertime source may be a strong generator of small-scale QM waves (Alexander, 1996).

QM waves might originate from regions of more-or-less incoherent broadband forcing. To produce coherent QM waves, selective amplification of frequency-wavenumber components within the frequency-wavenumber band of the disturbance is required. Selective amplification of this nature requires the existence of ducts that are tuned to some degree to the frequency-wavenumber band of the QM wave.

7.3. Tidal effects

As with the prevailing wind, tidal winds can increase or decrease the observability of QM waves in the mesopause region. Perhaps the most problematical aspect of long-distance north–south propagation in the LT duct is the effect of meridional tidal winds in the regions of small N above and below the duct. Tides also have an effect on the thermal structure of the LT duct, but these effects should not be as important as the Doppler effects due to the tidal winds. If the winds are sufficiently strong in the regions of low N they can annul the effects of thermal ducting. This is especially true for waves generated in the north at low latitudes. The regions of summertime convection in northern Australia are not too far equatorward of where the diurnal meridional wind in the mesosphere is maximum. Because the most readily ducted waves (those with large vertical wavelengths) can follow long oblique paths with shallow slopes (subject to refractive effects), a substantial fraction of these waves may gain access to the duct some distance poleward of where the diurnal wind is maximum. Also, the diurnal tide propagating up from below does not attain its maximum amplitude in the main part of the low-N region below the LT duct and is heavily damped before it reaches the low-N region above the duct; while the tide generated higher in the thermosphere has its maximum amplitudes well above the LT duct (Forbes, 1990 and references therein; Hecht et al., 1998; McLandress et al., 1986a,b). The effects of the semidiurnal tide are also significant, but tidal wind effects on meridional propagation in the LT duct should not be too severe, especially away from low latitudes (Hedin, 1996).

7.4. Data limitations and future work

We have argued that the directionality, prevalence and seasonality of the observed QM waves is consistent with an interpretation in terms of ducted waves. A definitive interpretation of the nature of the QM waves would involve knowledge of the vertical structure of waves and detailed knowledge of the thermal and wind structure along with wave propagation properties (period, direction, and horizontal wavelength). Knowledge of wave vertical structure indicates whether the wave is standing, evanescent, or freely propagating and knowledge of the wave background and properties gives an indication of whether a standing wave is resonant. Airglow data can give information on wave structure, in addition to information on wave propagation properties. A necessary condition for a ducted wave is wave trapping. When this gives standing waves, the phase relation between temperature and airglow emission fluctuations in a layer can be used as a diagnostic for ducted waves (Hines and Tarasick, 1994; Makhlouf et al., 1995, 1998). Temperature and intensity should be either in phase or in anti-phase. For emissions coming from different layers, trapping is indicated if the layer temperatures are in phase or in anti-phase. However, localized waves, as mentioned, can be trapped without necessarily self-interfering to give standing waves.

With the airglow instrument used in this study, standing wave behavior for small-scale QM waves could not be deduced from temperature measurements. This is because it was not possible to image temperature with enough signal to noise to distinguish QM temperature waves. Furthermore, there is about a 1–2-min time difference between images of intensity of the same airglow emission. This is a significant fraction of the period for some of the higher frequency QM features and introduces a significant phase difference between images. Therefore, dividing two intensity images to get a temperature image would introduce a significant error. It would be useful to develop airglow imagers which can image temperature on a much faster time scale.

Using the intensity of the emissions alone can involve serious ambiguities because chemical as well as dynamical effects can contribute to the phase difference between emissions. Furthermore, there is about a 1–2-min time difference between images of intensity for the different airglow emission. This can introduce a large difference between emissions for the faster QM waves observed. Also, in a visual examination of a given image it is difficult to accurately characterize the phase. The complications of chemistry and experimental uncertainties make the analysis of the present data set for direct evidence of standing wave behavior infeasible.

We suggest similar studies for different locations. A clear and consistent relationship between the seasonality of QM features and distant sources would provide strong

support for a ducting interpretation for small-scale QM waves. Also, we suggest the addition of temperature lidars to the instrument complement whenever possible. With winds and temperatures it should be possible to determine from modeling whether the QM waves observed in the airglow are consistent with ducted waves.

8. Conclusions

Observations of the mesopause region over Adelaide have shown a N–S anisotropy in the directionality of atmospheric gravity waves as detected by an airglow imager and an MF radar. In addition, the airglow imager data show that small scale (a few tens of kilometers horizontal wavelength) QM gravity waves propagate predominantly poleward in summer and equatorward in winter. We rule out local sources because it is implausible that local sources would produce the observed anisotropy and its seasonality. During summer when the anisotropy is most pronounced there is a paucity of sources close to Adelaide. Also because of the paucity of sources over the interior of Australia in the summer, it is likely that the QM waves in summer originate in the region of deep convection several thousands kilometers to the north. Since freely propagating small-scale gravity waves would travel a much smaller distance from the source than this before reaching the mesopause region, it is likely that the QM waves observed in this study have been strongly refracted by variations in the background atmosphere. The temperature structure in the lower thermosphere forms a thermal duct whose lower boundary is formed in proximity to the mesopause. As the mesopause is below the airglow region in summer and there is a prolific source of gravity waves in northern Australia in the summer, we argue that the observed summertime QM waves are trapped (ducted) waves originating in the region of convection far to the north.

To explore the thermal and Doppler effects on small-scale waves in the upper mesosphere and lower thermosphere a full-wave analysis was performed. It was found that zonal winds tend to either destroy the duct or greatly restrict access to the duct. The former is related to the Jones effect (Jones, 1972), whereby winds can detune a thermal duct. This effect can allow locally generated free access to the mesopause region. Increased access is at the expense of the residence time in the duct, decreasing the probability of seeing a given distantly generated wave in the mesopause region overhead. The Jones effect contributes along with other wind effects (attenuation by critical-levels, and wind-enhanced viscous absorption, wave breakdown and evanescence) to a viable explanation for the near absence of E–W propagating QM waves during both summer and winter. Meridionally propagating QM waves are not similarly affected because the meridional winds are much weaker than zonal winds below the thermal duct. Meridional winds in the lower thermosphere were found to increase the ducting of poleward waves in the summer, helping to explain the observed extreme N–S anisotropy, and have little effect on the duct in winter (Chimonas and Hines, 1986). In winter the observed equatorward travelling waves may be the evanescent tails of ducted waves from storm systems to the south of Adelaide.

Acknowledgments

Work at the Aerospace Corporation was supported by NASA Grants NAGW-2887 and NAG5-4528 and by NSF Grant ATM-9714648. Work at Clemson University was supported by NASA Grant NAG5-4762 and by NSF Grants ATM-9612819 and ATM-9711341. The support of the Australian Research Council for research by the University of Adelaide is acknowledged.

References

Allen, S.J., Vincent, R.A., 1995. Gravity wave activity in the lower stratosphere: Seasonal and latitudinal variations. J. Geophys. Res. 100, 1327–1350.

Alexander, M.J., 1996. A simulated spectrum of convectively generated gravity waves: Propagation from the tropopause to the mesopause and the effects on the middle atmosphere. J. of Geophys. Res. 101, 1571–1588.

Alexander, M.J., 1998. Interpretations of observed climatological patterns in stratospheric gravity wave variance. J. of Geophys. Res. 103, 8627–8640.

Chimonas, G., Hines, C.O., 1986. Doppler ducting of atmospheric gravity waves. J. Geophys. Res. 91, 1219–1230.

Forbes, J.M., 1990. Atmospheric tides between 80 and 120 km. Adv. Space Res. 10, 127–140.

Francis, S.H., 1973. Acoustic-gravity modes and large-scale traveling ionospheric disturbances of a realistic, dissipative atmosphere. J. Geophys. Res. 78, 2278–2301.

Gardner, C.S., Taylor, M.J., 1998. Observational limits for lidar, radar, and airglow imager measurements of gravity wave parameters. J. Geophys. Res. 103, 6327–6437.

Hecht, J.H., Walterscheid, R.L., Ross, M.N., 1994. First Measurements of the 2D Horizontal Wave Number Spectrum from CCD Images of the Nightglow. J. Geophys. Res. 99, 11449–11460.

Hecht, J.H., Ramsay Howat, S.K., Walterscheid, R.L., Isler, J.R., 1995. Observations of Spectra of Intensity Fluctuations of the OH Meinel Nightglow During ALOHA 93. Geophys. Res. Lett. 22, 2873–2876.

Hecht, J.H., Walterscheid, R.L., Woithe, J., Campbell, L., Vincent, R.A., Reid, I.M., 1997. Trends of Airglow Imager Observations Near Adelaide, Australia. Geophys. Res. Lett. 24, 587–590.

Hecht, J.H., Walterscheid, R.L., Roble, R.G., Lieberman, R.S., Talaat, E.R., Ramsey Howat, S.K., Lowe, R.P., Turnbull, D.N., Gardner, C.S., States, R., Dao, P.D., 1998. A comparison of atmospheric tides inferred from observations at the

mesopause during ALOHA-93 with the model predictions of the TIME-GCM. J. Geophys. Res. 103, 630–6312.

Hedin, A.E., 1991. Extension of the MSIS thermosphere model into the middle and lower atmosphere. J. Geophys. Res. 96, 1159.

Hedin, A.E., Fleming, E.L., Manson, A.H., Schmidlin, F.J., Avery, S.K., Clark, R.R., Franke, S.J., Fraser, G.J., Tsuda, T., Vial, F., Vincent, R.A., 1996. Empirical wind model for the upper, middle and lower atmosphere. J. Atmos. Terr. Phys. 58, 1421.

Hickey, M.P., Walterscheid, R.L., Taylor, M.J., Ward, W., Schubert, G., Zhou, Q., Garcia, F., Kelley, M.C., Shepherd, G.G., 1997. Numerical Simulations of Gravity Waves Imaged Over Arecibo During the 10-Day January 1993 Campaign. J. Geophys. Res. 102, 11,475–11,489.

Hickey, M.P., Taylor, M.J., Gardner, C.S., Gibbons, C.R., 1998. Full-wave modeling of small-scale gravity waves using Airborne Lidar and Observations of the Hawaiian Airglow (ALOHA-93) O(^{1}S) images and coincident Na wind/temperature lidar measurements. J. Geophys. Res. 103, 6439–6453.

Hines, C.O., Tarasick, D.W., 1994. Airglow response to vertically standing gravity waves. Geophys. Res. Lett. 21, 2729.

Isler, J.R., Taylor, M.J., Fritts, D.C., 1997. Observational evidence of wave ducting and evanescence in the mesosphere. J. Geophys. Res. 102, 26,301–26,313.

Jones, W.L., 1972. Ducting of Internal Gravity Waves on a Stable Layer with Shear. J. Geophys. Res. 77, 3879–3885.

Makhlouf, U.B., Picard, R.H., Winick, J.R., 1995. Photochemical-dynamical modeling of the measured response of airglow to gravity waves. 1. Basic model for OH airglow. J. Geophys. Res. 100, 11,289–11,311.

Makhlouf, U.B., Picard, R.H., Winick, J.R., Tuan, T.F., 1995. A model for the response of the atomic oxygen 557.7 nm and the OH Meinel airglow to atmospheric gravity waves in a realistic atmosphere. J. Geophys. Res. 103, 6261–6269.

McLandress, C., Shepherd, G.G., Solheim, B.H., 1996a. Satellite observations of thermospheric tides: Results from the wind imaging interferometer on UARS. J. Geophys. Res. 101, 4093–4114.

McLandress, C., Shepherd, G.G., Solheim, B.H., Burrage, M.D., Hays, P.B., Skinner, W.R., 1996b. Combined mesosphere/thermosphere winds using WINDII and HRDI data from the Upper Atmosphere Research Satellite. J. Geophys. Res. 101, 10,441–10,453.

Pitteway, M.L.V., Hines, C.O., 1965. The reflection and ducting of atmospheric acoustic-gravity waves. Canadian J. Phys., 43, 2222–2245.

Richmond, A.D., 1978. The nature of gravity wave ducting in the thermosphere. J. Geophys. Res. 83, 1385–1389.

She, C.Y., Yu, J.R., Krueger, D.A., Roble, R., Keckhut, P., Hauchecorne, A., Chanin, M.L., 1995. Vertical structure of the midlatitude temperature from stratosphere to mesopause. Geophys. Res. Lett. 22, 377–380.

Scheer, J.E., Reisin, E.R., 1990. Rotational temperatures for OH and O2 airglow bands measured simultaneously from El Leoncito (31°48'S). J. Atmos. Terr. Phys. 52, 47–57.

Schubert, G., Walterscheid, R.L., 1984. Propagation of small-scale acoustic gravity waves in the Venus atmosphere. J. Atmos. Sci. 41, 1202–1213.

Swenson, G.R., Taylor, M.J., Espy, P.J., Gardner, C.S., Tao, X., 1995. ALOHA-93 measurements of intrinsic gravity wave characteristics using the airborne airglow imager and ground-based Na wind/temperature lidar. Geophys. Res. Lett. 22, 2841–2844.

Taylor, M.J., Ryan, E.H., Tuan, T.F., Edwards, R., 1993. Evidence of Preferential Directions for Gravity Wave Propagation due to Wind Filtering in the Middle Atmosphere. J. Geophys. Res. 98, 6047–6057.

Taylor, M.J., Gu, Y.Y., Tao, X., Gardner, C.S., Bishop, M.B., 1995a. An investigation of intrinsic gravity wave signatures using coordinated lidar and nightglow measurements. Geophys. Res. Lett. 22, 2853–2856.

Taylor, M.J., Bishop, M.B., Taylor, V., 1995b. All-sky measurements of short period waves imaged in the OH (557.7 nm), Na (589.2 nm) and near infrared OH and O2(0,1) nightglow emissions during the ALOHA-93 campaign. Geophys. Res. Lett. 22, 2833–2836.

Vincent, R.A., Fritts, D.C., 1987. A climatology of gravity wave motions in the mesopause region at Adelaide, Australia. J. Atmos. Sci. 44, 748–760.

von Zahn, U., Höffner, J., Eska, V., Alpers, M., 1996. The Mesopause altitude: Only two distinct levels worldwide? Geophys. Res. Lett. 23, 3231–3234.

Wang, D.Y., Tuan, T.F., 1988. Brunt–Doppler ducting of small-period gravity waves. J. Geophys. Res. 93, 9916–9926.

Wu, Q., Killeen, T.L., 1996. Seasonal dependences of mesospheric gravity waves (<100 km) at Peach Mountain Observatory, Michigan. Geophys. Res. Lett. 23, 2211–2214.

References

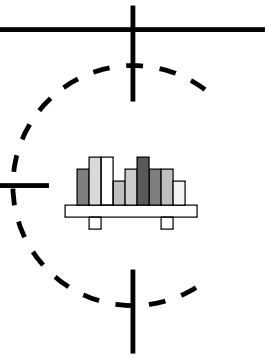

Andrews, D. G., Holton, J. R. & Leovy, C. B. (1987), *Middle atmosphere dynamics*, Academic Press, Orlando, Florida.

Angelats i Coll, M. & Forbes, J. M. (1998), 'Dynamical influences on atomic oxygen 5577Å emission rates in the lower thermosphere', *Geophysical Research Letters* **25**(4), 461–464.

Armstrong, E. B. (1982), 'The association of visible airglow features with a gravity wave', *Journal of Atmospheric and Terrestrial Physics* **44**(4), 325–336.

Barker, D. J. & Waddoups, R. O. (1967), 'Rocket measurements of midlatitude night airglow emissions', *Journal of Geophysical Research* **72**, 4881.

Barth, C. A. & Carter, D. A. (1961), 'The 5577A airglow emission mechanism', *Journal of Geophysical Research* **66**, 985.

Bates, D. R. (1981), 'The green light of the night sky', *Planetary and Space Science* **29**(10), 1061–1067.

Bates, D. R. & Moiseiwitsch, B. L. (1956), 'Origin of the Meinel hydroxyl system in the night airglow', *Journal of Atmospheric and Terrestrial Physics* **5**, 132.

Bates, D. R. & Nicolet, M. (1950), 'The photochemistry of atmospheric water vapour', *Journal of Geophysical Research* **55**, 301.

Beard, A. G., Mitchell, N. J., Williams, P. J. S. & Kunitake, M. (1999), 'Non-linear interactions between tides and planetary waves resulting in periodic tidal variability', *Journal of Atmospheric and Solar-Terrestrial Physics* **61**, 363–376.

Bender, C. M. & Orszag, S. A. (1978), *Advanced mathematical methods for scientists and engineers*, McGraw-Hill, New York.

Bevington, P. R. (1969), *Data Reduction and Error Analysis for the Physical Sciences*, McGraw-Hill Book Company.

Booker, H. G. (1956), 'Turbulence in the ionosphere with applications to meteor trails, radio star scintillation, auroral radar echos, and other phenomena', *Journal of Geophysical Research* **61**, 673–705.

Briggs, B. H. (1984), The analysis of spaced sensor records by correlation techniques, *in* 'Handbook for the Middle Atmosphere Program', Vol. 13, Special Committee for Solar-Terrestrial Physics Secretariat, pp. 166–186.

Briggs, B. H., Elford, W. G., Felgate, D. G., Golley, M. G., Rossiter, D. E. & Smith, J. W. (1969), 'Buckland Park aerial array', *Nature* **223**, 1321–1325.

Briggs, B. H., Phillips, G. J. & Shinn, D. H. (1950), 'The analysis of observations on spaced receivers of the fading of radio signals', *Proc. Phys. Soc. (London)* **B63**, 106.

Brinksma, E. J., Meijer, Y. J., McDermid, I. S., Cageao, R. P., Bergwerff, J. B., Swart, D. P. J., Ubachs, W., Matthews, W. A., Hogervorst, W. & Hovenier, J. W. (1998), 'First lidar observations of mesospheric hydroxyl', *Geophysical Research Letters* **25**(1), 51–54.

Bristow, W. A., Greenwald, R. A. & Villain, J. P. (1996), 'On the seasonal dependence of medium-scale atmospheric gravity waves in the upper atmosphere at high latitudes', *Journal of Geophysical Research* **101**(A7), 15685–15699.

Broadfoot, A. L. & Kendall, K. R. (1968), 'The airglow spectrum, 3100–10000Å', *Journal of Geophysical Research* **73**(1), 426–428.

Chakrabarti, S. (1998), 'Ground based spectroscopic studies of sunlit airglow and aurora', *Journal of Atmospheric and Solar-Terrestrial Physics* **60**, 1403–1423.

Chamberlain, J. W. (1961), *Physics of the Aurora and Airglow*, Academic Press, New York and London.

Chapman, S. (1931), 'Some phenomena of the upper atmosphere', *Proc. Roy. Soc. Lond. A* **132**, 353.

Chapman, S. (1967), History of aurora and airglow, *in* 'Aurora and Airglow: Proceedings of the NATO Advanced Study Institute, August 15–26, 1966', University of Keele, Straffordshire, England, pp. 15–26.

Chui, C. K. (1992), *An introduction to wavelets*, Academic Press, Inc., San Diego, California.

Clay, R. W., Wild, N. R., Bird, D. J., Dawson, B. R., Johnston, M., Patrick, R. & Sewell, A. (1998), 'A cloud monitoring system for remote sites', *Publications of the Astronomical Society of Australia* **15**(3), 332–335.

Connor, L. N. & Avery, S. K. (1996), 'A three-year gravity wave climatology of the mesosphere and lower thermosphere over Kauai', *Journal of Geophysical Research* **101**(D2), 4065–4077.

Daubechies, I. (1988), 'Orthonormal bases of compactly supported wavelets', *Communications on Pure and Applied Mathematics* **41**, 909–996.

de Deuge, M. A. (1990), Optical observations of gravity waves in the high-latitude thermosphere, Master's thesis, University of Adelaide, Adel., Australia.

de Deuge, M. A., Greet, P. A. & Jacka, F. (1994), 'Optical observations of gravity waves in the auroral zone', *Journal of Atmospheric and Terrestrial Physics* **56**(5), 617–629.

Dewan, E. M. & Ricard, R. H. (1998), 'Mesospheric bores', *Journal of Geophysical Research* **103**(D6), 6295–6305.

Downey, E. C. (1992), 'Xephem 3.2.2, ephemeris software for UNIX and Linux', Web site http://www.clearskyinstitute.com/xephem/xephem.html.

Evans, W. F. J. & Shepherd, G. G. (1996), 'A new airglow layer in the stratosphere', *Geophysical Research Letters* **23**(24), 3623–3626.

Fagundes, P. R., Takahashi, H., Sahai, Y. & Gobbi, D. (1995), 'Observations of gravity waves from multispectral mesospheric nightglow emissions observed at 23°S', *Journal of Atmospheric and Terrestrial Physics* **57**(4), 395–405.

Frederick, J. E. (1979), 'Influence of gravity wave activity on lower thermospheric photochemistry and composition', *Planetary and Space Science* **27**(12), 1469–1477.

Freund, J. T. & Jacka, F. (1979), 'Structure in the λ557.7nm [OI] airglow', *Journal of Atmospheric and Terrestrial Physics* **41**(1), 25–31.

Frey, H. U., Mende, S. B., Arens, J. F., McCullough, P. R. & Swenson, G. R. (2000), 'Atmospheric gravity wave signatures in the infrared hydroxyl OH airglow', *Geophysical Research Letters* **27**(1), 41–44.

Friend, A. W. (1949), 'Theory and practice of tropospheric sounding by radar', *Proceedings of the I.R.E.* **February**, 116–138.

Frigo, M. & Johnson, S. G. (1997), The fastest Fourier transform in the west, Technical Report MIT-LCS-TR-728, Massachusetts Institute of Technology, 77 Massachusetts Ave, 12-104, Cambridge, Massachusetts, U.S.A.

Frigo, M. & Johnson, S. G. (1998), FFTW: An adaptive software architecture for the FFT, *in* '1998 ICASSP conference proceedings', Vol. 3, p. 1381.

Fritts, D. C. (1984), 'Gravity wave saturation in the middle atmosphere: A review of theory and observations', *Reviews of geophysics and space physics* **22**, 275–308.

Fritts, D. C. (2000), 'Errant inferences of gravity wave momentum and heat fluxes using airglow and lidar instrumentation: corrections and cautions', *Journal of Geophysical Research* **105**(D17), 22355–22360.

Fritts, D. C., Isler, J. R., Thomas, G. & Andreassen, Ø. (1993), 'Wave breaking signatures in noctilucent clouds', *Geophysical Research Letters* **20**, 2039–2042.

Gardner, C. G., Coble, M., Papen, G. C. & Swenson, G. R. (1996), 'Observations of the unambiguous 2-dimensional horizontal wave number spectrum of OH intensity perturbations', *Geophysical Research Letters* **23**(25), 3739–3742.

Gardner, C. S. (1991), 'Introduction to ALOHA-90: the airborne lidar and observations of the Hawaiian airglow campaign', *Geophysical Research Letters* **18**(7), 1313–1316.

Gardner, C. S. (1998), 'Theoretical models for gravity wave horizontal wave number spectra: effects of wave field anisotropies', *Journal of Geophysical Research* **103**(D3), 6417–6425.

Gardner, C. S., Gulati, K., Zhao, Y. & Swenson, G. (1999), 'Measuring gravity wave momentum fluxes with airglow imagers', *Journal of Geophysical Research* **104**(D10), 11903–11915.

Gardner, C. S. & Taylor, M. J. (1998), 'Observational limits for lidar, radar and airglow imager measurements of gravity wave paramters', *Journal of Geophysical Research* **103**(D6), 6427–6437.

Gardner, F. F. & Pawsey, J. L. (1953), 'Study of the ionosphere D-region using partial reflections', *Journal of Atmospheric and Terrestrial Physics* **3**, 321–344.

Gavrilov, N., Fukao, S. & Nakamura, T. (2000), 'Average statistical characteristics of long gravity waves observed with the middle and upper atmosphere radar in the mesosphere', *Journal of Geophysical Research* **105**(D7), 9365–9379.

Gavrilov, N., Karmov, K. A., Mordvintsev, M. Y. & Semenov, V. K. (1978), 'Coherence of wave variations of O lambda 5577Å airglow and wind speed in the meteor zone', *Geomagnetism and Aeronomy* **18**, 248.

Gavrilov, N. & Shved, G. M. (1982), 'Study of internal gravity waves in the lower thermosphere from observations of the nocturnal sky Airglow [OI] 5577Å in Ashkhabad', *Annales Géophysique* **38**, 789.

Giers, D. H., Sahai, Y., Cogger, L. L. & Ryan, E. H. (1997), 'Occurrence characteristics of mesospheric gravity waves at 51°N', *Journal of Atmospheric and Solar-Terrestrial Physics* **59**(10), 1197–1203.

Gregory, J. B. (1956), 'Ionospheric reflections from heights below the E-region', *Australian Journal of Physics* **9**, 324–342.

Gulledge, I. S., Packer, D. M., Tillford, S. G. & Vanderslice, J. T. (1968), 'Intensity profile of the 6300Å and 5577Å OI lines in the night airglow', *Journal of Geophysical Research* **73**(17), 5535.

Hall, G. E., Meek, C. E. & Manson, A. H. (1995), 'Hodograph analysis of mesopause region winds observed by three MF radars in the Canadian Prairies', *Journal of Geophysical Research* **100**(D4), 7411–7421.

Hecht, J. H., Kane, T. J., Walterscheid, R. L., Gardner, C. S. & Tepley, C. A. (1993), 'Simultaneous nightglow and Na lidar observations at Arecibo during the AIDA-89 campaign', *Journal of Atmospheric and Terrestrial Physics* **55**, 409–423.

Hecht, J. H. & Walterscheid, R. L. (1991), 'Observations of the OH Meinel (6,2) and O_2 atmospheric (0,1) nightglow emissions from Maui during the ALOHA-90 campaign', *Geophysical Research Letters* **18**(7), 1341–1344.

Hecht, J. H., Walterscheid, R. L. & Ross, M. N. (1994), 'First measurements of two-dimensional horizontal wave number spectrum from CCD images of nightglow', *Journal of Geophysical Research* **99**(11), 11499–11460.

Hecht, J. H., Walterscheid, R. L., Woithe, J., Campbell, L., Vincent, R. A. & Reid, I. M. (1997), 'Trends of airglow imager obervations near Adelaide, Australia', *Geophysical Research Letters* **24**, 587–590.

Hecht, J. H., Walterscheild, R. L., Fritts, J. R., Isler, J. R., Senft, D. C., Gardner, C. S. & Franke, S. F. (1995), 'Wave breaking signatures in OH airglow and sodium densities and temperatures', *Journal of Geophysical Research* **102**(D6), 6655–6668.

Herzburg, G. (1950), *Molecular spectra and molecular structure*, Litton Educational Publishing, Inc.

Hickey, M. P., Taylor, M. J., Gardner, C. S. & Gibbons, C. R. (1998), 'Full-wave modeling of small-scale gravity waves using airborne lidar and observations of the Hawaiian airglow (ALOHA-93) O($1S$) images and coincident Na wind/temperature lidar measurements', *Journal of Geophysical Research* **103**(D6), 6439–6453.

Hickey, M. P., Walterscheid, R. L., Taylor, M. J., Ward, W., Schubert, G., Zhou, Q., Garcia, F., Kelly, M. C. & Shepherd, G. G. (1997), 'Numerical simulations of gravity waves imaged over Arecibo during the 10-day January 1993 campaign', *Journal of Geophysical Research* **102**(A6), 11475–11489.

Hines, C. O. (1960), 'Internal atmospheric gravity waves at ionospheric heights', *Canadian Journal of Physics* **38**, 1441–1481.

Hines, C. O. (1974), The upper atmosphere in motion, *in* 'The upper atmosphere in motion', American Geophysical Union, Washington, D.C., pp. 13–93.

Hines, C. O. (1993), 'Preface to Arecibo initiative in dynamics of the atmosphere, AIDA ACT '89', *Journal of Atmospheric and Terrestrial Physics* **55**(3), 197–199.

Hocke, K. (1998), 'Phase estimation with the Lomb-Scargle periodogram method', *Annales Géophysicae* **16**, 356–358.

Holdsworth, D. A. (1995), Signal analysis with applications to atmospheric radars, PhD thesis, University of Adelaide, Adel., Australia.

Holton, J. R. (1982), 'The role of gravity wave induced drag and diffusion in the momentum budget of the atmosphere', *Journal of the Atmospheric Sciences* **39**, 791–799.

Holton, J. R. (1983), 'The influence of gravity wave breaking on the general circulation of the middle atmosphere', *Journal of the Atmospheric Sciences* **40**, 2497–2507.

Horne, J. H. & Baliunas, S. L. (1986), 'A prescription for period analysis of unevenly spaced time series', *The Astrophysical Journal* **302**, 757–763.

Isler, J. R. & Fritts, D. C. (1996), 'Gravity wave variability and interaction with lower-frequency motions in the mesosphere and lower thermosphere over Hawaii', *Journal of the Atmospheric Sciences* **53**(1), 37–47.

Jacob, P. G. (1985), Manifestations of Atmospheric Gravity Waves in the Airglow at 95km, PhD thesis, University of Adelaide, Adel., Australia.

Jenkins, G. M. & Watts, D. G. (1968), *Spectral analysis and its applications*, Holden Day, San Fransisco.

Julian, P. R. (1974), 'Comments on the determination of significance levels of the coherence statistic', *Journal of the Atmospheric Sciences* **32**, 836–837.

Khattatov, B. V., Geller, M. A., Yudin, V. A., Hays, P. B., Skinner, W. R., Burrage, M. D., Franke, S. J., Fritts, D. C., Isler, J. R., Manson, A. H., Meek, C. E., McMurry, R., Singer, W., Hoffmann, P. & Vincent, R. A. (1996), 'Dynamics of the mesosphere and lower thermosphere as seen by MF radars and by the high-resolution Doppler imager/UARS', *Journal of Geophysical Research* **101**(D6), 10393–10404.

Krassovsky, V. I. (1971), 'The hydroxyl emission problem and paths of its solution', *Annales Géophysicae* **27**, 211.

Krassovsky, V. I. (1972), 'Infrasonic variations of the OH emission in the upper atmosphere', *Annales Géophysicae* **28**, 739.

Krassovsky, V. I., Potopov, B. P., Semenov, A. I., Shagaev, M. V., Shefov, N. N., Sobolev, V. G. & Toroshelidze, T. I. (1977), 'Internal gravity waves near the mesopause and the hydroxyl emission', *Annales Géophysicae* **33**(3), 347–356.

Kudeki, E. & Franke, S. J. (1998), 'Statistics of momentum flux estimation', *Journal of Atmospheric and Solar-Terrestrial Physics* **60**, 1549–1553.

Liang, J., Wan, W. & Yuan, H. (1998), 'Ducting of acoustic-gravity waves in a non-isothermal atmosphere around a spherical globe', *Journal of Geophysical Research* **103**(D10), 11229–11234.

Lomb, N. R. (1976), 'Least-squares frequency analysis of unequally spaced data', *Astrophysics and Space Science* **39**, 447–462.

Mallat, S. G. (1989), 'A theory for multiresolution signal decomposition: the wavelet representation', *IEEE Transactions on Pattern Analysis and Machine Intelligence* **11**, 674.

Manson, A. H., Meek, C. E., Flemming, E., Chandra, S., Vincent, R. A., Philips, A., Avery, S., Fraser, G. J., Smith, M. J., Fellous, J. L. & Massebeuf, M. (1991), 'Comparisons between satellite-derived gradient winds and radar-derived winds from the CIRA-86', *Journal of the Atmospheric Sciences* **48**, 441–428.

Manson, A. H., Meek, C. E. & Zhan, Q. (1997), 'Gravity wave spectra and directions statistics for the mesosphere as observed by MF radars in the Canadian Prairies (49°N–52°N) and at Tromsø (69°N)', *Journal of Atmospheric and Solar-Terrestrial Physics* **99**(9), 993–1009.

Marsh, D. R. & Skinner, W. R. (1999), 'Tidal influences on O_2 atmospheric band dayglow: HRDI observations vs. model simulations', *Geophysical Research Letters* **26**(10), 1369–1372.

McDade, I. C., Murtagh, D. P., Greer, R. G. H., Dickinson, P. H., Witt, G., Stegman, J., Llewellyn, E. J., Thomas, L. & Jenkins, D. B. (1986), 'Eton 2: Quenching parameters for the proposed percursors of $O_2(b^1\Sigma_g^+)$ and $O(^1S)$ in the terrestrial nightglow', *Planetary and Space Science* **34**, 789.

Meek, C. E., Reid, I. M. & Manson, A. H. (1985), 'Observations of mesospheric wind velocities 1: Gravity wave horizontal scales and phase velocities determined from spaced antenna wind observations', *Radio Science* **20**(6), 1363–1382.

Meinel, A. B. (1950), 'OH emission in the spectrum of the night sky', *The Astrophysical Journal* **111**, 555.

Melo, S. M. L., Lowe, R. P. & Takahashi, H. (1999), 'The nocturnal behavior of the hydroxyl airglow at the equatorial and low latitudes as observed by WINDII: comparison with ground-based measurements', *Journal of Geophysical Research* **104**(A11), 24657–24665.

Melo, S. M. L., Takahashi, H., Clemesha, B. R. & Simonich, D. M. (1997), 'An experimental study of the nightglow OH(8-3) band emission process in the equatorial mesosphere', *Journal of Atmospheric and Solar-Terrestrial Physics* **59**(5), 479–486.

Merriwether, J. W. (1975), 'High latitude airglow observations of correlated short term fluctuations in the hydroxyl Meinel 8-3 band intensity and rotational temperature', *Planetary and Space Science* **23**, 1211–1221.

Monserrat, S. & Thorpe, A. J. (1996), 'Use of ducting theory in an observed case of gravity waves', *Journal of the Atmospheric Sciences* **53**(12), 1724–1736.

Moreels, G. & Herse, H. (1977), 'Photographic evidence of waves around the 85 km level', *Planetary and Space Science* **25**(3), 265–273.

Mulligan, F. J., Horgan, D. F., Galligan, J. G. & Griffin, E. M. (1995), 'Mesopause temperatures and integrated band brightnesses calculated from airglow OH emissions recorded at Maynooth (53.2°N, 6.4°W) during 1993', *Journal of Atmospheric and Terrestrial Physics* **57**(13), 1623–1637.

Myrabø, H. K., Deehr, C. S. & Sivjee, G. G. (1983), 'Large-amplitude nightglow OH (8-3) band intensity and rotational temperature variations during a 24-hour period at 78°N', *Journal of Geophysical Research* **88**(A11), 9255–9259.

Nakamura, T., Tsuda, T. & Fukao, S. (1996a), 'Mean winds at 60–90km observed with the MU radar (35°N)', *Journal of Atmospheric and Terrestrial Physics* **58**(6), 655–660.

Nakamura, T., Tsuda, T., Fukao, S., Manson, A. H., Meek, C. E., Vincent, R. A. & Reid, I. M. (1996b), 'Mesospheric gravity waves at Saskatoon (52°N), Kyoto (35°N) and Adelaide (35°S)', *Journal of Geophysical Research* **101**(D3), 7005–7012.

Namboothiri, S. P., Tsuda, T. & Nakamura, T. (1999), 'Interannual variablility of mesospheric mean winds observed with the MU radar', *Journal of Atmospheric and Solar-Terrestrial Physics* **61**, 1111–1122.

O'Brien, B. J. (1967), Satellite observations of particle fluxes and atmospheric emissions, part II, *in* 'Aurora and Airglow: Proceedings of the NATO Advanced Study Institute, August 15–26, 1966', University of Keele, Straffordshire, England, pp. 634–642.

Offermann, D. & Drescher, A. (1973), 'Atomic oxygen densities in the lower thermosphere from in situ 5577Å night airglow and mass spectrometer measurements', *Journal of Geophysical Research* **78**(28), 6690.

Pancheva, D. & Mukhtarov, P. (2000), 'Wavelet analysis on transient behaviour of tital amplitude fluctuations observed by meteor radar in the lower thermosphere above Bulgaria', *Annales Géophysicae* **18**, 316–331.

Pawsey, J. L. (1935), 'Further investigations of the amplitude variations of downcoming wireless waves', *Proc. Cambridge Phil. Soc.* **31**, 125.

Plagmann, M., Marsh, S. H., Baggaley, W. J., Bennett, R. G. T., Deutsch, K. A., Fraser, G. J., Hernandez, G., Lawrence, B. N., Plank, G. E. & Smith, R. W. (1998), 'Annual variation of airglow heights derived from wind measurements', *Journal of Geophysical Research* **25**(24), 4457–4460.

Press, W. H., Flannery, B. P., Teukolsky, S. A. & Vetterling, W. T. (1986), *Numerical Recipes*, Cambridge University Press.

Press, W. H. & Rybicki, G. B. (1989), 'Fast algorithm for spectral analysis of unevenly sampled data', *The Astrophysical Journal* **338**, 277–280.

Qian, J., Gu, Y. Y., Papen, G. C. & Gardner, C. S. (1995), 'Horizontal wave number spectra of density and temperature perturbations in the mesosphere measured during the 4 August flight of ANCL-93', *Geophysical Research Letters* **22**(20), 2865–2868.

Ralph, F. M. (1997), 'Comments on "use of ducting theory in an observed case of gravity waves"', *Journal of the Atmospheric Sciences* **54**, 2237–2239.

Rau, M. N. M., Murty, G. S. N. & Jain, V. C. (1982), 'Altitude of peak emission of (OI) 5577Å in the lower thermosphere: Chapman versus Barth mechanisms', *Journal of Atmospheric and Terrestrial Physics* **44**(7), 559–566.

Rayleigh (1924), 'The light of the night sky: its intensity variations when analyzed by color filters', *Proc. Roy. Soc. Lond. A* **106**, 117–137.

Rayleigh (1935), 'The light of the night sky: Analysis of the intensity variations at three stations', *Proc. Roy. Soc. Lond. A* **151**, 22–55.

Rayner, J. N. (1971), *An introduction to spectral analysis*, Pion Limited, London.

Reid, I. M. (1984), Radar studies of atmospheric gravity waves, PhD thesis, University of Adelaide, Adel., Australia.

Reid, I. M. (1986), 'Gravity wave motions in the upper middle atmosphere (60–110km)', *Journal of Atmospheric and Terrestrial Physics* **48**(11–12), 1057–1072.

Reid, I. M., Vandepeer, B. G. W., Dillon, S. J. & Fuller, B. M. (1995), 'The New Adelaide MF Doppler Radar', *Radio Science* **30**(4), 1177–1189.

Reid, I. M. & Vincent, R. A. (1987a), 'Measurements of mesospheric gravity wave momentum fluxes and mean flow accelerations at Adelaide, Australia', *Journal of Atmospheric and Terrestrial Physics* **49**(5), 443–460.

Reid, I. M. & Vincent, R. A. (1987b), 'Measurements of horizontal scales and phase velocities of short period mesospheric gravity waves at Adelaide, Australia', *Journal of Atmospheric and Terrestrial Physics* **49**(10), 1033–1048.

Rogers, J. W., Murphy, R. E., Stair Jr, A. T., Ulwick, J. C., Baker, K. D. & Jensen, L. L. (1973), 'Rocket-borne radiometric measurements of OH in the auroral zone', *Journal of Geophysical Research* **78**, 7023.

Scargle, J. D. (1982), 'Studies in astronomical time series analysis. II. Statistical aspects of spectral analysis of unevenly spaced data', *The Astrophysical Journal* **263**, 835–853.

Scargle, J. D. (1989), 'Studies in atronomical time series analysis. III. Fourier transforms, autocorrelation functions and cross-correlation functions of unevenly spaced data', *The Astrophysical Journal* **343**, 874–887.

She, C. Y. & Lowe, R. P. (1998), 'Seasonal temperature variations in the mesopause region at mid-latitude: comparison of lidar and hydroxyl rotational temperatures using WINDII/UARS OH height profiles', *Journal of Atmospheric and Solar-Terrestrial Physics* **60**, 1573–1583.

Shepherd, G. G., Roble, R. G., McLandress, C. & Ward, W. E. (1997), 'WINDII observations of the 558nm emission in the lower thermosphere: the influence of dynamics on composition', *Journal of Atmospheric and Solar-Terrestrial Physics* **59**(6), 655–667.

Shepherd, G. G., Stegman, J., Espy, P., McLandress, C., Thuillier, G. & Wiens, R. H. (1999), 'Springtime transition in lower thermospheric atomic oxygen', *Journal of Geophysical Research* **104**(A1), 213–223.

Shimomai, T., Yamanaka, M. D. & Fukao, S. (1996), 'Application of wavelet analysis to wind disturbances observed with mst radar techniques', *Journal of Atmospheric and Terrestrial Physics* **58**, 683.

Smith, A. K. (1996), 'Longitudinal variations in mesospheric winds: evidence for gravity wave filtering by planetary waves', *Journal of the Atmospheric Sciences* **53**(8), 1156–1173.

Sridharan, R., Taori, A., Gurubaran, S., Rajaram, R. & Shepherd, M. G. (1999), 'First results on daytime mesopause OH rotational temperatures using ground-based photometry from equatorial latitudes', *Journal of Atmospheric and Solar-Terrestrial Physics* **61**, 1131–1142.

Swenson, G. R., Alexander, M. J. & Haque, R. (2000), 'Dispersion imposed limits on atmospheric gravity waves in the mesosphere: observations from OH airglow', *Geophysical Research Letters* **27**(6), 875–878.

Swenson, G. R. & Gardner, G. S. (1998), 'Analytical models for the responses of the mesospheric OH* and Na layers to atmospheric gravity waves', *Journal of Geophysical Research* **103**(D6), 6271–6294.

Swenson, G. R., Haque, R., Yang, W. & Gardner, C. S. (1999), 'Momentum and energy fluxes of monochromatic gravity waves observed by an OH imager at Starfire Optical Range, New Mexico', *Journal of Geophysical Research* **104**(D6), 6067–6080.

Swenson, G. R. & Liu, A. Z. (1998), 'A model for calculating acoustic gravity wave energy and momentum flux in the mesosphere from OH airglow', *Geophysical Research Letters* **25**(4), 477–480.

Swenson, G. R., Taylor, M. J., Espy, P. J., Gardner, C. & Tac, X. (1995), 'ALOHA-93 measurements of intrinsic AGW characteristics using airborne airglow imager and groundbased Na Wind/Temperature lidar', *Geophysical Research Letters* **22**(20), 2841–2844.

Takahashi, H. & Batista, P. P. (1981), 'Simultaneous measurements of OH(9,4), (8,3), (7,2), (6,2) and (5,1) bands in the airglow', *Journal of Geophysical Research* **86**(A4), 5632–5642.

Takahashi, H., Batista, P. P., Buriti, R. A., Gobbi, D., Nakamura, T., Tsuda, T. & Fukao, S. (1998), 'Simultaneous measurements of airglow OH emission and meteor wind by a scanning photometer and the MU radar', *Journal of Atmospheric and Solar-Terrestrial Physics* **60**, 1649–1668.

Takahashi, H., Clemesha, B. R. & Batista, P. P. (1995), 'Predominant semi-annual oscillation of the upper mesospheric airglow intensities and temperatures in the equatorial region', *Journal of Atmospheric and Terrestrial Physics* **57**(4), 407–414.

Takahashi, H., Melo, S. M. L., Clemesha, B. R. & Simonich, D. M. (1996), 'Atomic hydrogen and ozone concentrations derived from simultaneous lidar and rocket airglow measurements in the equatorial region', *Journal of Geophysical Research* **101**(D2), 4033–4040.

Taylor, M. J. & Bishop, M. B. (1995), 'All-sky measurements of short period waves imaged in the OI(557.7nm), Na(589.2nm) and near infrared OI and O_2(0,1) nightglow emissions during the ALOHA-93 campaign', *Geophysical Research Letters* **22**(20), 2833–2836.

Taylor, M. J., Fritts, D. C. & Isler, J. R. (1995), 'Determination of horizontal and vertical structure of an unusal pattern of short period gravity waves imaged during ALOHA-93', *Geophysical Research Letters* **22**(20), 2837–2840.

Taylor, M. J., Hapgood, M. A. & Rothwell, P. (1987), 'Observations of gravity wave propagation in the OI (557.7nm), Na (588.2nm) and near infra-red OH nightglow emissions', *Planetary and Space Science* **35**, 413.

Taylor, M. J., Ryan, E. H., Tuan, T. F. & Edwards, R. (1993), 'Evidence of preferential directions for gravity wave propagation due to wind filtering in the middle atmosphere', *Journal of Geophysical Research* **98**, 6047.

Taylor, M. J., Swenson, G. R. & Taylor, V. (1995b), 'Height measurements of OI(557.7nm) gravity wave structure over the Hawaiian Islands during ALOHA-93', *Geophysical Research Letters* **22**(20), 2881–2884.

Thayaparan, T., Hocking, W. K. & MacDougall, J. (1995), 'Observational evidence of tidal/gravity wave interactions using the UWO 2MHz radar', *Geophysical Research Letters* **22**(4), 373–376.

Thomas, R. J. & Young, R. A. (1981), 'Measurement of atomic oxygen and related airglows in the lower thermosphere', *Journal of Geophysical Research* **86**(C8), 7389–7393.

Tohmatsu, T. & Nagata, T. (1963), 'Dynamical studies of the oxygen green line in the airglow', *Planetary and Space Science* **10**, 103–116.

Torrence, C. & Compo, G. P. (1998), 'A practical guide to wavelet analysis', *Bulletin of the American Meteorological Society* **79**(1), 61–78.

Tridgell, A. et al. (1992-2000), 'Samba, Linux SMB/CIFS client/server software', Web site http://www.samba.org/.

Tsuda, T., Murayama, Y., Yamamoto, M., Kato, S. & Fukao, S. (1990), 'Seasonal variation of momentum flux in the mesosphere observed with the MU radar', *Geophysical Research Letters* **17**(6), 725–728.

Tsutsumi, M. (1995), A study of atmospheric dynamics near the mesopause using radio meteor echos, PhD thesis, Radio Atmospheric Science Centre, Kyōtō University.

Vandepeer, B. G. W. (1993), A new Doppler radar for upper atmospheric research, PhD thesis, University of Adelaide, Adel., Australia.

Veronis, G., Pasko, V. P. & Inan, U. (1999), 'Characteristics of mesospheric optical emissions produced by lightning discharges', *Journal of Geophysical Research* **104**(A6), 12645–12656.

Vincent, R. A. (1972), 'Ionospheric irregularities in the E-region', *Journal of Atmospheric and Terrestrial Physics* **34**, 1881–1898.

Vincent, R. A. (1984), 'Gravity-wave motions in the mesosphere', *Journal of Atmospheric and Terrestrial Physics* **46**(2), 119–128.

Vincent, R. A. & Reid, I. M. (1983), 'HF Doppler measurements of mesospheric gravity wave momentum fluxes', *Journal of the Atmospheric Sciences* **40**, 1321–1333.

von Zahn, U. & Höffner, J. (1996), 'Mesopause temperature profiling by potassium lidar', *Geophysical Research Letters* **23**(2), 141–144.

Walterscheid, R. L., Hecht, J. H., Vincent, R. A., Reid, I. M., Woithe, J. & Hickey, M. P. (1999), 'Analysis and interpretation of airglow and radar observations of quasi-monochromatic gravity waves in the upper mesosphere and lower thermosphere over Adelaide, Australia (35°S, 138°E)', *Journal of Atmospheric and Solar-Terrestrial Physics* **61**, 461–478.

Ward, W. E. (1999), 'A simple model of diurnal variations of the mesospheric oxygen nightglow', *Geophysical Research Letters* **26**(23), 3565–3568.

Ward, W. E., Solheim, B. H. & Shepherd, G. G. (1997), 'Two day wave induced variations in the oxygen green line volume emission rate: WINDII observations', *Geophysical Research Letters* **24**(9), 1127–1130.

Weinstock, J. (1978), 'Theory of the interaction of gravity waves with $O_2(^1\Sigma)$ airglow', *Journal of Geophysical Research* **83**, 5175.

Wiens, R. H., Wang, D. Y., Paterson, R. N. & Shepherd, G. G. (1997), 'Statistics of gravity waves seen in O_2 nightglow over Bear Lake observatory', *Journal of Geophysical Research* **102**(A4), 7319–7329.

Woithe, J. M. (1995), 'Optical observations of the upper atmosphere', Honours Thesis, University of Adelaide, Adel., Australia.

Wu, Q. & Killeen, T. L. (1996), 'Seasonal dependance of mesospheric gravity waves (<100km) at Peach Mountain Observatory, Michigan', *Geophysical Research Letters* **23**(17), 2211–2214.

Yeh, K. C. & Liu, C. H. (1981), 'The instability of atmospheric gravity waves through wave-wave interactions', *Journal of Geophysical Research* **86**, 9722–9728.

Zaragoza, G., López-Puertas, M., López-Valverde, M. Á. & Taylor, F. W. (1998), 'The detection of the hydroxyl nightglow layer in the mesosphere by ISAMS/UARS', *Geophysical Research Letters* **25**(13), 2417–2420.

Zhang, S. P., Peterson, R. N., Weins, R. H. & Shepherd, G. G. (1993), 'Gravity waves from O_2 nightglow during the AIDA '89 I: emission rate/temperature observations', *Journal of Atmospheric and Terrestrial Physics* **55**, 355–375.

Zhang, S. P., Wiens, R. H., Solheim, B. H. & Shepherd, G. G. (1998), 'Nightglow zenith emission rate variations in $O(^1S)$ at low latitudes from wind imaging interferometer (WINDII) observations', *Journal of Geophysical Research* **103**(D6), 6251–6259.